Nano/Micro-Assisted Regenerative Medicine

Edited by
Soo-Hong Lee

Printed Edition of the Special Issue Published in *IJMS*

MDPI

Nano/Micro-Assisted Regenerative Medicine

Nano/Micro-Assisted Regenerative Medicine

Special Issue Editor

Soo-Hong Lee

Special Issue Editor
Soo-Hong Lee
Dongguk University
Korea

This is a reprint of articles from the Special Issue published online in the open access journal *International Journal of Molecular Sciences* (ISSN 1422-0067) from 2017 to 2018 (available at: http://www.mdpi.com/journal/ijms/special_issues/nano_regenerative_medicine)

For citation purposes, cite each article independently as indicated on the article page online and as indicated below:

LastName, A.A.; LastName, B.B.; LastName, C.C. Article Title. *Journal Name* **Year**, *Article Number*, Page Range.

Contents

About the Special Issue Editor

Soo-Hong Lee is a Professor in the Department of Medical Biotechnology at Dongguk University. He received B.S. (1994), M.S. (1997), and Ph.D. (2002) degrees from the Department of Chemistry at Hanyang University. He was a Postdoctoral Research Associate at the Korea Institute of Science and Technology (KIST) and Rice University. His academic career started at the Department of Biomedical Science at CHA University (Assistant Professor, 2006–2010; Associate Professor, 2010–2014) and then was tenured as a Full Professor in 2015. Recently He has moved to Dongguk University. Dr. Lee's research group investigates biomaterials, tissue engineering, stem cell engineering, and cell therapy. He has published over 100 scientific papers and his papers have been cited over 4500 times (h-index = 31). He holds more than 20 granted or pending patents. He was awarded the Independent Investigator Award from the Korean Society for Biomaterials in 2017, the Contribution Award from the Korean Tissue Engineering and Regenerative Medicine Society in 2017, the Minister Citation from the Ministry of Science in 2014, the Best Research Evaluator from the National Research Foundation in 2013, the Macromolecular Rapid Communication Young Scientist Award in 2010. Moreover, he was recognized as the Best Scientist of CHA University in 2009, as well as counted among the National R&D 100 Best Researches from the Ministry of Education, Science, and Technology in 2008, and the R&D 100 Best Researches from the Korean Research Foundation in 2008. He has served as an associate editor at two journals, "Macromolecular Research", and "Tissue Engineering and Regenerative Medicine", and also as an editorial board member at "Tissue Engineering" over 5 years. He has also severed as an active member at "the Korean Society for Biomaterials" and also "the Korean Tissue Engineering and Regenerative Medicine Society" over 12 years.

Preface to "Nano/Micro-Assisted Regenerative Medicine"

Regenerative medicine is an emerging discipline aimed at repairing and reestablishing the normal functions of tissues and organs damaged by aging, disease, injury, or congenital disorders. Among the advanced technologies currently under investigation, such as cell therapy, tissue and biomaterial engineering, transplantation, nano/micro-technologies, either alone or in combination with specific cells, such as stem cells, have opened the prospect of nano/micro-assisted regenerative medicine, which has the potential to transform regenerative medicine.

Regenerative medicine is constantly evolving from advances in the development of new nano/micro-based materials, such as particles, fibers, composites, and surfaces. This evolution is bolstered by the multi- and inter-disciplinary efforts of scientists in areas such as biotechnology, biomaterials science, chemistry, physics, stem cell biology, developmental biology, and clinical medicine, as well as other areas.

In this book, promising applications of nano/micro-assisted regenerative medicine in tissue engineering or cancer treatment applications are introduced and strategies for the further development of this field are described. We are confident that progress in nano/micro technologies will continue to fertilize the emerging field of nano/micro-assisted regenerative medicine and provide a wide range of new and improved therapies for degenerative diseases. It is our hope that this book will help researchers in the field of nano/micro-assisted regenerative medicine.

Soo-Hong Lee
Special Issue Editor

Editorial

Nano/Micro-Assisted Regenerative Medicine

Bogyu Choi [1] and Soo-Hong Lee [1,2,*]

[1] Department of Biomedical Science, CHA University, 335 Pangyo-ro, Bundang-gu, Seongnam-si 13488, Korea; bgchoi@cha.ac.kr

[2] Department of Medical Biotechnology, Dongguk University 32 Dongguk-ro, Ilsandong-gu, Goyang-si, Gyeonggi-do 10326, Korea

* Correspondence: soohong@dongguk.edu; Tel.: +82-31-961-5153

Regenerative medicine is an emerging discipline aimed at repairing and reestablishing the normal functions of tissues and organs damaged by aging, disease, injury, or congenital disorders. Among the advanced technologies currently under investigation, such as cell therapy, tissue and biomaterial engineering, transplantation, nano/microtechnologies, either alone or in combination with specific cells, such as stem cells, have opened the prospect of nano/micro-assisted regenerative medicine, which has the potential to transform regenerative medicine.

This special issue, entitled "Nano/Micro-Assisted Regenerative Medicine" presents two reviews and 11 research articles highlighting recent advances in the use of nano/micro-assisted technologies in regenerative medicine. Kang et al. describe the application of nano and microengineering techniques for the fabrication of native tissue topographies as an alternative to silicone implants, which are known to cause capsular contractures via adverse immune reactions [1]. Bellinghen et al. report that temporomandibular joint regeneration can be improved by nano/micro-assisted functionalization [2]. Yun et al. show that labeling mesenchymal stem cells (MSCs) with superparamagnetic iron oxide nanoparticles (SPIONs) via magnetic retention enhances the homing efficiency of MSCs in olfactory-injured mice [3]. Jeong et al. describe the therapeutic effects of simvastatin-loaded porous microspheres (SIM/PMSs) on inflamed tenocytes in vitro and collagenase-induced Achilles tendinitis in vivo [4]. A new platform of three-dimensional (3D) graphene/arginine-glycine-aspartic acid (RGD) peptide nanoisland composites to enhance the osteogenesis of human adipose-derived MSCs is proposed by Kang et al. [5]. Lee et al. show that acid-degradable poly(ethylene glycol)-poly(amino ketal) (PEG-PAK)-based micelles can be used to improve stromal cell-derived factor-1α (*SDF-1α*) gene transfection efficacy and angiogenesis of human adipose-derived MSCs for the treatment of ischemic diseases [6]. Kim et al. demonstrate that a reduced graphene oxide-coated biphasic calcium phosphate bone graft material is effective for bone regeneration in rat calvarial defects [7]. Müller et al. demonstrate that amorphous polyphosphate nano/microparticles effectively block the neurotoxic effects of toxic amyloid β-protein fragment 25–35 by rebalancing the β-amyloid-induced decrease in adenosine triphosphate (ATP) levels [8]. Park et al. describe the development of in vitro cancer microtissue arrays on a fibroblast-layered nanofibrous membrane by inkjet printing and their applications to cancer drug screening and gradual 3D cancer studies [9]. Nagai et al. demonstrate that cilostazol ophthalmic nanodispersions have therapeutic effects on retinal disorders caused by diabetes mellitus in streptozotocin-induced diabetic rats [10]. Tatiparti et al. report the development of the carbonic anhydrase-IX selective nanocarrier, human serum albumin-paclitaxel-acetazolamide (HSA-PTX-ATZ), by copper-free 'click' chemistry-based synthesis for tumor hypoxia-targeted drug delivery that can be adapted to several types of cancers [11]. The cytotoxicity of peptide liposome incorporated citron-extract nanoparticles and turmeric extract incorporated oil-in-water nanoemulsions on various cell types is evaluated by Zhang et al. [12] and Yoon et al. [13], respectively.

Regenerative medicine is constantly evolving from advances in the development of new nano/micro-based materials, such as particles, fibers, composites, and surfaces. This evolution

is bolstered by the multidisciplinary and interdisciplinary efforts of scientists in areas such as biotechnology, biomaterials science, chemistry, physics, stem cell biology, developmental biology, and clinical medicine, as well as other areas. In this special issue, promising applications of nano/micro-assisted regenerative medicine in tissue engineering or cancer treatment are introduced, and strategies for the further development of this field are described. We are confident that progress in nano/microtechnologies will continue to fertilize the emerging field of nano/micro-assisted regenerative medicine and provide a wide range of new and improved therapies for the degenerative disease.

Conflicts of Interest: The authors declare no conflict of interest.

References

1. Kang, S.H.; Sutthiwanjampa, C.; Heo, C.Y.; Kim, W.S.; Lee, S.H.; Park, H. Current Approaches Including Novel Nano/Microtechniques to Reduce Silicone Implant-Induced Contracture with Adverse Immune Responses. *Int. J. Mol. Sci.* **2018**, *19*, 1171. [CrossRef] [PubMed]
2. Van Bellinghen, X.; Idoux-Gillet, Y.; Pugliano, M.; Strub, M.; Bornert, F.; Clauss, F.; Schwinte, P.; Keller, L.; Benkirane-Jessel, N.; Kuchler-Bopp, S.; et al. Temporomandibular Joint Regenerative Medicine. *Int. J. Mol. Sci.* **2018**, *19*, 446. [CrossRef] [PubMed]
3. Yun, W.S.; Choi, J.S.; Ju, H.M.; Kim, M.H.; Choi, S.J.; Oh, E.S.; Seo, Y.J.; Key, J. Enhanced Homing Technique of Mesenchymal Stem Cells Using Iron Oxide Nanoparticles by Magnetic Attraction in Olfactory-Injured Mouse Models. *Int. J. Mol. Sci.* **2018**, *19*, 1376. [CrossRef] [PubMed]
4. Jeong, C.; Kim, S.E.; Shim, K.S.; Kim, H.J.; Song, M.H.; Park, K.; Song, H.R. Exploring the In Vivo Anti-Inflammatory Actions of Simvastatin-Loaded Porous Microspheres on Inflamed Tenocytes in a Collagenase-Induced Animal Model of Achilles Tendinitis. *Int. J. Mol. Sci.* **2018**, *19*, 820. [CrossRef] [PubMed]
5. Kang, E.S.; Kim, D.S.; Han, Y.; Son, H.; Chung, Y.H.; Min, J.; Kim, T.H. Three-Dimensional Graphene-RGD Peptide Nanoisland Composites That Enhance the Osteogenesis of Human Adipose-Derived Mesenchymal Stem Cells. *Int. J. Mol. Sci.* **2018**, *19*, 669. [CrossRef] [PubMed]
6. Lee, T.J.; Shim, M.S.; Yu, T.; Choi, K.; Kim, D.I.; Lee, S.H.; Bhang, S.H. Bioreducible Polymer Micelles Based on Acid-Degradable Poly(ethylene glycol)-poly(amino ketal) Enhance the Stromal Cell-Derived Factor-1alpha Gene Transfection Efficacy and Therapeutic Angiogenesis of Human Adipose-Derived Stem Cells. *Int. J. Mol. Sci.* **2018**, *19*, 529. [CrossRef] [PubMed]
7. Kim, J.W.; Shin, Y.C.; Lee, J.J.; Bae, E.B.; Jeon, Y.C.; Jeong, C.M.; Yun, M.J.; Lee, S.H.; Han, D.W.; Huh, J.B. The Effect of Reduced Graphene Oxide-Coated Biphasic Calcium Phosphate Bone Graft Material on Osteogenesis. *Int. J. Mol. Sci.* **2017**, *18*, 1725. [CrossRef] [PubMed]
8. Müller, W.E.G.; Wang, S.; Ackermann, M.; Neufurth, M.; Steffen, R.; Mecja, E.; Munoz-Espi, R.; Feng, Q.; Schroder, H.C.; Wang, X. Rebalancing beta-Amyloid-Induced Decrease of ATP Level by Amorphous Nano/Micro Polyphosphate: Suppression of the Neurotoxic Effect of Amyloid beta-Protein Fragment 25-35. *Int. J. Mol. Sci.* **2017**, *18*, 2154. [CrossRef] [PubMed]
9. Park, T.M.; Kang, D.; Jang, I.; Yun, W.S.; Shim, J.H.; Jeong, Y.H.; Kwak, J.Y.; Yoon, S.; Jin, S. Fabrication of In Vitro Cancer Microtissue Array on Fibroblast-Layered Nanofibrous Membrane by Inkjet Printing. *Int. J. Mol. Sci.* **2017**, *18*, 2348. [CrossRef] [PubMed]
10. Nagai, N.; Deguchi, S.; Otake, H.; Hiramatsu, N.; Yamamoto, N. Therapeutic Effect of Cilostazol Ophthalmic Nanodispersions on Retinal Dysfunction in Streptozotocin-Induced Diabetic Rats. *Int. J. Mol. Sci.* **2017**, *18*, 1971. [CrossRef] [PubMed]
11. Tatiparti, K.; Sau, S.; Gawde, K.A.; Iyer, A.K. Copper-Free 'Click' Chemistry-Based Synthesis and Characterization of Carbonic Anhydrase-IX Anchored Albumin-Paclitaxel Nanoparticles for Targeting Tumor Hypoxia. *Int. J. Mol. Sci.* **2018**, *19*, 838. [CrossRef] [PubMed]

12. Zhang, X.; Yoon, H.J.; Kang, M.G.; Kim, G.J.; Shin, S.Y.; Baek, S.H.; Lee, J.G.; Bai, J.; Lee, S.Y.; Choi, M.J.; et al. Identification and Evaluation of Cytotoxicity of Peptide Liposome Incorporated Citron Extracts in an in Vitro System. *Int. J. Mol. Sci.* **2018**, *19*, 626. [CrossRef] [PubMed]

13. Yoon, H.J.; Zhang, X.; Kang, M.G.; Kim, G.J.; Shin, S.Y.; Baek, S.H.; Lee, B.N.; Hong, S.J.; Kim, J.T.; Hong, K.; et al. Cytotoxicity Evaluation of Turmeric Extract Incorporated Oil-in-Water Nanoemulsion. *Int. J. Mol. Sci.* **2018**, *19*, 280. [CrossRef] [PubMed]

Article

Enhanced Homing Technique of Mesenchymal Stem Cells Using Iron Oxide Nanoparticles by Magnetic Attraction in Olfactory-Injured Mouse Models

Wan Su Yun [1,†], Jin Sil Choi [2,3,†], Hyun Mi Ju [2,3], Min Hee Kim [2,3], Seong Jin Choi [4], Eun Seol Oh [1], Young Joon Seo [2,3,*] and Jaehong Key [1,*]

[1]   Department of Biomedical Engineering, Yonsei University, Wonju, Gangwon-do 26493, Korea; ip9801@naver.com (W.S.Y.); marchman10@hanmail.net (E.S.O.)

[2]   Laboratory of Smile Snail, Yonsei University Wonju College of Medicine, Wonju, Gangwon-do 26426, Korea; towtowtow92@naver.com (J.S.C.); skdi1082@naver.com (H.M.J.); mini.alice11234@gmail.com (M.H.K.)

[3]   Department of Otorhinolaryngology, Yonsei University Wonju College of Medicine, Wonju, Gangwon-do 26426, Korea

[4]   Department of Obstetrics and Gynecology, Yonsei University Wonju College of Medicine, Wonju, Gangwon-do 26426, Korea; choisj@yonsei.ac.kr

*   Correspondence: okas2000@hanmail.net (Y.J.S.); jkey@yonsei.ac.kr (J.K.); Tel.: +82-33-741-0644 (Y.J.S.); +82-33-760-2857 (J.K.)

†   Contributed equally to this work.

Abstract: Intranasal delivery of mesenchymal stem cells (MSCs) to the olfactory bulb is a promising approach for treating olfactory injury. Additionally, using the homing phenomenon of MSCs may be clinically applicable for developing therapeutic cell carriers. Herein, using superparamagnetic iron oxide nanoparticles (SPIONs) and a permanent magnet, we demonstrated an enhanced homing effect in an olfactory model. Superparamagnetic iron oxide nanoparticles with rhodamine B (IRBs) had a diameter of 5.22 ± 0.9 nm and ζ-potential of $+15.2 \pm 0.3$ mV. IRB concentration of 15 µg/mL was injected with SPIONs into MSCs, as cell viability significantly decreased when 20 µg/mL was used ($p \leq 0.005$) compared to in controls. The cells exhibited magnetic attraction in vitro. SPIONs also stimulated CXCR4 (C-X-C chemokine receptor type 4) expression and CXCR4-SDF-1 (Stromal cell-derived factor 1) signaling in MSCs. After injecting magnetized MSCs, these cells were detected in the damaged olfactory bulb one week after injury on one side, and there was a significant increase compared to when non-magnetized MSCs were injected. Our results suggest that SPIONs-labeled MSCs migrated to injured olfactory tissue through guidance with a permanent magnet, resulting in better homing effects of MSCs in vivo, and that iron oxide nanoparticles can be used for internalization, various biological applications, and regenerative studies.

Keywords: superparamagnetic iron oxide nanoparticles; CXCR4; homing; mesenchymal stem cells; intranasal delivery; olfactory-injured mouse model

1. Introduction

Stem cell-based therapy is actively studied and used in all areas of regenerative medicine. However, delivery of an appropriate number of intact cells to defective tissue remains difficult. Stem cells have self-renewal capability and can differentiate into various tissues [1]. In addition, stem cell migration to a damaged cell, known as the homing phenomenon, is an important part of stem cell research. Human mesenchymal stem cells (MSCs) communicate with other cells in the body and appear to 'home' to injured tissue in response to cellular damage signals known as homing factors [2].

Homing may be useful in clinically applying MSCs as cell carriers for therapeutic modalities. MSCs injected either topically or systematically have been used for cell therapy for various indications. Bone marrow MSCs are used to alleviate clinical symptoms of incomplete bone formation and infarcted myocardium [3,4] and been applied as immunomodulatory treatments for autoimmune diseases including Crohn's disease [5], multiple sclerosis [6], and rheumatoid arthritis [7]. Homing may be clinically applied with MSCs as cellular mediators for anti-cancer therapy in tumors. Maestroni et al. [8] showed that bone marrow MSCs significantly reduced the size and metastasis of lung cancer cells and melanoma cells in mice. Although the olfactory epithelium can regenerate continuously, few studies have examined restoration of the olfactory epithelium using stem cell techniques [9].

Although the precise mechanism of how MSCs select their target tissues is not completely understood, several previous studies suggested that chemokines and their receptors (e.g., CXCR4 and SDF-1) are important factors that induce homing of MSCs. To improve the effectiveness of MSC homing, several strategies have been developed. (1) Cultivate MSCs to have a higher migratory capability by adjusting the cell culture conditions. Shi et al. [10] showed that MSCs with a cocktail of cytokines in culture induced high surface expression of CXCR4, with chemotactic receptors of SDF-1α up-regulated in ischemic tissues. (2) Improve the capability of MSCs to respond to migratory stimuli. Several studies to modify MSCs or increase the expression of surface markers (CXCR4-SDF-1α axis) have been conducted to improve MSC migration. (3) Stimulate the target site for MSC mobilization. François et al. [11] applied whole body irradiation or additional local irradiation to the abdominal area or hindlimb of mice.

Recently, a "magnetic attraction" method for stem cells was developed. Two previous studies evaluated the magnetic attraction of stem cells to the brain. Song et al. [12] demonstrated that rats wearing an external magnet (0.32 T) on their skull for one week contained an increased number of stem cells labeled by superparamagnetic iron oxide (SPIO) after intravenous injection, resulting in a 3-fold or higher increase in the infarct area under the magnet as well as a significant decrease in the infarct size. Shen et al. [13] introduced another approach for magnetic stem cell attraction to injury sites after traumatic brain injury via intra-carotid delivery.

SPIOs are known to induce reactive oxygen species (ROS) [14,15], and ROS increases CXCR4 expression of MSCs derived from bone marrow [16]. Huang et al. demonstrated that internalization of SPIOs into MSCs strengthens the CXCR4-SDF-1α axis in a Transwell assay [17]. Taken together, our results show that magnetic retention of SPIO-labeled MSCs increased the migration and homing efficiency of MSCs with SPIO nanoparticles in vivo in mice with olfactory bulb injury (Scheme 1).
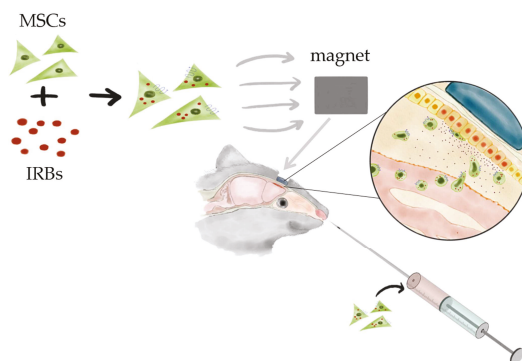
Scheme 1. Schematic illustration of mesenchymal stem cell (MSC) homing in olfactory mouse model using a permanent magnet. Iron oxide nanoparticles internalized in MSCs guide the cells to the defective site using an external permanent magnet.

2. Results

2.1. Characterization of Nanoparticles

The proposed SPIO nanoparticles with rhodamine B (IRBs) were comprised of an SPIO core coated with both oleic acid and rhodamine b, which were purchased from Ocean NanoTech (Springdale, AR, USA) [18] (Figure 1A). The sizes of IRBs were measured by transmission electron microscopy (TEM). A Zetasizer-ZS90 was utilized to measure the ζ-potential. TEM images showed that IRBs appeared as uniform spheres under completely dried conditions (Figure 1B). To analyze the IRB diameter, ImageJ software was used (NIH, Bethesda, MD, USA). After randomly sampling 255 particles, the IRB diameter was found to be 5.22 ± 0.9 nm (Figure 1C). The ζ-potential of IRBs was slightly positive in aqueous solution with a value of +15.2 ± 0.3 mV (Figure 1D).
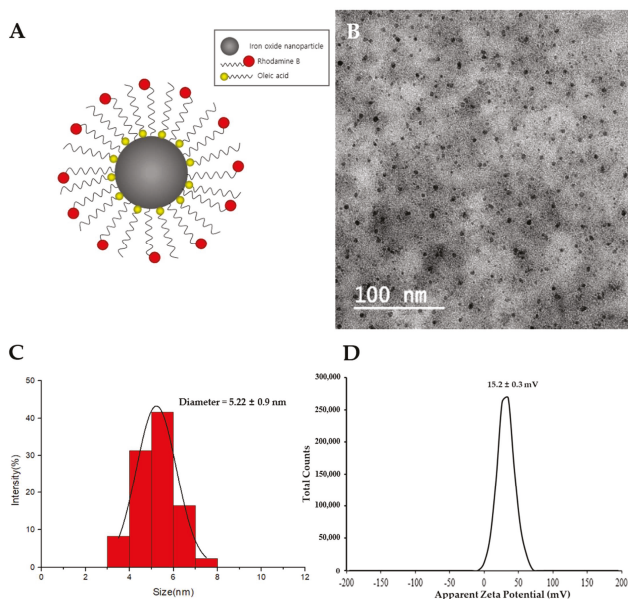
Figure 1. Characterization of superparamagnetic iron oxide (SPIO) nanoparticles with rhodamine B (IRBs). (**A**) Schematic illustration of IRBs used in this study. (**B**) Transmission electron microscope image of mono-dispersed IRBs. (**C**) Histogram analysis of the diameter of IRBs in transmission electron microscopy (TEM) images. (**D**) ζ-potential results of IRBs (*n* = 3) using Zetasizer-ZS90.

2.2. Internalization of IRBs (SPIO nanoparticles with rhodamine b) into MSCs (Mesenchymal stem cells) and Magnetic Properties

Cellular internalization of IRBs was characterized by measuring the red fluorescence of rhodamine B-labeled IRBs (Figure 2A). Green fluorescence indicated green fluorescent protein (GFP)-labeled MSCs. MSC nuclei were stained with 4′,6-diamidino-2-phenylindole (DAPI). MSCs in each image (Figure 2A (a)–(d)) were treated and incubated for 0, 3, 6, and 24 h with 15 μg/mL IRBs. Significant differences were observed in each image. With increasing incubation time, a greater number of IRBs gradually became internalized into the MSCs as measured at 580 nm. Thus, the group treated for 24 h with IRBs showed the largest number of IRBs in the MSCs. The ratio of IRB internalization in MSCs was measured with a fluorescence microscope (Figure 2B). The internalization ratios were 0% at 0 h, 52% at 3 h, 71.4% at 6 h, and 91.6% at 24 h. The results showed that as incubation time increased, the internalization percent also increased. Therefore, for sufficient internalization, 24-h IRB incubation was selected.
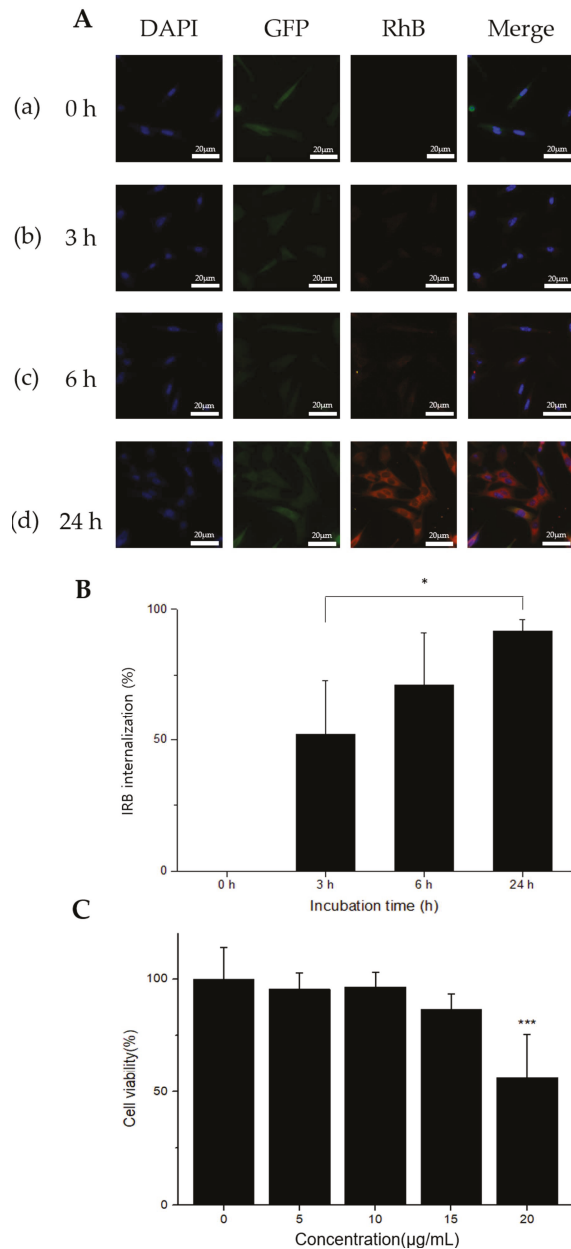
Figure 2. Cell internalization and viability analysis by IRBs. (**A**) Fluorescence microscopy images confirming IRB uptake at different incubation times. Each experimental group was incubated for 24 h. Time points of 0 h (**a**), 3 h (**b**), 6 h (**c**), and 24 h (**d**) in 15 µg/mL of IRBs (60× magnification, scale bar: 20 µm). (**B**) Ratio of IRB internalization in MSCs. IRB internalization was 0% at 0 h, 52% at 3 h, 71.4% at 6 h, and 91.6% at 24 h ($n = 4$, *: $p \leq 0.05$). (**C**) In vitro CCK-8 cytotoxicity analysis of IRBs in MSCs. Results presented as cell viability (mean ± SD) versus IRB concentration. Viability results were normalized to the control groups ($n = 9$, ***: $p \leq 0.005$).

The in vitro cytotoxicity of IRBs was measured by the (2-(2-methoxy-4-nitrophenyl)-3-(4-nitrophenyl)-5-(2,4-disulfophenyl)-2*H*-tetrazolium) (CCK-8) assay (Figure 2C). Cell viability in 20 μg/mL samples was significantly decreased ($p \leq 0.005$) compared to that in control samples. The results indicated that the highest concentration was considerably cytotoxic. Thus, 15 μg/mL of IRB was used for CXCR4 expression and further in vivo evaluation.

For magnet attraction experiments, magnetic flux and effective distances were tested. The permanent magnet used in this study was analyzed by both COMSOL (Burlington, MA, USA) simulation and a magnetometer. Figure 3A shows the simulation results. Magnetic flux was evaluated from a permanent cube-shape magnet, which revealed differences in magnetic flux depending on both the direction and distance. The maximum magnetic flux was 5087 Gauss and minimum flux was 1.626 Gauss. The result showed that the north and south magnetic fluxes changed symmetrically with distance. However, only very weak magnetic fluxes were observed on the sides. Therefore, only the north and south poles were evaluated by magnetometer analysis. To analyze the differences between the polar surface and non-polar surface, magnetic flux was measured with a magnetometer (KANETEC, Tokyo, Japan) at 1-mm intervals. The result showed that magnetic flux decreased significantly as the distance from the magnet increased (Figure 3B). Surface magnetic flux at the north pole was 0.32 T (3200 Gauss) and flux at the non-pole was nearly 0.03 T (264 Gauss) (Figure 3C). Thus, only the polar surface was considered for further experiments, considering the effective distance from the surface ($n = 9$, $p \leq 0.005$).
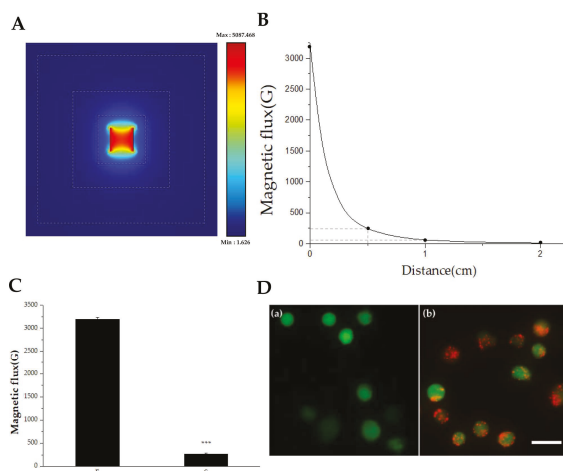
Figure 3. Measurement of magnetic flux and visualization of IRB-loaded MSCs. (**A**) Simulation analysis of a permanent cube-shape magnet. The dotted lines indicate the distances from the magnetic surface, which were 5, 10, and 20 mm. Different magnetic flux values depending on distances and directions. (**B**) Graph of magnetic flux versus distance. The actual values of magnetic flux from a permanent magnet applied in this study were measured. Magnetic flux values were 3200, 235, 60, and 10 Gauss at 0, 5, 10, and 20 mm, marked as a black dot, respectively. (**C**) Different surface magnetic flux was measured depending in polar (F) and non-polar directions (S) ($n = 9$, ***: $p \leq 0.005$). (**D**) IRB-loaded MSCs floating in the cell culture media were visualized with a fluorescence microscope, showing a clear difference between (**a**) MSCs without IRBs and (**b**) IRB-loaded MSCs (Scale bar: 25 μm).

It is important to evaluate whether MSCs hold IRBs under the floating condition because the MSCs were injected into the bloodstream and physically dragged to the injured area via an external magnet. To confirm that IRBs were internalized into MSCs under floating conditions, MSCs were incubated with IRBs at 37 °C for 24 h and treated with trypsin for 2 min. MSCs were observed by

fluorescence microscopy (Figure 3D). In contrast to MSCs without IRBs (Figure 3D (a)), MSCs with IRBs clearly showed internalized IRBs even in the floating state (Figure 3D (b)).

2.3. Enhanced Migration Capacity of Magnetized MSCs with IRBs In Vitro

Figure 4A shows that MSCs with IRBs were magnetically attracted. The fluorescence intensity of GFP-tagged MSCs was determined, and a normalized number of MSCs affected by the magnet was analyzed with ImageJ software (Figure 4B). MSCs without IRBs and 15 µg/mL magnetized MSCs were prepared in 6-well plates. After 24 h of incubation, fluorescence images were acquired at up to 15 mm at 1-mm intervals from the magnet (Figure 4A (a)–(b)). The cells were treated with trypsin and seeded into 6-well plates, which were attached by a magnet outside the wall. After 24 h of incubation, fluorescence images were captured using the same steps (Figure 4A (c)–(d)). In the plate without the magnet, 34.99% of cells without IRBs adhered in the range of 0–5 mm (front part), 33.54% adhered in 5–10 mm (middle part), and 31.46% adhered to 10–15 mm (back part); 35.02% of magnetized MSCs adhered to the front part, 32.68% adhered to the middle part, and 32.29% adhered to the back part. In the plate with a magnet, 34.57% of MSCs without IRBs adhered to the front part, 33.60% adhered to the middle part, and 31.82% adhered to the back part. In contrast, 42.42% of magnetized MSCs adhered to the front part, 32.61% adhered to the middle part, and 24.97% adhered to the back part (Figure 4B). As a result, only in the group treated with IRBs with an external magnet, MSCs were effectively attracted to the area showing the magnetic force because of magnetic flux. These results revealed magnetized MSC migration in vitro using a permanent magnet.
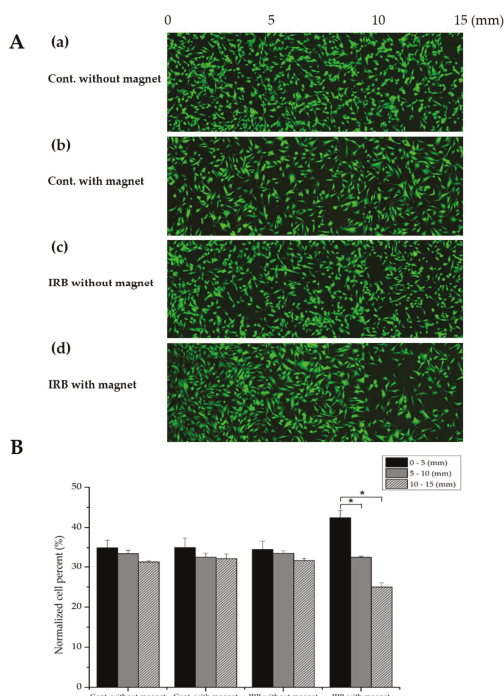
Figure 4. Visualization and quantitative analysis of magnetic dragging of MSCs. (**A**) (**a**)–(**c**): MSCs only, MSCs with a magnet, and IRB-loaded MSCs without a magnet showed no magnetic dragging. (**d**): IRB-loaded MSCs clearly showed magnetic dragging. (**B**) Normalized cell counting of MSCs depending on the distance from the magnet showed that only IRB-loaded MSCs were attracted by the magnet (approximately 43% of MSCs at 0–5 mm) ($n = 4$, *: $p \leq 0.05$).

2.4. Enhanced Expression of CXCR4 in Magnetized MSCs with IRBs and Reactive Oxygen Species (ROS) Analysis

CXCR4 expression in cells was increased by internalizing IRBs into the cells (Figure 5A). As the concentration of IRB increased, the amount of CXCR4 RNA was significantly increased by 10 μg/mL IRB compared to the control, which was increased by approximately 2-fold ($p \leq 0.005$) at an IRB concentration of 15 μg/mL. This pattern confirmed the results of protein quantification obtained by western blotting.

The relationship between ROS levels in magnetized MSCs and IRBs was evaluated (Figure 5B). ROS were measured as the normalized intensity of 2′,7′-dichlorodihydrofluorescein diacetate (H_2DCFDA) fluorescence. Immediately after IRBs were added to the MSCs, there were no differences among IRBs concentrations. However, after 3, 6, and 24 h of incubation, ROS values increased proportionally with IRB concentration. Changes in ROS levels were related to CXCR4 expression levels at 24 h. At 15 μg/mL IRBs at 24 h, the levels of ROS in MSCs were significantly increased by nearly 2-fold ($p \leq 0.005$) compared to in the control.
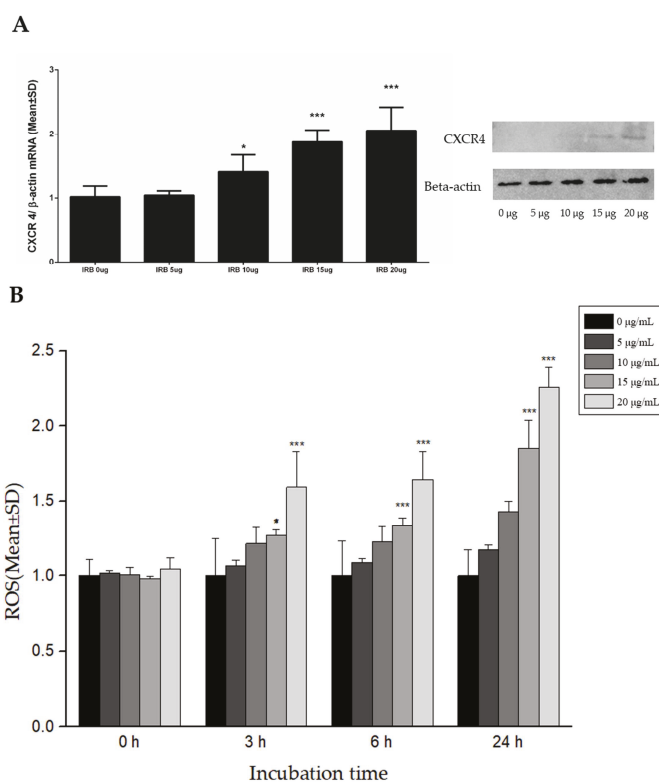
Figure 5. Expression of CXCR4 by Western blotting and measurement of reactive oxygen species (ROS) by H_2DCFDA using fluorescence intensity. (**A**) Different IRB concentrations induced different expression levels of CXCR4. At a concentration of 15 μg/mL, CXCR4 RNA was increased by approximately 2-fold ($n = 8$, *: $p \leq 0.05$, ***: $p \leq 0.005$). (**B**) Different IRB concentrations and IRB incubation time induced changes in ROS levels. After 3 h, 20 μg/mL IRBs clearly generated ROS compared to 0 μg/mL. After 24 h, 15 μg/mL induced a nearly 2-fold increase in ROS levels compared to in the control and 20 μg/mL induced a more than 2-fold increase in ROS levels compared to in the control. H_2DCFDA and IRBs were added to each well at the same time ($n = 9$, *: $p \leq 0.05$, ***: $p \leq 0.005$).

2.5. Enhanced Migration of Magnetized MSCs with IRBs In Vivo in Olfactory-Injured Mouse Models

Preparation of olfactory-injured mouse models and migration of magnetized MSCs with IRBs in mice were performed (Figure S1). To prepare olfactory-inured mouse models, the scalp bone was exposed by cutting the skin covering the skull with scissors. A 2-mm cranial window was opened on the exposed bone. Bipolar coagulation was used with a 1-mm depth for 100 ms on only one side of the olfactory bulb to induce olfactory injury. The result was confirmed by H&E (Hematoxylin and Eosin) staining and immunohistochemistry (Figure S2). The 5-mm cuboidal magnet was inserted into the scalp, and then the scalp was sutured. Injection of magnetized MSCs incubated with 15 µg/mL IRBs for 24 h into the olfactory-injured mouse model was performed with a 50-µL Hamilton syringe via each nostril (Supplementary Movie 1).

One week after MSC injection, the olfactory bulb was extracted to confirm the presence of stem cells in the damaged olfactory bulb. We compared the presence of MSCs in the damaged olfactory bulb under four different conditions: (a) control without MSC injection, (b) MSC injection without IRBs, (c) MSC injection with IRBs, (d) MSC injection with IRBs under magnetic fields. (a) Control showed neither GFP nor rhodamine signals in the injured area. (b) MSC injection without IRBs showed few GFP signals in the area. Only (c) and (d) showed both GFP and rhodamine signals (Figure 6A).

To quantify the results, we counted the number of MSCs in the injured area using both GFP signals from MSCs and rhodamine signals from IRBs in MSCs (Figure 6B). For counting by GFP, MSC injection with IRBs under a magnetic field showed significantly higher values compared to both MSC injection without IRBs and MSC injection with IRBs ($p \leq 0.005$). (Figure 6B, Left). For counting by rhodamine, MSC injection with IRBs under a magnetic field also showed a meaningful difference compared to MSC injection without IRBs ($p \leq 0.05$) (Figure 6B, Right). The different values between GFP and rhodamine counting may be explained by the optical sensitivity of the microscope used.

SDF-1 RNA and protein levels showed the greatest increase at 1 day after injury but remained higher than in the control after seven days (Figure 6C). This may explain why MSC injection with IRBs without magnetic fields showed higher homing effects than MSCs alone ($p \leq 0.05$) (Figure 6B-Left). Increased CXCR4 levels in the MSCs via the internalization of IRBs may improve the CXCR4-SDF-1 signaling pathway at the injured area (Figure 5A).
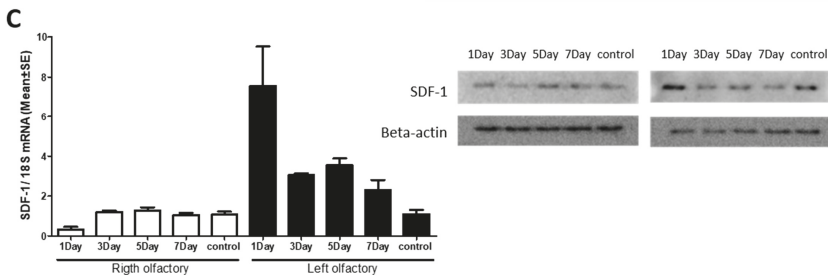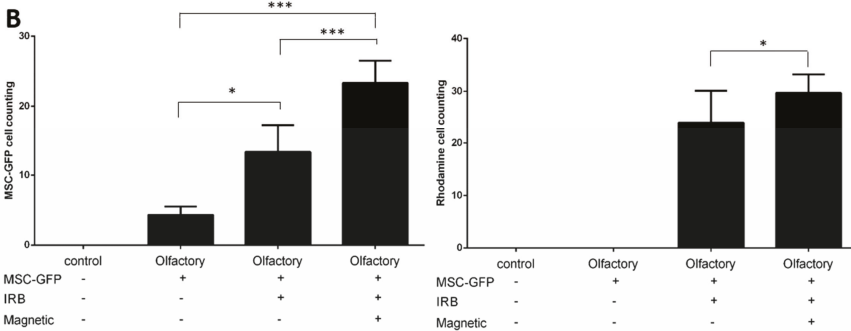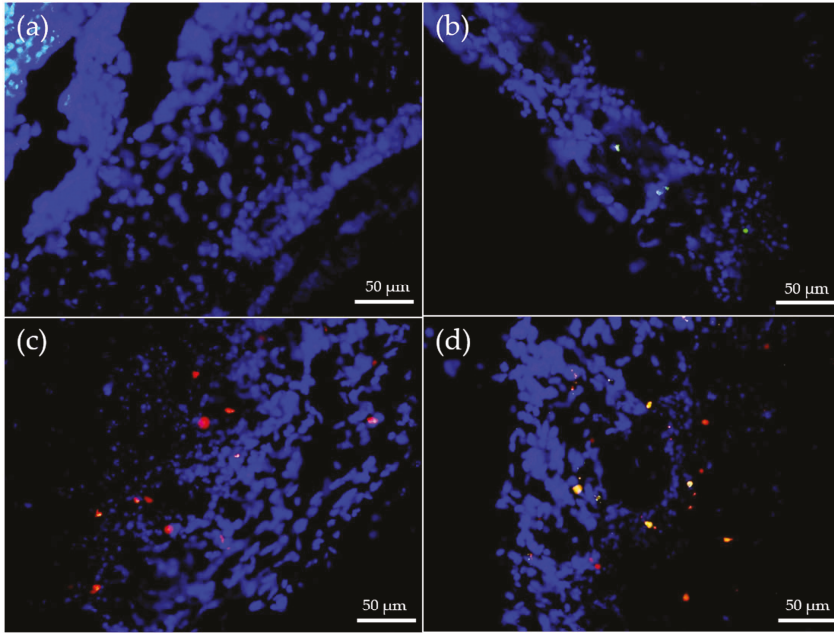
Figure 6. Enhanced migration of magnetized MSCs with IRBs in olfactory-injured mouse models. Green dots—GFP-tagged MSCs, Red dots—rhodamine-tagged (IRB) MSCs. (**A**) (**a**) control: injection without MSCs in normal mice, (**b**) MSC injection without IRBs, (**c**) magnetized MSC injection with IRBs, (**d**) magnetized MSC injection with IRBs under magnetic field (scale bar: 50 μm). (**B**) Graphs of MSC-GRP cell counting (**left**) and rhodamine cell counting (**right**) according to injection groups ($n = 8$, *: $p \leq 0.05$, ***: $p \leq 0.005$). (**C**) Increased expression of SDF-1 in injured olfactory bulb (**left**) determined by PCR and Western blotting (**right**) (control $n = 4$, experimental group $n = 12$).

3. Discussion

Our study reveals methods for improving the homing ability of magnetized MSCs with internalized IRBs in vivo. By internalizing the IRBs, the direct homing efficiency of MSCs to the wounded olfactory bulb was improved by promoting the homing factor of the CXCR4-SDF-1 axis, and additional MSCs were be homed to the desired site by using a magnetic field. Although IRB internalization may affect MSC proliferation or vitality at high doses, an appropriate amount of IRB did not inhibit the cells, but rather had a stimulatory effect, leading to increased ROS because of the hypoxic conditions, which may help CXCR4 to increase the homing of MSCs. A sufficient number of IRBs was internalized into the cell and responded to the magnetic field, which was useful for promoting MSC homing in vivo. Previous studies also introduced nanoparticles to enhance homing. Magnetic attraction of SPIO-labeled cells has been applied to enhance the delivery of stem cells to a wide range of target tissues including the liver, muscle, joints, heart, retina, and brain [13,15,19–21]. Studies observed increased cells in the target tissue as well as physiological improvement. Shen et al. [13] transported human SPIO-labeled neuroprogenitor cells (hNPCs) into post-traumatic brain injury animals in the presence of a static magnetic field. They revealed increased homing and retention of hNPCs to the injured cortex compared to in the control group in which hNPCs were injected in the absence of a static magnetic field. Li et al. [22] used endothelial progenitor cells loaded with SPIO as well as similar methods and magnet strength to deliver cells following brain infarction.

SPIO was reported to have low toxicity in the human body [23]. Iron oxide nanoparticles are also well-known to be harmless and non-cytotoxic under 100 µg/mL. Ankamwar et al. [24] reported that the toxicity of Fe_3O_4 NPs coated with tetramethylammonium 11-aminoundecanoate was concentration-dependent, showing non-toxicity over the concentration range of 0.1–10 µg/mL but cytotoxicity at 100 µg/mL. Shen et al. [13] reported no negative effects on hNPC viability, proliferation, and differentiation following labeling with MIRB. In this study, we found that magnetized MSCs under 15 µg/mL IRB at 24 h showed similar viability as non-labeled MSCs in vitro. Despite the presence of a static magnetic field, MSCs-IRBs showed normal viability, proliferation, and differentiation properties in vivo and in vitro.

Upon internalization into cells, SPIO can induce toxicity by generating ROS [14,15]. SPIO may be degraded into iron ions within lysosomes by hydrolyzing enzymes. This free iron can react with hydrogen peroxide and oxygen produced by the mitochondria after crossing the mitochondrial membrane. Therefore, iron overload from SPIO exposure may result in harmful cellular consequences, finally leading to cell death. A study demonstrated that the ROS produced by iron-nanoparticles induced GSK-3b (Glycogen synthase kinase 3β) inhibition by activating the Akt signaling pathway, altering actin dynamics such as cell migration [25]. Another study investigating the toxic effect of Ferucarbotran (Resovist) revealed that MSCs showed enhanced cell proliferation with changes in the expression of cell cycle control genes and a reduction in intracellular hydrogen peroxide [26]. One approach for improving the homing capacity of MSCs is to culture MSCs under hypoxic conditions. At 15 µg/mL IRB for 24 h in vitro, the thresholds of ROS in magnetized MSCs was increased by nearly 2-fold. The stimulated ROS system may help in the homing of magnetized MSCs to increase the expression of CXCR4 on the cell surface. Therefore, this result demonstrates that adding IRB to MSCs can increase homing without a magnetic field.

The CXCR4-SDF-1 axis is known as an important factor in bone marrow homing [27]. Overexpression of CXCR4 in MSCs by internalization of nanoparticles can increase in vivo homing of MSCs into ischemic areas of the myocardium [28]. Insulin-like growth factor-1 treatment of rat MSCs was revealed to increase MSC migration in response to SDF-1 via CXCR4 receptor signaling. The SDF-1/CXCR4 axis may also contribute to the migration of MSCs into the brain and towards glioma tissue in irradiated animals [29]. Induction of CXCR4 expression by a simple method in injured tissue, which increased the expression of SDF-1, suggests that iron oxide nanoparticles can be used for internalization, and iron oxide is expected to be useful for biological applications.

Intranasal delivery of MSCs to the olfactory bulb appears to be a promising approach for the therapy of central nervous system diseases. Recent studies reported the nasal system as a novel stem cell delivery route to the brain [30–32]. MSCs transported into the nasal cavity have been shown to migrate through the cribriform plate and into brain tissue via the olfactory and trigeminal pathways. Lusine et al. demonstrated that noninvasive intranasal delivery of MSCs is a promising approach for the therapeutic treatment of Parkinson's disease. The olfactory system has been widely applied as a model in studies of neural regeneration and axon rewiring [33]. Wounds to olfactory cells in the neuroepithelium are not reversible following damage of the basal cell layer, but when spared, regenerated basal cells lead to reconstruction of the sensory epithelium and subsequent restoration of olfactory function [9]. Therefore, intranasal delivery of magnetized MSCs in an injured olfactory mouse model is an effective method of demonstrating the homing phenomenon of MSCs using nanoparticles.

4. Materials and Methods

4.1. Characterization of NPs

Iron oxide nanoparticles with rhodamine B (IRBs) were obtained from Ocean Nanotech. The size and charge properties of IRBs were measured by TEM and with a Zetasizer-ZS90 (Malvern Instruments Ltd., Malvern, UK). IRBs were well-dispersed in an aqueous solution. For TEM analysis, after 10-min bath sonication, 2 μL IRBs were dropped on the carbon grid three times and completely dried. IRBs were observed by TEM (JEM-ARM 200F, JEOL, Tokyo, Japan). The diameter of IRBs was analyzed with ImageJ software (NIH, Bethesda, MD, USA). To obtain the ζ-potential of IRBs, 20 μL IRBs and 980 μL distilled water were mixed into a folded capillary cell (Malvern Instruments) after 10-min bath sonication.

4.2. Cell Culture

GFP-labeled MSCs derived from C57BL/6 mouse tibia bone marrow were obtained from Cyagen Biosciences, Inc. (cat. MUBMX-01101; Santa Clara, CA, USA), cultured in low-glucose DMEM (Hyclone, Logan, UT, USA) containing 2 ng/mL of basic fibroblast growth factor and 10% fetal bovine serum (Gibco, Grand Island, NY, USA), and maintained at 37 °C in a humidified atmosphere of 5% CO_2. The cell culture medium was replaced every three days, and bone marrow-derived MSCs were collected by trypsin (0.25%, Invitrogen, Carlsbad, CA, USA) digestion. All experiments were performed using MSCs at 3–5 passages.

4.3. Internalizing Iron Oxide Nanoparticles with Rhodamine B into MSCs

GFP-labeled MSCs were seeded onto confocal dishes (SPL Life Sciences, Gyeonggi-do, Korea) at 1×10^5 cells per well. After 24 h incubation, the culture media was exchanged with 2 mL of fresh media and cells were incubated for 0, 3, 6, and 24 h with 15 μg/mL IRBs. The MSCs were washed twice using PBS, fixed in 10% formalin, and stained with DAPI. Images were captured with a fluorescence microscope (Eclipse Ti-U, Nikon, Tokyo, Japan) and further analyzed to confirm the intracellular localization and quantity of IRBs. To quantify the internalization ratio in MSCs, all MSCs were counted in the fluorescence images. The number of RhB-positive cells was divided by the total number of cells.

4.4. Cytotoxicity of IRB-MSCs

MSCs were seeded into 96-well surface-treated plates at a density of 5×10^3 cells per well and incubated at 37 °C and 5% CO_2 for 24 h. The culture media were replaced with 100 μL of fresh media containing different concentrations of Fe in IRBs. Cells without IRBs were measured as a control. After 24 h of incubation, the cells were washed and incubated in cell culture media. In vitro cytotoxicity was evaluated by using the CCK-8 (Cell Counting Kit-8). For this assay, 10 μL CCK-8 was added to each well under light protection. After 1 h incubation, absorbance values at 450 nm were measured with a multimode reader (Synergy HTX, BioTek, Winooski, VT, USA).

4.5. Magnetic Field Effects on Magnetized MSCs In Vitro

To estimate the homing effect of MSCs using IRBs, magnetic flux properties were evaluated by both simulation (COMSOL Multiphysics software, Stockholm, Sweden) and a Tesla meter (TM-701, KANETEC) using a $5 \times 5 \times 5$ mm permanent regular hexahedron neodymium magnet. From the magnet, the magnetic pole surface showing north and south was used to attract the IRBs. MSCs on 6-well plates at a density of 1×10^5 per well were incubated for 3 h. Fluorescence images were captured with a fluorescence microscope. MSCs were treated for 12 h with 15 μg/mL IRBs. Images were captured to determine whether IRBs were internalized into the MSCs. Floating MSCs were incubated with the magnet for 24 h on six-well plates at a density of 1×10^5 per well and MSCs guided by the magnet were confirmed using a fluorescence microscope.

4.6. Analysis of Real-Time PCR

Total RNA was extracted from the magnetized MSCs in vitro to evaluate CXCR4 expression. In an animal study, total RNA was collected using TRIzol Reagent (Invitrogen) from the sensory epithelium of both olfactory bulbs of three mice, which were sacrificed seven days after treatment. Total RNA was subjected to reverse transcription using SYBR® Select master mix (Applied Biosystems, Foster City, CA, USA). Real-time RT-PCR was performed using the Applied Biosystem's sequence detection system 7900 to quantify SDF-1 levels. The following primers were used for sequencing: CXCR4, forward: 5′-CAG CAT CGA CTC CTT CAT CC-3′ and reverse: 5′-GGT TCA GGC AAC AGT GGA AG-3′ (119 base pairs), SDF-1, forward: 5′-CGC CAG AGC CAA CGT CAA GC-3′ and reverse: 5′-TTT GGG TCA ATG CAC ACT TG-3′; β-actin, forward: 5′-CGT GCG TGA CAT CCA AGA GAA-3′ and reverse: 5′-TGG ATG CCA CAG GAT TCC AT-3′. To detect the possibility of genomic DNA amplification, no-template controls were utilized and allowed when the C_t value was at least nine cycles greater than the template run. Duplicate measurements were performed and accepted if the difference in C_t values between the duplicates was less than 1. Real-time PCR data were normalized to the level of β-actin, and the relative quantity of mRNA was determined using the comparative cycle threshold method.

4.7. Western Blotting and Fluorescence-Activated Cell Sorting

MSCs were incubated with IRBs for 2 h and then washed twice with PBS. Fresh medium was utilized for different time periods. After collecting the cells, CXCR4 expression of MSCs was evaluated by fluorescence-activated cell sorting and western blotting.

Cells ($>10^5$) and olfactory tissue were lysed in Laemmli buffer according to the manufacturer's instructions (Invitrogen) and separated on a 12% sodium dodecyl sulfate polyacrylamide gel. Membranes were hybridized with rabbit anti-human CXCR4 at 1:1000 (sc-9046; Santa Cruz Biotechnology, Dallas, TX, USA), with SDF-1 (ab18919; Abcam, Cambridge, UK), or anti-β-actin (1:500; Sigma, St. Louis, MO, USA). Anti-rabbit horseradish peroxidase secondary antibody was used at 1:1000 (Dako, Glostrup, Denmark). Deglycosylation was carried out using *N*-glycosidase F according to the manufacturer's instructions (New England Biolabs, Ipswich, MA, USA).

To analyze CXCR4 expression in different subcellular protein fractions, MSCs were incubated with IRBs (108 μM) for 2 h. The cells were cultured for 22 h and the medium was replaced. After cell collection, the proteins expressed in cytoplasm, membrane, and nucleus were separated with a subcellular protein fractionation kit (Thermo Scientific, Waltham, MA, USA).

4.8. ROS Analysis

In vitro ROS analysis was conducted in 96-well surface-treated plates. MSCs were seeded at a density of 5×10^3 cells per well and incubated at 37 °C and 5% CO_2 for 24 h. After incubation, the cells were washed with PBS and 100 μL of fresh media containing different Fe concentrations in IRBs was added. Control groups did not contain added IRBs. After 24 h of incubation, MSCs were

washed twice with PBS and incubated in fresh media and 10 μL 0.2 mM H_2DCFDA PBS solution in the dark. Fluorescence values at 485 nm excitation/528 nm emission were measured with a multimode reader at each time point (0, 3, 6, and 24 h).

4.9. In Vivo Injection of Magnetized MSCs into Olfactory Injury Mouse Models

Twenty-four male C57BL/6 mice, including six control mice for the olfactory-injured model, were allowed free access to water and a regular mouse diet and kept at room temperature under a standard 12-h light/dark cycle for one week of acclimatization before the experiments. The animals were five weeks old and weighed approximately 18–25 g. Mice were anesthetized by intraperitoneal injection of 30 mg/kg tiletamine-zolazepam (Zoletil, 500 mg/vial; Virbac, Carros, France) and 10 mg/kg xylazine (Rompun; Bayer Korea, Ansan, Korea) and sacrificed by decapitation. Animal experiments were conducted in accordance with the guidelines of the Institutional Animal Care and Use Committee of Yonsei University, Korea (YWC-170721-1, 27 February 2017).

4.10. Immunofluorescence Staining in Olfactory Bulb

Normal and olfactory-injured mice were sacrificed after seven days of magnetized MSC injection. After cardiac perfusion, the skull bones were removed. Next, both olfactory bulbs were immersed in 4% paraformaldehyde (Biosesang Seongnam, Korea) in fixative for 24 h at 4 °C. The samples were embedded in optimal cutting temperature compound (Leica, Wetzlar, Germany) and sectioned at 2–10 μm thickness using a cryostat (Leica CM1850 Cryostat; Leica). A standard hematoxylin and eosin staining protocol was followed, with 1–3 min incubation in hematoxylin and 30–60 s staining with eosin, before mounting the samples.

Immunohistochemistry for SDF-1 was performed on cryosections of the cochlea in each group. Slide samples were incubated with appropriate primary antibodies as follows. An antibody against SDF-1 1 (cat# ab18919; Abcam) was used. Sections were incubated with the primary antibody overnight at 4 °C. After washing three times with 0.1 M PBS, the sections were incubated with an appropriate biotin-tagged secondary antibody at room temperature for 1 h. The sections were incubated in an avidin–biotin–peroxidase complex solution (Vector Laboratories, Inc., Burlingame, CA, USA) and developed with a diaminobenzidine substrate kit (Vector Laboratories, Inc.) after washing three times with 0.1 M PBS. The sections were dehydrated, mounted, and visualized with a BX50 microscope (Olympus, Tokyo, Japan), and digital images were captured.

4.11. Statistical Analysis

Statistical analysis was performed using SPSS statistical package version 17.0 (SPSS, Inc., Chicago, IL, USA). Descriptive results of continuous variables are expressed as the mean ± standard deviation (SD) for normally distributed variables. Means were compared by two-way analysis of variance. The level of statistical significance was set to 0.05.

5. Conclusions

Our study demonstrated that noninvasive intranasal delivery of magnetized MSCs with IRBs is a promising method for treating an olfactory-injured mouse model. Using complementary methods, we demonstrated the following: (i) migration of magnetized MSCs with IRBs under a magnetic field in vitro; (ii) increase in CXCR4 by internalizing IRBs into MSCs; and (iii) improvement in homing of magnetized MSCs into the injured olfactory epithelium in vivo. We are currently assessing the long-term effects (regeneration and cytotoxicity) of magnetized MSCs in olfactory-injured mice with different magnetic fields, nanoparticle concentrations, and nanoparticle shapes in MSCs.

Supplementary Materials: The following are available online at https://zenodo.org/record/1256264#.Ww9REVKSCJ0.

Abbreviations

MSCs	Mesenchymal stem cells
SPIO	Superparamagnetic iron oxide
IRBs	SPIO nanoparticles with rhodamine b
ROS	Reactive oxygen species
CXCR4	C-X-C chemokine receptor type 4
SDF-1	Stromal cell-derived factor 1
GFP	Green fluorescent protein

References

1. Bjornson, C.R.R.; Rietze, R.L.; Reynolds, B.A.; Magli, M.C.; Vescovi, A.L. Turning brain into blood: A hematopoietic fate adopted by adult neural stem cells in vivo. *Science* **1999**, *283*, 534–537. [CrossRef] [PubMed]
2. Kang, S.K.; Shin, I.S.; Ko, M.S.; Jo, J.Y.; Ra, J.C. Journey of mesenchymal stem cells for homing: Strategies to enhance efficacy and safety of stem cell therapy. *Stem Cells Int.* **2012**, *2012*, 1–11. [CrossRef] [PubMed]
3. Ripa, R.S.; Haack-Sorensen, M.; Wang, Y.; Jorgensen, E.; Mortensen, S.; Bindslev, L.; Friis, T.; Kastrup, J. Bone marrow derived mesenchymal cell mobilization by granulocyte-colony stimulating factor after acute myocardial infarction: Results from the stem cells in myocardial infarction (STEMMI) trial. *Circulation* **2007**, *116*, I24–I30. [CrossRef] [PubMed]
4. Kawada, H.; Fujita, J.; Kinjo, K.; Matsuzaki, Y.; Tsuma, M.; Miyatake, H.; Muguruma, Y.; Tsuboi, K.; Itabashi, Y.; Ikeda, Y. Nonhematopoietic mesenchymal stem cells can be mobilized and differentiate into cardiomyocytes after myocardial infarction. *Blood* **2004**, *104*, 3581–3587. [CrossRef] [PubMed]
5. Duijvestein, M.; Vos, A.C.; Roelofs, H.; Wildenberg, M.E.; Wendrich, B.B.; Verspaget, H.W.; Kooy-Winkelaar, E.M.; Koning, F.; Zwaginga, J.J.; Fidder, H.H.; et al. Autologous bone marrow-derived mesenchymal stromal cell treatment for refractory luminal crohn's disease: Results of a phase I study. *Gut* **2010**, *59*, 1662–1669. [CrossRef] [PubMed]
6. Zappia, E.; Casazza, S.; Pedemonte, E.; Benvenuto, F.; Bonanni, I.; Gerdoni, E.; Giunti, D.; Ceravolo, A.; Cazzanti, F.; Frassoni, F.; et al. Mesenchymal stem cells ameliorate experimental autoimmune encephalomyelitis inducing T-cell anergy. *Blood* **2005**, *106*, 1755–1761. [CrossRef] [PubMed]
7. Augello, A.; Tasso, R.; Negrini, S.M.; Cancedda, R.; Pennesi, G. Cell therapy using allogeneic bone marrow mesenchymal stem cells prevents tissue damage in collagen-induced arthritis. *Arthritis Rheumatol.* **2007**, *56*, 1175–1186. [CrossRef] [PubMed]
8. Maestroni, G.J.; Hertens, E.; Galli, P. Factor(s) from nonmacrophage bone marrow stromal cells inhibit lewis lung carcinoma and B16 melanoma growth in mice. *Cell. Mol. Life Sci.* **1999**, *55*, 663–667. [CrossRef] [PubMed]
9. Costanzo, R.M.; Yagi, S. Olfactory epithelial transplantation: Possible mechanism for restoration of smell. *Curr. Opin. Otolaryngol. Head Neck Surg.* **2011**, *19*, 54–57. [CrossRef] [PubMed]

10. Shi, M.; Li, J.; Liao, L.; Chen, B.; Li, B.; Chen, L.; Jia, H.; Zhao, R.C. Regulation of CXCR4 expression in human mesenchymal stem cells by cytokine treatment: Role in homing efficiency in nod/scid mice. *Haematologica* **2007**, *92*, 897–904. [CrossRef] [PubMed]

11. Francois, S.; Bensidhoum, M.; Mouiseddine, M.; Mazurier, C.; Allenet, B.; Semont, A.; Frick, J.; Sache, A.; Bouchet, S.; Thierry, D. Local irradiation not only induces homing of human mesenchymal stem cells at exposed sites but promotes their widespread engraftment to multiple organs: A study of their quantitative distribution after irradiation damage. *Stem Cells* **2006**, *24*, 1020–1029. [CrossRef] [PubMed]

12. Song, M.; Kim, Y.J.; Kim, Y.H.; Roh, J.; Kim, S.U.; Yoon, B.W. Using a neodymium magnet to target delivery of ferumoxide-labeled human neural stem cells in a rat model of focal cerebral ischemia. *Hum. Gene Ther.* **2010**, *21*, 603–610. [CrossRef] [PubMed]

13. Shen, W.B.; Plachez, C.; Tsymbalyuk, O.; Tsymbalyuk, N.; Xu, S.; Smith, A.M.; Michel, S.L.; Yarnell, D.; Mullins, R.; Gullapalli, R.P.; et al. Cell-based therapy in TBI: Magnetic retention of neural stem cells in vivo. *Cell Transpl.* **2016**, *25*, 1085–1099. [CrossRef] [PubMed]

14. Schulze, E.; Ferrucci, J.T., Jr.; Poss, K.; Lapointe, L.; Bogdanova, A.; Weissleder, R. Cellular uptake and trafficking of a prototypical magnetic iron oxide label in vitro. *Investig. Radiol.* **1995**, *30*, 604–610. [CrossRef]

15. Arbab, A.S.; Jordan, E.K.; Wilson, L.B.; Yocum, G.T.; Lewis, B.K.; Frank, J.A. In vivo trafficking and targeted delivery of magnetically labeled stem cells. *Hum. Gene Ther.* **2004**, *15*, 351–360. [CrossRef] [PubMed]

16. Liu, H.; Xue, W.; Ge, G.; Luo, X.; Li, Y.; Xiang, H.; Ding, X.; Tian, P.; Tian, X. Hypoxic preconditioning advances CXCR4 and CXCR7 expression by activating hif-1α in mscs. *Biochem. Biophys. Res. Commun.* **2010**, *401*, 509–515. [CrossRef] [PubMed]

17. Huang, X.; Zhang, F.; Wang, Y.; Sun, X.; Choi, K.Y.; Liu, D.; Choi, J.S.; Shin, T.H.; Cheon, J.; Niu, G.; et al. Design considerations of iron-based nanoclusters for noninvasive tracking of mesenchymal stem cell homing. *ACS Nano* **2014**, *8*, 4403–4414. [CrossRef] [PubMed]

18. William, W.Y.; Falkner, J.C.; Yavuz, C.T.; Colvin, V.L. Synthesis of monodisperse iron oxide nanocrystals by thermal decomposition of iron carboxylate salts. *Chem. Commun.* **2004**, 2306–2307.

19. Kamei, G.; Kobayashi, T.; Ohkawa, S.; Kongcharoensombat, W.; Adachi, N.; Takazawa, K.; Shibuya, H.; Deie, M.; Hattori, K.; Goldberg, J.L.; et al. Articular cartilage repair with magnetic mesenchymal stem cells. *Am. J. Sports Med.* **2013**, *41*, 1255–1264. [CrossRef] [PubMed]

20. Chen, J.; Huang, N.; Ma, B.; Maitz, M.F.; Wang, J.; Li, J.; Li, Q.; Zhao, Y.; Xiong, K.; Liu, X. Guidance of stem cells to a target destination in vivo by magnetic nanoparticles in a magnetic field. *ACS Appl. Mater. Interfaces* **2013**, *5*, 5976–5985. [CrossRef] [PubMed]

21. Luciani, A.; Wilhelm, C.; Bruneval, P.; Cunin, P.; Autret, G.; Rahmouni, A.; Clement, O.; Gazeau, F. Magnetic targeting of iron-oxide-labeled fluorescent hepatoma cells to the liver. *Eur. Radiol.* **2009**, *19*, 1087–1096. [CrossRef] [PubMed]

22. Li, Q.; Tang, G.; Xue, S.; He, X.; Miao, P.; Li, Y.; Wang, J.; Xiong, L.; Wang, Y.; Zhang, C.; et al. Silica-coated superparamagnetic iron oxide nanoparticles targeting of EPCs in ischemic brain injury. *Biomaterials* **2013**, *34*, 4982–4992. [CrossRef] [PubMed]

23. Karlsson, H.L.; Cronholm, P.; Gustafsson, J.; Moller, L. Copper oxide nanoparticles are highly toxic: A comparison between metal oxide nanoparticles and carbon nanotubes. *Chem. Res. Toxicol.* **2008**, *21*, 1726–1732. [CrossRef] [PubMed]

24. Ankamwar, B.; Lai, T.C.; Huang, J.H.; Liu, R.S.; Hsiao, M.; Chen, C.H.; Hwu, Y.K. Biocompatibility of Fe_3O_4 nanoparticles evaluated by in vitro cytotoxicity assays using normal, glia and breast cancer cells. *Nanotechnology* **2010**, *21*, 075102. [CrossRef] [PubMed]

25. Apopa, P.L.; Qian, Y.; Shao, R.; Guo, N.L.; Schwegler-Berry, D.; Pacurari, M.; Porter, D.; Shi, X.L.; Vallyathan, V.; Castranova, V.; et al. Iron oxide nanoparticles induce human microvascular endothelial cell permeability through reactive oxygen species production and microtubule remodeling. *Part. Fibre Toxicol.* **2009**, *6*, 1. [CrossRef] [PubMed]

26. Huang, D.M.; Hsiao, J.K.; Chen, Y.C.; Chien, L.Y.; Yao, M.; Chen, Y.K.; Ko, B.S.; Hsu, S.C.; Tai, L.A.; Cheng, H.Y.; et al. The promotion of human mesenchymal stem cell proliferation by superparamagnetic iron oxide nanoparticles. *Biomaterials* **2009**, *30*, 3645–3651. [CrossRef] [PubMed]

27. Moll, N.M.; Ransohoff, R.M. CXCL12 and CXCR4 in bone marrow physiology. *Expert Rev. Hematol.* **2010**, *3*, 315–322. [CrossRef] [PubMed]

28. Haider, H.K.; Jiang, S.; Idris, N.M.; Ashraf, M. IGF-1–Overexpressing mesenchymal stem cells accelerate bone marrow stem cell mobilization via paracrine activation of SDF-1α/CXCR4 signaling to promote myocardial repair. *Circ. Res.* **2008**, *103*, 1300–1308. [CrossRef] [PubMed]

29. Balyasnikova, I.V.; Prasol, M.S.; Ferguson, S.D.; Han, Y.; Ahmed, A.U.; Gutova, M.; Tobias, A.L.; Mustafi, D.; Rincon, E.; Zhang, L.J.; et al. Intranasal delivery of mesenchymal stem cells significantly extends survival of irradiated mice with experimental brain tumors. *Mol. Ther.* **2014**, *22*, 140–148. [CrossRef] [PubMed]

30. Reitz, M.; Demestre, M.; Sedlacik, J.; Meissner, H.; Fiehler, J.; Kim, S.U.; Westphal, M.; Schmidt, N.O. Intranasal delivery of neural stem/progenitor cells: A noninvasive passage to target intracerebral glioma. *Stem Cells Transl. Med.* **2012**, *1*, 866–873. [CrossRef] [PubMed]

31. Van Velthoven, C.T.; Kavelaars, A.; van Bel, F.; Heijnen, C.J. Nasal administration of stem cells: A promising novel route to treat neonatal ischemic brain damage. *Pediatr. Res.* **2010**, *68*, 419–422. [CrossRef] [PubMed]

32. Danielyan, L.; Schafer, R.; von Ameln-Mayerhofer, A.; Bernhard, F.; Verleysdonk, S.; Buadze, M.; Lourhmati, A.; Klopfer, T.; Schaumann, F.; Schmid, B.; et al. Therapeutic efficacy of intranasally delivered mesenchymal stem cells in a rat model of parkinson disease. *Rejuvenation Res.* **2011**, *14*, 3–16. [CrossRef] [PubMed]

33. Iwema, C.L.; Fang, H.; Kurtz, D.B.; Youngentob, S.L.; Schwob, J.E. Odorant receptor expression patterns are restored in lesion-recovered rat olfactory epithelium. *J. Neurosci.* **2004**, *24*, 356–369. [CrossRef] [PubMed]

Article

Exploring the In Vivo Anti-Inflammatory Actions of Simvastatin-Loaded Porous Microspheres on Inflamed Tenocytes in a Collagenase-Induced Animal Model of Achilles Tendinitis

Chandong Jeong [1,2,†], **Sung Eun Kim** [1,†], **Kyu-Sik Shim** [2], **Hak-Jun Kim** [1], **Mi Hyun Song** [1], **Kyeongsoon Park** [3,*] and **Hae-Ryong Song** [1,*]

1   Department of Orthopedic Surgery and Rare Diseases Institute, Korea University College of Medicine, Guro Hospital, Guro-dong, Guro-gu, Seoul 08308, Korea; cdjeong85@gmail.com (C.J.); sekim10@korea.ac.kr (S.E.K.); dakjul@korea.ac.kr (H.-J.K.); wwiiw@naver.com (M.H.S.)
2   Department of Biomedical Science, Korea University College of Medicine, Anam-dong, Seongbuk-gu, Seoul 02841, Korea; breakdown88@nate.com
3   Department of Systems Biotechnology, Chung-Ang University, Anseong, Gyeonggi-do 17546, Korea
*   Correspondence: kspark1223@cau.ac.kr (K.P.); songhae@korea.ac.kr (H.-R.S.); Tel.: +82-31-670-3357 (K.P.); +82-2-2626-2481 (H.-R.S.)
†   These authors contributed equally to this work.

Abstract: Tendon rupture induces an inflammatory response characterized by release of pro-inflammatory cytokines and impaired tendon performance. This study sought to investigate the therapeutic effects of simvastatin-loaded porous microspheres (SIM/PMSs) on inflamed tenocytes in vitro and collagenase-induced Achilles tendinitis in vivo. The treatment of SIM/PMSs in lipopolysaccharide (LPS)-treated tenocytes reduced the *mRNA* expressions of pro-inflammatory cytokines (Matrix metalloproteinase-3 (*MMP-3*), cyclooxygenase-2 (*COX-2*), interleukin-6 (*IL-6*), and tumor necrosis factor-α (*TNF-α*)). In addition, the local injection of SIM/PMSs into the tendons of collagenase-induced Achilles tendinitis rat models suppressed pro-inflammatory cytokines (*MMP-3*, *COX-2*, *IL-6*, *TNF-α*, and *MMP-13*). This local treatment also upregulated anti-inflammatory cytokines (*IL-4*, *IL-10*, and *IL-13*). Furthermore, treatment with SIM/PMSs also improved the alignment of collagen fibrils and effectively prevented collagen disruption in a dose-dependent manner. Therefore, SIM/PMSs treatment resulted in an incremental increase in the collagen content, stiffness, and tensile strength in tendons. This study suggests that SIM/PMSs have great potential for tendon healing and restoration in Achilles tendinitis.

Keywords: Achilles tendinitis; simvastatin; porous microspheres; anti-inflammation; tendon healing

1. Introduction

Most acute and chronic tendon injuries are the result of gradual wear and tear to the tendon from either overuse or aging. Tendon problems develop both in athletes and in the general population [1]. Achilles tendinitis is an inflammatory injury characterized by chronic pain and swelling [2]. Injured tendons induce a local inflammation response, which is mediated by the release of inflammation markers including pro-inflammatory cytokines (e.g., interleukin-1β (IL-1β), tumor necrosis factor-α (TNF-α)), matrix metalloproteinases (MMPs; MMP-2, -3, -9, and -13, etc.) and cyclooxygenase-2 (COX-2). Eventually, there is cell damage and/or death as well as disintegration of the extracellular matrix (ECM) at the injured sites. Ultimately, these changes decrease the biomechanical properties (i.e., tensile strength) of the tendon [3–6]. Given its inflammatory nature, non-steroidal

anti-inflammatory drugs (NSAIDs) are one of the treatment approaches for Achilles tendinitis. However, previous studies have found that the long-term use of oral NSAIDs can have adverse side effects, such as gastrointestinal bleeding, ulceration, and perforation [7]. In contrast, the local application of NSAIDs effectively reduced pain and swelling without many of these adverse events; however, their long-term effects are minimal [8,9].

Statins as 3-hyroxy-3-methylglutaryl coenzyme A (HMG-CoA) reductase inhibitors have pleiotropic effects, including anti-inflammatory, antioxidant, immune-modulatory, and angiogenesis stimulation effects [10,11]. Previous studies have found that statins inhibit the secretion of IL-6 and TNF-α in co-cultured human vascular smooth muscle cells (SMCs) and human mononuclear cells (MNCs) or macrophages [12,13]. Despite their positive effects, statins also have adverse effects on muscle, including myalgias, myositis, rhabdomyolysis, and myopathies [14–16]. Eliasson et al. recently reported that simvastatin and atorvastatin have negative effects on tendons due to the decreased mechanical properties of tendon constructs and catabolic changes in the *gene* expression pattern [17]. These adverse effects mainly occur in the setting of high statin doses.

In order to overcome these adverse effects and to investigate the enhanced therapeutic effects of Achilles tendinitis, injectable drug delivery systems have been developed for local application. For instance, porous microspheres are suitable for the controlled and long-term delivery of drugs and proteins [18–20]. We recently developed a porous microsphere using a simple fluidic device and a poly(lactic-co-glycolic acid) (PLGA) polymer as the drug delivery carrier [18–21]. This PLGA polymer is non-toxic, biocompatible, and biodegradable. It is also the Food and Drug Administration (FDA)-approved polymer for clinical applications [22]. In this study, we prepared simvastatin-loaded porous PLGA microspheres (SIM/PMSs). We investigated whether SIM/PMS systems showed anti-inflammatory effects in lipopolysaccharide (LPS)-treated tenocytes in vitro as well as in vivo anti-inflammation, tendon healing, and tissue restoration in a collagenase-induced Achilles tendinitis rat model.

2. Results

2.1. Characterizing PMSs and SIM/PMSs in an In Vitro Drug Release Study

The size, porosity, and shape of the prepared PMSs with or without simvastatin were analyzed using a scanning electron microscope (SEM). The prepared PMSs and two SIM/PMSs with different drug amounts had similar morphologies (Figure 1). The PMSs and SIM/PMSs were also similar in size, at approximately 250–300 μm in diameter. All of the PMSs and SIM/PMSs were highly porous structures. The pores were interconnected. The average pore sizes of the PMSs, SIM (1 mM)/PMSs, and SIM (5 mM)/PMSs were 25.37 ± 2.12 μm, 26.52 ± 3.49 μm, and 26.32 ± 2.08 μm, respectively. The loading amounts of simvastatin per 30 mg of PMSs were 143.51 ± 6.69 μg for SIM (1 mM)/PMSs and 730.88 ± 33.25 μg for SIM (5 mM)/PMSs. The in vitro release profiles of simvastatin from the SIM/PMSs are shown in Figure 2a. On the first day, there was 58.54 ± 0.98 μg of simvastatin released from SIM (1 mM)/PMSs and 184.31 ± 0.78 μg from SIM (5 mM)/PMSs. Over 28 days, the SIM (1 mM)/PMSs and SIM (5 mM)/PMSs released 92.39 ± 1.87 μg and 383.04 ± 4.13 μg of simvastatin, respectively.
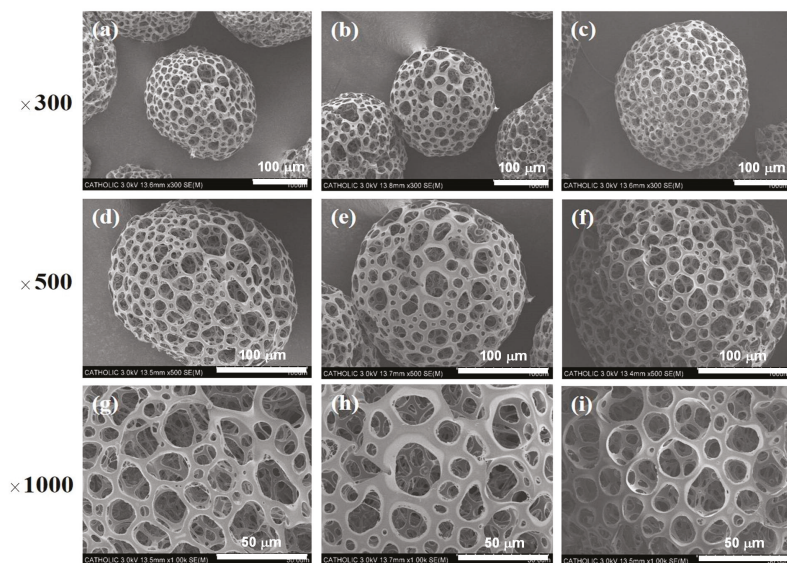
Figure 1. SEM images of porous microspheres (PMSs) (**a**,**d**,**g**), simvastatin (SIM) (1 mM)/PMSs (**b**,**e**,**h**), and SIM (5 mM)/PMSs (**c**,**f**,**i**).
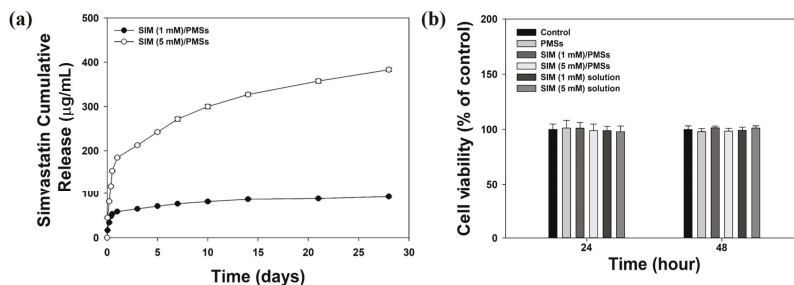
Figure 2. (**a**) In vitro release profiles of simvastatin from SIM (1 mM)/PMSs and SIM (5 mM)/PMSs. (**b**) Cytotoxicity of simvastatin (1 mM and 5 mM), PMSs, SIM (1 mM)/PMSs, and SIM (5 mM)/PMSs at 24 h and 48 h. Error bars represent the means $\pm$ SDs ($n = 5$).

2.2. In Vitro Cytotoxicity

Cytotoxicities for PMSs, simvastatin (1 mM or 5 mM), SIM (1 mM)/PMSs, and SIM (5 mM)/PMSs were measured using a CCK-8 assay kit (Dojindo Inc., Tokyo, Japan) at 24 h and 48 h. Cell viabilities in all groups were maintained at over 96%, indicating that PMSs, simvastatin, and SIM/PMSs had no toxic effects on tenocytes (Figure 2b).

2.3. Anti-Inflammatory Properties of SIM/PMSs in Inflamed Tenocytes

We sought to evaluate the in vitro anti-inflammatory effects of SIM/PMSs in LPS-stimulated tenocytes. The *mRNA* expression levels of pro-inflammatory cytokines, such as *MMP-3*, *COX-2*, *IL-6*, and *TNF-α*, were determined using real-time PCR on days 1 and 3 (Figure 3). The LPS-stimulated tenocytes had the highest *mRNA* levels of pro-inflammatory cytokines on days 1 and 3. The PMSs without simvastatin did not suppress the *mRNA* levels of pro-inflammatory cytokines as did those in the LPS-treated group. This finding suggests that the PMSs alone have no anti-inflammatory properties.

However, the SIM/PMSs significantly and dose-dependently decreased the *mRNA* levels of *MMP-3*, *COX-2*, *IL-6*, and *TNF-α* in LPS-stimulated tenocytes compared to those in the other groups on days 1 and 3 (** $p < 0.01$). This decrease implies that the released simvastatin from the microspheres can suppress inflammatory responses in LPS-stimulated tenocytes.

Figure 3. The relative *mRNA* expression levels of pro-inflammatory cytokines, including: (**a**) *MMP-3*, (**b**) *COX-2*, (**c**) *IL-6*, and (**d**) *TNF-α* in lipopolysaccharide (LPS)-stimulated tenocytes that were cultured with PMSs, SIM (1 mM)/PMSs, and SIM (5 mM)/PMSs on days 1 and 3. Error bars represent the means ± SDs (*n* = 5). (* $p < 0.05$ and ** $p < 0.01$).

2.4. Histopathological Evaluations

We developed collagenase-induced rat models of Achilles tendinitis. We used these animal models to confirm the in vivo suppression of tendon degeneration and anti-inflammatory responses of SIM/PMSs. Histopathological examination with Masson's trichrome staining was performed to determine whether SIM/PMSs can prevent tendon disruption. As shown in Figure 4a, normal tendons had well-aligned collagen fiber organization and no tendon disruption. In contrast, collagenase injection led to severe collagen matrix breakdown with an absence of well-aligned collagen fibers (Figure 4b). In PMSs treatment alone, the severe collagen matrix breakdown was still shown, suggesting that PMSs have no preventative effects on collagen disruption (Figure 4c). However, treatment with simvastatin and SIM/PMSs was sufficient to suppress collagen matrix disruption (Figure 4d–f). The SIM/PMSs treated groups exhibited much more aligned collagen fiber organization and effectively prevented collagen disruption in a dose-dependent manner compared to that of simvastatin. This result suggests that SIM/PMSs have better tendon restoration effects than does simvastatin (Figure 4e,f).
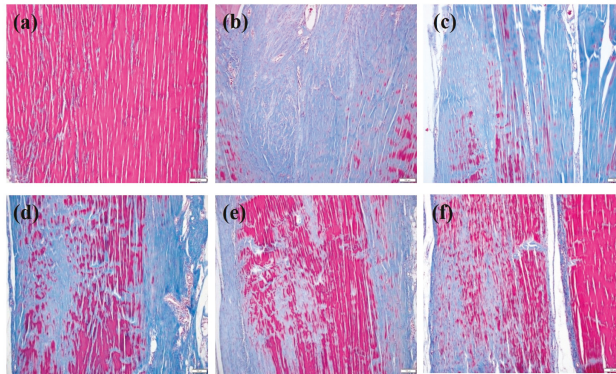
Figure 4. Masson's trichrome staining at 7 weeks after collagenase (Col (I)) injection into tendon tissues, and at 6 weeks after treatment with PMSs, simvastatin, SIM (1 mM)/PMSs, and SIM (5 mM)/PMSs. Groups are categorized as follows: (**a**) control (no treatment); (**b**) Col (I); (**c**) Col (I) + PMSs; (**d**) Col (I) + simvastatin; (**e**) Col (I) + SIM (1 mM)/PMSs, and (**f**) Col (I) + SIM (5 mM)/PMSs. Scale bar: 100 μm. Red: collagen fibers; Blue: collagen matrix breakdown.

2.5. In Vivo Tendon Restorative Effects of SIM/PMSs and Biomechanical Study

In order to further demonstrate the tendon restorative effects of SIM/PMSs, we performed biomechanical studies, including stiffness and tensile strengths, of tendon tissues. The stiffness and tensile strengths of the tendon tissues in the collagenase-treated group and PMSs-treated group were much lower than were those in the control (normal) group at 6 weeks (Figure 5). Simvastatin increased the stiffness and tensile strengths of the tendons compared to that of the collagenase-treated group and PMSs-treated group. However, the tendon healing effects of both SIM/PMSs groups were much more effective in a dose-dependent manner than were those of simvastatin (** $p < 0.01$). A hydroxyproline assay was performed at six weeks after the drug treatments in order to determine the change in collagen content in the Achilles tendinitis animal model. The hydroxyproline contents of the Achilles tendon in the collagenase-treated group and PMSs-treated group were significantly lowered than were those in the control (normal) group (Figure 6). Treatments with simvastatin and two SIM/PMSs increased the hydroxyproline content significantly more than did treatment in the collagenase-treated group and PMSs-treated group (** $p < 0.01$). The SIM/PMSs-treated groups also had much higher hydroxyproline content in a dose-dependent manner than did the simvastatin-treated group (** $p < 0.01$).
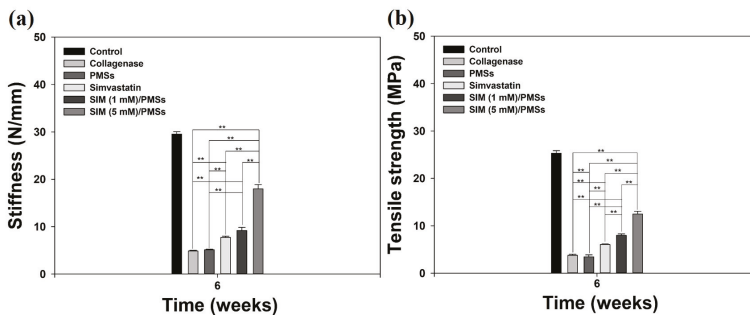
Figure 5. (**a**) Stiffness and (**b**) tensile strengths of Achilles tendon tissues isolated from collagenase-induced Achilles tendinitis rat models in each group at 6 weeks after treatments with PMSs, simvastatin, SIM (1 mM)/PMSs, and SIM (5 mM)/PMSs. Data represent means ± SDs ($n = 4$). (** $p < 0.01$).
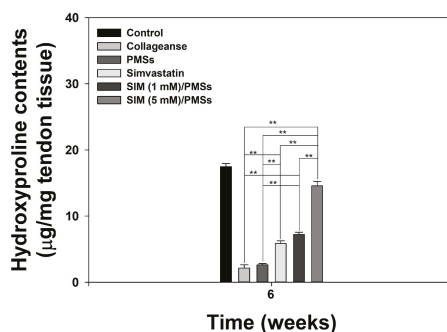
Figure 6. Hydroxyproline contents in Achilles tendon tissues from collagenase-induced Achilles tendinitis rat models 6 weeks after treatment with PMSs, simvastatin, SIM (1 mM)/PMSs, and SIM (5 mM)/PMSs. Data represent means ± SDs (*n* = 4), (** *p* < 0.01).

2.6. In Vivo Anti-Inflammatory Effects of SIM/PMSs

We next sought to further investigate the in vivo anti-inflammatory effects of SIM/PMSs in collagenase-induced Achilles tendinitis rat models. The *mRNA* levels of pro-inflammatory cytokines (*MMP-3*, *COX-2*, *IL-6*, *TNF-α*, and *MMP-13*), as well as anti-inflammatory cytokines (*IL-4*, *IL-10*, and *IL-13*), were measured in whole blood samples collected from the rats in each group. Figure 7 shows that the *mRNA* levels of all of pro-inflammatory cytokines in the collagenase-treated group were significantly upregulated (up to over 5-fold) compared to those in the control (normal) group. There were no significant differences in the *mRNA* levels between the collagenase-treated group and PMSs-treated group. At two weeks, the *mRNA* levels of pro-inflammatory cytokines in the two SIM/PMSs-treated groups were similar or slightly higher than those in the simvastatin-treated groups. However, at six weeks, the *mRNA* levels in both SIM/PMSs-treated groups were much lower than were those in the simvastatin-treated group, in a dose-dependent manner (** *p* < 0.01). The *mRNA* levels of anti-inflammatory cytokines (*IL-4*, *IL-10*, and *IL-13*) in the collagenase-treated group (or PMSs-treated groups) were similarly maintained or slightly lower than were those in the control (normal) group during the 6 weeks (Figure 8). In contrast, groups treated with simvastatin (the real treated dose; 105 µg/rat), SIM (1 mM)/PMSs (the real treated dose; 2.39 µg/rat), and SIM (5 mM)/PMSs (the real treated dose; 12.18 µg/rat) had increased *mRNA* levels of anti-inflammatory cytokines. Simvastatin had much higher levels than did the two SIM/PMSs-treated groups at two weeks. This result can be explained by the fact that the treated dose of simvastatin was much higher than were those of the two SIM/PMSs groups. However, the two SIM/PMSs-treated groups displayed much higher *mRNA* levels of anti-inflammatory cytokines in a dose-dependent manner than did the simvastatin-treated group at 6 weeks (** *p* < 0.01). These data suggest that SIM/PMSs were more effective than was simvastatin at suppressing the inflammatory responses induced by collagenase injection into tendon tissues. This result is mostly likely because SIM/PMSs gradually released simvastatin molecules from the microspheres over a long period of time. Simvastatin is a small molecular weight molecule that may passively cross into the blood stream and be easily excreted from local treatment sites. Therefore, the simvastatin group may have experienced a shorter exposure period to the simvastatin than did the SIM/PMSs groups.
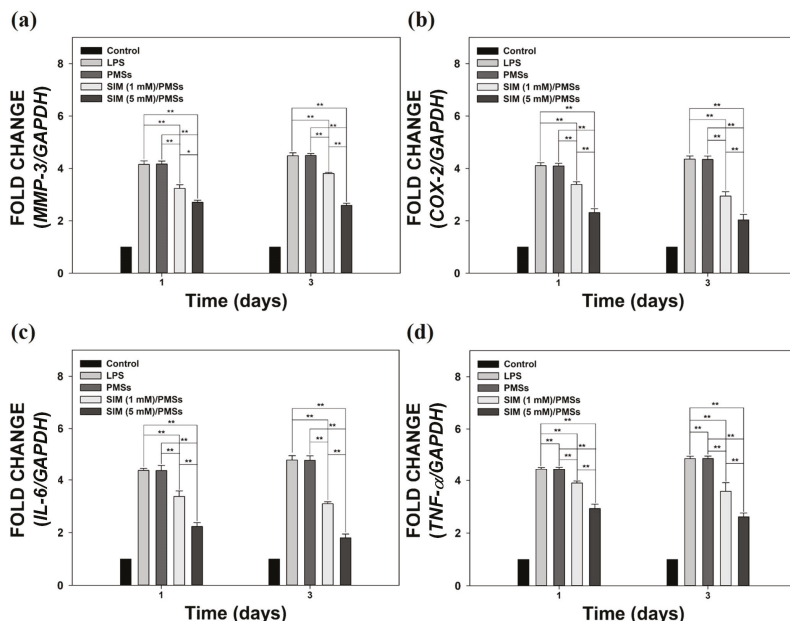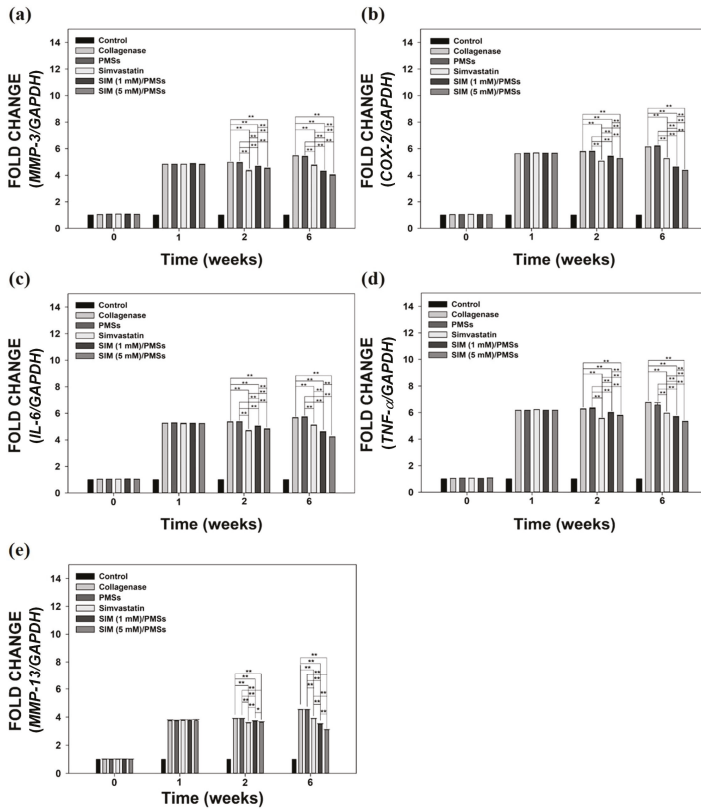
Figure 7. The relative *mRNA* expression levels of pro-inflammatory cytokines, including: (**a**) *MMP-3*; (**b**) *COX-2*, (**c**) *IL-6*, (**d**) *TNF-α*, and (**e**) *MMP-13* in whole blood samples from a collagenase-induced Achilles tendinitis rat model in each group. Whole blood samples were collected from collagenase-induced Achilles tendinitis rat models in each group at 0, 1, 2, and 6 weeks after treatments with PMSs, simvastatin, SIM (1 mM)/PMSs, and SIM (5 mM)/PMSs. Each *mRNA* expression level was determined using real time-PCR analysis. Data represent means ± SDs ($n = 4$), (* $p < 0.05$ and ** $p < 0.01$).
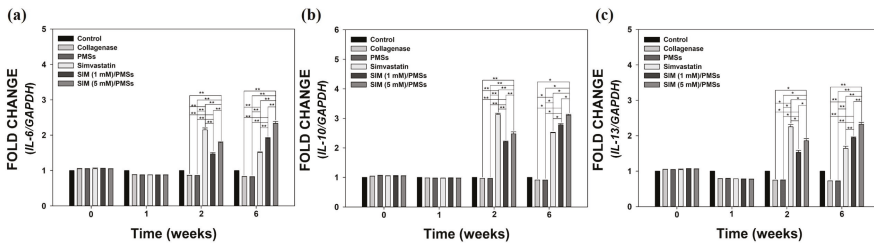
Figure 8. The relative *mRNA* expression levels of anti-inflammatory cytokines, including: (**a**) *IL-4*, (**b**) *IL-10*, and (**c**) *IL-13* in whole blood samples from the collagenase-induced Achilles tendinitis rat model in each group. Whole blood samples were collected from the rat models in each group at 0, 1, 2, and 6 weeks after treatment with PMSs, simvastatin, SIM (1 mM)/PMSs, and SIM (5 mM)/PMSs. Each *mRNA* expression level was determined using real time-PCR analysis. Data represent means ± SDs ($n = 4$), (* $p < 0.05$ and ** $p < 0.01$).

3. Discussion

Achilles tendinitis occurs in both active and inactive individuals due to overuse or aging. Achilles tendinitis is accompanied by pain, swelling, and impaired tendon function in its early stage [23]. It eventually can lead to partial or total tendon rupture. Tendon disruption and injury provokes local inflammation responses by inducing pro-inflammatory cytokines, MMPs, and ECM disintegration [6]. Ultimately, this inflammation impairs the biomechanical properties of the tendon tissues. Prior reports have suggested that statins, 3-hydroxy-3-methylglutaryl coenzyme A (HMG-CoA) reductase inhibitors, have pleiotropic effects including anti-inflammation, anti-oxidation, and immune-modulation effects [24,25]. Retrospective studies have reported that there are double-sided characteristics on statin-associated tendon disorders. Simvastatin may have a protective role in tendinopathies in patients with severe hyperlipidemia [26–28]. Treatment with statins may also enhance tendon healing through stimulation of the COX-2/prostaglandin E2 receptor 4 (PGE2 EP4) pathway. Statins may also enhance anterior cruciate ligament (ACL) healing through their effects on angiogenesis and osteogenesis [29]. In contrast, other studies have suggested that several common side effects of statins (i.e., muscle weakness and pain) actually increase the risk of tendinopathy and rupture [30,31] and tendon complications [26,30,32]. However, previous in vivo studies showed that statin treatment reduced the mechanical properties of tendon constructs and increased the *gene* expressions of *MMPs* (such as *MMP-1*, *MMP-3*, and *MMP-13*) in the ECM of tendons [31,32]. Ultimately, there remains active controversy regarding statins' role as either detrimental or beneficial to tendon healing.

In this study, we developed simvastatin-loaded porous microspheres (SIM/PMSs). These microspheres were built using a simple fluidic device consisting of a discontinuous phase channel (homogenized gelatin and PLGA solution with or without simvastatin) and a continuous phase channel (as previously described by our group) [18–21]. Simple fluidic devices are very useful to control the size and porosity of the microspheres. The prepared PMSs, with or without simvastatin, were spherical shapes approximately 250–300 μm in diameter. Their pores were interconnected and 25–30 μm in size. Hydrophobic simvastatin could be readily encapsulated within hydrophobic PLGA porous microspheres. Initially, the SIM/PMSs allowed fast drug release given the diffusion from the surface of highly porous microspheres. However, the release of simvastatin from the microspheres was incomplete over the four weeks given polymer degradation. This result suggests that SIM/PMSs are suitable for long-term drug delivery.

The in vitro anti-inflammatory effects of PMSs were investigated using tenocytes, because they are fibroblast-like differentiated cells found throughout the tendon structure. Tenocytes synthesize ECM and induce the assembly of early collagen fibers (as the basic units of the tendon). The in vitro inflammatory environment was mimicked by treating LPS to the tenocytes. As previously reported, the LPS-treated cells increased their expression of certain cytokines, including TNF-α, IL-6, and IL-1β. These cytokines further stimulate tenocytes to induce pro- and anti-inflammatory cytokines, including TNF-α, IL-6, IL-10, IL-1β, COX-2, and ECM-degrading enzymes, such as MMP-1, -3, and -13 [33,34]. Previous studies have reported that statins have anti-inflammatory activities on several cells. For example, LPS-stimulated macrophages that were exposed to statins decreased their expression of IL-6 and TNF-α [12,35]. Statins also inhibited macrophage production of IL-6, IL-8, MMP-1, -3, and -9 [36,37]. Consistent with the findings of previous studies, we also demonstrated that treatment of LPS-treated tenocytes with PMSs alone does not reduce the *mRNA* levels of pro-inflammatory cytokines (i.e., *MMP-3*, *COX-2*, *IL-6*, and *TNF-α*). In contrast, SIM/PMSs could significantly decrease their *mRNA* levels in a dose-dependent manner. These data suggest that SIM/PMSs suppress inflammation responses by downregulating the *mRNA* expression levels of multiple pro-inflammatory cytokines in inflamed tenocytes.

Injection of collagenase type I consistently leads to tendon disruption accompanied by an inflammatory response [38]. Therefore, collagenase injection serves as an adequate method of developing an Achilles tendinitis model. In particular, injection of collagenase into a tendon disrupts collagen fibers, changes the biochemical and biomechanical properties of the tendon, and more closely

resembles the main histopathologic features and dysfunctions of human tendinopathy [38]. Therefore, we used a collagenase-induced Achilles tendinitis rat model to study the in vivo anti-inflammatory and tendon-healing effects of SIM/PMSs. Under histological examination with Masson's trichrome staining, we found that tendon treatment with collagenase led to destruction of the well-aligned collagen fiber organization and severe collagen matrix breakdown. The PMSs did not prevent collagen matrix disruption. In contrast, SIM/PMSs effectively decreased the collagen disruption and repaired collagen organization in a dose-dependent manner. Although simvastatin also prevented collagen matrix disruption, its therapeutic effect is lower than those of the two SIM/PMSs groups. Previous study reported that an increase in the hydroxyproline content is directly correlated to early maturation of fibroblasts, early parallel arrangement of collagen fibers, and bundle formation [39]. This group also found that there is a close relationship between the absolute amount of collagen and mechanical strength. In this study, the local treatment of SIM/PMSs on collagenase-treated tendon tissues had beneficial effects on the healing tendon. SIM/PMSs enhanced the hydroxyproline content of the treated tendon tissues more so than did collagenase. This result correlated with increased collagen fibrin organization using Masson's trichrome stain. The collagen content increased after SIM/PMS treatment. Therefore, the stiffness and tensile strength of tendon tissues in the SIM/PMS-treated groups were markedly enhanced compared to those of the other groups (including collagenase, PMSs, and simvastatin-treated groups). These data suggest that using SIM/PMSs as a long-term simvastatin delivery system is useful for restoration of the tendon tissues in collagenase-induced Achilles tendinitis.

Tendon injuries (i.e., ruptures or tendinopathy) typically heal in three different phases. These are the inflammatory phase, proliferative phase or collagen-producing phase, and finally the remodeling phase [40,41]. During this healing process, the modulation of multiple pro- and anti-inflammatory cytokines plays an important role in improving tendon healing [42]. Excessive pro-inflammatory cytokines provoke inflammatory reactions, thereby leading to cell damage and ECM disintegration at injured sites [6]. In contrast, anti-inflammatory cytokines attract fibroblasts to restore the injured tissues [43]. In order to investigate the in vivo anti-inflammatory effects of SIM/PMSs on collagenase-induced Achilles tendinitis models, we monitored the *mRNA* levels of both pro-inflammatory cytokines (*MMP-3*, *COX-2*, *IL-6*, *TNF-α*, and *MMP-13*) and anti-inflammatory cytokines (*IL-4*, *IL-10*, and *IL-13*). We made these measurements from the blood at scheduled time points, because an indirect assessment of inflammatory markers in the blood can support the hypothesis of local inflammation at injured sites [44,45]. At 1, 2, and 6 weeks after collagenase injection, the *mRNA* levels of the pro-inflammatory cytokines were significantly increased. In contrast, the *mRNA* levels of anti-inflammatory cytokines did not increase. Compared to the collagenase-treated group, PMSs alone did not affect the *mRNA* expression levels of pro-inflammatory cytokines or anti-inflammatory cytokines, indicating that PMSs have no anti-inflammatory activity. In contrast, treatment with simvastatin and SIM/PMSs can downregulate pro-inflammatory cytokines and upregulate anti-inflammatory cytokines. However, the therapeutic effects of SIM/PMSs were superior to those of simvastatin.

This study demonstrates that SIM/PMSs have many beneficial therapeutic effects, including anti-inflammation and tendon healing effects, on a collagenase-induced Achilles tendinitis rat model. Interestingly, treatment with SIM/PMSs as a long-term simvastatin delivery system had much better therapeutic efficacy than did simvastatin alone. As our group has previously described, the biodegradation of microspheres (as a long-term drug delivery system) can be tailored from a few weeks to several months depending on the polymer compositions (such as the ratio of poly(lactic acid) to poly(glycolic acid)). These compositions ultimately influence the drug release rates from the drug delivery system [21]. Treatment with high doses of simvastatin alone also had positive effects on Achilles tendinitis at first. However, its therapeutic effects are short-lived, because this small molecular drug eventually passively diffuses into the blood stream and away from the injured sites. In order to achieve good therapeutic effects with a small molecular drug, therefore, repeated injections would be needed. Regardless, side effects and toxicities must be considered. Moreover, our study has some

limitations, including the lack of *mRNA* expression levels for pro- and anti-inflammatory cytokines in tissues as well as no pharmacokinetic data of simvastatin and SIM/PMSs after local treatments. Despite these limitations, our study showed that using SIM/PMSs as a long-term delivery system will have a great potential to suppress inflammatory responses and enhance healing and restoration of tendon tissues.

4. Materials and Methods

4.1. Materials

PLGA (50:50; Resomer® RG505) was supplied by Boehringer Ingelheim (Ingelheim, Germany). Poly vinyl alcohol (PVA, molecular weight: 13,000–23,000, 98% hydrolyzed), dichloromethane (DCM), gelatin from porcine skin, simvastatin (SIM), and LPS were obtained from Sigma-Aldrich (St. Louis, MO, USA). Cellulose-ester dialysis membrane (MWCO; 6–8 kDa) was obtained from Spectrum Laboratories (Milpitas, CA, USA). Dulbecco's modified Eagle's medium (DMEM), fetal bovine serum (FBS), phosphate-buffered saline (PBS), and penicillin-streptomycin were obtained from Gibco (Rockville, MD, USA).

4.2. Fabrication of SIM-Loaded Porous Microspheres (SIM/PMSs)

In order to fabricate SIM/PMSs, a fluidic device method was used, as previously described [18–21]. Briefly, PLGA (2 weight % (wt %)), with or without simvastatin (1 or 5 mM), was dissolved in DCM (7 mL). Gelatin (7.5 wt %) and PVA (2 wt %) were dissolved in deionized water (DW, 10 mL). Next, the gelatin (3 mL) and PVA (0.5 mL) solutions were added to the PLGA solution with or without SIM. These mixtures were emulsified with a homogenizer (Ultra-Turrax T-25 Basic, IKA, Woonsocket, RI, USA) at 13,500 rpm for 1 min. The emulsified solution was introduced into the discontinuous phase. Another PVA (2 wt %) solution was prepared as a continuous phase. In order to make PMSs, the continuous phase and discontinuous phase flow rates were 0.5 mL/min and 0.05 mL/min, respectively. The emulsion droplets were placed in warm water (45 °C) and gently stirred for 24 h to remove any residual gelatin within the microspheres and DCM. The fabricated microspheres were washed three times with warm DW, collected, and lyophilized for three days. The PMSs are designated according to the amount of simvastatin as PMSs (no simvastatin), SIM (1 mM)/PMSs, and SIM (5 mM)/PMSs, respectively.

4.3. Characterization of PMSs and SIM/PMSs

The morphologies of the PMSs, SIM (1 mM)/PMSs, and SIM (5 mM)/PMSs were observed using scanning electron microscopy (SEM, S-2300, Hitachi, Tokyo, Japan). Each sample was coated with platinum (Pt) using a sputter coater (Eiko IB, Tokyo, Japan), and examined at an accelerated voltage of 3 kV. The average pore sizes of randomly selected microspheres in each group ($n = 50$ pores/group) were determined using Image J (Ver. 1.2, Bethesda, MD, USA) based on the SEM images.

In order to determine the loading amount of simvastatin within SIM (1 mM)/PMSs and SIM (5 mM)/PMSs, 30 mg of each sample was dissolved in DCM. The loading amount of SIM was analyzed at 250 nm using the UV/Vis spectrophotometer (UV-1800, Shimadzu, Kyoto, Japan).

4.4. In Vitro Drug Release Study

In order to evaluate in vitro simvastatin release from the microspheres, the samples (10 mg) in each group were dispersed in a 50 mL conical tube including 1 mL PBS solution (pH 7.4) as the release medium. This mixture was gently shaken at a rate of 100 rpm in a shaking water bath at 37 °C. At the pre-determined time intervals, the PBS was replaced with fresh PBS medium. The amount of simvastatin that was released from the microspheres was determined at 250 nm using the UV/Vis spectrophotometer.

4.5. In Vitro Cytotoxicity

The cytotoxicity test of simvastatin, PMSs, and SIM/PMSs was evaluated in tenocytes. Tenocytes (5×10^4 cells/well) were seeded in 96-well tissue culture plates containing simvastatin (1 mM), simvastatin (5 mM), 10 mg of PMSs, SIM (1 mM)/PMSs, and SIM (5 mM)/PMSs and maintained with DMEM supplemented with 10% FBS and 1% antibiotics. After 1 day or 2 days, the medium was aspirated and CCK-8 proliferation reagents were added. According to the manufacturer's instructions, the cells were further incubated for 1 h at 37 °C. The optical density of the live cells was measured using a Flash Multimode Reader at 450 nm.

4.6. In Vitro Anti-Inflammatory Effects of SIM/PMSs on Inflamed Tenocytes

The in vitro anti-inflammatory effects of SIM/PMSs were tested using tenocytes that were isolated from the Achilles tendons of Sprague Dawley (SD) rats (8-week-old males, DooYeol Biotech, Seoul, Korea). The tenocyte isolation was performed as previously described [21]. The experimental protocol for this isolation was approved by the Institutional Animal Care and Use Committee of the Korea University Medical Center (KOREA-2016-0250, 29 November 2016).

In order to demonstrate the in vitro anti-inflammatory effects of SIM/PMSs on LPS-treated tenocytes, we analyzed the *mRNA* levels of *MMP-3*, *COX-2*, *IL-6*, and *TNF-α* using real-time PCR. Tenocytes (1×10^5 cells/mL/well) were carefully seeded on the PMSs (10 mg) or SIM (1 mM or 5 mM)/PMSs in 24-well tissue culture plates. After 24 h of incubation, LPS (1 µg/mL) was applied to the tenocytes in all groups. After three days, the cells were harvested. The total RNA was isolated from cells in each group using an RNeasy Plus Mini Kit (Qiagen, Valencia, CA, USA) according to the manufacturer's instructions. The total RNA (1 µg) was reverse-transcribed into cDNA using AccuPower RT PreMix (Bioneer, Daejeon, Korea) according to the manufacturer's instructions. The primers and PCR conditions used for amplification of *MMP-3*, *COX-2*, *IL-6*, and *TNF-α* are as follows: *MMP-3*; (F) 5′-ACC TGT CCC TCC AGA ACC TG-3′, (R) 5′-AAC TTC ATA TGC GGC ATC CA-3′, *COX-2*; (F) 5′-CAG CCA TAC TAT GCC TCG GA-3′, (R) 5′-GGA TGT CTT GCT CGT CGT TC-3′, *IL-6*; (F) 5′-CCG TTT CTA CCT GGA GTT TG-3′, (R) 5′-GTT TGC CGA GTA GAC CTC AT-3′, and *TNF-α*; (F) 5′-CTC CCA GAA AAG CAA GCA AC-3′, (R) 5′-CGA GCA GGA ATG AGA AGA GG-3′. PCR amplification and detection were performed using an ABI7300 Real-Time Thermal Cycler (Applied Biosystems, Foster, CA, USA). The relative *mRNA* levels of *MMP-3*, *COX-2*, *IL-6*, and *TNF-α* were normalized to those of glyceraldehyde 3-phophate dehydrogenase (*GAPDH*).

4.7. Animal Models of Collagenase-Induced Achilles Tendinitis

We established an Achilles tendinitis animal model (using collagenase injection) to demonstrate the in vivo anti-inflammatory and tendon healing effects of SIM/PMSs, as described in our previous study [21]. The in vivo animal experiments were performed and approved by the Institutional Animal Care and Use Committee of the Korea University Medical Center (KOREA-2016-0250, 29 November 2016). SD rats (8-week-old males, DooYeol Biotech, Seoul, Korea) were anesthetized with isoflurane (1% *w/v* in 2 L oxygen). The rats received a single injection of 50 µL of collagenase type I in the right Achilles tendon (Col I) (50 mg/mL inn PBS (pH 7.4)). Seven days after the collagenase injection, 10 mg of the microspheres were mixed with 1 mL of 2% carboxymethyl cellulose (CMC) solution. Randomly selected rats received an injection of 50 µL of CMC solution of the microspheres. The real treatment dosages of simvastatin in each SIM/PMS group were 2.39 µg/rat for SIM (1 mM)/PMSs and 12.18 µg/rat for SIM (5 mM)/PMSs. Simvastatin (105 µg/rat) was used as the drug control, and was injected into the Achilles tendon of control animals. Six weeks after treatment with PMSs, simvastatin, SIM (1 mM)/PMSs, and SIM (5 mM)/PMSs, the rats were euthanized for further analysis. The rats were divided into the following six groups: (I) control (no treatment), (II) Col (I) (collagenase treatment), (III) Col (I) + PMSs, (IV) Col (I) + simvastatin, (V) Col (I) + SIM (1 mM)/PMSs, and (VI) Col (I) + SIM (5 mM)/PMSs.

4.8. Histopathological Evaluations

The calcaneus-Achilles tendon specimens were harvested from the sacrificed rats and fixed in 3.7% (*v/v*) paraformaldehyde for histological evaluations. The specimens were then dehydrated in ethanol and embedded in paraffin. The tissue blocks were sectioned longitudinally in the rotary microtome (HM 355S automatic microtomes, Thermo Scientific, Waltham, MA, USA) at 5 μm thickness. These sliced tissue samples were stained with Masson's trichrome.

4.9. Biomechanical Test

The tendon specimens were fixed to a specially designed device, which allowed the specimen to be oriented such that a tensile load could be applied along the axis of the tendon. The fixed specimen device was tested on an Instron Mechanical Tester (AG-10KNX, Shimadzu, Kyoto, Japan) at a cross-head speed of 5 mm/min. A 1 newton load cell was used to measure the loading force. The ultimate tensile strength (defined as maximum stress or force per unit area) and stiffness (force required per unit displacement) were also obtained.

4.10. Hydroxyproline Assay

In order to investigate the Achilles tendon healing effects of SIM/PMSs, the collagen contents of Achilles tendon tissues in each group were demonstrated by measuring the hydroxyproline assay. In brief, 5 mg of Achilles tendon tissue was hydrolyzed with 6 normal HCl under heating at 110 °C for 12 h. The HCl was evaporated at 60 °C, and the hydrolyzed tissues were reconstituted in DW (20 mL) and neutralized with NaOH to pH 7.0. Chloramine T solution (50 μL, 60 mM) was mixed with 100 μL of standard hydroxyproline or samples in a 96-well plate to initiate hydroxyproline oxidation. After 20 min of incubation at room temperature (RT), the chloramine T was destroyed by adding 50 μL of perchloric acid (HClO$_4$) to each well. The absorbance was read using a Flash Multimode Reader (Thermo Scientific, San Jose, CA, USA) at 550 nm.

4.11. In Vivo Anti-Inflammatory Effects of SIM/PMSs on Collagenase-Induced Achilles Tendinitis

The in vivo anti-inflammatory effects of SIM/PMSs on Achilles tendinitis were investigated by analyzing the *gene* expressions of pro-inflammatory cytokines (*MMP-3*, *COX-2*, *IL-6*, *TNF-α*, and *MMP-13*) and anti-inflammatory cytokines (*IL-4*, *IL-10*, and *IL-13*) using real-time PCR. The *gene* expression levels of these pro- and anti-inflammatory cytokines were determined using the total RNA extracted from the whole blood in each group. The whole blood was collected from an ear vein of a rat in each group at weeks: 0 (no treatment), 1 (1 week after collagenase treatment, 2 (2 weeks after collagenase treatment and 1 week after treatment of SIM or PMSs with or without SIM), and 6 (7 weeks after collagenase treatment and 6 weeks after treatment of SIM or PMSs with or without SIM). The total RNA was extracted from the collected whole blood samples at the pre-determined time points using a QlAamp RNA Blood Mini Kit (Qiagen, Valencia, CA, USA). The total RNA concentration in each group was measured using a Nanodrop spectrometer (ND-1000 spectrometer, NanoDrop Technologies Inc., Wilmington, DE, USA). The total RNA (1 μg) was reverse-transcribed into cDNA. The same primer sequences for the pro-inflammatory cytokines (including *MMP-3*, *COX-2*, *IL-6*, and *TNF-α genes*) were used as described above for the in vitro anti-inflammatory studies. The primer sequence of *MMP-13* was as follows: *MMP-13*; (F) 5'-AAG GAG CAT GGC GAC TTC TA-3', (R) 5'-GGT CCT TGG AGT GGT CAA GA-3'. The primer sequences of the anti-inflammatory cytokines, including *IL-4*, *IL-10*, and *IL-13*, were as follows: *IL-4*; (F) 5'-ACA GGA GAA GGG ACG CCA T-3', (R) 5'-GAA GCC CTA CAG ACG AGC TCA-3', *IL-10*; (F) 5'-GGT TGC CAA GCC TTA TCG GA-3', (R) 5'-ACC TGC TCC ACT GCC TTG CT-3' and *IL-13*; (F) 5'-AGA CCA GAC TCC CCT GTG CA-3', (R) 5'-TGG GTC CTG TAG ATG GCA TTG-3'. PCR amplification and detection was performed using a ABI7300 Real-Time Thermal Cycler (Applied Biosystems) using a DyNAmo$^{\text{TM}}$ SYBR® Green qPCR Kit (Finnzymes, Espoo, Finland). The relative *gene* expression levels of pro-inflammatory cytokines (*MMP-3*, *COX-2*, *IL-6*,

TNF-α, and *MMP-13*) and anti-inflammatory cytokines (*IL-4*, *IL-10*, and *IL-13*) were normalized to those of *GAPDH*.

4.12. Statistical Analysis

Data are presented as means ± standard deviations. Statistical comparisons were carried out via one-way analysis of variance (ANOVA) using Systat software ver. 13 (SigmaPlot, IL, USA). Differences were considered statistically significant at * $p < 0.05$ and ** $p < 0.01$.

5. Conclusions

We used a simple fluidic device to develop a long-term simvastatin delivery system using porous microspheres. The SIM/PMSs are capable of long-term simvastatin delivery in a sustained manner. This treatment effectively and dose-dependently decreased the *mRNA* levels of pro-inflammatory cytokines in the LPS-treated tenocytes. In vivo studies demonstrated that SIM/PMSs significantly decreased the levels of pro-inflammatory cytokines, while they markedly increased anti-inflammatory cytokine levels. These anti-inflammatory effects of SIM/PMSs may ultimately allow improved tendon healing and restoration by increasing the collagen content, stiffness, and the tissue's overall tensile strength.

Author Contributions: Sung Eun Kim, Kyeongsoon Park, and Hae-Ryong Song conceived and designed the study; Chandong Jeong, Sung Eun Kim, and Kyu-Sik Shim performed the in vitro and in vivo experiments; Chandong Jeong, Sung Eun Kim, Hak-Jun Kim, Mi Hyun Song, and Kyeongsoon Park analyzed the in vivo data; and Chandong Jeong, Sung Eun Kim, and Kyeongsoon Park wrote the paper. All authors reviewed the final paper.

Conflicts of Interest: The authors declare no conflict of interest.

References

1. Lopez, R.G.; Jung, H.G. Achilles tendinosis: Treatment options. *Clin. Orthop. Surg.* **2015**, *7*, 1–7. [CrossRef] [PubMed]
2. Maffulli, N.; Khan, K.M.; Puddu, G. Overuse tendon conditions: Time to change a confusing terminology. *Arthroscopy* **1998**, *14*, 840–843. [CrossRef]
3. Sharma, P.; Maffulli, N. Tendon injury and tendinopathy: Healing and repair. *J. Bone Jt. Surg. Am.* **2005**, *87*, 187–202.
4. Nagase, H.; Visse, R.; Murphy, G. Structure and function of matrix metalloproteinases and timps. *Cardiovasc. Res.* **2006**, *69*, 562–573. [CrossRef] [PubMed]
5. Langberg, H.; Boushel, R.; Skovgaard, D.; Risum, N.; Kjaer, M. Cyclo-oxygenase-2 mediated prostaglandin release regulates blood flow in connective tissue during mechanical loading in humans. *J. Physiol.* **2003**, *551*, 683–689. [CrossRef] [PubMed]
6. Schulze-Tanzil, G.; Al-Sadi, O.; Wiegand, E.; Ertel, W.; Busch, C.; Kohl, B.; Pufe, T. The role of pro-inflammatory and immunoregulatory cytokines in tendon healing and rupture: New insights. *Scand. J. Med. Sci. Sports* **2011**, *21*, 337–351. [CrossRef] [PubMed]
7. Moore, R.A.; Tramer, M.R.; Carroll, D.; Wiffen, P.J.; McQuay, H.J. Quantitative systematic review of topically applied non-steroidal anti-inflammatory drugs. *BMJ* **1998**, *316*, 333–338. [CrossRef] [PubMed]
8. Fredberg, U.; Stengaard-Pedersen, K. Chronic tendinopathy tissue pathology, pain mechanisms, and etiology with a special focus on inflammation. *Scand. J. Med. Sci. Sports* **2008**, *18*, 3–15. [CrossRef] [PubMed]
9. Smidt, N.; van der Windt, D.A.; Assendelft, W.J.; Deville, W.L.; Korthals-de Bos, I.B.; Bouter, L.M. Corticosteroid injections, physiotherapy, or a wait-and-see policy for lateral epicondylitis: A randomised controlled trial. *Lancet* **2002**, *359*, 657–662. [CrossRef]

10. Tsai, W.C.; Yu, T.Y.; Lin, L.P.; Cheng, M.L.; Chen, C.L.; Pang, J.H. Prevention of simvastatin-induced inhibition of tendon cell proliferation and cell cycle progression by geranylgeranyl pyrophosphate. *Toxicol. Sci.* **2016**, *149*, 326–334. [CrossRef] [PubMed]

11. McFarland, A.J.; Davey, A.K.; Anoopkumar-Dukie, S. Statins reduce lipopolysaccharide-induced cytokine and inflammatory mediator release in an in vitro model of microglial-like cells. *Med. Inflamm.* **2017**, *2017*, 2582745. [CrossRef] [PubMed]

12. Rosenson, R.S.; Tangney, C.C.; Casey, L.C. Inhibition of proinflammatory cytokine production by pravastatin. *Lancet* **1999**, *353*, 983–984. [CrossRef]

13. Loppnow, H.; Zhang, L.; Buerke, M.; Lautenschlager, M.; Chen, L.; Frister, A.; Schlitt, A.; Luther, T.; Song, N.; Hofmann, B.; et al. Statins potently reduce the cytokine-mediated IL-6 release in SMC/MNC cocultures. *J. Cell. Mol. Med.* **2011**, *15*, 994–1004. [CrossRef] [PubMed]

14. Marschner, I.C.; Colquhoun, D.; Simes, R.J.; Glasziou, P.; Harris, P.; Singh, B.B.; Friedlander, D.; White, H.; Thompson, P.; Tonkin, A.; et al. Long-term risk stratification for survivors of acute coronary syndromes. Results from the long-term intervention with pravastatin in ischemic disease (lipid) study. Lipid study investigators. *J. Am. Coll. Cardiol.* **2001**, *38*, 56–63. [CrossRef]

15. Hayem, G. Statins and muscles: What price glory? *Jt. Bone Spine* **2002**, *69*, 249–251. [CrossRef]

16. Kashani, A.; Sallam, T.; Bheemreddy, S.; Mann, D.L.; Wang, Y.; Foody, J.M. Review of side-effect profile of combination ezetimibe and statin therapy in randomized clinical trials. *Am. J. Cardiol.* **2008**, *101*, 1606–1613. [CrossRef] [PubMed]

17. Eliasson, P.; Svensson, R.B.; Giannopoulos, A.; Eismark, C.; Kjaer, M.; Schjerling, P.; Heinemeier, K.M. Simvastatin and atorvastatin reduce the mechanical properties of tendon constructs in vitro and introduce catabolic changes in the gene expression pattern. *PLoS ONE* **2017**, *12*, e0172797. [CrossRef] [PubMed]

18. Kim, S.E.; Yun, Y.P.; Shim, K.S.; Park, K.; Choi, S.W.; Shin, D.H.; Suh, D.H. Fabrication of a BMP-2-immobilized porous microsphere modified by heparin for bone tissue engineering. *Coll. Surf. B Biointerfaces* **2015**, *134*, 453–460. [CrossRef] [PubMed]

19. Park, J.W.; Yun, Y.P.; Park, K.; Lee, J.Y.; Kim, H.J.; Kim, S.E.; Song, H.R. Ibuprofen-loaded porous microspheres suppressed the progression of monosodium iodoacetate-induced osteoarthritis in a rat model. *Coll. Surf. B Biointerfaces* **2016**, *147*, 265–273. [CrossRef] [PubMed]

20. Lee, J.Y.; Kim, S.E.; Yun, Y.P.; Choi, S.W.; Jeon, D.I.; Kim, H.J.; Park, K.; Song, H.R. Osteogenesis and new bone formation of alendronate-immobilized porous plga microspheres in a rat calvarial defect model. *J. Ind. Eng. Chem.* **2017**, *52*, 277–286. [CrossRef]

21. Kim, S.E.; Yun, Y.P.; Shim, K.S.; Jeon, D.I.; Park, K.; Kim, H.J. In vitro and in vivo anti-inflammatory and tendon-healing effects in achilles tendinopathy of long-term curcumin delivery using porous microspheres. *J. Ind. Eng. Chem.* **2018**, *58*, 123–130. [CrossRef]

22. Hollinger, J.O.; Battistone, G.C. Biodegradable bone repair materials. Synthetic polymers and ceramics. *Clin. Orthop. Relat. Res.* **1986**, 290–305.

23. Maffulli, N.; Wong, J.; Almekinders, L.C. Types and epidemiology of tendinopathy. *Clin. Sports Med.* **2003**, *22*, 675–692. [CrossRef]

24. Weber, C.; Erl, W.; Weber, K.S.; Weber, P.C. HMG-CoA reductase inhibitors decrease CD11b expression and CD11b-dependent adhesion of monocytes to endothelium and reduce increased adhesiveness of monocytes isolated from patients with hypercholesterolemia. *J. Am. Coll. Cardiol.* **1997**, *30*, 1212–1217. [CrossRef]

25. Buchwald, H.; Campos, C.T.; Boen, J.R.; Nguyen, P.A.; Williams, S.E. Disease-free intervals after partial ileal bypass in patients with coronary heart disease and hypercholesterolemia: Report from the program on the surgical control of the hyperlipidemias (posch). *J. Am. Coll. Cardiol.* **1995**, *26*, 351–357. [CrossRef]

26. Contractor, T.; Beri, A.; Gardiner, J.C.; Tang, X.; Dwamena, F.C. Is statin use associated with tendon rupture? A population-based retrospective cohort analysis. *Am. J. Ther.* **2015**, *22*, 377–381. [CrossRef] [PubMed]

27. Beri, A.; Dwamena, F.C.; Dwamena, B.A. Association between statin therapy and tendon rupture: A case-control study. *J. Cardiovasc. Pharmacol.* **2009**, *53*, 401–404. [CrossRef] [PubMed]

28. Lin, T.T.; Lin, C.H.; Chang, C.L.; Chi, C.H.; Chang, S.T.; Sheu, W.H. The effect of diabetes, hyperlipidemia, and statins on the development of rotator cuff disease: A nationwide, 11-year, longitudinal, population-based follow-up study. *Am. J. Sports Med.* **2015**, *43*, 2126–2132. [CrossRef] [PubMed]

29. Dolkart, O.; Liron, T.; Chechik, O.; Somjen, D.; Brosh, T.; Maman, E.; Gabet, Y. Statins enhance rotator cuff healing by stimulating the COX2/PGE2/EP4 pathway: An in vivo and in vitro study. *Am. J. Sports Med.* **2014**, *42*, 2869–2876. [CrossRef] [PubMed]

30. Hoffman, K.B.; Kraus, C.; Dimbil, M.; Golomb, B.A. A survey of the FDA's AERS database regarding muscle and tendon adverse events linked to the statin drug class. *PLoS ONE* **2012**, *7*, e42866. [CrossRef] [PubMed]

31. De Oliveira, L.P.; Vieira, C.P.; Guerra, F.D.; Almeida, M.S.; Pimentel, E.R. Structural and biomechanical changes in the achilles tendon after chronic treatment with statins. *Food Chem. Toxicol.* **2015**, *77*, 50–57. [CrossRef] [PubMed]

32. Marie, I.; Delafenetre, H.; Massy, N.; Thuillez, C.; Noblet, C. Network of the French Pharmacovigilance Centers. Tendinous disorders attributed to statins: A study on ninety-six spontaneous reports in the period 1990–2005 and review of the literature. *Arthritis Rheum.* **2008**, *59*, 367–372. [CrossRef] [PubMed]

33. Tsuzaki, M.; Guyton, G.; Garrett, W.; Archambault, J.M.; Herzog, W.; Almekinders, L.; Bynum, D.; Yang, X.; Banes, A.J. IL-1 beta induces COX2, MMP-1, -3 and -13, ADAMTS-4, IL-1 beta and IL-6 in human tendon cells. *J. Orthop. Res.* **2003**, *21*, 256–264. [CrossRef]

34. John, T.; Lodka, D.; Kohl, B.; Ertel, W.; Jammrath, J.; Conrad, C.; Stoll, C.; Busch, C.; Schulze-Tanzil, G. Effect of pro-inflammatory and immunoregulatory cytokines on human tenocytes. *J. Orthop. Res.* **2010**, *28*, 1071–1077. [CrossRef] [PubMed]

35. Niwa, S.; Totsuka, T.; Hayashi, S. Inhibitory effect of fluvastatin, an hmg-coa reductase inhibitor, on the expression of adhesion molecules on human monocyte cell line. *Int. J. Immunopharmacol.* **1996**, *18*, 669–675. [CrossRef]

36. Kothe, H.; Dalhoff, K.; Rupp, J.; Muller, A.; Kreuzer, J.; Maass, M.; Katus, H.A. Hydroxymethylglutaryl coenzyme a reductase inhibitors modify the inflammatory response of human macrophages and endothelial cells infected with chlamydia pneumoniae. *Circulation* **2000**, *101*, 1760–1763. [CrossRef] [PubMed]

37. Luan, Z.; Chase, A.J.; Newby, A.C. Statins inhibit secretion of metalloproteinases-1, -2, -3, and -9 from vascular smooth muscle cells and macrophages. *Arterioscler. Thromb. Vasc. Biol.* **2003**, *23*, 769–775. [CrossRef] [PubMed]

38. Hast, M.W.; Zuskov, A.; Soslowsky, L.J. The role of animal models in tendon research. *Bone Jt. Res.* **2014**, *3*, 193–202. [CrossRef] [PubMed]

39. Patterson-Kane, J.C.; Firth, E.C.; Parry, D.A.; Wilson, A.M.; Goodship, A.E. Effects of training on collagen fibril populations in the suspensory ligament and deep digital flexor tendon of young thoroughbreds. *Am. J. Vet. Res.* **1998**, *59*, 64–68. [PubMed]

40. Rosso, F.; Bonasia, D.E.; Marmotti, A.; Cottino, U.; Rossi, R. Mechanical stimulation (pulsed electromagnetic fields "pemf" and extracorporeal shock wave therapy "eswt") and tendon regeneration: A possible alternative. *Front. Aging Neurosci.* **2015**, *7*, 211. [CrossRef] [PubMed]

41. Aspenberg, P. Stimulation of tendon repair: Mechanical loading, gdfs and platelets. A mini-review. *Int. Orthop.* **2007**, *31*, 783–789. [CrossRef] [PubMed]

42. Ricchetti, E.T.; Reddy, S.C.; Ansorge, H.L.; Zgonis, M.H.; Van Kleunen, J.P.; Liechty, K.W.; Soslowsky, L.J.; Beredjiklian, P.K. Effect of interleukin-10 overexpression on the properties of healing tendon in a murine patellar tendon model. *J. Hand Surg. Am.* **2008**, *33*, 1843–1852. [CrossRef] [PubMed]

43. Lichtnekert, J.; Kawakami, T.; Parks, W.C.; Duffield, J.S. Changes in macrophage phenotype as the immune response evolves. *Curr. Opin. Pharmacol.* **2013**, *13*, 555–564. [CrossRef] [PubMed]

44. Jeong, Y.J.; Kim, I.; Cho, J.H.; Park, D.W.; Kwon, J.E.; Jung, M.W.; Meng, X.; Jo, S.M.; Song, H.S.; Cho, Y.M.; et al. Anti-osteoarthritic effects of the litsea japonica fruit in a rat model of osteoarthritis induced by monosodium iodoacetate. *PLoS ONE* **2015**, *10*, e0134856. [CrossRef] [PubMed]

45. Xu, Y.; Liu, Q.; Liu, Z.L.; Lim, L.; Chen, W.H.; Lin, N. Treatment with simiaofang, an anti-arthritis chinese herbal formula, inhibits cartilage matrix degradation in osteoarthritis rat model. *Rejuvenation Res.* **2013**, *16*, 364–376. [CrossRef] [PubMed]

Article

Three-Dimensional Graphene–RGD Peptide Nanoisland Composites That Enhance the Osteogenesis of Human Adipose-Derived Mesenchymal Stem Cells

Ee-Seul Kang [1], Da-Seul Kim [1], Yoojoong Han [1], Hyungbin Son [1], Yong-Ho Chung [2], Junhong Min [1,*] and Tae-Hyung Kim [1,3,*]

[1] School of Integrative Engineering, Chung-Ang University, Seoul 06974, Korea; eeseul94@cau.ac.kr (E.-S.K.); dptmf4011@cau.ac.kr (D.-S.K.); handbwnd@naver.com (Y.H.); being@cau.ac.kr (H.S.)

[2] Department of Chemical Engineering, Hoseo University, Asan City, Chungnam 31499, Korea; yhchung@hoseo.edu

[3] Integrative Research Center for Two-Dimensional Functional Materials, Institute of Interdisciplinary Convergence Research, Chung-Ang University, Seoul 06974, Korea

* Correspondence: junmin@cau.ac.kr (J.M.); thkim0512@cau.ac.kr (T.-H.K.); Tel.: +82-2-820-5469

Abstract: Graphene derivatives have immense potential in stem cell research. Here, we report a three-dimensional graphene/arginine-glycine-aspartic acid (RGD) peptide nanoisland composite effective in guiding the osteogenesis of human adipose-derived mesenchymal stem cells (ADSCs). Amine-modified silica nanoparticles (SiNPs) were uniformly coated onto an indium tin oxide electrode (ITO), followed by graphene oxide (GO) encapsulation and electrochemical deposition of gold nanoparticles. A RGD–MAP–C peptide, with a triple-branched repeating RGD sequence and a terminal cysteine, was self-assembled onto the gold nanoparticles, generating the final three-dimensional graphene–RGD peptide nanoisland composite. We generated substrates with various gold nanoparticle–RGD peptide cluster densities, and found that the platform with the maximal number of clusters was most suitable for ADSC adhesion and spreading. Remarkably, the same platform was also highly efficient at guiding ADSC osteogenesis compared with other substrates, based on gene expression (alkaline phosphatase (ALP), runt-related transcription factor 2), enzyme activity (ALP), and calcium deposition. ADSCs induced to differentiate into osteoblasts showed higher calcium accumulations after 14–21 days than when grown on typical GO-SiNP complexes, suggesting that the platform can accelerate ADSC osteoblastic differentiation. The results demonstrate that a three-dimensional graphene–RGD peptide nanoisland composite can efficiently derive osteoblasts from mesenchymal stem cells.

Keywords: graphene oxide; silica nanoparticles; gold nanoparticles; RGD peptide; differentiation; mesenchymal stem cells; adipose-derived stem cells; osteogenesis

---

1. Introduction

Stem cells have emerged as a promising source in the field of regenerative medicine, because of their innate ability to produce a variety of desired cell types in the human body [1,2]. Among stem cells, mesenchymal stem cells (MSCs) have predominated in clinical trials and commercialization, since they are relatively easy to obtain from various sources (e.g., adipose tissue, bone marrow, dental tissue), free from ethical issues, and most importantly, have a low risk of teratoma formation after transplantation [3]. MSCs are also attractive because of their capability to generate various types of cells (e.g., osteoblasts, chondrocytes, adipocytes), all of which are fundamental for the reconstruction

and regeneration of most body components [4–6]. However, to maximize regeneration efficiency, the characteristics of MSCs should be properly adjusted to the desired cell type through differentiation, because their multipotency may also result in the production of unwanted cell types [7–9].

The differentiation of stem cells is conventionally controlled by soluble cues; that is, the use of defined culture media containing multiple growth factors (e.g., bone morphogenetic proteins, insulin, peroxisome proliferator-activated receptor γ) and biomolecules (e.g., dexamethasone, ascorbic acid, glycerophosphate) [10–14]. However, recent findings suggest that biophysical cues, such as the physicochemical characteristics of the underlying substrate, to which the cells attach and actively interact with as they grow, can also play key roles in steering the transformation of MSCs into specific cell types [15–18]. Mechanical stimulation, a biophysical cue that can affect cell behavior, is generally initiated by cell–substrate interactions, which alter cytoskeletal dynamics and consequently affect gene expression in the cells [12,15,19–25]. To provide favorable biophysical stimulation to stem cells, nanostructures, micropatterns, and functional composite materials have been utilized to control stem cell behavior, particularly differentiation, with and without the use of soluble factors [26–31]. Among such materials, graphene and graphene oxide (GO) have recently been shown to effectively provide the necessary physical stimulation for stem cell differentiation [32–36]. The distinct physicochemical characteristics of graphene derivatives were found to successfully initiate several specific MSC differentiation routes, such as adipogenesis [37], osteogenesis [38,39], and neurogenesis [40]. The multifarious surface chemistry, controllable amphiphilicity, and unique honeycomb carbon structure were reported to affect several cellular aspects such as spreading, growth, and morphology, as well as the absorption kinetics of proteins and chemicals in the differentiation medium [32,33,41–44].

In addition to graphene derivatives, natural polymers such as extracellular matrix (ECM) proteins (e.g., fibronectin, laminin, and vitronectin) and peptides are also excellent candidates for controlling stem cell behavior [45,46]. Among the various available materials, peptides containing a repeating arginine–glycine–aspartic acid (RGD) sequence, which is often found in ECM proteins, have been widely applied not only to increase the uptake of materials and molecules of interest into specific types of cells, but also to enhance cell adhesion to artificial platforms such as synthetic polymers and metallic surfaces [47–49]. Interestingly, RGD-containing peptides immobilized onto substrates enhanced the adhesion strength of MSCs, ultimately resulting in increased osteogenic differentiation, as cell adhesion is a key factor guiding osteogenic lineage commitment [50,51].

In this study, we report a three-dimensional graphene/RGD peptide nanoisland composite that is highly effective in controlling the osteogenic differentiation of human-adipose-derived mesenchymal stem cells (ADSCs; Figure 1). ADSC differentiation was controlled by four independent factors: (i) GOs that contribute to the absorption of several differentiation factors; (ii) RGD–MAP–C peptides that enhance cell adhesion; (iii) nanopatterns with randomly-distributed geometry and iv) height variations of underlying substrates that facilitate cell–GO and cell–peptide interactions (Figure 1). The physical and chemical properties of the three-dimensional nanocomposites were first characterized by X-ray photoelectron spectroscopy (XPS) and Raman spectroscopy. Thereafter, ADSCs were cultivated on GO surfaces with varying numbers of nanoparticle–RGD peptides and their adhesion, spreading, and proliferation were analyzed. Furthermore, the effects of nanoparticle–RGD peptides complexes on ADSC osteogenesis were characterized by assaying mRNA expression and calcification levels. Finally, to better understand the effects of nanoparticle–RGD peptides on the osteogenic differentiation of ADSCs, a four-week time course was performed in the presence of culture medium with and without differentiation factors.
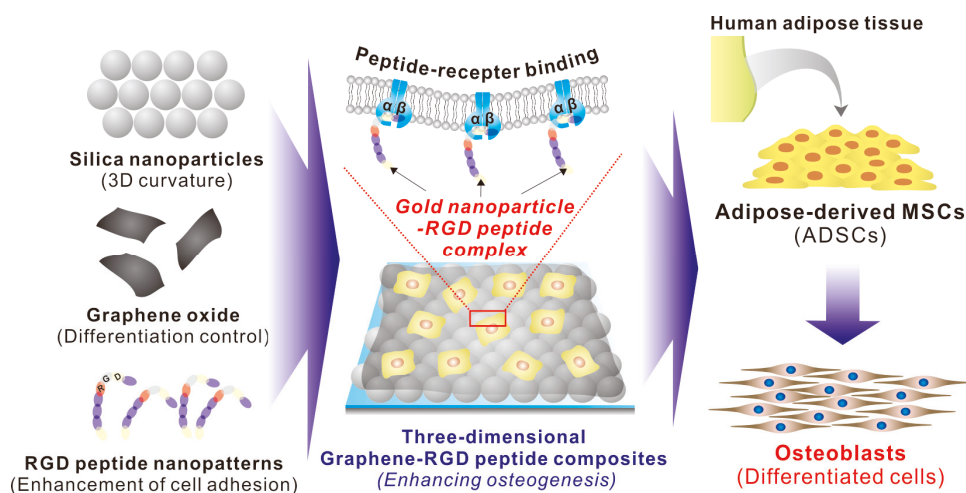
Figure 1. Schematic diagram of three-dimensional graphene/arginine-glycine-aspartic acid (RGD) peptide composites for enhancement of adipose-derived mesenchymal stem cell (ADSC) osteogenesis.

2. Results

2.1. Fabrication of Silica-Nanoparticle–Graphene-Oxide Composites on an Indium Tin Oxide (ITO) Substrate

To enhance cell–substrate interactions, we hypothesized that the generation of RGD nanopattern ripples on the graphene surface would facilitate both $\alpha_v\beta_3$ ligand–RGD peptide and GO–cell membrane interactions, which ultimately affect stem cell behavior. There are several methods that could be utilized to fabricate three-dimensional environments on a GO surface. Photolithography is a representative tool suitable for the fabrication of various nano- and micro-structures with precisely controlled geometry [52,53]. However, this technique includes laborious and time-consuming steps such as photomask fabrication, photoresist coating, cleaning, and etching/metal deposition. Moreover, residual photoresist on the substrates could result in unexpected toxic effects on stem cells. Hence, silica nanoparticles (SiNPs), a material proven to be nontoxic and safe for use with most cell lines [54,55], were used as a coating material to generate height variations on the ITO substrate prior to GO modification. We then attached amine-functionalized SiNPs to the negatively charged GO via electrostatic interactions. As shown in Figure 2a, GO-coated SiNPs were uniformly coated onto the ITO substrate, and the ITO/GO substrate showed the typical wrinkle-like structure of graphene, different from the bare ITO substrate. In addition, XPS spectra revealed that the chemical structure of GO sheets on SiNPs were similar to those on the ITO substrate, showing C–C, C–O and C=O bonding, which are all typically found on the GO surface (Figure 2b and Figure S1). Raman spectroscopy was used to investigate GO oxidation. It has been reported that the G band represents the in-plane structure (sp^2-bonded carbon) while the D band indicates structural defects, such as oxidized carbon. Based on this, the structural defects and carbon-to-oxygen ratio were analyzed. Figure 2c and Figure S2 show clear D (1350 cm^{-1}) and G (1600 cm^{-1}) peaks for ITO/SiNP/GOs, demonstrating the successful absorption of GO sheets onto amine-modified SiNP surfaces. The I_D/I_G values of ITO/GOs and ITO/SiNP/GOs were calculated to be 0.96 and 0.97, indicating that both GOs were highly oxidized, with C–C and C–O/C=O/O=C–O ratios of approximately 1:1. GO sheets embedded on the surface of SiNPs not only act as a conducting layer to enable electrochemical deposition of gold nanoparticles (GNPs) onto the SiNPs, but also helped attract gold chloride ions, resulting in the formation of the seed for GNP synthesis. Hence, it can be concluded that the fabricated GO-SiNP composite is a suitable

platform for the generation of GNPs via electrochemical deposition, which could be further utilized to control stem cell behavior.
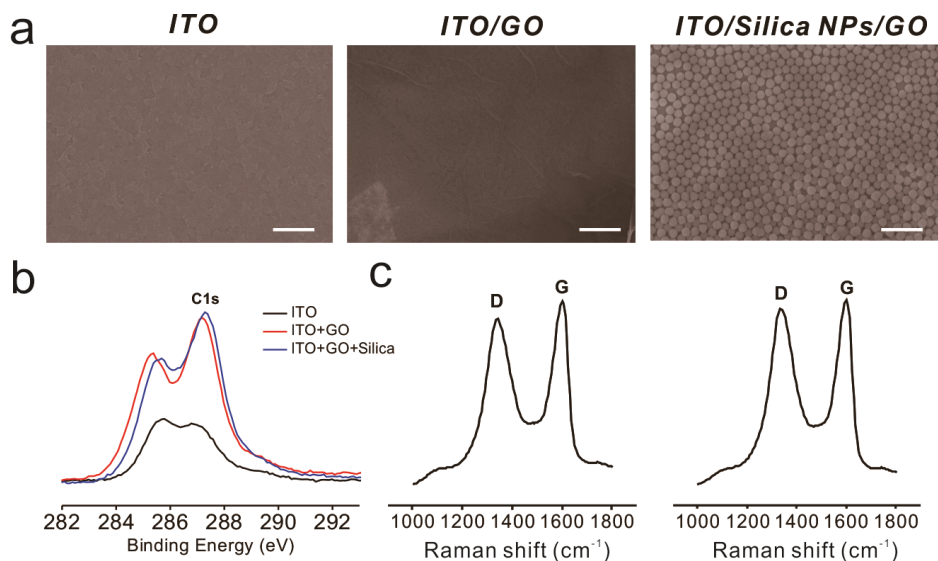
Figure 2. Characterization of the basic substrates. (**a**) Scanning electron microscopy images of indium tin oxide (ITO) (left), ITO/graphene oxide (GO) (middle), and ITO/GO/silica nanoparticles (SiNPs) (right). Scale bars = 1 μm; (**b**) X-ray photoelectron spectroscopy (XPS) results for each substrate; (**c**) Raman spectroscopy data for ITO/GO (left) and ITO/GO/SiNPs (right).

2.2. Fabrication of a 3D Graphene–RGD Peptide Nanoisland Composite for Stem Cell Cultures

Cell adhesion is controlled by transmembrane glycoproteins, including integrins, selectins, and cadherins [56–58]. Integrins are core materials that actively regulate the anchoring of the cell membrane to the extracellular environment, and are hugely affected by the physicochemical properties of the underlying substrates [59,60]. A number of studies have reported that nanotopographic features influence many key cellular activities, including cell migration, proliferation, differentiation, and even apoptosis [61–64]. Specifically, since the size of the integrin subunits that are located in the outside of the cell membrane (α and β chains) is around 23nm and the final N-termini of each chain is around 5nm, the materials whose sizes are in the nanometer range could result in the changes of integrin-mediated cell anchoring [62,65]. Consequently, this causes cytoskeletal rearrangements of cells adhered to the nanomaterial surfaces, resulting in changes of cell signaling pathways, which ultimately affect cell growth, spreading and differentiation. In the case of MSCs, nanopattern geometry and arrangement are critical for both multipotency maintenance and differentiation. Dalby et al. reported that nanopatterns with random arrangements can effectively guide MSC osteogenesis, while the same nanopatterns with homogeneous arrangements maintain their multipotency in long-term cultures [65]. Based on this, we generated GNPs on GO-coated SiNPs via electrochemical deposition, as shown in Figure 3a. Due to the presence of the conducting GO layer, GNPs of 10–20 nm in diameter were successfully generated on the non-conducting SiNPs. Interestingly, the I_D/I_G values of Raman spectra were calculated to be 1.01, 1.04, 1.18, and 1.2 after 0, 40, 80, and 120 s of deposition, respectively, indicating that GO oxidation increased with increased electrochemical deposition (Figure S2). As the RGD-containing peptides (RGD–MAP–C) contain a terminal cysteine residue, they can be easily self-assembled on the surface of the GNPs. In addition, by varying the electrochemical deposition time, the size and density of GNPs could be varied, resulting in different RGD–MAP–C peptide arrangements, which would ultimately

alter the cytoskeletal dynamics of stem cells. To investigate this, ADSCs were seeded onto each platform at different GNP densities, and therefore with different RGD–MAP–C peptide arrangements. As shown in Figure 3b, the GO-SiNP-GNP-RGD peptide composites with the highest GNP density (deposition time = 120 s) showed more active filopodia interaction with the underlying platform, indicating that this substrate might effectively enhance cell adhesion and migration, improving ADSC osteogenesis. To further study the effects of GNP-RGD peptide composites on ADSCs, the substrates were divided into two groups: (i) GO-SiNP-GNPs and (ii) GO-SiNP-GNP-RGD peptide composites. After two days of culture, the cytoskeletal structures and nuclei of ADSCs were visualized by phalloidin and Hoechst 33342 staining to calculate the rates of cell spreading and growth by fluorescence microscopy (Figure 4a,b and Figure S3). Cell growth was not affected by the presence of RGD–MAP–C peptides (Figure 4c), while cell spreading was highly enhanced on all the substrates possessing GNP-RGD peptide composites (Figure 4d). Cell spreading was 118, 128, and 110% higher on GNP-RGD composites compared to GNPs only, after 40, 80, and 120 s of deposition, respectively. Cell spreading seemed to increase with increased GNP density; however, owing to the limitations in the area in which cells could attach and grow, the enhancement of cell spreading was saturated with medium GNP density. Interestingly, cell spreading was not enhanced by RGD–MAP–C peptide modifications to the GO-SiNP platform, because of the absence of GNPs, which mediate RGD–MAP–C peptide immobilization via an Au–S bond. Accordingly, based on the cell adhesion, spreading, and proliferation results, we conclude that GNP-RGD peptide modifications to the GO-SiNP platform positively affect ADSC adhesion, and can thus be considered a candidate platform to control stem cell differentiation.
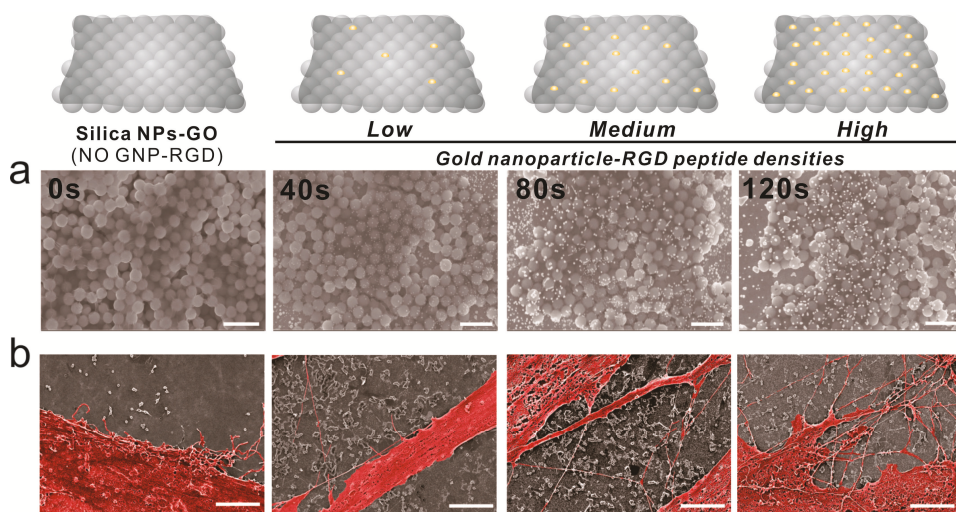
Figure 3. Scanning electron microscopy (SEM) images of ADSCs on gold-deposited substrates. (**a**) From left to right, SEM images of gold deposition. Scale bars = 1 μm; (**b**) Pseudocolor SEM images of ADSCs showing cell spreading. Scale bars = 3 μm.

2.3. Guiding ADSC Osteogenesis Using Graphene–RGD Peptide Nanoisland Composites

As cell adhesion and spreading were highly enhanced by GNP-RGD peptide modifications, we next investigated whether these differences in cell behavior affected ADSC osteogenesis. Differentiation was performed in medium containing well-known osteogenic differentiation factors (β-glycerophosphate, ascorbic acid, and dexamethasone; Figure 5). After four weeks of differentiation, ADSC osteogenesis levels were analyzed using several markers, including alkaline phosphatase (ALP) enzyme activity, ALP and runt-related transcription factor 2 (RUNX2) expression, and osteogenesis

mineralization. ALP regulates the dephosphorylation of several biomolecules and is an indicator of pre-osteogenesis stem cells, while RUNX2 is critical for osteoblastic differentiation. Based on reverse transcription-quantitative polymerase chain reaction (RT-qPCR) results, remarkably, the expression of both genes was highly enhanced on GO-SiNPs with high levels of GNP-RGD peptides compared with bare 3D GO-SiNPs and the same substrate with low and medium GNP-RGD peptide densities (263% and 295% higher than low density of gold deposition for ALP and RUNX2, respectively (Figure 5b). Next, to confirm the superiority of 3D GO-RGD peptide nanoisland composites with high GNP density in ADSC osteogenic differentiation, the ALP enzyme activity and calcification levels were evaluated, using para-nitrophenylphosphate and Alizarin Red S (ARS) as colorimetric reagents, respectively. MSCs accumulation of calcium phosphate (hydroxyapatite mineral ($Ca_{10}(PO_4)_6$)), an essential material for building bone structure, is an indicator of osteogenesis. As shown in Figure 5a, all ADSCs cultured in osteogenic medium successfully differentiated into cells displaying calcium deposits. Three-dimensional GO-RGD peptide nanoisland composites with high GNP density showed the best osteogenic differentiation efficiency based on ALP and ARS levels, which were 148% and 158% higher than with bare GO-SiNP platforms (Figure 5c,d). This is consistent with a previous study reporting that modifications to ECM-derived RGD-glycoproteins (e.g., fibronectin, vitronectin, and osteopontin) on cell culture substrates are critical for MSC osteogenic differentiation. Hence, it is highly likely that the increase in RGD–MAP–C peptide density in combination with the three-dimensional GO sheets on the SiNPs synergistically enhance ADSC osteogenesis via increased cell adhesion and absorption of differentiation factors. Based on these observations, we can logically conclude that the developed graphene–RGD peptide nanoislands are a promising platform to guide the differentiation of stem cells into specific lineages.
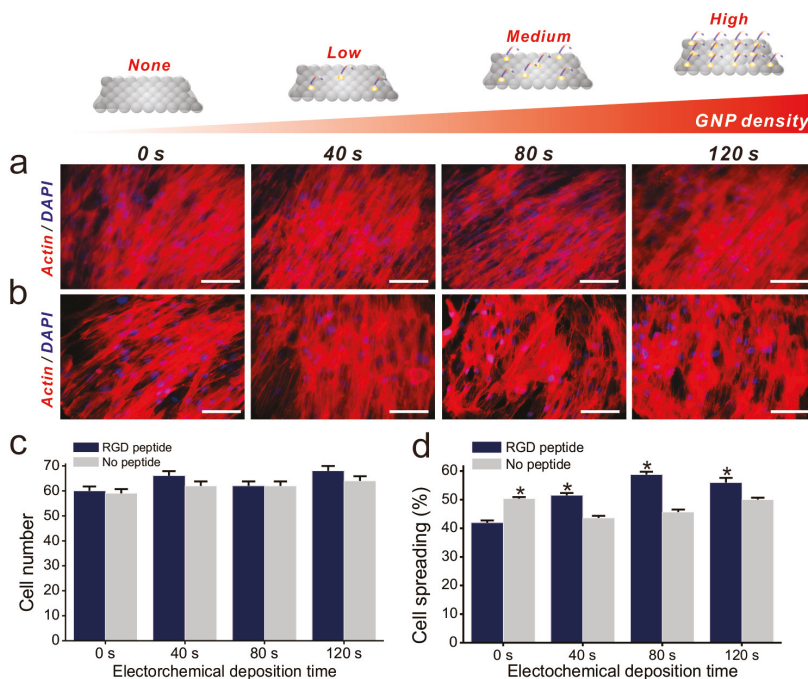
Figure 4. Fluorescence images of all substrates Fluorescence images of each substrate with (**a**) and without (**b**) RGD peptide. Scale bars = 100 μm; (**c**) Number of cells on each substrate after 2 day of incubation; (**d**) Spreading of proliferated cells. * Student's *t*-test, $p < 0.05$, $n = 3$.
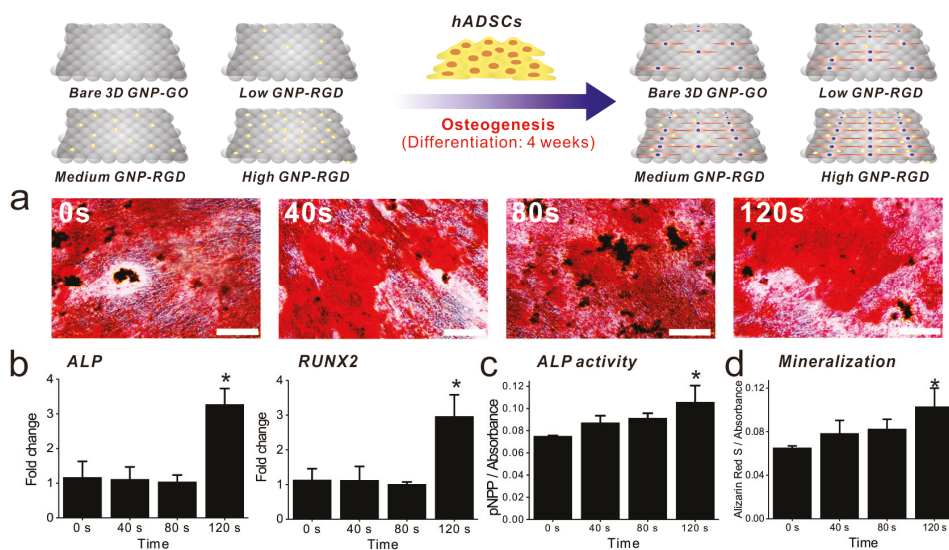
Figure 5. Confirmation of ADSC osteogenic differentiation. (**a**) Alizarin Red S staining of all substrates. Scale bars = 200 μm; (**b**) RT-qPCR data for alkaline phosphatase (ALP), and RUNX2; (**c**) The ALP activity of each substrate; (**d**) Absorbance rates after Alizarin Red S (ARS) staining. * Student's *t*-test, $p < 0.05$, $n = 3$.

2.4. Time Course of ADSC Osteogenic Differentiation on Graphene–RGD Peptide Nanoislands

After confirming that the graphene–RGD peptide nanoislands with high GNP density are highly effective in guiding ADSC osteogenesis, we next investigated whether the platform could accelerate ADSC osteogenesis. This is important to study, because accelerated differentiation is needed to supply osteoblasts to the patients requiring urgent orthopedic surgery. In fact, it takes up to four weeks to generate bone cells from stem cells, and this is an obstacle in the clinical use of stem-cell-derived osteoblasts. Osteogenic ADSC differentiation was induced using typical osteogenic medium, and ARS staining was performed weekly to evaluate the osteoblastic differentiation of ADSCs grown on GO-SiNP/GNPs with and without RGD–MAP–C peptides. For the first 14 days, there was no discernable increase in osteoblast mineralization (Figure 6a). However, after two weeks of differentiation, the difference was apparent, especially between days 14 and 21 (Figure 6 and Figure S4). Specifically, the conversion of MSCs into osteoblasts on the GO-SiNP/GNP/RGD–MAP–C substrate was 120% and 160% higher than on the same substrate without GNP-RGD–MAP–C composites at days 21 and 28, respectively. Interestingly, the osteoblastic mineralization of ADSCs was highly enhanced at day 21 on the GO-SiNP/GNP/RGD–MAP–C substrate compared to on typical GO-SiNP substrates, indicating that the platform might be useful to more rapidly generate osteoblasts from stem cells, which could help meet timely clinical demands (Figure 6b). More studies regarding the gene expression levels of adhesion-related proteins (e.g., integrins, vinculin, focal adhesion kinase, paxillin, and talin) and osteogenic differentiation (e.g., osteocalcin, osteonectin, osteopontin) should be performed to validate the aforementioned results.
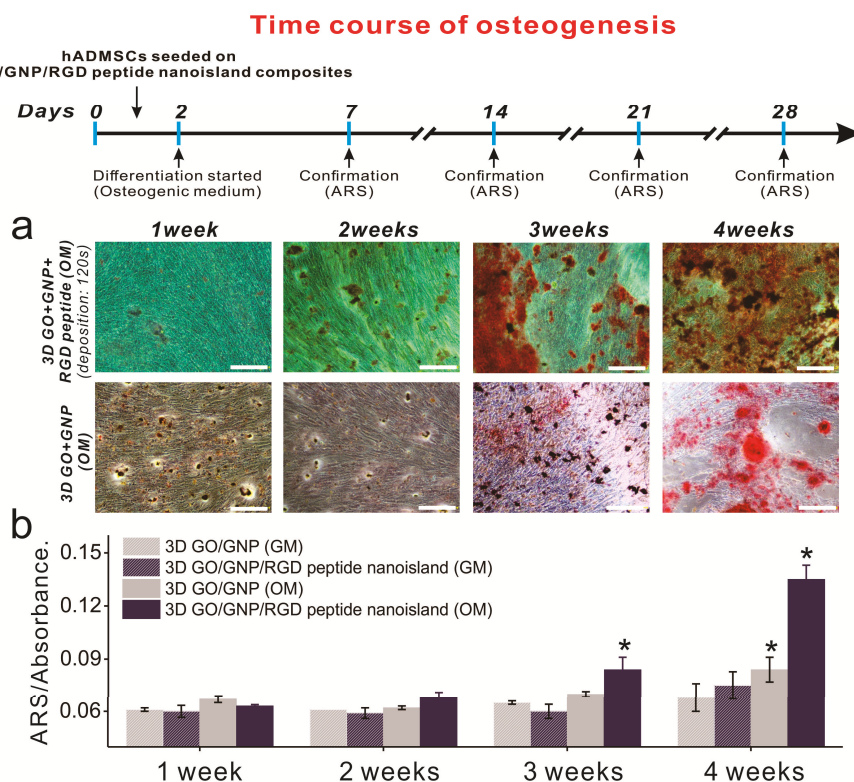
Figure 6. Time course of osteogenesis with and without RGD–MAP–C peptides. (**a**) ADSC differentiation was monitored every 7 d. Scale bars = 200 μm; (**b**) ARS absorbance changes in the presence of gold and different media. * Student's *t*-test, $p < 0.05$, $n = 3$.

3. Discussion

In this study, we report a new platform that enables the stable long-term culture of ADSCs and guides their osteogenic differentiation. Among the various substrates fabricated, the three-dimensional GO-SiNP platform with high GNP-RGD peptide density, which we have termed the graphene–RGD peptide nanoisland composite, was best at enhancing stem cell adhesion and spreading on the artificial surface. Furthermore, this substrate was superior to other platforms, including bare GO-SiNPs and GO-SiNPs with low and medium densities of GNP-RGD peptides, at guiding ADSC osteogenesis. Specifically, the RNA expression levels of ALP (a pre-osteogenic marker) and RUNX2 (an osteogenic marker) in ADSCs grown on graphene–RGD peptide nanoisland composite were 2.63- and 2.95-fold higher than on bare 3D GO-SiNPs after four weeks of differentiation. Other osteogenic differentiation indicators, such as ALP enzyme activity and calcium accumulation, were also highly enhanced, 1.48- and 1.58-fold higher than with bare 3D GO-SiNPs, proving the excellence of 3D graphene–RGD peptide nanoisland composite for steering ADSC osteogenesis. Moreover, ADSCs grown on the developed composites showed increased osteoblastic mineralization between days 14–21, 1.2-fold higher than on bare GO-SiNPs, exhibiting the potential of the developed platform to accelerate stem cell osteogenesis.

The 3D graphene–RGD peptide nanoisland composite shows great promise in stem cell research, and more advanced studies based on our findings will be required to improve the platform through the incorporation of different types of nanomaterials (e.g., polystyrene beads, glass beads) and peptides

(cyclic RGD peptide, iRGD peptide). Other types of stem cells, such as pluripotent stem cells and neural stem cells, could also be applied to fully investigate the potential of 3D graphene–peptide nanoislands as a stable platform for long-term stem cell culture [66,67]. The desired cell types achieved from various stem cell lines using 3D graphene–peptide nanoisland composites as the culture platforms would then be usefully applied for clinical study, especially for the regeneration of damaged parts of human organs/tissues. Taken together, we can logically conclude that the developed platform, graphene–peptide complexes, could make remarkable contributions in the field of stem-cell-based regenerative medicine.

4. Materials and Methods

4.1. Materials

SiNPs were purchased from NanoComposix (San Diego, CA, USA). GO was obtained from Graphene Supermarket (Calverton, NY, USA). ADSCs and cell engineering for origin (CEFO) ADSC growth media supplemented with 10% fetal bovine serum and 1% penicillin/streptomycin were obtained from CEFO Bio (Seoul, Korea). Dexamethasone, L-ascorbic acid, β-glycerophosphate, and gold chloride trihydrate were purchased from Sigma Aldrich (St. Louis, MO, USA). RGD peptide was purchased from Peptron (Daejeon, Korea). ITO was purchased from UID (Sejong, Korea).

4.2. Fabrication of Three-Dimensional Hybrid Structures

First, ITO was prepared by sonication in 1% Triton X-100 in distilled water (DW) and pure ethanol for 20 min each. The ITO was spin-coated at 2000 rpm for 20 sec using 300 nm silica nanoparticles in 70% ethanol. After coating the substrates, 250 μg/mL GO solution was dropped onto the ITO and baked in a 70 °C oven for 1 h, after which the substrates were washed with DW. A chamber of 0.8 cm diameter was placed on the ITO substrates, using Polydimethylsilozane (PDMS) for cold deposition. A 0.5 mM gold solution was electrochemically treated at an initial voltage of −1.3 at 0, 40, 80, and 120 s. After electrical deposition, the chamber was washed with PBS, and coated with 0.05 mg/mL RGD peptide overnight at 4 °C.

4.3. Substrate Characterization

The silica-coated substrates were characterized by a variety of analytical techniques, including scanning electron microscopy (SEM, SIGMA, Carl Zeiss, Oberkochen, Germany), XPS (K-alpha+, Waltham, MA, USA; Thermo Fisher Scientific, Waltham, MA, USA.), and Raman spectroscopy.

4.4. Cell Proliferation and Spreading Analysis

ADSCs (6000 cells/cm^2) were cultured on the 3D hybrid substrates in growth medium for 2 day. Before staining, cells were fixed in neutral buffered formalin (Sigma Aldrich) and permeabilized with 0.1% Triton X-100 for 5 min. After staining with Alexa Fluor 568 phalloidin (Life Technology, Carlsbad, CA, USA) and Hoechst 33342 (Thermo Scientific, Waltham, MA, U.S.A), cells were imaged by fluorescence microscopy. Cell proliferation and spreading were analyzed using ImageJ software.

4.5. Osteogenesis of ADSCs

The osteogenic differentiation medium contained 50 μM L-ascorbic acid, 10 mM β-glycerophosphate, and 100 nM dexamethasone. ADSCs were seeded in chambers, and the medium was changed every 2 days for 4 weeks. After the induction of osteogenesis, differentiation was confirmed by assaying calcium deposition with ARS. Cells were stained with ARS for 20 min, washed with DW, and imaged on an optical microscope. Subsequently, 10% cetylpyridinium chloride in 10 mM sodium phosphate was added, and the solution was incubated at 25 °C for 15 min. ARS extraction was measured at 562 nm on a microplate reader. In the case of alkaline phosphatase (ALP) analysis, ALP activity was measured based on the conversion of p-nitrophenyl phosphate (pNPP) into p-nitrophenol. First, the cell lysates achieved and

were added in to 96 well plate with reaction reagent (pNPP). The plates were then incubated at 25 °C for 15 min while protecting the plates from light. Finally, the reaction was terminated with the addition of 3 M NaOH, followed by reading the absorbance at 405 nm using the plate reader.

4.6. Osteogenic Marker Expression Analysis

Total RNA was extracted from osteogenic cells using an RNeasy Mini Kit (Qiagen, Hilden, Germany) according to the manufacturer's instructions, and cDNA was synthesized from 1 μg of total RNA with SuperScript II Reverse Transcriptase (Invitrogen, Carlsbad, CA, U.S.A). RT-qPCR was performed with SYBR Premix Ex Taq (Takara, Shiga, Japan) in a StepOnePlus RT-PCR system.

Author Contributions: Tae-Hyung Kim and Junhong Min conceived and designed the experiments; Ee-Seul Kang, Da-Seul Kim, and Yoojoong Han performed the experiments; Tae-Hyung Kim, Ee-Seul Kang and Hyungbin Son analyzed the data; Tae-Hyung Kim, Hyungbin Son and Junhong Min contributed reagents/materials/analysis tools; Ee-Seul Kang, Tae-Hyung Kim, Yoojoong Han, Yong-Ho Chung, and Junhong Min wrote the paper.

Conflicts of Interest: The authors declare no conflict of interest. The founding sponsors had no role in the design of the study; in the collection, analyses, or interpretation of data; in the writing of the manuscript, and in the decision to publish the results.

Abbreviations

ADSC	Adipose-derived mesenchymal stem cells
ALP	Alkaline phosphatase
ARS	Alizarin red S
DW	Distilled water
ECM	Extracellular matrix
ITO	Indium tin oxide
GNP	Gold nanoparticle
GO	Graphene oxide
PDMS	Polydimethylsilozane
RGD	Arginine-glycine-aspartic acid
RT-qPCR	Reverse transcription quantitative polymerase chain reaction
RUNX2	Runt-related transcription factor 2
SEM	Scanning electron microscopy
SiNPs	Silica nanoparticles
XPS	X-ray photoelectron spectroscopy

References

1. Segers, V.F.; Lee, R.T. Stem-cell therapy for cardiac disease. *Nature* **2008**, *451*, 937–942. [CrossRef] [PubMed]
2. Strauer, B.E.; Kornowski, R. Stem cell therapy in perspective. *Circulation* **2003**, *107*, 929–934. [CrossRef] [PubMed]
3. Ankrum, J.; Karp, J.M. Mesenchymal stem cell therapy: Two steps forward, one step back. *Trends Mol. Med.* **2010**, *16*, 203–209. [CrossRef] [PubMed]
4. Lee, K.B.; Hui, J.H.; Song, I.C.; Ardany, L.; Lee, E.H. Injectable mesenchymal stem cell therapy for large cartilage defects—A porcine model. *Stem Cells* **2007**, *25*, 2964–2971. [CrossRef] [PubMed]
5. Crisan, M.; Yap, S.; Casteilla, L.; Chen, C.-W.; Corselli, M.; Park, T.S.; Andriolo, G.; Sun, B.; Zheng, B.; Zhang, L.; et al. A perivascular origin for mesenchymal stem cells in multiple human organs. *Cell Stem Cell* **2008**, *3*, 301–313. [CrossRef] [PubMed]

6. Campagnoli, C.; Roberts, I.A.; Kumar, S.; Bennett, P.R.; Bellantuono, I.; Fisk, N.M. Identification of mesenchymal stem/progenitor cells in human first-trimester fetal blood, liver, and bone marrow. *Blood* **2001**, *98*, 2396–2402. [CrossRef] [PubMed]

7. Karnoub, A.E.; Dash, A.B.; Vo, A.P.; Sullivan, A.; Brooks, M.W.; Bell, G.W.; Richardson, A.L.; Polyak, K.; Tubo, R.; et al. Mesenchymal stem cells within tumour stroma promote breast cancer metastasis. *Nature* **2007**, *449*, 557–563. [CrossRef] [PubMed]

8. Curran, J.M.; Chen, R.; Hunt, J.A. The guidance of human mesenchymal stem cell differentiation in vitro by controlled modifications to the cell substrate. *Biomaterials* **2006**, *27*, 4783–4793. [CrossRef] [PubMed]

9. Suhito, I.R.; Han, Y.; Min, J.; Son, H.; Kim, T.-H. In situ label-free monitoring of human adipose-derived mesenchymal stem cell differentiation into multiple lineages. *Biomaterials* **2018**, *154*, 223–233. [CrossRef] [PubMed]

10. Majumdar, M.K.; Keane-Moore, M.; Buyaner, D.; Hardy, W.B.; Moorman, M.A.; McIntosh, K.R.; Mosca, J.D. Characterization and functionality of cell surface molecules on human mesenchymal stem cells. *J. Biomed. Sci.* **2003**, *10*, 228–241. [CrossRef] [PubMed]

11. Caplan, A.I.; Bruder, S.P. Mesenchymal stem cells: Building blocks for molecular medicine in the 21st century. *Trends Mol. Med.* **2001**, *7*, 259–264. [CrossRef]

12. Engler, A.J.; Sen, S.; Sweeney, H.L.; Discher, D.E. Matrix elasticity directs stem cell lineage specification. *Cell* **2006**, *126*, 677–689. [CrossRef] [PubMed]

13. Mackay, A.M.; Beck, S.C.; Murphy, J.M.; Barry, F.P.; Chichester, C.O.; Pittenger, M.F. Chondrogenic differentiation of cultured human mesenchymal stem cells from marrow. *Tissue Eng.* **1998**, *4*, 415–428. [CrossRef] [PubMed]

14. Oh, M.; Kim, Y.J.; Son, Y.J.; Yoo, H.S.; Park, J.H. Promotive effects of human induced pluripotent stem cell-conditioned medium on the proliferation and migration of dermal fibroblasts. *Biotechnol. Bioproc. Eng.* **2017**, *22*, 561–568. [CrossRef]

15. Shih, Y.R.V.; Tseng, K.F.; Lai, H.Y.; Lin, C.H.; Lee, O.K. Matrix stiffness regulation of integrin-mediated mechanotransduction during osteogenic differentiation of human mesenchymal stem cells. *J. Bone Miner. Res.* **2011**, *26*, 730–738. [CrossRef] [PubMed]

16. Kilian, K.A.; Bugarija, B.; Lahn, B.T.; Mrksich, M. Geometric cues for directing the differentiation of mesenchymal stem cells. *Proc. Natl. Acad. Sci. USA* **2010**, *107*, 4872–4877. [CrossRef] [PubMed]

17. Knippenberg, M.; Helder, M.N.; Zandieh, D.B.; Semeins, C.M.; Wuisman, P.I.; Klein-Nulend, J. Adipose tissue-derived mesenchymal stem cells acquire bone cell-like responsiveness to fluid shear stress on osteogenic stimulation. *Tissue Eng.* **2005**, *11*, 1780–1788. [CrossRef] [PubMed]

18. Shin, Y.M.; Park, J.-S.; Jeong, S.I.; An, S.-J.; Gwon, H.-J.; Lim, Y.-M.; Nho, Y.-C.; Kim, C.-Y. Promotion of human mesenchymal stem cell differentiation on bioresorbable polycaprolactone/biphasic calcium phosphate composite scaffolds for bone tissue engineering. *Biotechnol. Bioproc. Eng.* **2014**, *19*, 341–349. [CrossRef]

19. Nava, M.M.; Raimondi, M.T.; Pietrabissa, R. Controlling self-renewal and differentiation of stem cells via mechanical cues. *Biom. Res. Int.* **2012**, *2012*. [CrossRef] [PubMed]

20. Connelly, J.T.; Gautrot, J.E.; Trappmann, B.; Tan, D.W.-M.; Donati, G.; Huck, W.T.; Watt, F.M. Actin and serum response factor transduce physical cues from the microenvironment to regulate epidermal stem cell fate decisions. *Nat. Cell Biol.* **2010**, *12*, 711–718. [CrossRef] [PubMed]

21. Kuo, S.-W.; Lin, H.-I.; Ho, J.H.-C.; Shih, Y.-R.V.; Chen, H.-F.; Yen, T.-J.; Lee, O.K. Regulation of the fate of human mesenchymal stem cells by mechanical and stereo-topographical cues provided by silicon nanowires. *Biomaterials* **2012**, *33*, 5013–5022. [CrossRef] [PubMed]

22. Lutolf, M.P.; Gilbert, P.M.; Blau, H.M. Designing materials to direct stem-cell fate. *Nature* **2009**, *462*, 433–441. [CrossRef] [PubMed]

23. Sun, Y.; Chen, C.S.; Fu, J. Forcing stem cells to behave: A biophysical perspective of the cellular microenvironment. *Ann. Rev. Biophys.* **2012**, *41*, 519–542. [CrossRef] [PubMed]

24. Xue, R.; Li, J.Y.S.; Yeh, Y.; Yang, L.; Chien, S. Effects of matrix elasticity and cell density on human mesenchymal stem cells differentiation. *J. Orthop. Res.* **2013**, *31*, 1360–1365. [CrossRef] [PubMed]

25. Suhito, I.R.; Han, Y.; Kim, D.-S.; Son, H.; Kim, T.-H. Effects of two-dimensional materials on human mesenchymal stem cell behaviors. *Biochem. Biophys. Res. Commun.* **2017**, *493*, 578–584. [CrossRef] [PubMed]

26. Ragetly, G.R.; Griffon, D.J.; Lee, H.-B.; Fredericks, L.P.; Gordon-Evans, W.; Chung, Y.S. Effect of chitosan scaffold microstructure on mesenchymal stem cell chondrogenesis. *Acta Biomater.* **2010**, *6*, 1430–1436. [CrossRef] [PubMed]

27. Park, J.; Kim, P.; Helen, W.; Engler, A.J.; Levchenko, A.; Kim, D.-H. Control of stem cell fate and function by engineering physical microenvironments. *Integr. Biol.* **2012**, *4*, 1008–1018. [CrossRef]

28. Huri, P.Y.; Cook, C.; Hutton, D.; Goh, B.; Gimble, J.; DiGirolamo, D.; Grayson, W.L. Biophysical cues enhance myogenesis of human adipose derived stem/stromal cells. *Biochem. Biophys. Res. Commun.* **2013**, *438*, 180–185. [CrossRef] [PubMed]

29. Huang, C.; Dai, J.; Zhang, X.A. Environmental physical cues determine the lineage specification of mesenchymal stem cells. *Biochim. Biophys. Acta Gen. Subj.* **2015**, *1850*, 1261–1266. [CrossRef] [PubMed]

30. Keung, A.J.; Healy, K.E.; Kumar, S.; Schaffer, D.V. Biophysics and dynamics of natural and engineered stem cell microenvironments. *Wiley Interdiscip. Rev. Syst. Biol. Med.* **2010**, *2*, 49–64. [CrossRef] [PubMed]

31. Chueng, S.-T.D.; Yang, L.; Zhang, Y.; Lee, K.-B. Multidimensional nanomaterials for the control of stem cell fate. *Nano. Converg.* **2016**, *3*, 23. [CrossRef] [PubMed]

32. Lee, W.C.; Lim, C.H.Y.; Shi, H.; Tang, L.A.; Wang, Y.; Lim, C.T.; Loh, K.P. Origin of enhanced stem cell growth and differentiation on graphene and graphene oxide. *ACS Nano* **2011**, *5*, 7334–7341. [CrossRef] [PubMed]

33. Nayak, T.R.; Andersen, H.; Makam, V.S.; Khaw, C.; Bae, S.; Xu, X.; Ee, P.-L.R.; Ahn, J.-H.; Hong, B.H.; Pastorin, G.; et al. Graphene for controlled and accelerated osteogenic differentiation of human mesenchymal stem cells. *ACS Nano* **2011**, *5*, 4670–4678. [CrossRef] [PubMed]

34. Park, S.Y.; Park, J.; Sim, S.H.; Sung, M.G.; Kim, K.S.; Hong, B.H.; Hong, S. Enhanced differentiation of human neural stem cells into neurons on graphene. *Adv. Mater.* **2011**, *23*. [CrossRef] [PubMed]

35. Kang, E.-S.; Kim, D.-S.; Suhito, I.R.; Choo, S.-S.; Kim, S.-J.; Song, I.; Kim, T.H. Guiding osteogenesis of mesenchymal stem cells using carbon-based nanomaterials. *Nano Converg.* **2017**, *4*, 2. [CrossRef] [PubMed]

36. Kim, T.-H.; Lee, T.; El-Said, W.A.; Choi, J.-W. Graphene-based materials for stem cell applications. *Materials* **2015**, *8*, 8674–8690. [CrossRef] [PubMed]

37. Janderová, L.; McNeil, M.; Murrell, A.N.; Mynatt, R.L.; Smith, S.R. Human mesenchymal stem cells as an in vitro model for human adipogenesis. *Obesity* **2003**, *11*, 65–74. [CrossRef] [PubMed]

38. Luu, Y.K.; Capilla, E.; Rosen, C.J.; Gilsanz, V.; Pessin, J.E.; Judex, S.; Rubin, C.T. Mechanical stimulation of mesenchymal stem cell proliferation and differentiation promotes osteogenesis while preventing dietary-induced obesity. *J. Bone. Miner Res.* **2009**, *24*, 50–61. [CrossRef] [PubMed]

39. Bruder, S.P.; Fink, D.J.; Caplan, A.I. Mesenchymal stem cells in bone development, bone repair, and skeletal regeneration therapy. *J. Cell Biochem.* **1994**, *56*, 283–294. [CrossRef] [PubMed]

40. Wei, L.; Fraser, J.L.; Lu, Z.-Y.; Hu, X.; Yu, S.P. Transplantation of hypoxia preconditioned bone marrow mesenchymal stem cells enhances angiogenesis and neurogenesis after cerebral ischemia in rats. *Neurobiol. Dis.* **2012**, *46*, 635–645. [CrossRef] [PubMed]

41. Mooney, E.; Dockery, P.; Greiser, U.; Murphy, M.; Barron, V. Carbon nanotubes and mesenchymal stem cells: Biocompatibility, proliferation and differentiation. *Nano Lett.* **2008**, *8*, 2137–2143. [CrossRef] [PubMed]

42. Park, S.Y.; Namgung, S.; Kim, B.; Im, J.; Kim, J.; Sun, K.; Lee, K.B.; Nam, J.M.; Park, Y.; Hong, S. Carbon nanotube monolayer patterns for directed growth of mesenchymal stem cells. *Adv. Mater.* **2007**, *19*, 2530–2534. [CrossRef]

43. Baik, K.Y.; Park, S.Y.; Heo, K.; Lee, K.B.; Hong, S. Carbon nanotube monolayer cues for osteogenesis of mesenchymal stem cells. *Small* **2011**, *7*, 741–745. [CrossRef] [PubMed]

44. Akhavan, O.; Ghaderi, E.; Emamy, H.; Akhavan, F. Genotoxicity of graphene nanoribbons in human mesenchymal stem cells. *Carbon* **2013**, *54*, 419–431. [CrossRef]

45. Trappmann, B.; Gautrot, J.E.; Connelly, J.T.; Strange, D.G.; Li, Y.; Oyen, M.L.; Cohen Stuart, M.A.; Boehm, H.; Li, B.; Vogel, V.; et al. Extracellular-matrix tethering regulates stem-cell fate. *Nat. Mater.* **2012**, *11*, 642–649. [CrossRef] [PubMed]

46. Watt, F.M.; Huck, W.T. Role of the extracellular matrix in regulating stem cell fate. *Nat. Rev. Mol. Cell Biol.* **2013**, *14*, 467–473. [CrossRef] [PubMed]

47. Sawyer, A.; Hennessy, K.; Bellis, S. Regulation of mesenchymal stem cell attachment and spreading on hydroxyapatite by RGD peptides and adsorbed serum proteins. *Biomaterials* **2005**, *26*, 1467–1475. [CrossRef] [PubMed]

48. Kim, T.G.; Park, T.G. Biomimicking extracellular matrix: Cell adhesive RGD peptide modified electrospun poly (D, L-lactic-co-glycolic acid) nanofiber mesh. *Tissue Eng.* **2006**, *12*, 221–233. [CrossRef] [PubMed]

49. Kim, T.-H.; Lee, D.; Choi, J.-W. Live cell biosensing platforms using graphene-based hybrid nanomaterials. *Biosens. Bioelectron.* **2017**, *94*, 485–499. [CrossRef] [PubMed]

50. You, M.; Peng, G.; Li, J.; Ma, P.; Wang, Z.; Shu, W.; Peng, S.; Chen, G.-Q. Chondrogenic differentiation of human bone marrow mesenchymal stem cells on polyhydroxyalkanoate (PHA) scaffolds coated with PHA granule binding protein PhaP fused with RGD peptide. *Biomaterials* **2011**, *32*, 2305–2313. [CrossRef] [PubMed]

51. Sawyer, A.; Weeks, D.; Kelpke, S.; McCracken, M.S.; Bellis, S. The effect of the addition of a polyglutamate motif to RGD on peptide tethering to hydroxyapatite and the promotion of mesenchymal stem cell adhesion. *Biomaterials* **2005**, *26*, 7046–7056. [CrossRef] [PubMed]

52. Cao, H.; Tegenfeldt, J.O.; Austin, R.H.; Chou, S.Y. Gradient nanostructures for interfacing microfluidics and nanofluidics. *Appl. Phys. Lett.* **2002**, *81*, 3058–3060. [CrossRef]

53. Lowe, C.R. Nanobiotechnology: The fabrication and applications of chemical and biological nanostructures. *Curr. Opin. Struct. Biol.* **2000**, *10*, 428–434. [CrossRef]

54. Lu, C.-W.; Hung, Y.; Hsiao, J.-K.; Yao, M.; Chung, T.-H.; Lin, Y.-S.; Wu, S.H.; Hsu, S.C.; Liu, H.M.; Mou, C.Y.; et al. Bifunctional magnetic silica nanoparticles for highly efficient human stem cell labeling. *Nano Lett.* **2007**, *7*, 149–154. [CrossRef] [PubMed]

55. Bharali, D.J.; Klejbor, I.; Stachowiak, E.K.; Dutta, P.; Roy, I.; Kaur, N.; Bergey, E.J.; Prasad, P.N.; Stachowiak, M.K. Organically modified silica nanoparticles: A nonviral vector for in vivo gene delivery and expression in the brain. *Proc. Natl. Acad. Sci. USA* **2005**, *102*, 11539–11544. [CrossRef] [PubMed]

56. Hynes, R.O. Integrins: Versatility, modulation, and signaling in cell adhesion. *Cell* **1992**, *69*, 11–25. [CrossRef]

57. Grinnell, B.W.; Hermann, R.B.; Yan, S.B. Human protein C inhibits selectin-mediated cell adhesion: Role of unique fucosylated oligosaccharide. *Glycobiology* **1994**, *4*, 221–225. [CrossRef] [PubMed]

58. Takeichi, M. Cadherins: A molecular family important in selective cell-cell adhesion. *Annu. Rev. Biochem.* **1990**, *59*, 237–252. [CrossRef] [PubMed]

59. Albelda, S. Role of integrins and other cell adhesion molecules in tumor progression and metastasis. *Lab. Investig.* **1993**, *68*, 4–17. [PubMed]

60. Chapman, H.A. Plasminogen activators, integrins, and the coordinated regulation of cell adhesion and migration. *Curr. Opin. Cell Biol.* **1997**, *9*, 714–724. [CrossRef]

61. Kim, D.-H.; Provenzano, P.P.; Smith, C.L.; Levchenko, A. Matrix nanotopography as a regulator of cell function. *J. Cell Biol.* **2012**, *197*, 351–360. [CrossRef] [PubMed]

62. Yim, E.K.; Darling, E.M.; Kulangara, K.; Guilak, F.; Leong, K.W. Nanotopography-induced changes in focal adhesions, cytoskeletal organization, and mechanical properties of human mesenchymal stem cells. *Biomaterials* **2010**, *31*, 1299–1306. [CrossRef] [PubMed]

63. McNamara, L.E.; McMurray, R.J.; Biggs, M.J.; Kantawong, F.; Oreffo, R.O.; Dalby, M.J. Nanotopographical control of stem cell differentiation. *J. Tissue Eng. Regen. Med.* **2010**, *1*, 120623. [CrossRef] [PubMed]

64. Kim, H.N.; Jiao, A.; Hwang, N.S.; Kim, M.S.; Kim, D.-H.; Suh, K.-Y. Nanotopography-guided tissue engineering and regenerative medicine. *Adv. Drug Deliv. Rev.* **2013**, *65*, 536–558. [CrossRef] [PubMed]

65. Dalby, M.J.; Gadegaard, N.; Tare, R.; Andar, A.; Riehle, M.O.; Herzyk, P.; Wilkinson, C.D.W.; Oreffo, R.O.C. The control of human mesenchymal cell differentiation using nanoscale symmetry and disorder. *Nat. Mater.* **2007**, *6*, 997–1003. [CrossRef] [PubMed]

66. Shah, S. The nanomaterial tookit for neuroengineering. *Nano Converg.* **2016**, *3*, 25. [CrossRef] [PubMed]

67. Jeong, H.-C.; Choo, S.-S.; Kim, K.-T.; Hong, K.-S.; Moon, S.-H.; Cha, H.-J.; Kim, T.-H. Conductive hybrid matrigel layer to enhance electrochemical signals of human embryonic stem cells. *Sens. Actuator B Chem.* **2017**, *424*, 224–230. [CrossRef]

Article

Bioreducible Polymer Micelles Based on Acid-Degradable Poly(ethylene glycol)-poly(amino ketal) Enhance the Stromal Cell-Derived Factor-1α Gene Transfection Efficacy and Therapeutic Angiogenesis of Human Adipose-Derived Stem Cells

Tae-Jin Lee [1], Min Suk Shim [2], Taekyung Yu [3], Kyunghee Choi [4,5], Dong-Ik Kim [6], Soo-Hong Lee [7,8,*] and Suk Ho Bhang [1,*]

[1]   School of Chemical Engineering, Sungkyunkwan University, Suwon 16419, Korea; eclatwiz@hotmail.com
[2]   Division of Bioengineering, Incheon National University, Incheon 406-772, Korea; msshim@inu.ac.kr
[3]   Department of Chemical Engineering, College of Engineering, Kyung Hee University, Youngin 17104, Korea; tkyu@khu.ac.kr
[4]   Department of Pathology and Immunology, Washington University School of Medicine, St. Louis, MO 63110, USA; kchoi@wustl.edu
[5]   Developmental, Regenerative, and Stem Cell Biology Program, Washington University School of Medicine, St. Louis, MO 63110, USA
[6]   Division of Vascular Surgery, Samsung Medical Center, Sungkyunkwan University School of Medicine, Seoul 06351, Korea; dikim@skku.edu
[7]   Department of Biomedical Science, CHA University, Seongnam-si 13488, Korea
[8]   Department of Medical Biotechnology, Dongguk University, Gyeonggi-do 10326, Korea
[*]   Correspondence: soohong@dongguk.edu (S.-H.L.); sukhobhang@skku.edu (S.H.B.); Tel.: ++82-31-961-5153 (S.-H.L.); +82-31-290-7242 (S.H.B.)

Abstract: Adipose-derived stem cells (ADSCs) have the potential to treat ischemic diseases. In general, ADSCs facilitate angiogenesis by secreting various pro-angiogenic growth factors. However, transplanted ADSCs have a low therapeutic efficacy in ischemic tissues due to their poor engraftment and low viability. Stromal cell-derived factor-1α (SDF-1α) improves the survival rate of stem cells transplanted into ischemic regions. In this study, we developed acid-degradable poly(ethylene glycol)-poly(amino ketal) (PEG-PAK)-based micelles for efficient intracellular delivery of *SDF-1α* plasmid DNA. The *SDF-1α gene* was successfully delivered into human ADSCs (hADSCs) using PEG-PAK micelles. Transfection of *SDF-1α* increased *SDF-1α*, vascular endothelial growth factor, and basic fibroblast growth factor gene expression and decreased apoptotic activity in hADSCs cultured under hypoxic conditions in comparison with conventional gene transfection using polyethylenimine. *SDF-1α*-transfected hADSCs also showed significantly increased *SDF-1α* and VEGF expression together with reduced apoptotic activity at 4 weeks after transplantation into mouse ischemic hindlimbs. Consequently, these cells improved angiogenesis in ischemic hindlimb regions. These PEG-PAK micelles may lead to the development of a novel therapeutic modality for ischemic diseases based on an acid-degradable polymer specialized for gene delivery.

Keywords: angiogenesis; bioreducible polymer; gene therapy; hADSCs; *SDF-1α*

1. Introduction

Adipose-derived stem cells (ADSCs) have the potential to treat ischemic diseases. These cells facilitate angiogenesis by secreting various pro-angiogenic growth factors such as vascular endothelial

growth factor (VEGF) and fibroblast growth factor (FGF) [1]. Moreover, ADSCs can be easily obtained from adipose tissues [1]. However, ADSCs transplanted into ischemic region have a low therapeutic efficacy due to their poor engraftment and low viability [2]. To improve the therapeutic efficacy, the survival of ADSCs must be enhanced, which would increase the secretion of paracrine pro-angiogenic factors.

Ischemic tissues secrete various cytokines, chemokines, proteins, and growth factors [3]. Among these, stromal cell-derived factor-1α (SDF-1α) induces the recruitment and migration of stem cells [3]. SDF-1α can enhance cell survival by inactivating the cell death molecular pathway and increasing the transcription of cell survival genes [4,5]. Moreover, SDF-1α improves the survival rate of transplanted mesenchymal stem cells (MSCs) [6,7]. Cationic polymer-based nanoparticles have been researched for gene delivery [8]. Polyethylenimine (PEI), a polycation with a high cationic charge density, is a highly efficient gene delivery vector [8]. Cationic polymers can condense negatively charged nucleic acids and protect them from nuclease-induced degradation [9]. However, high-molecular-weight PEI is associated with problems such as non-biodegradability and high cytotoxicity [10]. To overcome these problems and increase the efficiency of gene delivery, biodegradable and nontoxic polymers that can efficiently release nucleic acids in response to cellular stimuli are required [11].

In this study, poly(ethylene glycol)-poly(amino ketal) (PEG-PAK), an acid-degradable cationic polymer whose backbone contains ketal linkages, was used to deliver *SDF-1α* plasmid DNA (pDNA) into human adipose-derived stem cells (hADSCs). PEG-PAK micelles efficiently delivered *SDF-1α* pDNA into the cytoplasm of hADSCs in comparison with conventional gene carriers and exhibited significantly reduced cytotoxicity. When transplanted into the ischemic hindlimbs of mice, *SDF-1α*-transfected hADSCs demonstrated improved viability and therapeutic angiogenesis. These PEG-PAK micelles may lead to the development of a novel therapeutic modality for ischemic diseases based on an acid-degradable polymer specialized for gene delivery.

2. Results

2.1. Characterization and Gene Transfection Efficiency of PEG-PAK Micelles

Acid-degradable poly(amino ketal) (PAK) was synthesized for efficient DNA delivery (Figure 1A). Before acid hydrolysis, pDNA/PEG-PAK micelles were spherical (Figure 1B, left). After 8h of acid hydrolysis, the structure of pDNA/PEG-PAK micelles was loosened and disrupted (Figure 1B, right). Intracellular dissociation of pDNA from pDNA/PEG-PAK micelles was confirmed by confocal laser scanning microscopy. A high level of pDNA (green dots) dissociated from PEG-PAK micelles (red dots) was found in the cytosol and perinuclear region (Figure 1B). The gene transfection efficiency of *SDF-1α* pDNA/PEG-PAK micelles was evaluated by incubating them with hADSCs for 48 h under hypoxic conditions. *SDF-1α* mRNA expression was measured and quantified (Figure 1C,D). mRNA expression of *SDF-1α* was significantly higher in the SDF-1α-PEG-PAK group than in the other groups.

2.2. Decreased Apoptosis and Enhanced Secretion of Pro-Angiogenic Factors in hADSCs Overexpressing SDF-1α

The anti-apoptotic effect of *SDF-1α* overexpression using PEG-PAK micelles was investigated in hADSCs cultured under hypoxic conditions. Expression of the anti-apoptotic gene *Bcl-2* and the pro-apoptotic gene *p53* was quantified by reverse transcription-polymerase chain reaction (RT-PCR) (Figure 2A,B). *Bcl-2* and *p53* expression was increased and decreased, respectively, in hADSCs transfected with *SDF-1α* pDNA/PEG-PAK micelles. The total amount of DNA was higher in these cells than in the other groups (Figure 2C). Moreover, hADSCs transfected with SDF-1α pDNA/PEG-PAK micelles secreted higher levels of *SDF-1α*, VEGF, and FGF2 than cells in the other groups (Figure 2D–F).
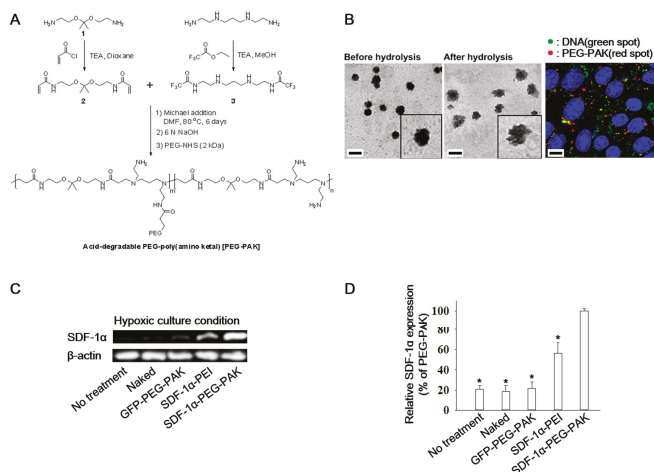
Figure 1. (**A**) Scheme of the synthesis of acid-degradable PEG-PAK; (**B**) Transmission electron microscopy images of *SDF-1α*/PEG-PAK micelles before and after acid hydrolysis (pH 5.0 for 8 h at 37 °C, scale bars indicate 200 nm) and confocal laser scanning microscopy images showing the intracellular colocalization of Alexa Fluor 488-labeled *SDF-1α* pDNA (green) and Cy3-labeled PEG-PAK (red) in hADSCs (blue indicates nuclei stained with DRAQ5, scale bar indicates 10 μm); (**C**) RT-PCR analysis and (**D**) quantification of SDF-1α expression in hADSCs transfected with SDF-1α using various methods under hypoxic culture conditions (* $p < 0.05$ compared with SDF-1α-PEG-PAK group). PEG-PAK: poly(ethylene glycol)-poly(amino ketal); SDF-1α: stromal cell-derived factor-1α; RT-PCR: reverse transcription-polymerase chain reaction; hADSCs: human adipose-derived stem cells; GFP: green fluorescence protein.
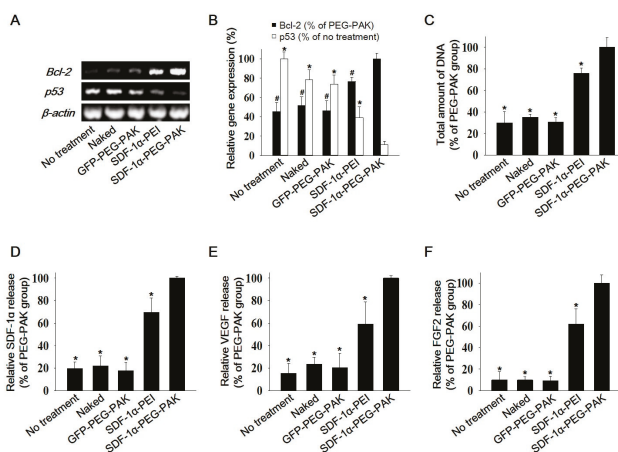
Figure 2. Apoptotic activity and pro-angiogenic growth factor secretion in hADSCs transfected with SDF-1α using PEG-PAK micelles. (**A**) RT-PCR analysis of the anti-apoptotic factor *Bcl-2* and the pro-apoptotic factor *p53* and (**B**) quantification of their expression in hADSCs transfected with *SDF-1α* using various methods. (**C**) Total amount of DNA in each group showing relative cell viability. Relative levels of (**D**) SDF-1α, (**E**) VEGF, and (**F**) FGF2 secretion by hADSCs transfected with *SDF-1α* using various methods. Secretion was quantified via enzyme-linked immunosorbent assays. (*,# $p < 0.05$ compared with SDF-1α-PEG-PAK group). VEGF: vascular endothelial growth factor; FGF2: basic fibroblast growth factor.

2.3. Effect of hADSCs Transfected with SDF-1α pDNA/PEG-PAK Micelles in Ischemic Limbs

The therapeutic efficacy of hADSCs transfected with *SDF-1α* pDNA/PEG-PAK micelles was evaluated in a mouse hindlimb ischemia model. After induction of ischemia, the mice were treated with hADSCs or those transfected with *SDF-1α* pDNA/PEG-PAK micelles (PEG-PAK + hADSC), *SDF-1α* pDNA/PEI polyplexes (PEI + hADSC), or naked *SDF-1α* pDNA (naked). Mice with ischemic injury were also injected with phosphate-buffered saline (PBS) as a control (no treatment). *SDF-1α* expression in ischemic limbs was significantly increased in the PEG-PAK + hADSC group at 21 days after treatment (Figure 3A). Consistently, VEGF expression was also increased in this group (Figure 3B).

Cell survival in ischemic limbs was investigated by double immunofluorescence staining of caspase-3 and human nuclear antigen (HNA) (Figure 3C). There were fewer caspase-3-positive cells (apoptotic cells in the ischemic limb) and HNA/caspase-3 double-positive cells (apoptotic hADSCs) in the PEG-PAK + hADSC group than in the other groups (Figure 3C–E). Moreover, mRNA expression of human *Bcl-2* and *p53* was higher and lower, respectively, in the PEG-PAK + hADSC group than in the PEI + hADSC, hADSC, and naked groups (Figure 3F). Similarly, mRNA expression of mouse *Bcl-2* and *p53* expression was higher and lower, respectively, in the PEG-PAK + hADSC group than in the other groups (Figure 3F).
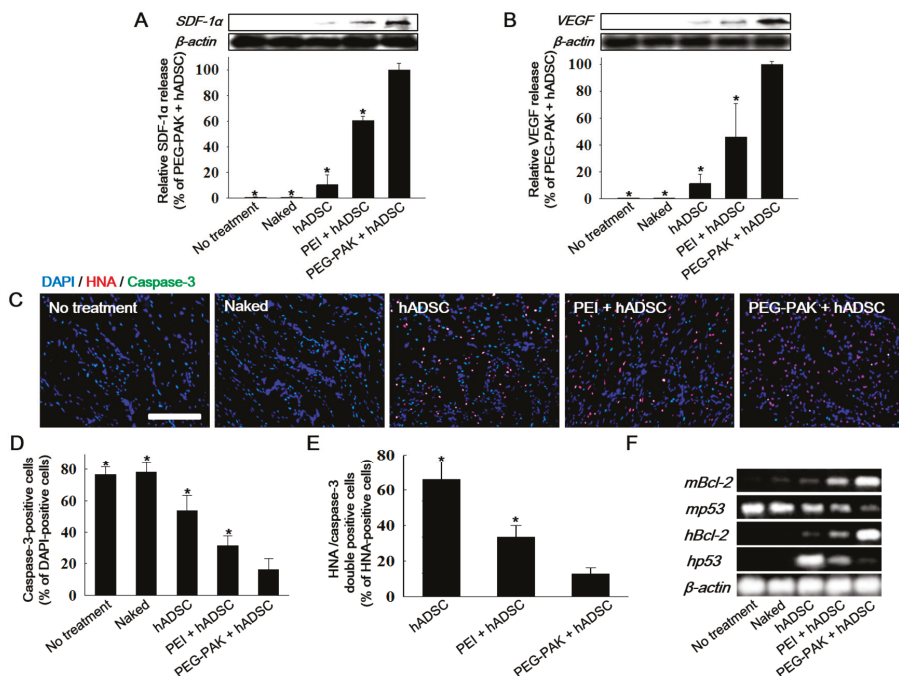
Figure 3. Western blot analysis and quantification of (**A**) SDF-1α and (**B**) VEGF expression in the mouse hindlimb ischemia model 3 days after the various treatments; (**C**) Immunofluorescence staining of caspase-3 (green) and HNA (red) in ischemic limb tissues retrieved 3 days after treatment (blue indicates nuclei stained with 4′,6-diamidino-2-phenylindole (DAPI), scale bar = 100 μm). Percentages of (**D**) caspase-3-positive cells (apoptotic cells) among DAPI-positive cells (total cells) and (**E**) HNA/caspase-3 double-positive cells (apoptotic hADSCs) among HNA-positive cells (hADSCs) in the ischemic region (* $p < 0.05$ compared with PEG-PAK + hADSC group); (**F**) RT-PCR analysis of human and mouse *Bcl-2* (anti-apoptotic factor) and *p53* (pro-apoptotic factor) in ischemic limbs.

2.4. In Vivo Pro-Angiogenic Effect of hADSCs Transfected with SDF-1α pDNA/PEG-PAK Micelles

Fibrotic tissue formation in ischemic hindlimb regions was reduced in the PEG-PAK + hADSC group (Figure 4). Moreover, blood perfusion in ischemic limbs was significantly higher in the PEG-PAK + hADSC group than in the other groups (Figure 4B,C). Furthermore, limb salvage was observed in 60% of mice in the PEG-PAK + hADSC group (Figure 4D). The density of CD31-positive microvessels was significantly higher in the PEG-PAK + hADSC group than in the other groups at 21 days after treatment (Figure 5A,C). Moreover, the density of smooth muscle (SM)-α actin-positive vessels was significantly higher in the PEG-PAK + hADSC group than in the other groups (Figure 5B,D). Transplantation of hADSCs transfected with *SDF-1α* pDNA/PEG-PAK micelles increased expression of the proteoglycan NG2, a marker of pericytes, in ischemic limbs, which was related to the stabilization of microvessels (Figure 5E,H). Expression of intercellular adhesion molecule (ICAM) and vascular cell adhesion molecule (VCAM) was also increased in the PEG-PAK + hADSC group (Figure 5E,H). This indicates that the number of activated endothelial cells was increased, which may promote the recruitment of endothelial progenitor cells (EPCs) into ischemic regions. Indeed, CD34 expression in ischemic limbs was higher in the PEG-PAK + hADSC group than in the other groups, providing strong evidence that the recruitment of EPCs into ischemic regions was increased (Figure 6).
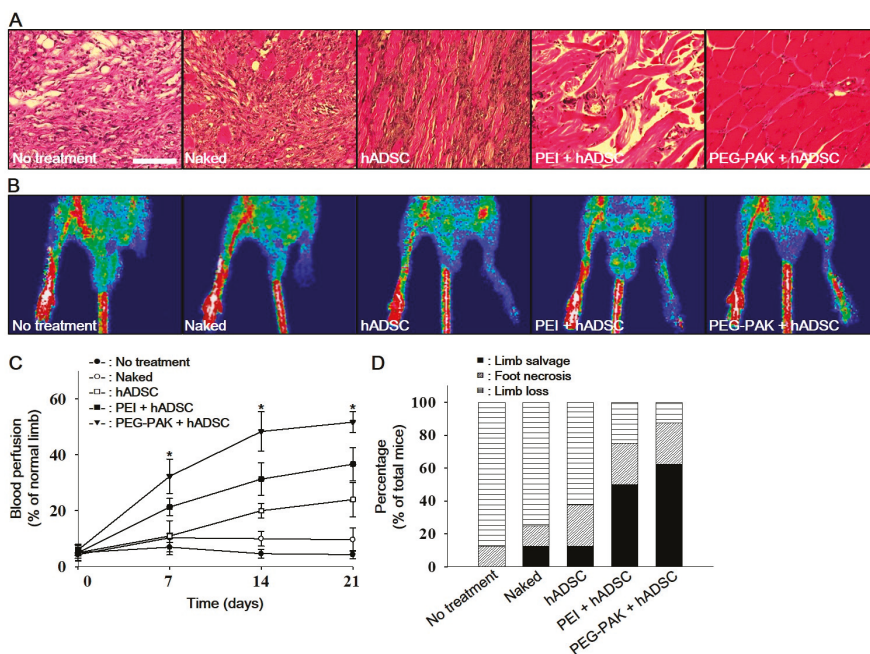
Figure 4. (**A**) Hematoxylin and eosin staining of hindlimb tissues obtained 21 days after ischemic injury (scale bars indicate 100 μm). (**B**) Representative laser Doppler perfusion imaging analysis performed at 21 days after treatment. (**C**) Blood perfusion of ischemic limbs relative to that of normal limbs at 0, 7, 14, and 21 days after treatment (* $p < 0.01$ compared with other groups). (**D**) Percentage of mice displaying limb salvage at 21 days after treatment.
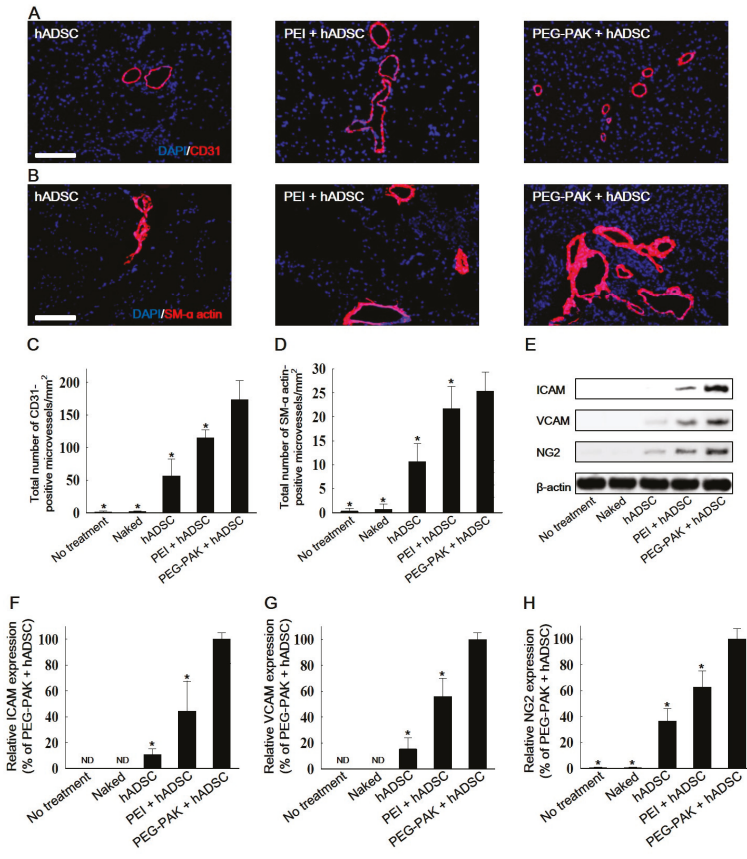
Figure 5. Representative immunohistochemical images of microvessels positive for (**A**) CD31 (red) and (**B**) smooth muscle (SM) α-actin (red) retrieved from hindlimb tissues 21 days after treatment (blue indicates nuclei stained with DAPI, scale bars indicate 100 μm). Quantification of microvessels positive for (**C**) CD31 and (**D**) SM α-actin in hindlimb tissues (* $p < 0.05$ compared with PEG-PAK + hADSC group); (**E**) Western blot analysis and quantification of (**F**) ICAM, (**G**) VCAM, and (**H**) NG2 expression in hindlimb tissues at 21 days after treatment. ICAM: intercellular adhesion molecule; VCAM: vascular cell adhesion molecule.
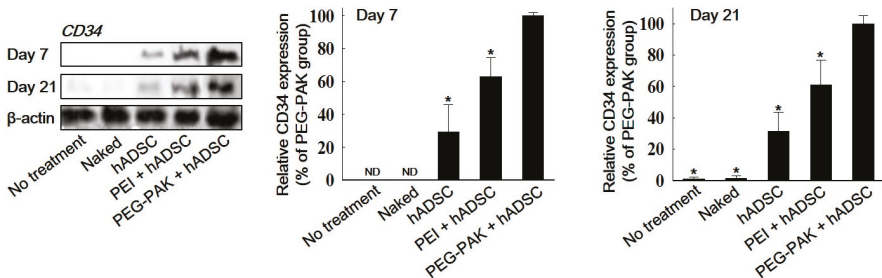
Figure 6. Western blot analysis and quantification of CD34 expression in ischemic hindlimb tissues at 7 and 21 days after treatment (* $p < 0.05$ compared with PEG-PAK + hADSC group).

3. Discussion

One of the major obstacles in stem cell-based therapy is the poor engraftment and low viability of transplanted stem cells, leading to a low therapeutic efficacy [2,12,13]. Various attempts have been made to overcome this problem [14–17]. Gene modifications, including overexpression of the serine/threonine protein kinase Akt, the proto-oncogene with serine/threonine-protein kinase activity Pim-1, or heme oxygenase-1, have been used to improve the survival of transplanted cells [18–20]. Along with these anti-apoptotic genes, expression of the well-known pro-angiogenic factor SDF-1α also improves the survival of transplanted stem cells such as MSCs and EPCs [6,21]. Therefore, we hypothesized that transfection of *SDF-1α* would enhance the survival and therapeutic efficacy of hADSCs. As expected, *SDF-1α* transfection decreased apoptotic activity in hADSCs cultured under hypoxic conditions (Figure 2) and transplanted into ischemic regions (Figure 3). Moreover, VEGF secretion was enhanced in *SDF-1α*-transfected hADSCs (Figures 2 and 3). This result shows that SDF-1α released from transplanted hADSCs transfected with SDF-1α pDNA/PEG-PAK micelles stimulated VEGF secretion [6,22]. Along with the improved survival of transplanted hADSCs, their enhanced secretion of pro-angiogenic factors might help to decrease ischemic damage and improve angiogenesis (Figure 4).

Recruitment of EPCs by SDF-1α-transfected hADSCs enhanced the angiogenic efficacy. EPC recruitment into ischemic regions, as represented by CD34 expression in ischemic limbs, was enhanced at 7 and 21 days following transplantation of SDF-1α-transfected hADSCs (Figure 6). SDF-1α release in ischemic limbs was increased by transplantation of hADSCs and was further amplified by transplantation of *SDF-1α*-transfected hADSCs (Figure 3). In addition, transplantation of SDF-1α-transfected hADSCs increased expression of ICAM and VCAM in ischemic tissues (Figure 5E–H). SDF-1a is a major chemoattractant for EPCs [23], and local release of SDF-1α increases homing of these cells [24]. ICAM and VCAM also contribute to EPC homing [25,26]. These results suggest that the increases in SDF-1α, ICAM, and VCAM expression upon transplantation of *SDF-1α*-transfected hADSCs led to the recruitment of EPCs, which facilitated angiogenesis in ischemic regions.

In summary, we have developed an acid-degradable non-viral carrier for efficient intracellular delivery. PEG-PAK micelles successfully delivered SDF-1α pDNA into hADSCs. SDF-1α-transfected hADSCs demonstrated increased SDF-1α, VEGF, and FGF2 expression and decreased apoptotic activity when cultured under hypoxic conditions. Similarly, SDF-1α-transfected hADSCs exhibited enhanced SDF-1α and VEGF expression and decreased apoptotic activity when transplanted into ischemic tissues. Finally, the enhanced viability of hADSCs increased the angiogenic efficacy in ischemic tissues. This study may offer a clever strategy to treat ischemic diseases using an acid-degradable polymer specialized for gene delivery.

4. Materials and Methods

4.1. Materials

Acryloyl chloride (C_3H_3ClO, Ward Hill, MA, USA) was obtained from Alfa Aesar. *N,N′-bis*(2-aminoethyl)-1,3-propanediamine, ethyl trifluoroacetate($C_4H_5F_3O_2$), 25 kDa branched polyethylenimine (B-PEI), trimethylamine(C_3H_9N), 3-(4,5-dimethyl-2-thiazolyl)-2,5-diphenyltetrazoliumbromide (MTT), and sodium hydroxide were prepared from Sigma Aldrich (St. Louis, MO, USA). PD-10 desalting columns were purchased from GE Healthcare (Piscataway, NJ, USA). Alexa Fluor 488 nucleic acid-labeling kit were purchased from Invitrogen (Eugene, OR, USA).

4.2. Synthesis of Acid-Degradable (PEG-PAK)

4.2.1. Synthesis of Acid-Degradable Ketal Crosslinker (Compound **2**)

Compound **1** was prepared as previously reported [27]. Compound **1** (0.83 g, 5.14 mmol, 1 equiv) in 20 mL of dioxane was mixed with 2.60 g of triethylamine (25.70 mmol, 5 equiv) on ice. Then acryloyl chloride (1.86 g, 20.56 mmol, 4 equiv) in 20 mL of dioxane was added dropwise to the mixture with continuous stirring. After the mixture was stirred for 30 min, the crude product was extracted with ethyl acetate and then purified by silica gel chromatography using a gradient from hexane to 1/1 hexane/ethyl acetate to obtain the yellow product (0.48 g, 1.79 mmol, 35% yield).

4.2.2. Synthesis of Compound **3**

N,N'-bis(2-aminoethyl)-1,3-propanediamine (2.00 g, 12.48 mmol, 1 equiv) and triethylamine (3.79 g, 37.44 mmol, 3 equiv) were dissolved in 100 mL of methanol. Ethyl trifluoroacetate (4.43 g, 31.20 mmol, 2.5 equiv), which selectively protects primary amine groups in *N,N'*-bis(2-aminoethyl)-1,3-propanediamine, was added to the mixture and stirred for 24 h at room temperature. After the reaction solvent was evaporated, the mixture was purified by silica gel chromatography using an eluent gradient from ethyl acetate to methanol to yield the product as a white solid (3.12 g, 8.86 mmol, 71% yield).

4.2.3. Synthesis of Acid-Degradable PEG-PAK

PAK was synthesized by reacting compound **3** (0.47 g, 1.33 mmol, 1 equiv) with acid degradable ketal crosslinker (compound **2**, 0.36 g, 1.33 mmol, 1 equiv) in 10 mL of dimethylformamide (DMF) via Michael addition conjugation. Afterwards, the mixtures were stirred for 6 days at 80 °C, and the polymer was precipitated into anhydrous diethyl ether and dried under vacuum. The precipitated polymer was dissolved in 10 mL of 1:9 methanol/6 N NaOH solution and stirred for 6 h to deprotect trifluoroacetate groups. The crude polymer was purified by dialysis (MW cutoff = 6 kDa) against DI water at 4 °C. Then, the polymer was dissolved in deionized (DI) water and amine-reactive 2 kDa PEG-NHS (Laysan Bio, Arab, AL, USA) was added to solution for pegylation. After the pegylation, the polymer was purified by a PD-10 desalting column (MW cutoff = 5 kDa), followed by flash dialysis against DI water (MW cutoff = 6 kDa). The final product was obtained as a powder with a hint of yellow color after lyophilization (0.18 g). Figure 1A shows a summary of the total synthetic process.

4.3. Transmission Electron Microscopy (TEM)

One microgram of *SDF-1α* pDNA was complexed with 20 µL of PEG-PAK in DI water (N/P ratio = 100). Two microliters of mixture solution was dropped on a carbon-coated copper TEM grid and air dried for 10 min at room temperature. To observe size and morphological changes of the polyplexes upon acidic condition, 18 µL of *SDF-1α* pDNA/PEG-PAK polyplex solution was mixed with 36 µL of pH 5.0 buffer and further incubated for 8 h at 37 °C. Then 2 µL of polyplex solution was deposited on a TEM grid and dried. TEM images were acquired using a FEI Tecnai G2 Spirit microscope (FEI Company, Hillsboro, OR, USA) operated at 120 kV.

4.4. hADSCs Culture

hADSCs were purchased (Lonza, Basel, Switzerland) and cultured in Dulbecco's Modified Eagle Medium (Gibco BRL, Gaithersburg, MD, USA) supplemented with 100 units/mL of penicillin (Gibco BRL), 10% (*v/v*) fetal bovine serum (FBS, Gibco BRL), and 100 µg/mL of streptomycin (Gibco BRL). All experiments were performed using hADSCs within five passages. To induce hypoxic condition in vitro, hADSCs were cultured under 1% oxygen and serum-free medium, as previously described [28].

4.5. In Vitro SDF-1α Transfection

hADSCs were seeded at a density of 3×10^5 cells/well 24 h prior to transfection. *SDF-1α* pDNA PEG-PAK polyplexes were prepared by mixing 8 μg (=600 pmol) of *SDF-1α* pDNA dissolved in 300 μL of DI water with a desired amount of PEG-PAK polymer in 300 μL of DI water to obtain the N/P ratio of 100. *SDF-1α* pDNA/PEI polyplexes at the N/P ratio of 10 were prepared as a control. After 30 min of incubation at room temperature, the culture medium in the dish was replaced with 5.4 mL of FBS-free Dulbecco Modified Eagle Medium (DMEM). Then 600 μL of polplex solution (or naked SDF-1α pDNA) was added to the cells to obtain a final concentration of 100 nM. After 4 h of incubation, the medium in the dish was replaced with fresh medium containing 10% FBS, followed by further incubation for 48 h.

4.6. Confocal Laser Scanning Microscopy

For fluorescence labeling of pDNA/PEG-PAK polyplexes, the desired amount of PEG-PAK (N/P = 100) was mixed with 5 μg of Alexa Fluor 488-labeled DNA in DI water (final volume of 500 μL). After 30 min of incubation, the polyplexes were labeled with amine-reactive Cy3 dye by following the manufacturer's instructions. Labeled pDNA/ PEG-PAK polyplexes were purified by a PD-10 size exclusion column. hADSCs were seeded at a density of 2×10^4 cells/well in a Falcon 8-well culture slide, 15 h prior to the incubation with the fluorescently labeled polyplexes. After the medium was replaced with 250 μL of fresh DMEM, 50 μL of polyplex solution containing 0.5 μg of Alexa Fluor 488-labeled DNA was incubated with the cells in a well. After 8 h of incubation, the cells were washed with PBS, followed by fixation with 2% paraformaldehyde for 30 min at 4 °C. Then the nuclei of the cells were counter-stained with 1 μM DRAQ5 solution in PBS. The intracellular localization and disassembly of pDNA/PEG-PAK polyplexes in hADSCs were observed under a confocal laser scanning microscope (Olympus Fluoview 500, Olympus America, Melville, NY, USA) using a 60× water immersion Plan-Apochromat objective lens. Fluorescence images of Alexa Fluor 488-labeled pDNA (green) were acquired using a 488 nm excitation light from a multiple argon laser. A krypton laser with 568 nm excitation was used to scan the images of the Cy3-labeled PEG-PAK (red). Images of DRAQ5-stained nuclei (blue) were acquired using a 633 nm helium-neon laser. Images were scanned at mid z-axis point of the cells to differentiate the fluorescence from the polyplexes adsorbed on the cell surface.

4.7. Reverse Transcription-Polymerase Chain Reaction (RT-PCR)

hADSCs were homogenized and lysed in TRIzol reagent. Total ribonucleic acid (RNA) was extracted from hADSCs 5 days after hypoxic culture using chloroform. After the extracted RNA was precipitated with 80% (v/v) isopropanol, the RNA pellet was washed with 75% (v/v) ethanol, air-dried, and dissolved in 0.1% (v/v) diethyl pyrocarbonate-treated water. RNA concentration was determined by measuring the absorbance at 260 nm using a spectrophotometer. Reverse transcription was performed using 5 μg of pure total RNA and SuperScriptTM II reverse transcriptase, followed by PCR amplification of the synthesized complementary deoxyribonucleic acid. The deoxyribonucleic acid concentration of all the samples in the different experimental sets was measured with a NanoDrop ND-1000 (NanoDrop Technologies, Rockland, Denmark). PCR consisted of 35 cycles of denaturing (94 °C, 30 s), annealing (58 °C, 45 s), and extension (72 °C, 45 s), with a final extension at 72 °C for 10 min. PCR was followed by electrophoresis on a 2% (w/v) agarose gel and visualization by ethidium bromide staining. PCR products were analyzed using a gel documentation system (Gel Doc 1000, Bio-Rad, Hercules, CA, USA). *β-actin* served as an internal control.

4.8. Western Blot Analysis

The retrieved samples were lysed in ice-cold lysis buffer (15 mM Tris·HCl (pH 8.0), 0.25 M sucrose, 15 mM NaCl, 1.5 mM MgCl₂, 2.5 mM ethylenediaminetetraacetic acid (EDTA), 1 mM ethylene glycol tetraacetic acid (EGTA), 1 mM DTT, 2 mM NaPPi, 1 μg/mL pepstatin A, 2.5 μg/mL aprotinin,

5 µg/mL leupeptin, 0.5 mM phenylmethylsulfonyl fluoride, 0.125 mM Na_3VO_4, 25 mM NaF, and 10 µM lactacystin). After protein concentration was determined using a bicinchoninic acid assay (BCA) kit, equal protein concentration from each sample as mixed with Laemmli sample buffer, loaded, and separated by sodium dodecyl sulfate-polyacrylamide gel electrophoresis (SDS-PAGE) on a 10% (*v*/*v*) resolving gel. Proteins separated by SDS-PAGE were applied to an Immobilon-P membrane (Millipore Corp., Billerica, MA, USA) and then probed with antibody against SDF-1α (Abcam, Cambridge, UK) for 1 hour at room temperature. The membranes were incubated with horseradish peroxidase-conjugated secondary antibody (Santa Cruz Biotechnology, Santa Cruz, CA, USA) for 1 hour at room temperature. The blots were developed using an enhanced chemiluminescence detection system (Amersham Bioscience, Piscataway, NJ, USA). Luminescence was recorded on X-ray film (Fuji super RX, Fujifilm Medical Systems, Tokyo, Japan), and bands were detected using a densitometer (Model GS-690, BioRad, Hercules, CA, USA).

4.9. Enzyme-Linked Immunosorbent Assay (ELISA)

Concentrations of angiogenic growth factors in conditioned media obtained from hADSCs cultures were determined using ELISA kits for human SDF-1α, VEGF, and FGF2 (R&D Systems, Minneapolis, MN, USA) according to the manufacturer's protocol.

4.10. Model of Mouse Hindlimb Ischemia

Hindlimb ischemia was induced in mice as previously described [29]. Four-week old female athymic mice (20–25 g body weight, Bar Harbor, ME, USA) were anesthetized with xylazine (10 mg/kg) and ketamine (100 mg/kg). The femoral artery and its branches were ligated via skin incision using a 6-0 silk suture (Ethicon, Somerville, NJ, USA), along with the external iliac artery and all upstream arteries. The femoral artery was then excised from its proximal origin as a branch of the external iliac artery to the distal point whereupon it bifurcates into the saphenous and popliteal arteries. The use and care of all animals in this study were approved by the Institutional Animal Care and Use Committee of Washington University in St. Louis Medical School (No. 20110260, 6 February 2011) and Sungkyunkwan University (No. SKKUIACUC-17-5-3-3, 3 May 2017).

4.11. Transplantation of SDF-1α Transfected hADSC into Ischemic Mouse Hindlimbs

After arterial dissection, mice were randomly divided into six groups (*n* = 8 for each group). Naked *SDF-1α* pDNA, hADSC, *SDF-1* pDNA/PEI transfected hADSCs, or *SDF-1* pDNA/PEG-PAK transfected hADSC (3×10^6 cells/limb) were intramuscularly injected into the gracilis muscle of the medial thigh.

4.12. Histology and Laser Doppler Imaging Analysis

Ischemic limb muscles retrieved 21 days post-treatment were fixed with a formaldehyde solution, dehydrated with a graded ethanol series, and embedded in paraffin. Next, 4-µm sections obtained from the specimens were stained with hematoxylin and eosin (H&E) to examine muscle degeneration and tissue inflammation. Laser Doppler imaging analysis (LDPI) was performed as described previously [29]. A laser Doppler perfusion imager (Moor Instruments, Devon, UK) was used for serial noninvasive physiological evaluation of neovascularization. Mice were monitored by serial scanning of surface blood flow in hindlimbs on days 0, 7, 14, and 21 after treatment. Digital color-coded images were scanned and analyzed to quantify a blood flow in ischemic regions from the knee joint to the toe. Mean values of perfusion were subsequently calculated.

4.13. Immunohistochemistry

Ischemic limb muscles harvested 21 days post-treatment were embedded in optimal cutting temperature compound (O.C.T. compound, TISSUE-TEK® 4583, Sakura Finetek USA Inc., Torrance,

CA, USA), followed by freezing and slicing into 10 μm-thick sections at −22 °C. After all the samples were completely sectioned, ten slides were selected out of the beginning, middle, and end part of each sample. Immunofluorescent staining with anti-human nuclear antigen (HNA) (Chemicon, Temecula, CA, USA) was conducted to detect transplanted human cells from the sections. Immunofluorescent staining with caspase-3 (Abcam, Cambridge, UK) was used to detect apoptotic cells. For the detection of capillaries and arterioles in ischemic regions, sections were immunofluorescently stained with anti-CD31 (PECAM, Abcam) and anti-smooth muscle (SM) α-actin (Abcam), respectively, followed by being examined using a fluorescent microscope (Nikon TE2000, Tokyo, Japan). Twenty different images per slide were randomly acquired from three different samples and analyzed at ×200 magnification. CD31-positive vessels with single-layered round morphology and SM α-actin-positive vessels with multiple-layered round morphology were counted, respectively. Fluorescent vessels with round morphology were counted and calculated as vessel number per mm^2. Rhodamine- (red) or FITC- (green) conjugated secondary antibodies (Jackson ImmunoResearch Laboratories, West Grove, PA) were used to visualize the stained vessels. Cellular nuclei were counter-stained with DAPI (Vector Laboratories, Burlingame, CA).

4.14. Statistical Analysis

GraphPad Prism 7 Software (GraphPad Prism 7, GraphPad Software, San Diego, CA, USA) was used for performing statistical analysis. Triplicate data were analyzed using with one-way analysis of variance (ANOVA) with a Bonferroni test for comparing more than two groups in all experiments (Figures 1–6). A *p*-value of <0.05 was considered to be significant. Data are presented as mean with standard deviation for all the measurements.

Author Contributions: Suk Ho Bhang designed and performed the experiments; Suk Ho Bhang, Tae-Jin Lee, Min Suk Shim, Taekyung Yu, and Soo-Hong Lee analyzed the data. Tae-Jin Lee, Suk Ho Bhang, and Soo-Hong Lee wrote the manuscript. Kyunghee Choi, Dong-Ik Kim, and Soo-Hong Lee revised the manuscript. Suk Ho Bhang provided overall supervision and coordinated all the experimental activities.

Conflicts of Interest: The authors declare no conflict of interest.

References

1. Gimble, J.M.; Katz, A.J.; Bunnell, B.A. Adipose-derived stem cells for regenerative medicine. *Circ. Res.* **2007**, *100*, 1249–1260. [CrossRef] [PubMed]
2. Nakagami, H.; Maeda, K.; Morishita, R.; Iguchi, S.; Nishikawa, T.; Takami, Y.; Kikuchi, Y.; Saito, Y.; Tamai, K.; Ogihara, T.; et al. Novel autologous cell therapy in ischemic limb disease through growth factor secretion by cultured adipose tissue-derived stromal cells. *Arterioscler. Thromb. Vasc. Biol.* **2005**, *25*, 2542–2547. [CrossRef] [PubMed]
3. Li, Q.; Zhang, A.; Tao, C.; Li, X.; Jin, P. The role of SDF-1-CXCR4/CXCR7 axis in biological behaviors of adipose tissue-derived mesenchymal stem cells in vitro. *Biochem. Biophys. Res. Commun.* **2013**, *441*, 675–680. [CrossRef] [PubMed]
4. Liu, X.; Duan, B.; Cheng, Z.; Jia, X.; Mao, L.; Fu, H.; Che, Y.; Ou, L.; Liu, L.; Kong, D. SDF-1/CXCR4 axis modulates bone marrow mesenchymal stem cell apoptosis, migration and cytokine secretion. *Protein Cell* **2011**, *2*, 845–854. [CrossRef] [PubMed]
5. Lataillade, J.J.; Clay, D.; Bourin, P.; Hérodin, F.; Dupuy, C.; Jasmin, C.; le Bousse-Kerdilès, M.C. Stromal cell-derived factor 1 regulates primitive hematopoiesis by suppressing apoptosis and by promoting G^0/G^1 transition in CD34$^+$ cells: Evidence for an autocrine/paracrine mechanism. *Blood* **2002**, *99*, 1117–1129. [CrossRef] [PubMed]

6. Zhang, M.; Mal, N.; Kiedrowski, M.; Chacko, M.; Askari, A.T.; Popovic, Z.B.; Koc, O.N.; Penn, M.S. SDF-1 expression by mesenchymal stem cells results in trophic support of cardiac myocytes after myocardial infarction. *FASEB J.* **2007**, *21*, 3197–3207. [CrossRef] [PubMed]

7. Cheng, Z.; Ou, L.; Zhou, X.; Li, F.; Jia, X.; Zhang, Y.; Liu, X.; Li, Y.; Ward, C.A.; Melo, L.G.; et al. Targeted migration of mesenchymal stem cells modified with *CXCR4* gene to infarcted myocardium improves cardiac performance. *Mol. Ther.* **2008**, *16*, 571–579. [CrossRef] [PubMed]

8. Ji, M.; Li, P.; Sheng, N.; Liu, L.; Pan, H.; Wang, C.; Cai, L.; Ma, Y. Sialic acid-targeted nanovectors with phenylboronic acid-grafted polyethylenimine robustly enhance siRNA-based cancer therapy. *ACS Appl. Mater. Interfaces* **2016**, *8*, 9565–9576. [CrossRef] [PubMed]

9. Park, T.G.; Jeong, J.H.; Kim, S.W. Current status of polymeric gene delivery systems. *Adv. Drug Deliv. Rev.* **2006**, *58*, 467–486. [CrossRef] [PubMed]

10. Fischer, D.; Bieber, T.; Li, Y.; Elsässer, H.P.; Kissel, T. A novel non-viral vector for DNA delivery based on low molecular weight, branched polyethylenimine: Effect of molecular weight on transfection efficiency and cytotoxicity. *Pharm. Res.* **1999**, *16*, 1273–1279. [CrossRef] [PubMed]

11. Lin, Y.L.; Jiang, G.; Birrell, L.K.; El-Sayed, M.E. Degradable, pH-sensitive, membrane-destabilizing, comb-like polymers for intracellular delivery of nucleic acids. *Biomaterials* **2010**, *31*, 7150–7166. [CrossRef] [PubMed]

12. Song, H.; Song, B.W.; Cha, M.J.; Choi, I.G.; Hwang, K.C. Modification of mesenchymal stem cells for cardiac regeneration. *Expert Opin. Biol. Ther.* **2010**, *10*, 309–319. [CrossRef] [PubMed]

13. Menasche, P. Stem cells for clinical use in cardiovascular medicine: Current limitations and future perspectives. *Thromb. Haemost.* **2005**, *94*, 697–701. [CrossRef] [PubMed]

14. Sekine, H.; Shimizu, T.; Dobashi, I.; Matsuura, K.; Hagiwara, N.; Takahashi, M.; Kobayashi, E.; Yamato, M.; Okano, T. Cardiac cell sheet transplantation improves damaged heart function via superior cell survival in comparison with dissociated cell injection. *Tissue Eng. Part A* **2011**, *17*, 2973–2980. [CrossRef] [PubMed]

15. Ishii, M.; Shibata, R.; Numaguchi, Y.; Kito, T.; Suzuki, H.; Shimizu, K.; Ito, A.; Honda, H.; Murohara, T. Enhanced angiogenesis by transplantation of mesenchymal stem cell sheet created by a novel magnetic tissue engineering method. *Arterioscler. Thromb. Vasc. Biol.* **2011**, *31*, 2210–2215. [CrossRef] [PubMed]

16. Bhang, S.H.; Cho, S.W.; La, W.G.; Lee, T.J.; Yang, H.S.; Sun, A.Y.; Baek, S.H.; Rhie, J.W.; Kim, B.S. Angiogenesis in ischemic tissue produced by spheroid grafting of human adipose-derived stromal cells. *Biomaterials* **2011**, *32*, 2734–2747. [CrossRef] [PubMed]

17. Bhang, S.H.; Lee, S.; Shin, J.Y.; Lee, T.J.; Kim, B.S. Transplantation of cord blood mesenchymal stem cells as spheroids enhances vascularization. *Tissue Eng. Part A* **2012**, *18*, 2138–2147. [CrossRef] [PubMed]

18. Mangi, A.A.; Noiseux, N.; Kong, D.; He, H.; Rezvani, M.; Ingwall, J.S.; Dzau, V.J. Mesenchymal stem cells modified with Akt prevent remodeling and restore performance of infarcted hearts. *Nat. Med.* **2003**, *9*, 1195–1201. [CrossRef] [PubMed]

19. Fischer, K.M.; Cottage, C.T.; Wu, W.; Din, S.; Gude, N.A.; Avitabile, D.; Quijada, P.; Collins, B.L.; Fransioli, J.; Sussman, M.A. Enhancement of myocardial regeneration through genetic engineering of cardiac progenitor cells expressing Pim-1 kinase. *Circulation* **2009**, *120*, 2077–2087. [CrossRef] [PubMed]

20. Tang, Y.L.; Tang, Y.; Zhang, Y.C.; Qian, K.; Shen, L.; Phillips, M.I. Improved graft mesenchymal stem cell survival in ischemic heart with a hypoxia-regulated heme oxygenase-1 vector. *J. Am. Coll. Cardiol.* **2005**, *46*, 1339–1350. [CrossRef] [PubMed]

21. Kalka, C.; Masuda, H.; Takahashi, T.; Kalka-Moll, W.M.; Silver, M.; Kearney, M.; Li, T.; Isner, J.M.; Asahara, T. Transplantation of ex vivo expanded endothelial progenitor cells for therapeutic neovascularization. *Proc. Natl. Acad. Sci. USA* **2000**, *97*, 3422–3427. [CrossRef] [PubMed]

22. Salcedo, R.; Oppenheim, J.J. Role of chemokines in angiogenesis: CXCL12/SDF-1 and CXCR4 interaction, a key regulator of endothelial cell responses. *Microcirculation* **2003**, *10*, 359–370. [CrossRef] [PubMed]

23. Lau, T.T.; Wang, D.A. Stromal cell-derived factor-1 (SDF-1): Homing factor for engineered regenerative medicine. *Expert Opin. Biol. Ther.* **2011**, *11*, 189–197. [CrossRef] [PubMed]

24. Yamaguchi, J.; Kusano, K.F.; Masuo, O.; Kawamoto, A.; Silver, M.; Murasawa, S.; Bosch-Marce, M.; Masuda, H.; Losordo, D.W.; Isner, J.M.; et al. Stromal cell–derived factor-1 effects on ex vivo expanded endothelial progenitor cell recruitment for ischemic neovascularization. *Circulation* **2003**, *107*, 1322–1328. [CrossRef] [PubMed]

25. Duan, H.; Cheng, L.; Sun, X.; Wu, Y.; Hu, L.; Wang, J.; Zhao, H.; Lu, G. LFA-1 and VLA-4 involved in human high proliferative potential endothelial progenitor cells homing to ischemic tissue. *Thromb. Haemost.* **2006**, *96*, 807–815. [CrossRef] [PubMed]

26. Peled, A.; Grabovsky, V.; Habler, L.; Sandbank, J.; Arenzana-Seisdedos, F.; Petit, I.; Ben-Hur, H.; Lapidot, T.; Alon, R. The chemokine SDF-1 stimulates integrin-mediated arrest of CD34$^+$ cells on vascular endothelium under shear flow. *J. Clin. Investig.* **1999**, *104*, 1199–1211. [CrossRef] [PubMed]

27. Shim, M.S.; Kwon, Y.J. Controlled delivery of plasmid DNA and siRNA to intracellular targets using ketalized polyethylenimine. *Biomacromolecules* **2008**, *9*, 444–455. [CrossRef] [PubMed]

28. Riis, S.; Newman, R.; Ipek, H.; Andersen, J.I.; Kuninger, D.; Boucher, S.; Vemuri, M.C.; Pennisi, C.P.; Zachar, V.; Fink, T. Hypoxia enhances the wound-healing potential of adipose-derived stem cells in a novel human primary keratinocyte-based scratch assay. *Int. J. Mol. Med.* **2017**, *39*, 587–594. [CrossRef] [PubMed]

29. Cho, S.W.; Moon, S.H.; Lee, S.H.; Kang, S.W.; Kim, J.; Lim, J.M.; Kim, H.S.; Kim, B.S.; Chung, H.M. Improvement of postnatal neovascularization by human embryonic stem cell derived endothelial-like cell transplantation in a mouse model of hindlimb ischemia. *Circulation* **2007**, *116*, 2409–2419. [CrossRef] [PubMed]

Article

The Effect of Reduced Graphene Oxide-Coated Biphasic Calcium Phosphate Bone Graft Material on Osteogenesis

Jeong-Woo Kim [1,†], Yong Cheol Shin [2,†], Jin-Ju Lee [1,†], Eun-Bin Bae [1], Young-Chan Jeon [1], Chang-Mo Jeong [1], Mi-Jung Yun [1], So-Hyoun Lee [1], Dong-Wook Han [2] and Jung-Bo Huh [1,*]

[1]   Department of Prosthodontics, Dental Research Institute, Institute of Translational Dental Sciences, BK21 PLUS Project, School of Dentistry, Pusan National University, Yangsan 50612, Korea; niceguy9790@hanmail.net (J.-W.K.); ljju1112@hanmail.net (J.-J.L.); 0228dmqls@hanmail.net (E.-B.B.); jeonyc@paran.com (Y.-C.J.); cmjeong@pusan.ac.kr (C.-M.J.); p-venus79@hanmail.net (M.-J.Y.); romilove7@hanmail.net (S.-H.L.)

[2]   Department of CognoMechatronics Engineering, Pusan National University, Busan 46241, Korea; choel15@naver.com (Y.C.S.); nanohan@pusan.ac.kr (D.-W.H.)

*   Correspondence: huhjb@pusan.ac.kr; Tel.: +82-10-8007-9099

†   These authors contributed equally to this work.

Abstract: This study was conducted to evaluate the effect of biphasic calcium phosphate (BCP) coated with reduced graphene oxide (rGO) as bone graft materials on bone regeneration. The rGO-coated BCP bone graft material was fabricatied by mixing rGO and BCP at various concentrations. The surface charge of rGO-coated BCP was measured to be -14.43 mV, which formed a static electrostatic interaction. Cell viabilities were significantly diminished at higher concentrations of ≥ 100 μg/mL. The calvarial defects of 48 rats were implanted rGO-coated BCPs at a weight ratio of 2:1000 (rGO2), 4:1000 (rGO4), and 10:1000 (rGO10), repectively. BCP was used as a control group. The micro-CT and histological analysis were performed to evaluate new bone formation at 2 and 8 weeks after surgery. The results showed that the new bone volume (mm^3) was significantly higher in the experimental groups than in the control group. Histological analysis showed that new bone areas (%) were significantly higher in the rGO2 and rGO10 than in the control, and significantly higher in rGO4 than in the rGO2 and rGO10. Conclusively, the rGO-coated BCP was found to be effective on osteogenesis and the concentration of the composite was an important factor.

Keywords: reduced graphene oxide; biphasic calcium phosphate; bone regeneration; concentration; rat

1. Introduction

Graft materials for alveolar bone augmentation can be classified based on the source of the bone as: autogenous, allogeneic, xenogeneic, or alloplastic bone grafts [1]. Autogenous bone grafts are the recognized gold standard, as they encourage osteogenesis and minimize cellular and humoral immune reactions [2]. However, the availability of autogenous bone is limited and harvesting requires additional surgery [3]. Allogeneic bone grafts are not limited with respect to the amount of bone harvested and do not require second surgery, but they do present the risk of disease transmission and raise ethical issues [4]. Xenogeneic bone grafts are easily obtained and manufactured, but they pose infection risks and have low osteoinductive capacities [5]. On the other hand, alloplastic bone grafts, like xenogeneic bone grafts, are readily available but raise concerns about inflammatory reactions and have poor osteoinductive potentials [6].

Alloplastic bone grafts are derived from non-living materials and are manufactured industrially. These grafts are composed of hydroxyapatite (HA) or β-tricalcium phosphate (β-TCP) [7]. Biphasic calcium phosphate (BCP, a mixture of hydroxyapatite and β-tricalcium phosphate) is used widely to control resorption rate and provide space maintenance [8]. Alloplastic bone can be manufactured without restriction and poses no risks of infection or immune response, but its osteoinductive potential is poor [6]. As a result, many studies have been conducted to enhance the bone regeneration performance of alloplastic grafts [9–14]. Bone morphogenetic protein-2 and -3 (BMP-2 and -3), β-glycerophosphate, and ascorbate are known osteogenic differentiation-inducing agents [10,11].

Nowdays, graphene is being studied as a means of enhancing bone regeneration [15,16]. At the atomic level, graphene is a flat monolayer of carbon atoms tightly packed into a two-dimensional (2D) honeycomb lattice [17]. Graphene has unique mechanical, electrical, thermal, and optical properties, and thus, has applications in many fields, such as, electronics, semiconductors, energy production, polymer science, and biotechnology [18]. The potential of graphene and its derivatives to enhance stem cell differentiation is of particular interest. To enhance stem cell differentiation, graphene and its derivatives function as planar culture platforms to differentiate stem cells towards osteogenic, neurogenic, myogenic, and chondrogenic lineages [19–24]. There are three types of graphene: pristine graphene, graphene oxide (GO), and reduced graphene oxide (rGO). Pristine graphene is a thin layer of pure carbon produced mainly by chemical vapor deposition (CVD), by the exfoliation of graphite [25]. GO is a hydrophilic oxidized form of graphene, and as its name implies, contains oxygen-containing groups [26]. rGO is obtained from reduction of GO, which removes oxygen-containing groups [27]. Of the three different forms of graphene, rGO has been focused on more so as a biomaterial that enhances cellular behaviors, because rGO is biocompatible and has some reactive functional groups [27–29]. Furthermore, the toxicity of GO can be minimized by controlling GO reduction [28]. In one in vitro study, graphene was found to enhance the adherence and growth of mesenchymal stem cells and osteoblasts [30], and in an animal study, rGO hydroxyapatite nanocomposites enhanced osteogenesis, though the particle size of hydroxyapatite used was considerably smaller than that typical of clinical bone graft materials [31].

Accordingly, using a combination of graphene and alloplastic bone graft in dental clinics was considered to enhance bone regeneration. In the present study, a biphasic calcium phosphate bone graft material was mixed in different ratios with rGO and these materials were evaluated to investigate the effects of rGO on bone regeneration.

2. Results

2.1. In Vitro Results

2.1.1. Characterizations of Reduced Graphene Oxide (rGO)-Coated Biphasic Calcium Phosphate (BCP) Bone Graft Materials

The surface morphology of a BCP microparticle (Bio-C) and of a rGO-coated BCP bone graft material are shown in Figure 1. A field emission scanning electron microscope (FE-SEM, Hitachi S-4700, Hitachi, Tokyo, Japan) showed rGO-coated BCP microparticles had an irregular granule-like shape with diameters of several microns, and were partly covered by an interconnected network of rGO nanoplatelets (Figure 1D).
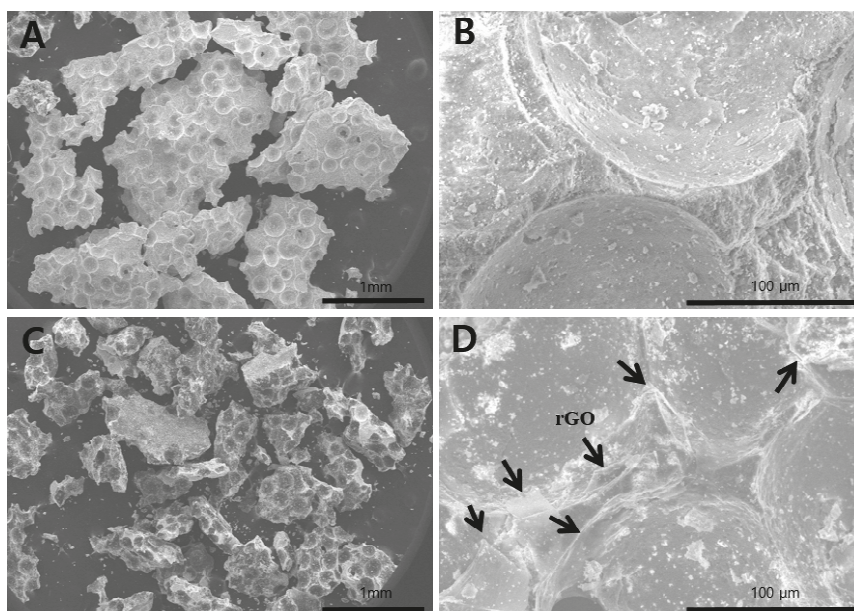
Figure 1. Field emission scanning electron microscope (FE-SEM) images of biphasic calcium phosphate (BCP) microparticles (magnification: 30× (**A**); 500× (**B**)) and reduced graphene oxide (rGO)-coated BCP bone graft materials (magnification: 30× (**C**); 500× (**D**)). Arrows indicate the rGO nanoplatelets.

The ζ potential analysis showed that BCP microparticles in deionized water (pH 7.0) were charged at about +2.17 mV, whereas rGO nanoplatelets were charged at about −34.5 mV (Figure 2). The surface charge of rGO-coated BCP was be around −14.43 mV. These results indicate that rGO-coated BCP bone graft material was probably formed by electrostatic interactions between BCP microparticles and rGO nanoplatelets.
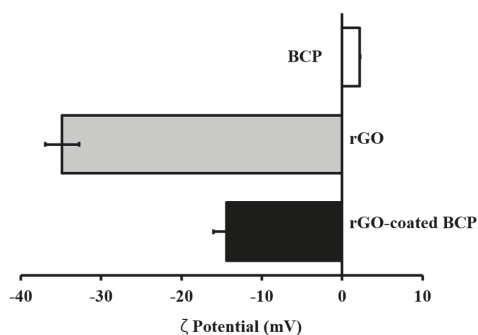
Figure 2. The surface charge of BCP, RGO, and rGO-coated BCP by the ζ potential analysis.

The Raman spectra of rGO-coated BCP and BCP are presented in Figure 3. In the Raman spectrum of rGO-coated BCP, characteristic bands of rGO nanoplatelets, corresponding to the D and G bands of rGO nanoplatelets, were observed at ~1350 and ~1600 cm^{-1}, respectively. On the other hand, no notable peak was observed in the Raman spectrum of BCP microparticles [32,33].
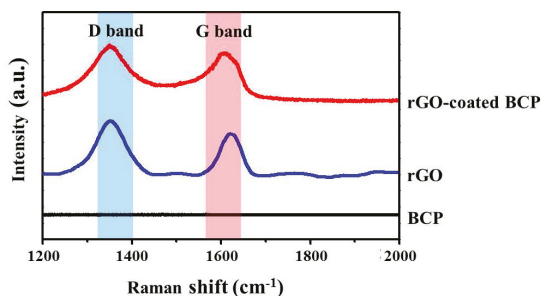
Figure 3. The Raman spectrum of rGO-coated BCP were observed at 1350 and 1600 cm^{-1}, corresponding to the D and G bands of rGO nanoplatelets.

2.1.2. Cytotoxicity of rGO Nanoplatelets

The viabilities of MC3T3-E1 osteoblasts decreased on increasing rGO nanoplatelet concentration (Figure 4). Cell viabilities were slightly affected at concentrations <62.5 µg/mL, but were significantly ($p < 0.05$) diminished at higher concentrations ($\geq$100 µg/mL). At an rGO nanoplatelet concentration of 500 µg/mL, MC3T3-E1 osteoblast viability fell to ~40% of non-treated controls.
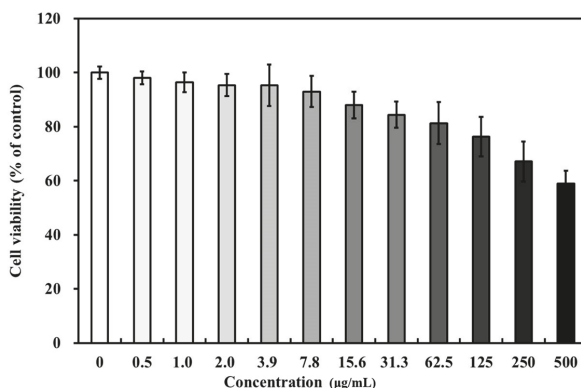
Figure 4. The viability of MC3T3-E1 osteoblasts according to increasing rGO nanoplatelet concentration (µg/mL).

2.2. *In Vivo Results*

2.2.1. Clinical Findings

Forty-eight male Sprague–Dawley rats survived the experimental procedure, and all 48 defects were harvested without problem. During the treatment period after surgery, no collagen membrane was exposed or lost, and no other abnormal findings, such as infection or inflammation, were observed.

2.2.2. Micro-Computed Tomography (Micro-CT) Findings

Total volumes of new bone within regions of interest (ROIs) were measured using the micro-CT scanner at 8 weeks after surgery. Micro-CT images showed the bone graft material was well positioned in defects (Figure 5). No macroscopic difference was observed between the control and experimental groups. New bone volumes, determined by micro-CT, are summarized in Table 1 and Figure 6. At 8 weeks after surgery, mean ($\pm$SD) new bone volumes (mm^3) in the control, rGO2, rGO4, and

rGO10 groups was 2.59 ± 1.10, 7.43 ± 1.40, 7.65 ± 1.39, and 5.43 ± 1.12, respectively, and new bone volumes in the experimental groups were significantly different ($p < 0.001$). Furthermore, new bone volume was significantly greater in the three experimental groups than in the control group at week 8 ($p < 0.05$). The rGO4 group exhibited the greatest amount of new bone volume, and the control group the least. The three experimental groups tended to have significantly greater new bone volume values than the control group.
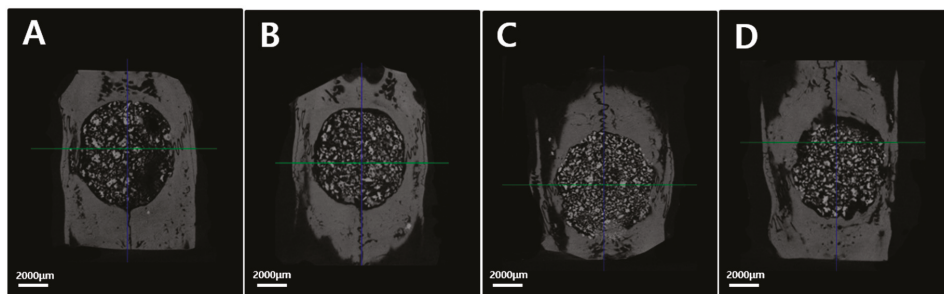
Figure 5. Micro-computed tomographic images. (**A**) Control group; (**B**) rGO2 group; (**C**) rGO4 group; (**D**) rGO10 group.

Table 1. New bone volumes within regions of interest ($n = 6$; mm^3).

Group	Mean ± SD	Median
Control	2.59 ± 1.10	2.40
rGO2	7.43 ± 1.40	7.08
rGO4	7.65 ± 1.39	7.51
rGO10	5.43 ± 1.12	5.77
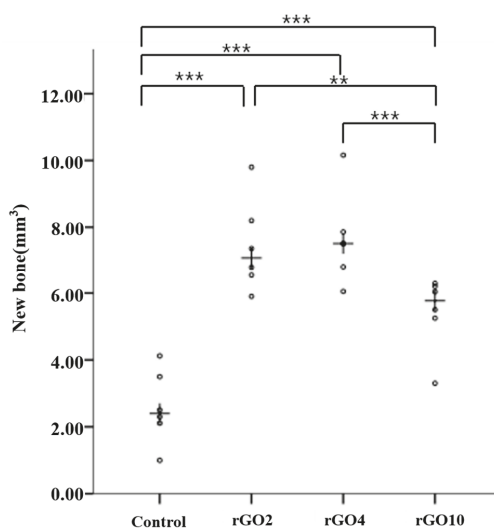
Figure 6. Scatter plot and median values (the crosses) of new bone volumes (mm^3) (** $p < 0.01$, *** $p < 0.001$).

2.2.3. Histologic Findings

No abnormal findings, such as inflammation, were noted in any group. In the three experimental groups, bone graft materials were well positioned in calvarial defect sites, presumably due to the presence of the collagen membrane.

At 2 weeks after surgery (Figure 7), the early phase of new bone formation was observed around existing bone in calvarial defects in the control and experimental groups, but most of the new bone tissues were immature. In the control group, large quantities of fibrous and connective tissues were observed without inflammation in entire calvarial defect sites. Whereas in the rGO4 group, a large quantity of new bone formation from existing bone around the bone graft material was observed. As compared with the control group, the bone formation in the three rGO groups was enhanced.

At 8 weeks after surgery (Figure 8), new bone formation and calcification were observed in the control and experimental groups. In most specimens, new bone formation was observed around existing bone and surrounded bone graft materials. At 8 weeks, in the rGO4 group, a large quantity of new bone from existing old bone surrounded bone graft materials. As compared with the control group, all three rGO groups showed obviously more new bone formation at 8 weeks after surgery.
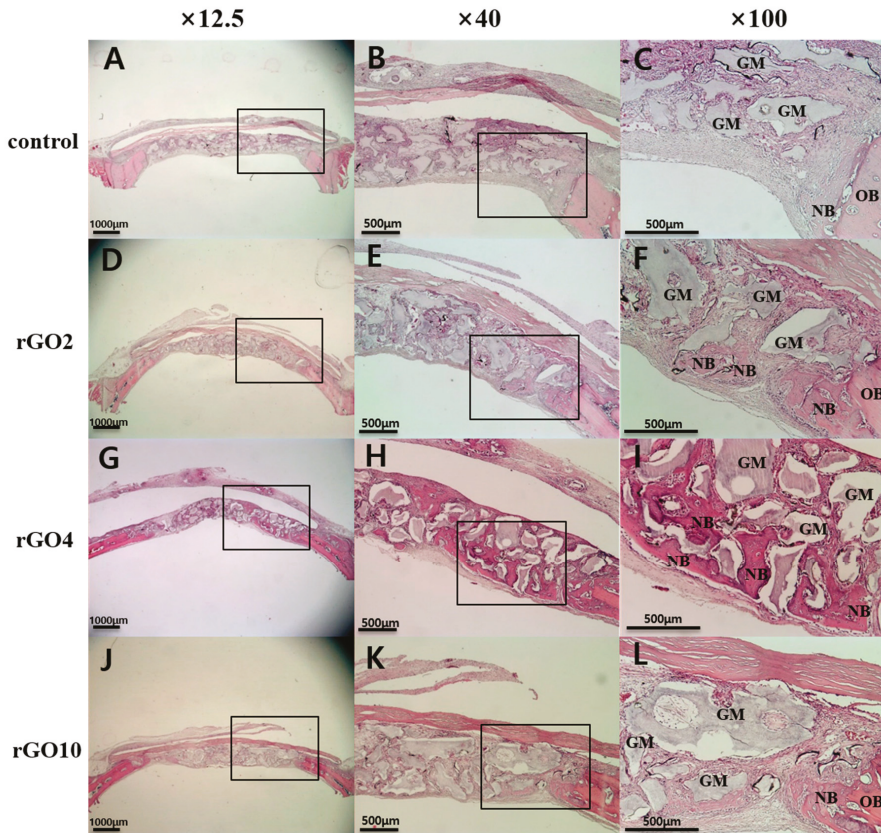
Figure 7. Histological view of hematoxylin and eosin (H&E) stained specimens obtained at 2 weeks after surgery. Black box is the area of interest. (**A–C**) Control group; (**D–F**) rGO2 group; (**G–I**) rGO4 group; (**J–L**) rGO10 group; OB: old bone, NB: new bone, GM: bone graft material (Original magnifications: 12.5× (**A,D,G,J**), 40× (**B,E,H,K**), 100× (**C,F,I,L**)).
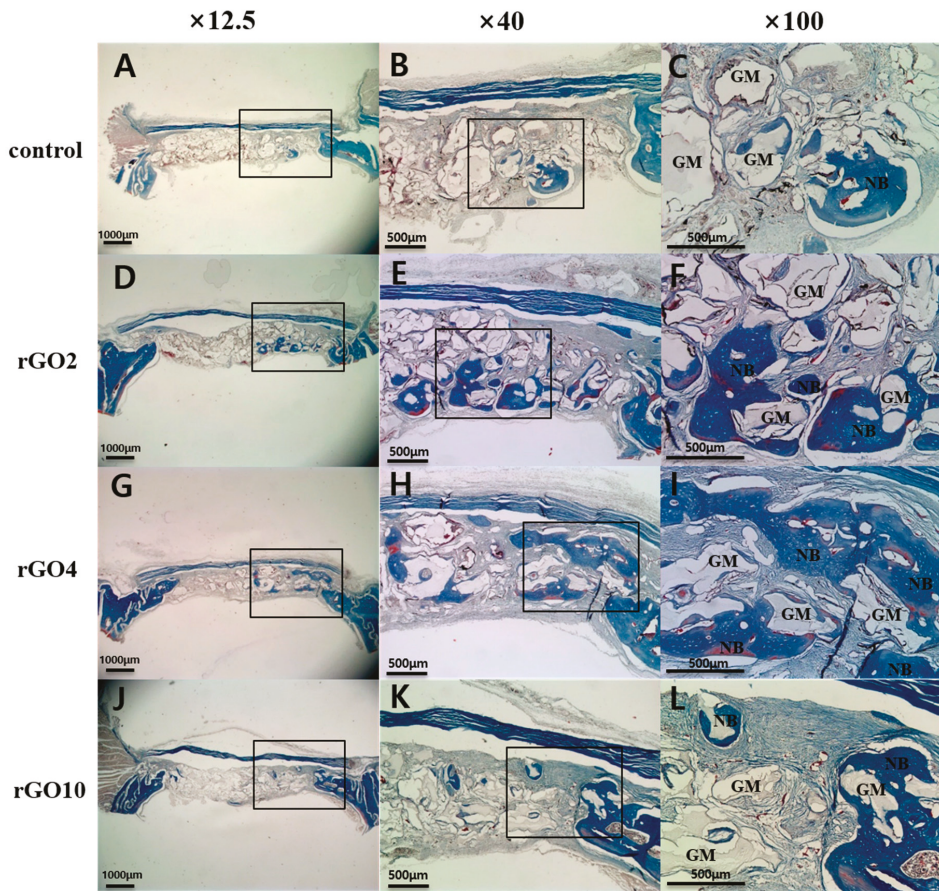
Figure 8. Histological view of Masson's trichrome stained sections at 8 weeks after surgery. Black box is the area of interest. (**A–C**) Control group; (**D–F**) rGO2 group; (**G–I**) rGO4 group; (**J–L**) rGO10 group; OB: old bone, NB: new bone, GM: bone graft material (Original magnifications: 12.5× (**A,D,G,J**), 40× (**B,E,H,K**), 100× (**C,F,I,L**)).

2.2.4. Histometric Findings

Histometric measurements are summarized in Table 2 and Figures 9 and 10. Differences in new bone area percentages (%) were significant between groups ($p < 0.001$).

At 2 weeks, mean ($\pm$ SD) new bone area percentages (%) in the control, rGO2, rGO4, and rGO10 groups were 0.81 ± 0.64, 3.67 ± 1.13, 5.08 ± 1.02, and 1.90 ± 0.95, respectively. The rGO4 group had the highest new bone area percentage (%), and the control group showed the lowest. New bone area percentages were significantly higher in the experimental groups than in the control group at 2 weeks ($p < 0.05$).

At 8 weeks, mean ($\pm$SD) new bone area percentages (%) in the control, rGO2, rGO4, and rGO10 groups were 1.88 ± 0.93, 5.66 ± 1.71, 6.11 ± 1.83, and 2.34 ± 0.79, respectively. New bone area percentages were significantly higher in the rGO2 and rGO10 experimental groups than in the control group, and significantly higher in rGO4 group than in the rGO2 and rGO10 groups ($p < 0.05$).

Table 2. New bone area percentages within the areas of interest ($n = 6$; %).

Week	Group	Mean $\pm$ SD	Median
2	Control	0.81 ± 0.64	0.57
	rGO2	3.67 ± 1.13	3.52
	rGO4	5.08 ± 1.02	4.86
	rGO10	1.90 ± 0.95	1.64
8	Control	1.88 ± 0.93	1.83
	rGO2	5.66 ± 1.71	4.90
	rGO4	6.11 ± 1.83	5.87
	rGO10	2.34 ± 0.79	2.31
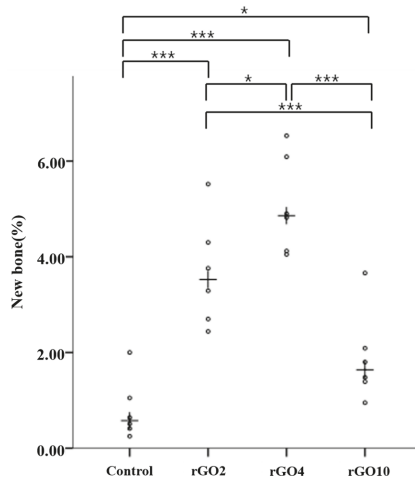
Figure 9. Scatter plot and medians (crosses) of new bone area percentages (%) at 2 weeks after surgery (* $p < 0.05$, *** $p < 0.001$).
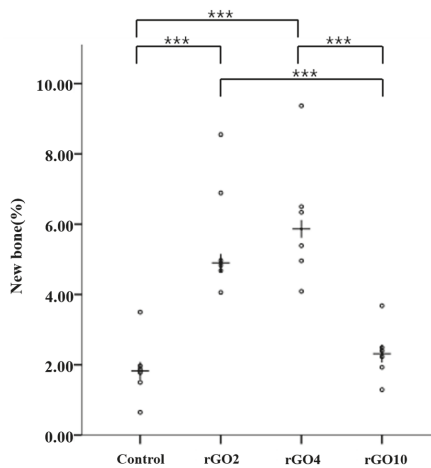
Figure 10. Scatter plot and medians (crosses) of new bone area percentages (%) at 8 weeks after surgery (*** $p < 0.001$).

3. Discussion

Graphene is composed of a single layer of carbon atoms that are tightly bonded in a hexagonal honeycomb lattice, which is the basic building block of all graphitic materials [17]. Graphene is used in many different biomedical fields, such as, drug delivery, gene delivery, biosensing, phototherapy for cancer, and bioimaging [34–39]. Graphene and its derivates allow the attachment of stem cells and stimulate their growth and their differentiation to the osteogenic lineage [40]. According to Kalbacova, graphene enhances the adherence and growth of mesenchymal stem cells and osteoblasts, but is not cytotoxic to these cells, and also has the potential to differentiate mesenchymal stem cells to the osteoblastic lineage [30]. Shin et al. [41] reported that rGO hydroxyapatite nanocomposites function as effective bone fillers that stimulate the osteogenesis of preosteoblasts.

In this study, BCP was coated at different levels with rGO, and this was confirmed by FE-SEM. In FE-SEM images, BCP was partially covered and interconnected by an rGO network. Previous studies have reported that osteoblasts adhered well to and proliferated on rGO- or graphene-hydroxyapatite hybrid materials, which suggests that these materials induce the three dimensional (3D) adhesion of osteoblast cells and maintain cell viability by providing a microenvironment similar to that found in vivo [42]. ζ potential analysis was used to determine surface potentials, and the results obtained suggested that rGO-coated BCP composite had a stable surface and a surface charge of −14.43 mV, which indicated rGO-coated BCP bone graft material was formed by electrostatic interactions between BCP and rGO. In the Raman spectrum of the rGO-coated materials, the intensity ratio of the D and G bands (ID/IG) is commonly used to characterize graphene and its derivatives [43]. The G band is attributed to the in-plane stretching vibration of graphene, while the D band represents structural defects in sp2-bonded carbon domains [44,45]. Therefore, the ID/IG value of rGO is larger than 1. As shown in Figure 3, the ID/IG value of rGO-coated BCP composite was larger than 1 (~1.05), indicating that the rGO nanoplatelets were successfully prepared, and the structure of rGO nanoplatelets were maintained in the rGO-coated BCP. Therefore, considering the FE-SEM images (Figure 1) together with Raman spectra (Figure 3), it is indicated that the rGO-coated BCP was successfully prepared. The influence of rGO on cell growth is largely dependent on its size, structure, and concentration [46–49]. In the present study, the cytotoxicity of rGO was evaluated using a cell counting kit-8 (CCK-8) assay, which is based on mitochondrial activity. According to a previous study, the cytotoxicity of rGO involves the generation of an oxidative stress response [46]. rGO has been reported to exhibit dose-dependent cytotoxicity but showed no apparent cytotoxicity at low concentration [47,48]. In the present study, cell viability was significantly decreased at rGO concentrations >100 μg/mL, but was maintained above 80% at concentrations <62.5 μg/mL. These results suggest rGO has no harmful effects and is non-cytotoxic at concentrations <62.5 μg/mL.

At 8 weeks after surgery, total volumes of new bone (mm^3) were measured by micro-CT, and it showed that the rGO-coated BCP groups exhibited significantly more new bone formation than the control group. The rGO4 group involved the use of a rGO and BCP 4:1000 mixture and it showed the greatest total volume of new bone. Micro-CT and histometric analysis showed that the rGO4 group showed the highest new bone area percentage, and somewhat surprisingly the rGO10 group had a lower new bone area percentage than the rGO2 group. These results suggest as the percentage of rGO is increased, bone regeneration ability is enhanced, but when the rGO percentage exceeds a certain threshold level, rGO cytotoxicity decreases osteoblast viability.

The physical and chemical characteristics of graphene are presumably responsible for its enhancement of osteogenic differentiation. In particular, the wrinkles and ripples present on graphene surfaces may affect osteogenic differentiation [40,50], as these features assist cell anchorage and increase cytoskeletal tension [50,51]. In addition, graphene can adsorb proteins (β-glycerophosphate) and biomolecules (dexamethasone) and these could promote cell differentiation [38].

In this study, we found that rGO-coated BCP bone graft material accelerated new bone formation. We suggest further studies be undertaken to determine the optimal concentration of rGO.

4. Materials and Methods

4.1. In Vitro Study

4.1.1. Preparation of rGO Nanoplatelets

GO was prepared from flake graphite using the modified Hummers and Offeman method (Figure 11) [41,52]. A small amount of graphite flakes (Grade 1721, Asbury Carbon, Asbury, NJ, USA) was placed into a glass beaker and heated for 10 s in a microwave oven. Separately, H_2SO_4 (50 mM) was added to a flask, which was then placed in a cold water bath (0 °C) with stirring. Microwave treated graphite flakes (2 g) were then slowly added to this flask, and this was followed by slowly adding 6 g $KMnO_4$ powder. This mixture was then heated for 2 h at 35 °C with stirring. Deionized water was then slowly added to the mixture, which was maintained at a temperature of <70 °C. To eliminate the $KMnO_4$, H_2O_2 (30 wt %) was then added gradually. At this stage the color of the mixture changed from a dark brown to a brilliant yellow. The mixture was filtered several times and diluted with deionized water to completely remove acid until its pH reached 6. GO was obtained by drying the resulting suspension for 12 h. To prepare rGO nanoplatelets, the prepared GO suspension (1 g in 1 L deionized water) was sonicated for 2 h, and then 10 mL hydrazine hydrate ($N_2H_4 \cdot H_2O$) was added to the GO suspension. The reaction was conducted at 100 °C for 24 h, and the suspension obtained was filtered several times and washed with ethanol–water solutions. rGO nanoplatelets were prepared by drying under vacuum conditions at 80 °C for 12 h [52].
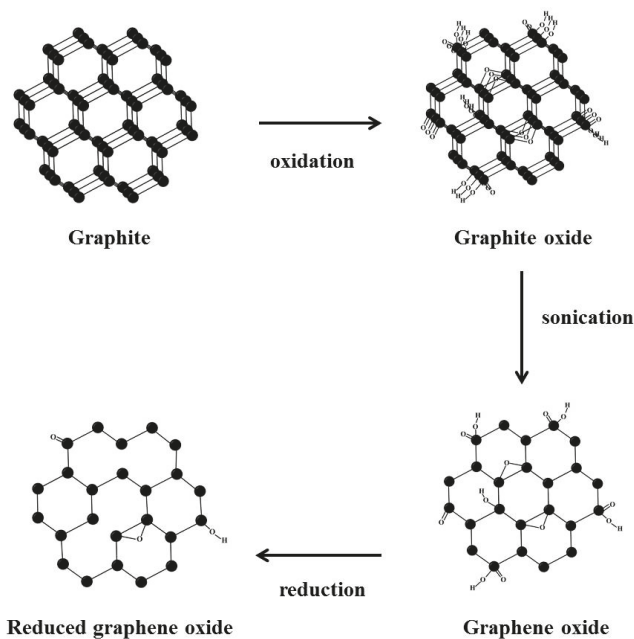
Figure 11. Schematic images of the process used to produce reduced graphene oxide (rGO).

4.1.2. Preparation of rGO-coated BCP Bone Graft Material

The BCP microparticles (MP; Bio-C, Cowellmedi, Seoul) used in this study were a mixture of HA and β-TCP (3:7 by weight). To prepare rGO-coated BCP graft material, as-prepared rGO in deionized water was sonicated for 2 h, and then mixed with BCP suspended in deionized water at rGO to BCP weight ratios of 2:1000, 4:1000, or 10:1000. The rGO-coated BCP graft material was obtained by

vigorously mixing colloidal dispersions of rGO nanoplatelets and BCP microparticles for 10 min and slow air-drying at room temperature overnight.

4.1.3. Characterizations of the rGO-Coated BCP Bone Graft Materials

The morphologies of rGO-coated BCPs were studied using a FE-SEM (Hitachi S-4700, Hitachi, Tokyo, Japan) at an accelerating voltage of 5 kV. The surface potentials of the rGO-coated BCPs were obtained using a Zetasizer (Malvern Instruments, Nano ZS, Worcestershire, UK). The Raman spectra of rGO-coated BCP, rGO nanoplatelets, and BCP were obtained by a Raman spectrometer (Micro Raman PL Mapping System, Dongwoo Optron Co., Kwangju, Korea) with excitation a 514.5 nm using an Ar-ion laser at a radiant power of 5 mW.

4.1.4. Cytotoxicity of rGO Nanoplatelets

A murine preosteoblastic cell line (MC3T3-E1 cells from C57BL/6 mouse calvaria) was purchased from the American Type Culture Collection (CRL-2593™; ATCC, Rockville, MD, USA). This cell-line is an established osteoblast model and has been widely used to investigate osteogenesis and bone formation [53,54]. Cells were maintained in complete α-minimum essential medium supplemented with 10% fetal bovine serum and 1% antibiotic antimycotic solution (all from Sigma-Aldrich, St Louis, MO, USA) in a humid 5% CO_2 atmosphere at 37 °C. The cytotoxic effects of rGO nanoplatelets on MC3T3-E1 cells were assessed using a cell counting kit-8 (CCK-8) (Dojindo, Kumamoto, Japan), according to the manufacturer's instructions. Numbers of viable cells were found to be directly proportional to the metabolic reaction products obtained in the CCK-8 assay. Briefly, the MC3T3-E1 cells were seeded at a density of 5×10^4 cells/mL on 24-well plates and incubated for 24 h. The rGO nanoplatelets were then added at concentrations from 0 to 500 µg/mL, and the cells were further cultured for 24 h. Subsequently, the cells were incubated with a CCK-8 solution for the last 2 h of the culture period (24 h) at 37 °C in the dark. Absorbances were measured at 450 nm using an ELISA reader (SpectraMax 340, Molecular Device Co., Sunnyvale, CA, USA).

4.2. In Vivo Study

4.2.1. Experimental Animals and Design

Forty-eight 12- to 13-week-old male Sprague–Dawley rats (250–300 g) were used in this study. Before starting, rats were allowed and a minimum adaption period of 7 days. During all procedures, rats were housed in plastic cages (maximum of 3 rats per cage) under controlled conditions (25 ± 1 °C and RH 55 ± 7%). All animals had access to a rodent diet and water ad libitum. The experimental protocol was approved beforehand by the Pusan National University Institutional Animal Care and Use Committee (PNU-2016-1407, 7 January 2016) and performed at the Laboratory Animal Resource Center of Pusan National University.

The animals were divided into four groups depending on bone graft material used.

1. Control group (*n* = 12)
     : only BCP;
2. rGO2 group (*n* = 12)
     : a mixture of rGO and BCP at a ratio of 2:1000 (Concentration of rGO: 28 µg/mL);
3. rGO4 group (*n* = 12)
     : a mixture of rGO and BCP at a ratio of 4:1000 (Concentration of rGO: 56 µg/mL);
4. rGO10 group (*n* = 12)
     : a mixture of rGO and BCP at a ratio of 10:1000 (Concentration of rGO: 140 µg/mL).

4.2.2. Surgical Procedures

All surgical procedures were performed under general anesthesia. A mixture of tiletamine-zolazepam (Zoletil 50, Virbac, Carros, France) and xylazine (Rompun, Bayer Korea, Seoul) at 6:4 was anesthetized by intramuscular injection into animals. 0.2 mL of anesthetic per rat was used [55]. Surgical sites on rat crania were shaved and disinfected with alcohol and povidone-iodine (Betadine, Korea Pharma Co., Seoul, Korea). Local anesthesia was performed using 2% lidocaine containing 1:100,000 epinephrine (Yu-Han Co., Gunpo, Korea) at surgical sites.

A 15-mm incision was made at midline and the skin and periosteum were dissected to expose parietal bones. An 8-mm diameter bone defect was then formed in the middle of calvaria using a trephine bur (external diameter 8 mm, 3i Implant Innovation, Palm Beach Garden, FL, USA) under saline irrigation. In the control group, 0.03 ± 0.002 g of Bio-C was placed on the calvarial defect using a micro spoon (Karl Hammacher GmbH Co., Cologne, Germany), and in the three experimental groups, the same amount of rGO-coated BCP was placed in the same manner. After completing the bone grafting, a collagen membrane (GCM2030, GENOSS, Suwon, Korea) was cut into square shape (10 mm $\times$ 10 mm) and used to cover the defect (Figure 12). Periosteum at the incision site was sutured using a 4-0 absorbable suture (Vicryl, Ethicon, Somerville, NJ, USA) and skin was sutured with 4-0 black silk.
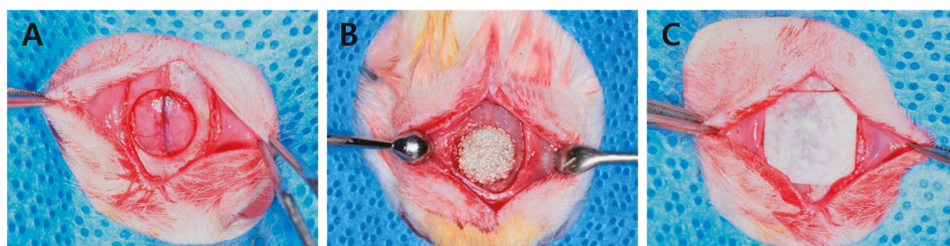
Figure 12. Surgical procedures. (**A**) A defect was formed in the middle of calvaria using a trephine bur; (**B**) Bone graft material was placed; (**C**) A collagen membrane was placed on the defect.

Animals were allowed to recover for 2 or 8 weeks after surgery. In the three experimental groups, animals were sacrificed by CO_2 inhalation at 2 or 8 weeks after surgery. To collect specimens, skin was removed, and defect sites were harvested with surrounding bone. Collected specimens were immediately immersed in neutral buffered formalin (Sigma-Aldrich) for 2 weeks and prepared for micro-computed tomographic (micro-CT) and histomorphometric analyses.

4.2.3. Micro-Computed Tomography Analysis

Harvested calvaria were scanned using a micro-CT scanner (Skyscan-1173, version 1.6, Bruker-CT Co., Kontich, Belgium) at 8 weeks after surgery (Figure 13). Harvested calvaria were wrapped in film (Parafilm M, Bemis Co., Neenah, WI, USA) to prevent evaporation of fixative solution during scans. Scanning was performed at 130 kV, 60 µA, at a pixel resolution of 7.10 µm using a bromine filter (0.25 mm). The Nrecon reconstruction program (version 1.6.10.1, Bruker-CT Co., Kontich, Belgium) was used to reconstruct images. Identical parameters were used for all specimens. A cylindrical region of interest (ROI; 8 mm diameter; the same size as the original defect) was established, and total volume of new bone volume (NBV; mm^3), that is, the volume occupied by new bone within the region of interest, was measured.
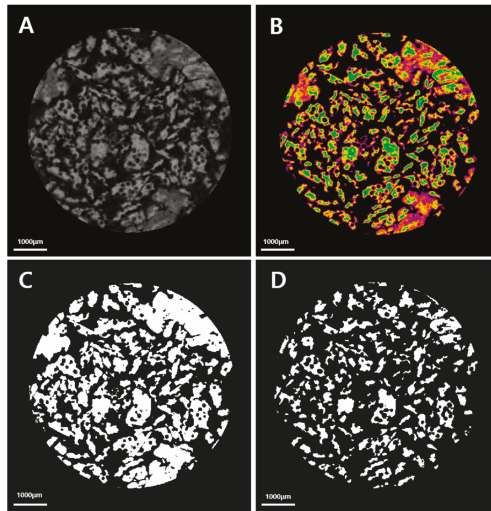
Figure 13. Micro-computed tomographic (CT) images of regions of interest. (**A**) Reconstructed image; (**B**) Color image (yellow and green-bone graft material and orange and purple-new bone); (**C**) Total bone (bone graft material and new bone) image; (**D**) Bone graft material image.

4.2.4. Histologic and Histometric Analysis

Specimens were decalcified in 10% ethylenediaminetetraacetic acid (EDTA) solution (pH 8.0) for 2 weeks at 4 °C. After dehydration, specimens were embedded in paraffin, and sectioned longitudinally at 4 µm through the largest defect diameter using a microtome. Slides were stained with hematoxylin-eosin and Masson's trichrome stain for histologic and histometric analyses to observe newly regenerated bone tissues, and photographed under an optical microscope (BX51, OLYMPUS, Tokyo, Japan) connected to a computer. Captured images were analyzed using an image analysis program (i-solution ver. 8.1, IMT, Vancouver, BC, Canada). For histologic and histometric analyses, specimen images were observed at magnifications of 12.5×, 40×, and 100×. Histologic and histometric analyses were performed by the same blinded investigator. Total area of new bone was defined as the area occupied by new bone within a defect (Figure 14), and new bone area (%) (NBA %) was defined as the area occupied by new bone expressed as a percentage of total defect area.
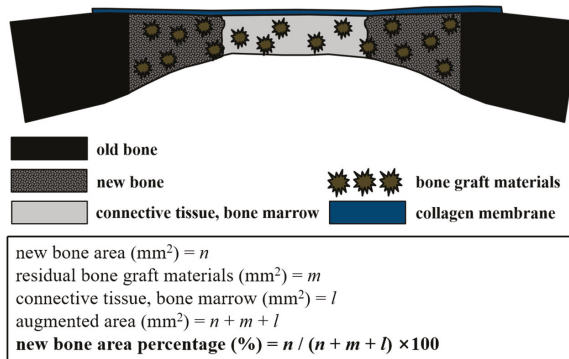
Figure 14. Schematic illustration of the histometric analysis.

4.2.5. Statistical Analysis

Results are expressed as means, standard deviations, and medians. The analysis was conducted using the statistical software package R ver. 3.1.3 (The R Foundation, Vienna, Austria). To compare group micro-CT and histomorphometric results, we used the non-parametric analysis devised by Brunner & Langer. The statistical significance was accepted for *p* values of <0.05.

5. Conclusions

The in vitro results obtained in the present study indicate that reduced graphene oxide-coated biphasic calcium phosphate is a safe and stable bone graft material. The reduced graphene oxide-coated biphasic calcium phosphate enhanced bone regeneration better than biphasic calcium phosphate alone. In addition, new bone formation appeared to be influenced by the concentration of reduced graphene oxide in the composite. We suggest further studies be undertaken to determine the optimum concentration of reduced graphene oxide in the composite.

Author Contributions: Jung-Bo Huh, Dong-Wook Han, Young-Chan Jeon and Chang-Mo Jeong conceived and designed the experiments; Mi-Jung Yun, So-Hyoun Lee, Yong Cheol Shin and Jin-Ju Lee performed experiments; Jeong-Woo Kim, Eun-Bin Bae and Jung-Bo Huh analyzed the data; Jung-Woo Kim, Yong Cheol Shin and Jung-Bo Huh wrote the manuscript. All authors reviewed the final manuscript.

Conflicts of Interest: The authors declare no conflict of interest.

Abbreviations

BCP	Biphasic calcium phosphate
rGO	Reduced graphene oxide
HA	Hydroxyapatite
β-TCP	β-Tricalcium phosphate
BMP	Bone morphogenetic protein
2D	Two-dimensional
GO	Graphene oxide
Bio-C	BCP microparticle
FE-SEM	Field emission-scanning electron microscopy
H&E	Hematoxylin and eosin
3D	Three dimensional
ID/IG	Intensity ratio of the D and G bands
micro-CT	Micro-computed tomographic
ROI	Region of interest
NBV	New bone volume
EDTA	Ethylenediaminetetraacetic acid
NBA	New bone area

References

1. Hoexter, D.L. Bone regeneration graft materials. *J. Oral Implantol.* **2002**, *28*, 290–294. [CrossRef]
2. Blokhuis, T.; Arts, J.C. Bioactive and osteoinductive bone graft substitutes: Definitions, facts and myths. *Injury* **2011**, *42*, S26–S29. [CrossRef] [PubMed]
3. Cypher, T.J.; Grossman, J.P. Biological principles of bone graft healing. *J. Foot Aankle Surg.* **1996**, *35*, 413–417. [CrossRef]
4. Carter, G. Harvesting and implanting allograft bone. *AORN J.* **1999**, *70*, 659–670. [CrossRef]
5. Araújo, M.; Linder, E.; Lindhe, J. Effect of a xenograft on early bone formation in extraction sockets: An experimental study in dog. *Clin. Oral Implants Res.* **2009**, *20*, 1–6. [CrossRef] [PubMed]

6. La Gatta, A.; de Rosa, A.; Laurienzo, P.; Malinconico, M.; de Rosa, M.; Schiraldi, C. A novel injectable poly (ε-caprolactone)/calcium sulfate system for bone regeneration: Synthesis and characterization. *Macromol. Biosci.* **2005**, *5*, 1108–1117. [CrossRef] [PubMed]

7. Zimmermann, G.; Moghaddam, A. Allograft bone matrix versus synthetic bone graft substitutes. *Injury* **2011**, *42*, S16–S21. [CrossRef] [PubMed]

8. Greenwald, A.S.; Boden, S.D.; Goldberg, V.M.; Khan, Y.; Laurencin, C.T.; Rosier, R.N. Bone-graft substitutes: Facts, fictions, and applications. *J. Bone Jt. Surg Am.* **2001**, *83*, S98–S103. [CrossRef]

9. Moore, W.R.; Graves, S.E.; Bain, G.I. Synthetic bone graft substitutes. *ANZ J. Surg.* **2001**, *71*, 354–361. [CrossRef] [PubMed]

10. Mostafa, N.Z.; Fitzsimmons, R.; Major, P.W.; Adesida, A.; Jomha, N.; Jiang, H.; Uludağ, H. Osteogenic differentiation of human mesenchymal stem cells cultured with dexamethasone, vitamin D3, basic fibroblast growth factor, and bone morphogenetic protein-2. *Connect. Tissue Res.* **2012**, *53*, 117–131. [CrossRef] [PubMed]

11. Zhou, D.; Ito, Y. Inorganic material surfaces made bioactive by immobilizing growth factors for hard tissue engineering. *RSC Adv.* **2013**, *3*, 11095–11106. [CrossRef]

12. Iannazzo, D.; Pistone, A.; Espro, C.; Galvagno, S. Drug Delivery Strategies for Bone Tissue Regeneration. In *Biomimetic Approaches for Tissue Healing*; Panseri, S., Taraballi, F., Cunha, C., Eds.; OMICS International: Foster City, CA, USA, 2015; Volume 1, pp. 1–39.

13. Pistone, A.; Iannazzo, D.; Espro, C.; Galvagno, S.; Tampieri, A.; Montesi, M.; Panseri, S.; Sandri, M. Tethering of Gly-Arg-Gly-Asp-Ser-Pro-Lys peptides on Mg-doped hydroxyapatite. *Engineering* **2017**, *3*, 55–59. [CrossRef]

14. Pistone, A.; Iannazzo, D.; Panseri, S.; Montesi, M.; Tampieri, A.; Galvagno, S. Hydroxyapatite-magnetite-mwcnt nanocomposite as a biocompatible multifunctional drug delivery system for bone tissue engineering. *Nanotechnology* **2014**, *25*, 425701. [CrossRef] [PubMed]

15. Holt, B.D.; Wright, Z.M.; Arnold, A.M.; Sydlik, S.A. Graphene oxide as a scaffold for bone regeneration. *Wiley Interdiscip. Rev. Nanomed. Nanobiotechnol.* **2017**, *9*. [CrossRef] [PubMed]

16. Wu, C.; Xia, L.; Han, P.; Xu, M.; Fang, B.; Wang, J.; Chang, J.; Xiao, Y. Graphene-oxide-modified β-tricalcium phosphate bioceramics stimulate in vitro and in vivo osteogenesis. *Carbon* **2015**, *93*, 116–129. [CrossRef]

17. Geim, A.K.; Novoselov, K.S. The rise of graphene. *Nat. Mater.* **2007**, *6*, 183–191. [CrossRef] [PubMed]

18. Singh, V.; Joung, D.; Zhai, L.; Das, S.; Khondaker, S.I.; Seal, S. Graphene based materials: Past, present and future. *Prog. Mater. Sci.* **2011**, *56*, 1178–1271. [CrossRef]

19. Xia, L.; Lin, K.; Jiang, X.; Fang, B.; Xu, Y.; Liu, J.; Zeng, D.; Zhang, M.; Zhang, X.; Chang, J. Effect of nano-structured bioceramic surface on osteogenic differentiation of adipose derived stem cells. *Biomaterials* **2014**, *35*, 8514–8527. [CrossRef] [PubMed]

20. Zhao, J.; Shen, G.; Liu, C.; Wang, S.; Zhang, W.; Zhang, X.; Zhang, X.; Ye, D.; Wei, J.; Zhang, Z. Enhanced healing of rat calvarial defects with sulfated chitosan-coated calcium-deficient hydroxyapatite/bone morphogenetic protein 2 scaffolds. *Tissue Eng. Part A* **2011**, *18*, 185–197. [CrossRef] [PubMed]

21. Lee, W.C.; Lim, C.H.Y.; Shi, H.; Tang, L.A.; Wang, Y.; Lim, C.T.; Loh, K.P. Origin of enhanced stem cell growth and differentiation on graphene and graphene oxide. *ACS Nano* **2011**, *5*, 7334–7341. [CrossRef] [PubMed]

22. Zhang, Y.; Nayak, T.R.; Hong, H.; Cai, W. Graphene: A versatile nanoplatform for biomedical applications. *Nanoscale* **2012**, *4*, 3833–3842. [CrossRef] [PubMed]

23. Alford, A.I.; Hankenson, K.D. Matricellular proteins: Extracellular modulators of bone development, remodeling, and regeneration. *Bone* **2006**, *38*, 749–757. [CrossRef] [PubMed]

24. Ivaska, K.K.; Hentunen, T.A.; Vääräniemi, J.; Ylipahkala, H.; Pettersson, K.; Väänänen, H.K. Release of intact and fragmented osteocalcin molecules from bone matrix during bone resorption in vitro. *J. Biol. Chem.* **2004**, *279*, 18361–18369. [CrossRef] [PubMed]

25. Goncalves, G.; Marques, P.; Vila, M. *Graphene-Based Materials in Health and Environment*; Springer: New York, NY, USA, 2017.

26. Dreyer, D.R.; Park, S.; Bielawski, C.W.; Ruoff, R.S. The chemistry of graphene oxide. *Chem. Soc. Rev.* **2010**, *39*, 228–240. [CrossRef] [PubMed]

27. Park, S.; Ruoff, R.S. Chemical methods for the production of graphenes. *Nat. Nanotechnol.* **2009**, *4*, 217–224. [CrossRef] [PubMed]

28. Das, S.; Singh, S.; Singh, V.; Joung, D.; Dowding, J.M.; Reid, D.; Anderson, J.; Zhai, L.; Khondaker, S.I.; Self, W.T. Oxygenated functional group density on graphene oxide: Its effect on cell toxicity. *Part. Part. Syst. Charact.* **2013**, *30*, 148–157. [CrossRef]

29. Zanin, H.; Saito, E.; Marciano, F.R.; Ceragioli, H.J.; Granato, A.E.C.; Porcionatto, M.; Lobo, A.O. Fast preparation of nano-hydroxyapatite/superhydrophilic reduced graphene oxide composites for bioactive applications. *J. Mater. Chem. B* **2013**, *1*, 4947–4955. [CrossRef]

30. Kalbacova, M.; Broz, A.; Kong, J.; Kalbac, M. Graphene substrates promote adherence of human osteoblasts and mesenchymal stromal cells. *Carbon* **2010**, *48*, 4323–4329. [CrossRef]

31. Lee, J.H.; Shin, Y.C.; Lee, S.-M.; Jin, O.S.; Kang, S.H.; Hong, S.W.; Jeong, C.-M.; Huh, J.B.; Han, D.-W. Enhanced osteogenesis by reduced graphene oxide/hydroxyapatite nanocomposites. *Sci. Rep.* **2015**, *5*. [CrossRef] [PubMed]

32. Zhou, Y.; Yang, J.; He, T.; Shi, H.; Cheng, X.; Lu, Y. Highly stable and dispersive silver nanoparticle–graphene composites by a simple and low-energy-consuming approach and their antimicrobial activity. *Small* **2013**, *9*, 3445–3454. [CrossRef] [PubMed]

33. Eda, G.; Fanchini, G.; Chhowalla, M. Large-area ultrathin films of reduced graphene oxide as a transparent and flexible electronic material. *Nat. Nanotechnol.* **2008**, *3*, 270–274. [CrossRef] [PubMed]

34. Loh, K.P.; Bao, Q.; Ang, P.K.; Yang, J. The chemistry of graphene. *J. Mater. Chem.* **2010**, *20*, 2277–2289. [CrossRef]

35. Song, Y.; Wei, W.; Qu, X. Colorimetric biosensing using smart materials. *Adv. Mater.* **2011**, *23*, 4215–4236. [CrossRef] [PubMed]

36. Feng, L.; Liu, Z. Graphene in biomedicine: Opportunities and challenges. *Nanomedicine* **2011**, *6*, 317–324. [CrossRef] [PubMed]

37. Kostarelos, K.; Novoselov, K.S. Exploring the interface of graphene and biology. *Science* **2014**, *344*, 261–263. [CrossRef] [PubMed]

38. Goenka, S.; Sant, V.; Sant, S. Graphene-based nanomaterials for drug delivery and tissue engineering. *J. Control. Release* **2014**, *173*, 75–88. [CrossRef] [PubMed]

39. Liu, J.; Cui, L.; Losic, D. Graphene and graphene oxide as new nanocarriers for drug delivery applications. *Acta Biomater.* **2013**, *9*, 9243–9257. [CrossRef] [PubMed]

40. Dubey, N.; Bentini, R.; Islam, I.; Cao, T.; Castro Neto, A.H.; Rosa, V. Graphene: A versatile carbon-based material for bone tissue engineering. *Stem Cells Intern.* **2015**, *2015*, 1–12. [CrossRef] [PubMed]

41. Shin, Y.C.; Lee, J.H.; Jin, O.S.; Kang, S.H.; Hong, S.W.; Kim, B.; Park, J.-C.; Han, D.-W. Synergistic effects of reduced graphene oxide and hydroxyapatite on osteogenic differentiation of MC3T3-E1 preosteoblasts. *Carbon* **2015**, *95*, 1051–1060. [CrossRef]

42. Kim, S.; Ku, S.H.; Lim, S.Y.; Kim, J.H.; Park, C.B. Graphene–biomineral hybrid materials. *Adv. Mater.* **2011**, *23*, 2009–2014. [CrossRef] [PubMed]

43. Jiao, L.; Zhang, L.; Wang, X.; Diankov, G.; Dai, H. Narrow graphene nanoribbons from carbon nanotubes. *Nature* **2009**, *458*, 877–880. [CrossRef] [PubMed]

44. Kudin, K.N.; Ozbas, B.; Schniepp, H.C.; Prud'Homme, R.K.; Aksay, I.A.; Car, R. Raman spectra of graphite oxide and functionalized graphene sheets. *Nano Lett.* **2008**, *8*, 36–41. [CrossRef] [PubMed]

45. Tran, D.N.; Kabiri, S.; Losic, D. A green approach for the reduction of graphene oxide nanosheets using non-aromatic amino acids. *Carbon* **2014**, *76*, 193–202. [CrossRef]

46. Zanni, E.; De Bellis, G.; Bracciale, M.P.; Broggi, A.; Santarelli, M.L.; Sarto, M.S.; Palleschi, C.; Uccelletti, D. Graphite nanoplatelets and caenorhabditis elegans: Insights from an in vivo model. *Nano Lett.* **2012**, *12*, 2740–2744. [CrossRef] [PubMed]

47. Zhang, L.; Wang, Z.; Lu, Z.; Shen, H.; Huang, J.; Zhao, Q.; Liu, M.; He, N.; Zhang, Z. Pegylated reduced graphene oxide as a superior ssrna delivery system. *J. Mater. Chem. B* **2013**, *1*, 749–755. [CrossRef]

48. Miao, W.; Shim, G.; Kang, C.M.; Lee, S.; Choe, Y.S.; Choi, H.-G.; Oh, Y.-K. Cholesteryl hyaluronic acid-coated, reduced graphene oxide nanosheets for anti-cancer drug delivery. *Biomaterials* **2013**, *34*, 9638–9647. [CrossRef] [PubMed]

49. Lv, M.; Zhang, Y.; Liang, L.; Wei, M.; Hu, W.; Li, X.; Huang, Q. Effect of graphene oxide on undifferentiated and retinoic acid-differentiated SH-SY5Ycells line. *Nanoscale* **2012**, *4*, 3861–3866. [CrossRef] [PubMed]

50. Nayak, T.R.; Andersen, H.; Makam, V.S.; Khaw, C.; Bae, S.; Xu, X.; Ee, P.-L.R.; Ahn, J.-H.; Hong, B.H.; Pastorin, G. Graphene for controlled and accelerated osteogenic differentiation of human mesenchymal stem cells. *ACS Nano* **2011**, *5*, 4670–4678. [CrossRef] [PubMed]

51. Xie, H.; Cao, T.; Gomes, J.V.; Neto, A.H.C.; Rosa, V. Two and three-dimensional graphene substrates to magnify osteogenic differentiation of periodontal ligament stem cells. *Carbon* **2015**, *93*, 266–275. [CrossRef]

52. Lee, J.H.; Shin, Y.C.; Jin, O.S.; Kang, S.H.; Hwang, Y.-S.; Park, J.-C.; Hong, S.W.; Han, D.-W. Reduced graphene oxide-coated hydroxyapatite composites stimulate spontaneous osteogenic differentiation of human mesenchymal stem cells. *Nanoscale* **2015**, *7*, 11642–11651. [CrossRef] [PubMed]

53. Sudo, H.; Kodama, H.-A.; Amagai, Y.; Yamamoto, S.; Kasai, S. In vitro differentiation and calcification in a new clonal osteogenic cell line derived from newborn mouse calvaria. *J. Cell Biol.* **1983**, *96*, 191–198. [CrossRef] [PubMed]

54. Chatterjee, K.; Lin-Gibson, S.; Wallace, W.E.; Parekh, S.H.; Lee, Y.J.; Cicerone, M.T.; Young, M.F.; Simon, C.G. The effect of 3D hydrogel scaffold modulus on osteoblast differentiation and mineralization revealed by combinatorial screening. *Biomaterials* **2010**, *31*, 5051–5062. [CrossRef] [PubMed]

55. Choi, H.R.; Ko, J.H.; Lee, H.B.; Lee, J.M. Anesthesia for the experimental rats. *J. Korean Soc. Microsurg.* **2013**, *22*, 1–6.

Rebalancing *β*-Amyloid-Induced Decrease of ATP Level by Amorphous Nano/Micro Polyphosphate: Suppression of the Neurotoxic Effect of Amyloid *β*-Protein Fragment 25-35

Werner E. G. Müller [1],*, Shunfeng Wang [1], Maximilian Ackermann [2], Meik Neufurth [1], Renate Steffen [1], Egherta Mecja [1], Rafael Muñoz-Espí [3], Qingling Feng [4], Heinz C. Schröder [1] and Xiaohong Wang [1],*

[1]   ERC Advanced Investigator Grant Research Group at the Institute for Physiological Chemistry, University Medical Center of the Johannes Gutenberg University, Duesbergweg 6, D-55128 Mainz, Germany; shunwang@uni-mainz.de (S.W.); mneufurt@uni-mainz.de (M.N.); steffen@uni-mainz.de (R.S.); egherta@gmail.com (E.M.); hschroed@uni-mainz.de (H.C.S.)

[2]   Institute of Functional and Clinical Anatomy, University Medical Center of the Johannes Gutenberg University, Johann Joachim Becher Weg 13, D-55099 Mainz, Germany; maximilian.ackermann@uni-mainz.de

[3]   Institute of Materials Science (ICMUV), Universitat de València, C/Catedràtic José Beltrán 2, 46980 Paterna, València, Spain; rafael.munoz@uv.es

[4]   Key Laboratory of Advanced Materials of Ministry of Education of China, School of Materials Science and Engineering, Tsinghua University, Beijing 100084, China; biomater@mail.tsinghua.edu.cn

*   Correspondence: wmueller@uni-mainz.de (W.E.G.M.); wang013@uni-mainz.de (X.W.); Tel.: +49-6131-39-25910 (W.E.G.M. & X.W.)

Abstract: Morbus Alzheimer neuropathology is characterized by an impaired energy homeostasis of brain tissue. We present an approach towards a potential therapy of Alzheimer disease based on the high-energy polymer inorganic polyphosphate (polyP), which physiologically occurs both in the extracellular and in the intracellular space. Rat pheochromocytoma (PC) 12 cells, as well as rat primary cortical neurons were exposed to the Alzheimer peptide Aβ25-35. They were incubated in vitro with polyphosphate (polyP); ortho-phosphate was used as a control. The polymer remained as Na^+ salt; or complexed in a stoichiometric ratio to Ca^{2+} (Na-polyP[Ca^{2+}]); or was processed as amorphous Ca-polyP microparticles (Ca-polyP-MP). Ortho-phosphate was fabricated as crystalline Ca-phosphate nanoparticles (Ca-phosphate-NP). We show that the pre-incubation of PC12 cells and primary cortical neurons with polyP protects the cells against the neurotoxic effect of the Alzheimer peptide Aβ25-35. The strongest effect was observed with amorphous polyP microparticles (Ca-polyP-MP). The effect of the soluble sodium salt; Na-polyP (Na-polyP[Ca^{2+}]) was lower; while crystalline orthophosphate nanoparticles (Ca-phosphate-NP) were ineffective. Ca-polyP-MP microparticles and Na-polyP[Ca^{2+}] were found to markedly enhance the intracellular ATP level. Pre-incubation of Aβ25-35 during aggregate formation, with the polyP preparation before exposure of the cells, had a small effect on neurotoxicity. We conclude that recovery of the compromised energy status in neuronal cells by administration of nontoxic biodegradable Ca-salts of polyP reverse the β-amyloid-induced decrease of adenosine triphosphate (ATP) level. This study contributes to a new routes for a potential therapeutic intervention in Alzheimer's disease pathophysiology.

Keywords: β-amyloid; calcium polyphosphate; microparticles; neurotoxic effect; adenosine triphosphate level; PC12 cells; primary rat cortex neurons

1. Introduction

Alzheimer's disease (AD), a neurodegenerative disorder characterized by deposition of amyloid-β (Aβ) peptides in the brain, leads to progressive memory loss and dementia [1,2]. The two proteins, amyloid β-protein and Tau, are characteristic signatures of AD [3]. Amyloid β-protein is a small peptide fragment generated through cleavage from the amyloid precursor protein (APP) [4]. Due to the fact that the etiologic agent(s) and the metabolic targets for AD have not been identified unequivocally, no causative cure can be offered. Five agents have been accepted with sufficient safety and efficacy to allow marketing approval: four cholinesterase inhibitors [5] and memantine [6]. We could demonstrate that memantine prevents neuronal apoptosis due to modulation of the NMDA (*N*-methyl-D-aspartate) receptor [7,8].

In general neurons and glial cells consume high levels of ATP in the brain. Since no energy storage system is available in the central nervous system, there is a high demand for a continuous adenosine triphosphate (ATP) supply that must be guaranteed to maintain energy homeostasis [9,10]. In our previous studies, we reported that the level of inorganic polyphosphate (polyP) in the brain of rats decrease with age [11,12]. Especially the latter finding is interesting since it might imply that the reduced polyP concentration in the brain of older specimens (rats) might have an etiological role or represent a predisposition for Alzheimer's disease. polyP, consisting of up to 1000 phosphoanhydride bond-linked phosphate monomers, has been detected in all prokaryotic and eukaryotic organisms; the concentration in mammalian tissues is approximately 50 μM, equivalent to 5 mg/g of tissue [13]. Intracellularly, polyP is present in the cytosol and in 100–200 nm sized acidocalcisomes, and is secreted into the extracellular space by platelets, astrocytes, and bacteria [14]. During hydrolysis of polyP by the enzyme alkaline phosphatase energy-rich anhydride bonds are cleaved that are proposed to give rise to metabolic energy ADP and/or ATP [15,16].

Recently, it has been published that polyP accelerates the fibril formation of both bacterial and human proteins [16,17]. Furthermore, experiments showed that the intracellular level of polyP might confer to a protection against cell death, including the β-amyloid peptide induced Ca^{2+}-dependent apoptosis [18]. Now, we used rat pheochromocytoma cells [PC12 cells], as well as primary cortical neurons, to study the effect of the soluble Na^+ salt of polyP (Na-polyP) and of amorphous microparticles fabricated from the Ca^{2+} salt of polyP (Ca-polyP-MP) to determine the neuroprotective potency of these two polymer preparations. As an inducer of amyloid β-protein-related cell toxicity, we applied a fragment of the amyloid β-protein, displaying amyloidogenic ability, primarily Aβ25-35 [19,20]. In a previous study, we reported that the Aβ peptide should stay in distilled water in a stock solution (900 μM) for five days (5 day) to develop full toxicity [21,22]. In the present study, we added Aβ25-35 at the clinical relevant dose of 5 μM (see: [23]) to PC12 cells. This Aβ25-35 peptide was found to reduce the cell survival during a 6 h incubation period. Concurrently, the ATP level of the cells dropped in the presence of Aβ25-35 by more than 50%. Both this toxic effect and the drop of the ATP pool size could be partially reversed by Na-polyP and almost completely by Ca-polyP-MP. We conclude that polyP rebalances of the β-amyloid-induced decrease in ATP level and in turn abrogate the neurotoxic effect displayed by Aβ25-35.

2. Results

2.1. Fabrication and Morphology of the Particles

In previous studies, it had been suspected that polyP microparticles are taken up by endocytosis [15,16], while the soluble polyP interacts with cell-surface receptors, followed by a signal-transduction pathway [24]. Therefore, the studies, summarized here had to be performed in parallel with both soluble (Na-polyP[Ca^{2+}]) and particulate (Ca-phosphate-NP, Ca-polyP-MP) phosphate samples.

The particles were fabricated using a previously developed precipitation method from $CaCl_2$ and an aqueous polyphosphate solution at an approximate weight ratio of 2:1 [15]. Under these weight

conditions, polyP was found to form microspheres. This procedure was applied both for Na-polyP, with a chain length of ~40 P_i units, and tri-sodium (ortho)-phosphate. The $CaCl_2$ solution was added dropwise to the respective phosphate solution. Na-polyP[Ca^{2+}] was prepared as described under "Materials and Methods".

The fabricated particles, both Ca-phosphate-NP and Ca-polyP-MP, had a powder like consistency (Figure 1A,B). At a higher magnification they appear as homogeneous grains (Figure 1C,E). At the nanoscale, the Ca-phosphate-NP show a largely homogeneous morphology with a diameter of the particles of 35 ± 8 nm ($n = 20$) (Figure 1D). In contrast, the spherical Ca-polyP-MP showed an average size of 170 ± 87 nm (Figure 1F).
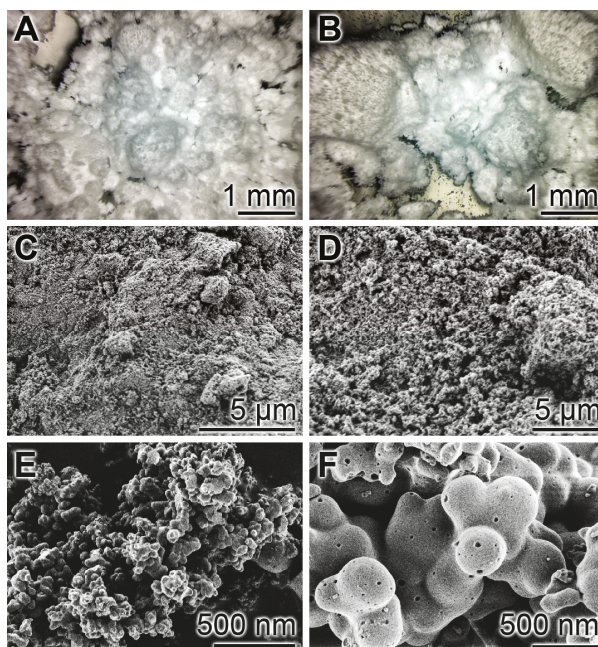
Figure 1. Micrographs of Ca-phosphate nanoparticles (Ca-phosphate-NP) and of Ca-polyP microparticles (Ca-polyP-MP); (**A,B**) optical microscopy; (**C–F**) Scanning electron microscopy (SEM) (**A,C,D**) The Ca-phosphate-NP appear as homogeneous material and as spherical particles of a size around 35 nm at high magnification; (**B,E,F**) The Ca-polyP-MP particles are a likewise homogenous powder at lower magnification and spherical particles at high power scanning electron microscopy (SEM).

2.2. Characterization by Fourier Transform Infrared and X-ray Diffraction

The Fourier Transform Infrared (FTIR) spectra of the Ca-phosphate-NP (Figure 2A) and the Ca-polyP-MP (Figure 2C) show characteristic differences. The Ca-phosphate-NP exhibit a spectrum indicative for carbonated apatite [25]. The spectrum comprises the typical ν_4 bending vibrations of PO_4^{3-} at 557 and 600 cm^{-1}, the ν_1 symmetric PO_4^{3-} stretching at 960 cm^{-1} (to be published), as well as the ν_3 asymmetric stretching at 1018 cm^{-1}. The occurrence of the latter band is also proven to be a marker for ortho-phosphate [26]. Additionally, bands originating from carbonate are visible at 877 cm^{-1} (ν_2 bending vibration) and 1415 cm^{-1} as well as 1455 cm^{-1} (ν_3 asymmetric stretching vibration; double band). The occurrence of these CO_3^{2-} bands is characteristic for type B apatite [27,28]. In contrast, the spectrum of the Ca-polyP-MP (Figure 2C) only shows the characteristic signals for

polyP, as described before [15]. These can be ascribed with 1245 cm^{-1} for ν_{as} $(PO_2)^-$, 1104 cm^{-1} for ν_{as} $(PO_3)^{2-}$, 997 cm^{-1} for ν_{sym} $(PO_3)^{2-}$, 905 cm^{-1} for ν_{as} (P-O-P) and 735 cm^{-1} for ν_{sym} (P–O–P). Vibrations indicative for carbonate are not present.

The X-Ray Diffraction (XRD) pattern for Ca-phosphate-NP shows that the mineral is crystalline (Figure 2B). This must be deduced from the recorded pattern between 20° and 57°; there, sharp reflections are seen with the maximum peak at 26.4°. In contrast, the XRD pattern for Ca-polyP-MP indicates that this material is amorphous (Figure 2D).
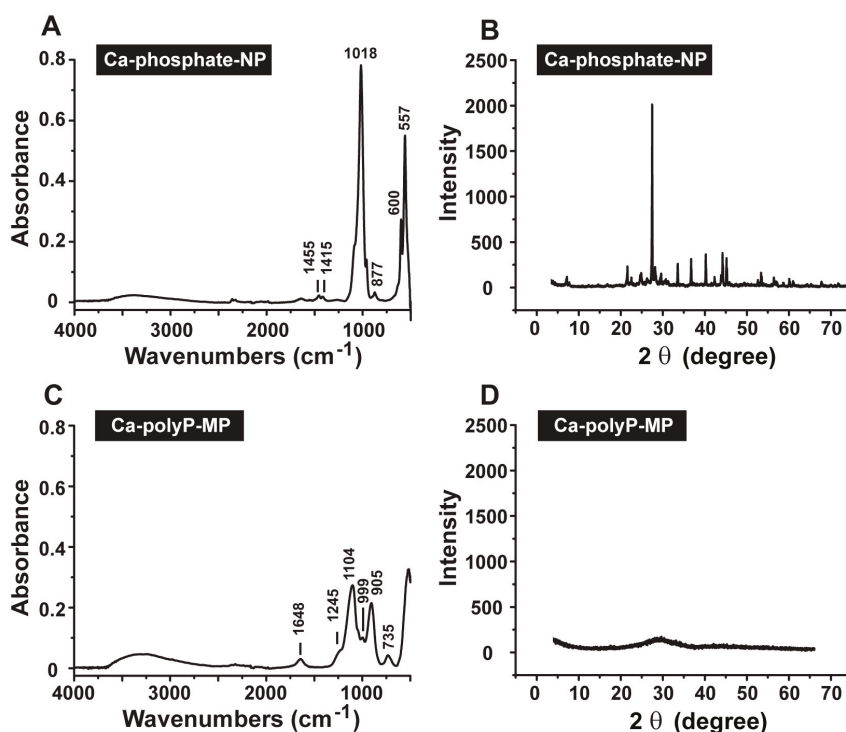
Figure 2. Characterization of the (**A**,**B**) Ca-phosphate-NP and (**C**,**D**) Ca-polyP-MP particles. The analyses were performed by (**A**,**C**) Fourier Transform Infrared (FTIR) and (**B**,**D**) X-Ray Diffraction (XRD).

2.3. Cell viability after Exposure to Phosphate or polyP Preparations

PC12 cells were exposed to three different phosphate preparations (concentration 30 µg/mL), first against Na-polyP[Ca^{2+}], then against Ca-phosphate-NP, and finally against Ca-polyP-MP (Figure 3). In the controls, no phosphate sample was added. The incubation in the 48-well plates was for 72 h; the seeding concentration was 2×10^4 cells/mL. At the end of the incubation period, the cells were harvested and subjected to the 3-[4,5-dimethyl thiazole-2-yl]-2,5-diphenyl tetrazolium (MTT) assay; the amount of formazan crystals was quantitated as described under "Materials and Methods". As seen the viability, measured on the basis of the enzymatic reaction, was found to be for all three preparations not significantly different if compared to the control (without phosphate or polyP); Figure 3. In more detailed viability tests the different phosphate and polyP samples were tested in the concentration range of 3 to 100 µg/mL. In none of the assays the viability in the controls was significantly different than those in the test series (to be published).
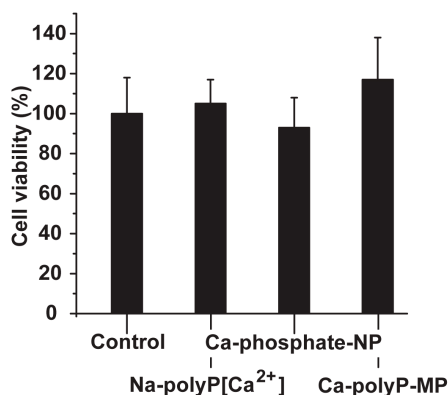
Figure 3. Viability of PC12 cells seeded into 48-well plates for a period of 72 h. Cell viability was determined using the MTT (3-[4,5-dimethyl thiazole-2-yl]-2,5-diphenyl tetrazolium) assay. The concentrations of Na-polyP[Ca^{2+}], Ca-phosphate-NP and Ca-polyP-MP in the assays were identical (30 µg/mL); the controls did not contain additional phosphate or polyP. Data represent mean ± SD of ten independent experiments; no significant differences are calculated ($p > 0.05$).

2.4. Induced Toxicity by the Amyloid β-Protein Peptide (Time-Dependent Pre-Incubation of Aβ25-35 in Water)

In order to assess at which conditions Aβ25-35 should be used for the toxicity/protection assays using PC12 cells one series of experiments were performed with Na-polyP[Ca^{2+}] and Aβ25-35. The peptide had been pre-incubated for a different period of time (0 to 24 h). The Aβ25-35 peptide was dissolved in distilled water (900 µM). Then, the peptide was added either immediately to the cells or was pre-incubated for 6 to 24 h in water and then added to the PC12 cells; the final concentration of the Aβ25-35 peptide was 5 µM. The concentration of cells was adjusted to 8×10^4 cells/mL. Subsequently, the cells were incubated for 12 h followed by the determination of the viability, using the MTT assay system. The results (Figure 4) show that the Aβ25-35 peptide, pre-incubated for 6 h or longer, caused a significant reduction of the PC12 cell number (measured on the basis of the viability of the cells in the assay), by approximately 50–60%. In order to assess the toxic effect of Aβ25-35, in dependence of the period of pre-incubation, the PC12 cells were exposed to Aβ25-35 peptide, which had been pre-incubated with 30 µg/mL of Na-polyP[Ca^{2+}] for 0 to 24 h. In this series only the values for the 6 h pre-incubation period showed a significant difference between the polyP-untreated and polyP-pretreated fragment. The results show that the Aβ25-35, fragment pre-incubated with polyP, is about 15% more toxic (Figure 4). At the present state of knowledge, we attribute this increase in the toxicity to a transient stabilization/conformational change due to the binding of polyP to the peptide of the amyloid β-protein, as outlined before [17]. This intensifying effect (toxicity) of Na-polyP[Ca^{2+}] on the cell growth/viability could not been detected with Ca-phosphate-NP, or Ca-polyP-MP, under otherwise identical conditions.

In a preliminary series of experiments we did not find any change of the degree of toxicity of amyloid β-protein after incubation of the peptide with polyP nanoparticles. Aβ25-35 had been incubated with the nanoparticles for 30 min followed by a centrifugation step (100,000 *g*/30 min); then the supernatant was tested for toxicity (to be published).
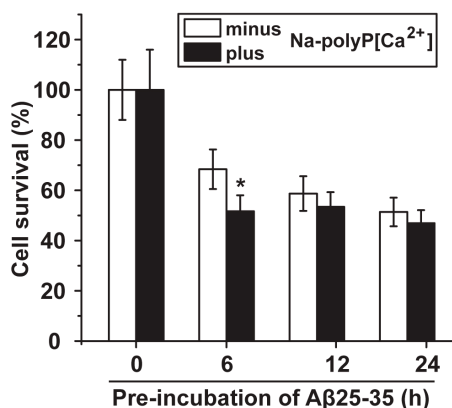
Figure 4. Viability of PC12 cells incubated with the amyloid β-protein fragment Aβ25-35 that had been pre-incubated with Na-polyP[Ca^{2+}]. The peptide had been pre-incubated in distilled water for 6 to 24 h, or was immediately used after solubilization. During the pre-incubation period Aβ25-35 remained untreated or was treated with 30 μg/mL of Na-polyP[Ca^{2+}] (minus/plus Na-polyP[Ca^{2+}]), as described under "Materials and Methods". After that, the respective peptide sample was added to the cell culture (8×10^4 PC12 cells/mL) at a concentration of 5 μM and incubated for 12 h. Then the viability of the cells was determined by the MTT assay; the cell survival rate was calculated and is given as % to the corresponding control culture. Data (±SD) have been based on ten independent experiments; (*) the significance has been calculated ($p < 0.05$).

2.5. Protection against Aβ25-35-Caused Toxicity by polyP

Based on the preceding results, we determined the (potential) cytoprotective effect of polyP, by using an Aβ25-35 sample that had been pre-incubated for 6 h in aqueous solution. In parallel, the PC12 cells were pre-incubated with 30 μg/mL of the phosphate/polyP samples (either Na-polyP[Ca^{2+}], Ca-phosphate-NP, or Ca-polyP-MP) for 24 h. Then, the phosphate-pre-incubated cells assays were mixed with Aβ25-35 (5 μM Aβ25-35 (final concentration)). In the controls to these experiments, the cells were only exposed to the toxic peptide.

The results with PC12 cells (8×10^4 cells/mL) show that in the assays with 5 μM Aβ25-35, the phosphate (Ca-phosphate-NP) pre-treated cells did not show any significant increase in cell survival compared to the control. However, the cells that had been pre-incubated with Na-polyP[Ca^{2+}] or Ca-polyP-MP show a significant resistance against the toxic effect of Aβ25-35 (Figure 5A). Striking is the effect of Ca-polyP-MP on cells during the pre-incubation period. Those cells reached the same survival rate, when compared to cells that are not incubated with the fragment Aβ25-35.

In order to support and express the cytoprotective effect of the Ca-polyP-MP towards the peptide the PC12 cells remained either untreated or were pre-treated with 30 μg/mL of Na-polyP[Ca^{2+}], Ca-phosphate-NP or Ca-polyP-MP (24 h) Then, the cells were treated with 5 μM Aβ25-35 for 6 h followed by staining with Calcein AM. The fluorescence images from the untreated (Figure 6A) and Ca-phosphate-NP-treated cells (Figure 6C) exhibit only relatively few cells, while the cultures treated with Na-polyP[Ca^{2+}] (Figure 6B) and especially those incubated with Ca-polyP-MP (Figure 6D) display markedly more cells in the microscopic view-frame.
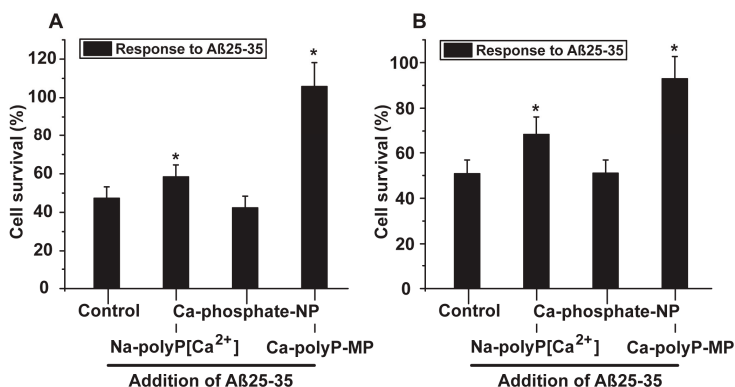
Figure 5. Protective effect of polyP against the toxic effect displayed by the fragment of the amyloid β-protein; the experiments were performed with (**A**) PC12 cells or with (**B**) primary rat cortex neurons. The cells remained either untreated, or were pre-incubated with 30 μg/mL of the phosphate/polyP samples (either Na-polyP[Ca^{2+}], Ca-phosphate-NP, or Ca-polyP-MP) for 24 h. Then the cells, at a concentration of 8×10^4 cells/mL, were incubated with the 6 h pre-incubated Aβ25-35 fragment. After a following period of 12 h the viability of the cells in the respective assays was determined with the MTT assay. From those values, the cell survival rate was calculated and the values are given in % of the respective controls (without phosphate/polyP and Aβ25-35). Data ± SD (ten independent experiments) are give; the significance (*) is calculated $p < 0.05$.
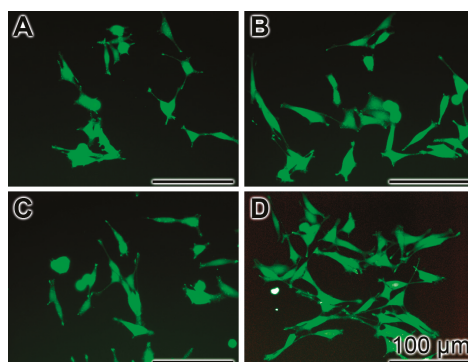
Figure 6. Frequency of cells in a microscopic view-frame pre-treated with phosphate/polyP (24 h) and treated with Aβ25-35 (6 h). The PC12 cell cultures remained untreated (**A**) or were pre-treated with 30 μg/mL of Na-polyP[Ca^{2+}] (**B**); Ca-phosphate-NP (**C**); or Ca-polyP-MP (**D**). After staining with Calcein AM the cells were inspected by fluorescence microscopy.

The results of these experiments were corroborated with primary rat cortex neurons (Figure 5B). Also those neurons (8×10^4 cells/mL), pre-incubated with 30 μg/mL of Na-polyP[Ca^{2+}] or Ca-polyP-MP for 24 h, showed a significant higher survival rate after exposure to Aβ25-35, when compared to the non-treated controls (not pre-treated). While cells, which remained untreated or had been pre-treated with 30 μg/mL of Ca-phosphate-NP showed a survival rate towards the toxic effect of Aβ25-35 of only ~50%, this value increased to 69% (for Na-polyP[Ca^{2+}]) or even 92% (Ca-polyP-MP).

In preliminary studies we found that a co-addition of phosphate nanoparticles to the Aβ25-35 only marginally, and not significantly, elicit a cytoprotective effect seen for the polyP nanoparticles, if added during a pre-incubation period (to be published).

Furthermore, it is well established that among the different peptides of the amyloid β-protein, besides of the Aβ25-35 peptide, also the Aβ1-42 form is toxic to neuronal cells in vitro [29,30]. Exposure primary rat cortex neurons with 5 μM of Aβ1-42 for 24 h resulted in a strong reduction of the number of viable cells to 35.7%, as compared to the untreated controls. However, if neurons that had been pre-incubated for 24 h with 30 μg/mL of Na-polyP[Ca^{2+}], were applied and exposed to Aβ1-42 the number of viable cells increased to 82.7% (when compared to the controls).

2.6. Modulation of the Intracellular ATP Pool in Cells in the Absence or Presence of Aβ25-35 and Phosphate/polyP

The PC12 cells (8 × 10^4 cells/mL) were incubated in the absence or presence of Aβ25-35 and then used for the determination of the intracellular ATP pool. In the absence of the peptide and also the absence of the phosphate samples (control), the ATP measures 2.27 ± 0.28 pmol of (intracellular) ATP (10^3 cells). The addition of Na-polyP[Ca^{2+}] significantly increased the level by 34%, while Ca-phosphate-NP caused no effect (an insignificant drop by 6%). However, if the cells were supplemented with Ca-polyP-MP, a significant increase of the pool by 91% is measured (Figure 7).
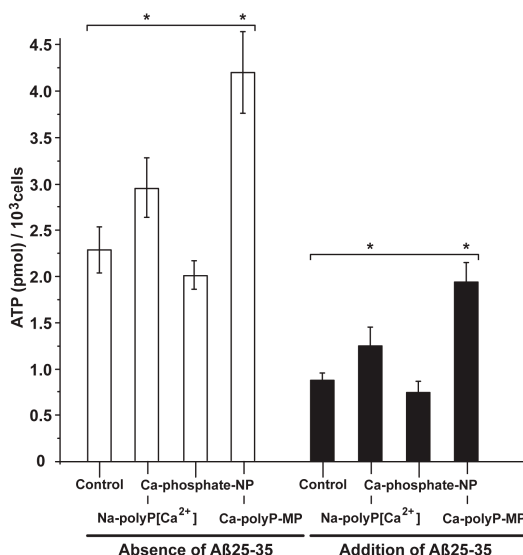
Figure 7. Change of the intracellular ATP pool in PC12 cells in dependence on the exposure to phosphate/polyP and/or Aβ25-35. In the first series the cells were exposed only to phosphate/polyP and not to Aβ25-35; open bar. In the Aβ25-35 test series (closed bars) the cells were treated with 5 μM of the peptide and remained either untreated (control) or were exposed to 30 μg/mL of Na-polyP[Ca^{2+}], Ca-phosphate-NP, or Ca-polyP-MP, as indicated. The values came from five parallel assays; the means as well as the standard deviations are given. The significant differences between the values (control [minus phosphate/polyP]) and the test samples (Na-polyP[Ca^{2+}] and Ca-polyP-MP) are indicated (*) *p* < 0.01.

If the cells were incubated for 24 h in the presence of 5 μM Aβ25-35 the ATP pool dropped to 0.87 ± 0.09 pmol (10^3 cells). If the cultures were treated together with the peptide and 30 μg/mL of Ca-phosphate-NP no significant change was measured. However, if they were treated with polyP and together with the peptide a significant increase was seen; with Na-polyP[Ca^{2+}] the level increases to 1.26 ± 0.02 pmol (10^3 cells), and with Ca-polyP-MP to 1.94 ± 0.21 pmol (10^3 cells); Figure 7.

3. Discussion

One of the hallmarks of AD is the presence of two specific structures in the brain the senile plaques and the neurofibrillary tangles, which are correlated and accompanied with neuron death [31]. While Aβ25-35 is one main component of the senile plaques it is the Tau protein, in its phosphorylated form, which is the main component of the neurofibrillary tangles [32]. In the extracellular space, an abnormal deposition of wrongly processed and aggregated amyloid β-protein/peptides and Tau proteins occurs [33]. Recent studies revealed that during AD pathogenesis misformation/misfolding of Tau protein proceeds downstream of amyloid β-protein accumulation [34]. The misfolded amyloid β-protein/peptides has been implicated as a major component involved in initiation of apoptotic neuronal cell death [21,35,36]. In turn, efforts have been undertaken to develop new potential therapeutics that prevent neuronal death through the prevention of misfolding of amyloid β-protein and Tau, as well as of the subsequent apoptotic process [37]. Flupirtine [38] and memantine [8] have been elaborated by us as modulators of the NMDA receptor and consequently as neuroprotective agents, a finding that has later been confirmed by others [39,40]. Memantine has even been proposed to be applied in human as both mild and moderate-to-severe AD.

It has been demonstrated that heat shock protein(s) can reduce the neurotoxic activity of Tau [41] and amyloid β-protein/peptides [42]. Those heat shock protein(s) require energy for the folding process, usually in form of ATP [43]. They function not only intracellularly, but also extracellularly [44]. ATP is surely present also in the extracellular space but there it is prone to hydrolytic dephosphorylation through the enzyme alkaline phosphatase (ALP; [45]). The extracellular polyP has recently been proposed to act as "metabolic fuel" [15,16,46], and could provide a further depot for biochemically useful energy. This inorganic polymer has also been identified in the central nervous system at concentrations between 25 and 120 μM (~5 μg/mL, with respect to phosphate) [13,47]. Since for many years, polyP has been proven to function as a modulator of the transient receptor potential cation channel A/1 (TRPA1) and of the transient receptor potential cation channel subfamily M/8 (TRPM8), it has been suggested that polyP is involved in neuronal signaling [14]. Furthermore, experiments suggested that short and medium size polyP (chain length up to 100 phosphate units) does not activate apoptotic cascade in neurons and astrocytes [48]. Soluble polyP has been suggested to interact with the P2Y purinoceptor 1 through which it leads to an activation of the phospholipase C, resulting in a release of inositol 3 phosphate and an elevation of Ca^{2+} level in the cytosol [48]. On the other side, the Ca-polyP nanoparticles/microparticles are most likely taken up by the cells via endocytosis [16].

It is well established that mitochondrial dysfunction in AD is associated not only with enhanced oxidative stress, but also with reduced ATP generation [49]. Based on our resent finding showing that amorphous Ca-polyP induces ATP synthesis in bone-like cells [46], we raised now the question if brain-like cells, PC12 cells neuron-related cells and/or primary rat cortex neurons, can be protected against the toxic effect elicited by Aβ25-35 through the upregulation of the ATP pool. In our approach, we applied three phosphate formulations, Na-polyP, complexed to Ca^{2+} (Na-polyP[Ca^{2+}]), orthophosphate nanoparticles (Ca-phosphate-NP), and finally Ca-polyP microparticles (Ca-polyP-MP). While Na-polyP[Ca^{2+}] is highly soluble and acts by binding to a cell-surface receptor, the two particle preparations, Ca-phosphate-NP and Ca-polyP-MP, are less soluble. Ca-polyP-MP will be taken up into the cells by endocytosis [15,16]. It is important to stress that, under the conditions applied, the orthophosphate particles are crystalline, while the polyP particles are amorphous. In general, minerals in the amorphous state are functionally more active that crystalline mineral deposits, due to their higher solubility, and in turn their more efficient signaling potential [50–52]. The applied Ca-polyP-MP, similar to those that are physiologically present in the acidocalcisomes [14], are also prone to hydrolytic attack to the intra- as well as the extracellular ALP [46,53]. It should be mentioned that Ca-polyP has lost its Na^+-chelating propensity and consequently the adverse functions of this polymers on cells [54].

The three phosphate formulations, at the concentration used (30 μg/mL), did not cause any significant effect on viability of PC12 cells. If the cells were exposed to the Aβ25-35 fragment an about

50% reduction of cell survival was measured after 6 h incubation. This Aβ25-35-mediated cell toxicity was significantly reduced by Na-polyP[Ca^{2+}] by 20% if the polymer was added to the cells 24 h prior to the addition of the fragment of the amyloid β-protein. No toxic effect was measured if the cells were exposed to Aβ25-35 after pre-incubation with Ca-polyP-MP for 24 h. The cytoprotective effect of Ca-polyP-MP against Aβ25-35 exposure was confirmed with primary embryonic rat cortex neurons. Furthermore, we used also the Aβ peptide Aβ1-42 and confirmed the effects, seen with Aβ25-35. The degree of toxicity displayed by Aβ25-35 was dependent on the time of pre-incubation in aqueous solution, as described before [21,22]. The maximum of toxicity was reached already during the first 6 h; longer pre-incubation phases did not change the degree of neurotoxicity. During this time of dissolution, the fragment of the amyloid β-protein underwent spontaneous aggregation [55].

In a preceding study, it has been reported that exposure of mammalian cells, in that study SaOS-2 cells have been used [46], to amorphous Ca^{2+}-polyP nanoparticles with a globular size of ~100 nm causes a ~2.5-fold increase of the intracellular ATP level, and an even ~10-fold rise in the extracellular ATP concentration. The determinations, presented here, show that PC12 cells respond to a 24 h-incubation with Ca-polyP-MP with a doubling of the intracellular ATP pool. All of the other phosphate formulations did not cause any significant alteration.

The reaction/signal transduction chain through which polyP, if extracellularly applied, changes the intracellular metabolism, is not yet known. From studies with isolated mitochondria, it is known that the permeability of mitochondrial membranes is altered in response to polyP [56]. At physiological concentrations, polyP can regulate calcium concentration by mitochondrial permeability transition pore opening, suggesting a potential regulatory role during apoptosis. As mentioned above, polyP is assumed to bind to P2Y purinoceptor 1, resulting in a modulation of the intracellular Ca^{2+} level. In our previous studies, we found that microparticles prepared from Ca-polyP are most likely taken up by the cells via endocytosis [16,46]. In addition, unpublished studies revealed that the polyP microparticles undergo an intracellular sequential disintegration [16,57]. During this process, polyP is surely released and undergoes enzymatic cleavage by the intracellular ALP. In analogy with the recent findings that extracellular polyP is prone to hydrolytic degradation by the ALP [11], resulting in an upregulation of the intracellular, as well as the extracellular ATP [46,58], we propose that also intracellularly, this inorganic polymer can function in the same reaction chain and transfers the metabolic energy stored in its energy-rich phosphoanhydride bonds to adenosine monophosphate (AMP) or ADP; the additional enzyme required for this process, the adenylate kinase, also exists in this compartment [59].

4. Materials and Methods

4.1. Materials

Sodium polyphosphate (Na-polyP of an average chain of 40 phosphate units) was obtained from Chemische Fabrik Budenheim (Budenheim; Germany).

4.2. Phosphate/Polyphosphate Sample Fabrication

The polyP particles were prepared as described before [15]. In brief, Na-polyP (2 g) was dissolved in 100 mL of distilled water; the resulting pH value was increased from pH 3.4 to 10 with 2 N NaOH. Then 60 mL of a $CaCl_2$ solution (5.6 g $CaCl_2 \cdot 2H_2O$; #C3306 Sigma, Taufkirchen; München, Germany) were added dropwise to the polyP solution. After stirring for 12 h the particles formed were collected by filtration through Nalgene Filter Units (pore size 0.45 µm; Cole-Parmer, Kehl/Rhein; Wertheim-Mondfel, Germany). Then the particles were washed twice with ethanol to remove the unbound Ca^{2+}. Finally, the amorphous microparticles, "Ca-polyP-MP", were dried at 60 °C overnight.

The particles formed from sodium orthophosphate (tri-sodium phosphate; Sigma #342483) were prepared in the same way. Two g of tri-sodium phosphate were dissolved in 100 mL of water; the pH value was adjusted to pH 10; then 60 mL of the $CaCl_2$ solution (containing 5 g $CaCl_2$) were added. The resulting crystalline particles, Ca-phosphate-NP, were processed as described above.

4.3. Fourier Transformed Infrared Spectroscopy and X-ray Diffraction

Fourier transformed infrared (FTIR) spectroscopy was performed with a Varian 660-IR spectrometer with Golden Gate ATR auxiliary (Agilent, Darmstadt, Germany). X-ray diffraction (XRD) of the dried powder samples was conducted in a Philips PW1820 diffractometer with monochromatic Cu-Kα radiation (λ = 1.5418 Å, 40 kV, 30 mA, 5 s, $\Delta\theta$ = 0.02) [60].

4.4. Microscopy

Scanning electron microscopy (SEM) was conducted with a HITACHI SU8000 electron microscope (Hitachi High-Technologies Europe, Krefeld, Germany). Light microscopy was performed with a VHX-600 Digital Microscope from KEYENCE (Neu-Isenburg, Germany).

4.5. PC12 Cells

Rat pheochromocytoma cells (PC12 cells) were obtained from Sigma (#88022401) and cultivated in RPMI 1640 medium (Sigma) and heat-inactivated horse serum (10%)/heat-inactivated fetal bovine serum (5%), together with gentamicin; incubation was performed in a humidified atmosphere of air (95%) and CO_2 (5%). The cells were plated at a density 4×10^3 cells in 96-well (working volume 200 µL)- or 4×10^4 cells in 6-well (2 mL) plate for the indicated periods of time.

Three different phosphate preparations were added to the culture: (i) Na-polyP complexed in a stoichiometric ratio to Ca^{2+} (molar ratio of 2 (with respect to the phosphate monomer); abbreviated as Na-polyP[Ca^{2+}]), as described in [54]; (ii) Ca-phosphate-NP; and, (iii) Ca-polyP-MP (40 phosphoanhydride bond-linked phosphate units). The concentrations are given with the respective experiments and were usually 30 µg/mL.

For microscopic visualization the cells were stained with 5 µM Calcein AM (Sigma). Then they were inspected by fluorescence microcopy at an excitation wavelength of 494 nm and an emission of 540 nm.

4.6. Cell Viability Assays

The toxicity of the phosphate preparations was determined after an incubation period of the PC12 cells in medium/serum for 72 h. The cells were seeded into 48-well plates at an initial density 2×10^4 cells/mL. Then, the viability of the cells was determined with the 3-[4,5-dimethyl thiazole-2-yl]-2,5-diphenyl tetrazolium (MTT; #M2128, Sigma) assay. The cells were detached (by carefully pipetting up and down with a 10 mL pipette) and a 2 mL cell suspension was aspirated and subsequently incubated with fresh medium containing 200 µL of MTT for 4 h in the dark. Subsequently, the remaining MTT dye was removed and 200 µL of dimethyl sulfoxide (DMSO) was added to solubilize the formazan crystals. Finally, the optical densities (OD) at 570 nm were measured using an enzyme-linked immunosorbent assay (ELISA) reader/spectrophotometer [61]. Cell viability was expressed as a percentage of the untreated control (without phosphate/polyP). Ten parallel experiments were performed.

4.7. Aβ-Induced Cell Toxicity

Previously, we found that the Aβ25-35 sample, should be pre-incubated in a stock solution (900 µM in distilled water) for five days to develop the full toxicity [21]. In the present study, we performed a time kinetics to assess the toxicity elicited by Aβ25-35 (#A4559, Sigma) by pre-incubating the Aβ25-35 stock solution in distilled water for a period between 6 and 24 h in the absence or presence of polyP. The polymer, Na-polyP[Ca^{2+}], was added at a concentration of 30 µg/mL. Subsequently, the corresponding volume of the sample was taken and added to PC12 cells (2×10^4 cells/mL) to reach a final concentration of 5 µM in the cell assays. The cells were incubated for 12 h. After termination, the viability of the cells in the culture was determined by the MTT assay (see above). From those results, the cell survival rate in % of the controls (without Aβ25-35), was calculated.

For testing the toxicity of the Aβ25-35 peptide, the stock solution was diluted to a final concentration in the toxicity assays of 5 μM [21,22]. Prior to the addition of Aβ25-35 the cells were pre-incubated for 24 h in medium/serum at a final concentrations of 30 μg/mL with Na-polyP[Ca^{2+}], Ca-phosphate-NP or Ca-polyP-MP; the controls were incubated in parallel and did not contain any phosphate sample. Then, the medium was removed and the Aβ25-35 sample was added. Incubation was performed for 12 h; finally, the viability of the cells was determined with MTT. Cell viability is given in percent of the untreated control (without Aβ25-35 and without phosphate/polyP).

In one series of experiments, the Aβ1-42 fragment (#A9810, Sigma) had been used in parallel to the toxicity studies. Again, a stock solution (900 μM in distilled water) had been prepared. After keeping for 24 h, aliquots had been taken and added to primary rat cortex neurons to reach a final concentration of 5 μM. After incubation for 24 h, in the absence or presence of 30 μg/mL Na-polyP[Ca^{2+}] the cell number was determined.

4.8. Primary Culture of Cortical Neurons

Primary rat cortex neurons isolated from 18-day old rat embryos were obtained from GIBCO/Thermo Fisher Scientific (Langenselbold, Wiesbaden, Germany). They were cultivated in Neurobasal Medium (from GIBCO/Thermo Fisher Scientific), as described in [38,62]. Five days old cultures were used for the studies. The experiments were performed in 96-well/or 6-well plates.

The assay regimen with Aβ25-35 as well as the pre-incubation protocol of the cells with the phosphate samples was the same as for PC12 cells.

Cell toxicity was determined after 12 h with the MTT assay [63].

4.9. Determination of the ATP Level in PC12 Cells

PC12 cells were cultivated in 12-well plates until they reached about 75% of confluency (8×10^4 cells/mL). Then, the cells were continued to be incubated for 24 h in the absence of any polyP, or the presence of the three phosphate samples in the absence of presence of Aβ25-35. Finally, ATP was extracted from the cells [64–66], and the ATP concentration was determined by using the ATP luminescence kit (NO. LL-100-1, Kinshiro, Toyo Ink; Fukuoka, Japan), as described in [46]. After establishing a standard curve for given ATP concentrations, the absolute amount of ATP was extrapolated and is given as pmol/10^3 viable cells. In parallel assays, the number of viable cells were determined by the MTT cell viability assay [67].

Prior to the ATP determination the cells were pre-incubated for 24 h with 30 μg/mL of Na-polyP[Ca^{2+}], Ca-phosphate-NP or Ca-polyP-MP; again, the controls were incubated in parallel and they did not contain any phosphate sample.

4.10. Statistical Analysis

After verifying that the respective values follow a standard normal Gaussian distribution and that the variances of the respective groups are equal, the results were statistically evaluated using the independent two-sample Student's *t*-test [68].

5. Conclusions

The described experiments in the present study indicate that the physiologically occurring polyP microparticles/nanoparticles, prepared from Ca-polyP, can effectively block the toxic effect elicited by the toxic peptide fragment Aβ25-35; see scheme in Figure 8. This inhibition is attributed to an elevation of intracellular ATP level, which has been described to be one factor for neuronal cell death in AD, or in AD-model systems. Surely further studies are required to elucidate if the observed effect of the polyP microparticles/nanoparticles to increase the ATP level intracellularly and can also be extended to the extracellular ATP pool [58]. Also, in this extracellular compartment ATP, or equivalent metabolic energy, is required for the heat shock protein-mediated folding of proteins in general and

of the amyloid precursor protein and/or it derivatives [69]. There, in the extracellular space, ADP (or perhaps also ATP) could feed, e.g., the chaperone clusterin with its ADP binding motif [70], with energy prevent misfolding of the amyloid precursor protein. Intracellularly, the polyP microparticles are enzymatically hydrolyzed via the ALP.
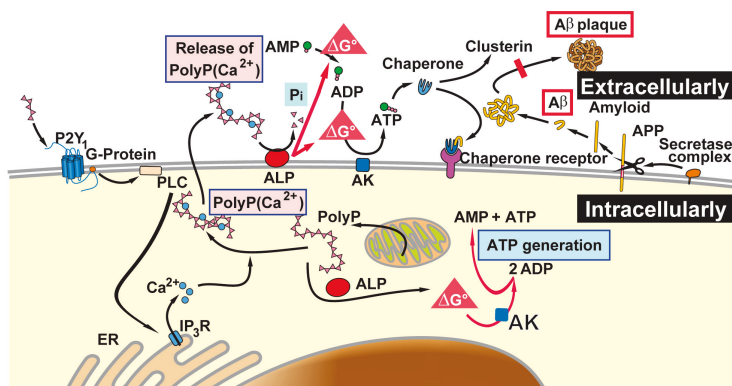

Figure 8. As outlined, polyP microparticles that can be taken up by the cells, or formed there intracellularly, are prone to the alkaline phosphatase (ALP). In analogy to the acidocalcisomes, polyP microparticles are also formed intracellularly, and can subsequently be released by the cells. It is sketched that the (proposed) pathways of ATP generate both intra- and extracellularly Gibbs free energy that is released during the hydrolysis of the anhydride bond in polyP into both compartments. This process can occur both extracellularly [58] and intracellularly. Those adenosine nucleotides provide the energy for the extracellular chaperones which might prevent misfolding of amyloid plaques (abbreviated as Aβ). AK: adenylate kinase; AMP: adenosine monophosphate; ADP: adenosine diphosphate; ATP: adenosine triphosphate; ER: endoplasmic reticulum.

The data reported in this contribution might help to develop new routes for a therapeutic intervention in AD pathophysiology. Methods have been worked out to deliver drugs, encapsulated into nanoparticles/microparticles, which can cross the blood-brain barrier [71,72]. Through this route, the delivery of the potential polyP compound across the blood-brain barrier appears to be promising, since this structural barrier undergoes dysfunction during the AD progression, facilitating particle transport [73,74]. This conclusion is also strengthened by a previous report [17], showing that polyP is not only stabilizing the structure of the amyloid β-protein but also might have a beneficial effect on the progression of the Alzheimer's disease in patients. However, future in vitro studies must be performed to determine, if cells pretreated with the peptide of the amyloid β-protein and are in the process to undergo apoptosis can be rescued by soluble or particulate polyP. In case such a rescuing effect cannot be found, polyP still remains a candidate molecule for prevention. But even then, polyP might be possible to lower the amyloid β-protein/fragments load in patients; recent studies suggest that peptides of the amyloid β-protein act as seeding molecules and start an amyloid β-protein seeding cascade [75].

Author Contributions: Werner E. G. Müller, Maximilian Ackermann, Qingling Feng, Heinz C. Schröder and Xiaohong Wang conceived and designed the experiments; Shunfeng Wang, Maximilian Ackermann, Meik Neufurth, Renate Steffen, Egherta Mecja and Rafael Muñoz-Espí performed the experiments;

Abbreviations

AD	Alzheimer's disease
Aβ	Amyloid β-peptides
Aβ25-35	amyloid β-protein fragment 25-35
ADP	adenosine diphosphate
AMP	adenosine monophosphate
ATP	adenosine triphosphate
Ca-polyP-MP	Ca-polyP microparticles
DMSO	dimethyl sulfoxide
ELISA	enzyme-linked immunosorbent assay
MTT	3-[4,5-dimethyl thiazole-2S-yl]-2,5-diphenyl tetrazolium
Na-polyP	Sodium polyphosphate
Na-polyP[Ca^{2+}]	Na^+ salt of polyP complexed in a stoichiometric ratio to Ca^{2+}
PC12 cells	Pheochromocytoma cells
polyP	Polyphosphate
SEM	Scanning electron microscopy
TRPA1	Transient receptor potential cation channel A/1
TRPM8	Cation channel subfamily M/8

References

1. Selkoe, D.J. The molecular pathology of Alzheimer's disease. *Neuron* **1991**, *6*, 487–498. [CrossRef]
2. Alzheimer, A. Über eine eigenartige Erkrankung der Hirnrinde. *Allg. Zschr. Psychiatr. Psych. Gerichtl. Med.* **1907**, *64*, 146–148.
3. Wolf, A.; Bauer, B.; Hartz, A.M. ABC transporters and the Alzheimer's disease enigma. *Front. Psychiatry* **2012**, *3*, 54. [CrossRef] [PubMed]
4. Hardy, J.; Selkoe, D.J. The amyloid hypothesis of Alzheimer's disease: Progress and problems on the road to therapeutics. *Science* **2002**, *297*, 353–356. [CrossRef] [PubMed]
5. Chase, T.N. High-dose cholinesterase inhibitor treatment of Alzheimer's disease. *Alzheimers. Dement.* **2015**, *11*, S466–S467. [CrossRef]
6. Informed Health Online. Alzheimer's Disease: Does Memantine Help? Available online: https://www.ncbi.nlm.nih.gov/pubmedhealth/PMH0072540/ (accessed on 2 August 2016).
7. Rytik, P.G.; Eremin, V.F.; Kvacheva, Z.B.; Poleschuk, N.N.; Popov, A.S.; Schröder, H.C.; Weiler, B.E.; Bachmann, M.; Müller, W.E.G. Susceptibility of human astrocytes to human immunodeficiency virus infection in vitro; Anti-HIV activity of memantine. *AIDS Res. Hum. Retrov.* **1991**, *7*, 89–95.
8. Müller, W.E.G.; Schröder, H.C.; Ushijima, H.; Dapper, J.; Bormann, J. Gp120 of HIV-1 induces apoptosis in rat cortical cell cultures: Prevention by memantine. *Eur. J. Pharmacol.* **1992**, *226*, 209–214. [CrossRef]
9. Khatri, N.; Man, H.Y. Synaptic activity and bioenergy homeostasis: Implications in brain trauma and neurodegenerative diseases. *Front. Neurol.* **2013**, *4*, 199. [CrossRef] [PubMed]
10. Li, Y.P.; Yang, G.J.; Jin, L.; Yang, H.M.; Chen, J.; Chai, G.S.; Wang, L. Erythropoietin attenuates Alzheimer-like memory impairments and pathological changes induced by amyloid β42 in mice. *Brain Res.* **2015**, *1618*, 159–167. [CrossRef] [PubMed]
11. Lorenz, B.; Schröder, H.C. Mammalian intestinal alkaline phosphatase acts as highly active exopolyphosphatase. *Biochim. Biophys. Acta* **2001**, *1547*, 254–261. [CrossRef]
12. Lorenz, B.; Münkner, J.; Oliveira, M.P.; Kuusksalu, A.; Leitão, J.M.; Müller, W.E.G.; Schröder, H.C. Changes in metabolism of inorganic polyphosphate in rat tissues and human cells during development and apoptosis. *Biochim. Biophys. Acta* **1997**, *1335*, 51–60. [CrossRef]

13. Morrissey, J.H.; Choi, S.H.; Smith, S.A. Polyphosphate, An ancient molecule that links platelets, coagulation, and inflammation. *Blood* **2012**, *119*, 5972–5979. [CrossRef] [PubMed]

14. Holmström, K.M.; Marina, N.; Baev, A.Y.; Wood, N.W.; Gourine, A.V.; Abramov, A.Y. Signalling properties of inorganic polyphosphate in the mammalian brain. *Nat. Commun.* **2013**, *4*, 1362. [CrossRef] [PubMed]

15. Müller, W.E.G.; Tolba, E.; Schröder, H.C.; Wang, X.H. Polyphosphate: A morphogenetically active implant material serving as metabolic fuel for bone regeneration. *Macromol. Biosci.* **2015**, *15*, 1182–1197. [CrossRef] [PubMed]

16. Wang, X.H.; Schröder, H.C.; Müller, W.E.G. Polyphosphate as a metabolic fuel in Metazoa: A foundational breakthrough invention for biomedical applications. *Biotechnol. J.* **2016**, *11*, 11–30. [CrossRef] [PubMed]

17. Cremers, C.M.; Knoefler, D.; Gates, S.; Martin, N.; Dahl, J.U.; Lempart, J.; Xie, L.; Chapman, M.R.; Galvan, V.; Southworth, D.R.; et al. Polyphosphate: A Conserved modifier of amyloidogenic processes. *Mol. Cell* **2016**, *63*, 768–780. [CrossRef] [PubMed]

18. Abramov, A.Y.; Fraley, C.; Diao, C.T.; Winkfein, R.; Colicos, M.A.; Duchen, M.R.; French, R.J.; Pavlov, E. Targeted polyphosphatase expression alters mitochondrial metabolism and inhibits calcium-dependent cell death. *Proc. Natl. Acad. Sci. USA* **2007**, *104*, 18091–18096. [CrossRef] [PubMed]

19. Masilamoni, J.G.; Jesudason, E.P.; Jesudoss, K.S.; Murali, J.; Paul, S.F.D.; Yayakumar, R. Role of fibrillar Aβ25-35 in the inflammation induced rat model with respect to oxidative vulnerability. *Free Rad. Res.* **2005**, *6*, 603–612. [CrossRef] [PubMed]

20. Tsai, H.H.; Lee, J.B.; Shih, Y.C.; Wan, L.; Shieh, F.K.; Chen, C.Y. Location and conformation of amyloid β(25-35) peptide and its sequence-shuffled peptides within membranes: Implications for aggregation and toxicity in PC12 cells. *ChemMedChem* **2014**, *9*, 1002–1011. [CrossRef] [PubMed]

21. Zeng, Z.; Xu, J.; Zheng, W. Artemisinin protects PC12 cells against β-amyloid-induced apoptosis through activation of the ERK1/2 signaling pathway. *Redox Biol.* **2017**, *12*, 625–633. [CrossRef] [PubMed]

22. Müller, W.E.G.; Romero, F.J.; Perović, S.; Pergande, G.; Pialoglou, P. Protection of flupirtine on ß-amyloid-induced apoptosis in neuronal cells in vitro. Prevention of amyloid-induced glutathione depletion. *J. Neurochem.* **1997**, *68*, 2371–2377. [CrossRef] [PubMed]

23. Müller, W.E.G.; Pialoglou, P.; Romero, F.J.; Perovic, S.; Pergande, G. Protective effect of the drug flupirtine on β-amyloid-induced apoptosis in primary neuronal cells in vitro. *J. Brain Res.* **1996**, *37*, 575–577. [CrossRef]

24. Dinarvand, P.; Hassanian, S.M.; Qureshi, S.H.; Manithody, C.; Eissenberg, J.C.; Yang, L.; Rezaie, A.R. Polyphosphate amplifies proinflammatory responses of nuclear proteins through interaction with receptor for advanced glycation end products and P2Y1 purinergic receptor. *Blood* **2014**, *123*, 935–945. [CrossRef] [PubMed]

25. Figueiredo, M.M.; Gamelas, J.A.F.; Martins, A.G. Characterization of Bone and Bone-Based Graft Materials Using FTIR Spectroscopy. In *Infrared Spectroscopy—Life and Biomedical Sciences*; Theophanides, T., Ed.; InTech: Rijeka, Croatia, 2012; pp. 315–338. Available online: https: //www.intechopen.com/books/infrared-spectroscopy-life-and-biomedical-sciences/characterization-of-bone-and-bone-based-graft-materials-using-ftir-spectroscopy (accessed on 1 June 2017). [CrossRef]

26. Khoshmanesh, A.; Cook, P.L.; Wood, B.R. Quantitative determination of polyphosphate in sediments using Attenuated Total Reflectance-Fourier Transform Infrared (ATR-FTIR) spectroscopy and partial least squares regression. *Analyst* **2012**, *137*, 3704–3709. [CrossRef] [PubMed]

27. Landi, E. Carbonated hydroxyapatite as bone substitute. *J. Eur. Ceram. Soc.* **2003**, *23*, 2931–2937. [CrossRef]

28. Fleet, M.E. Infrared spectra of carbonate apatites: ν2-region bands. *Biomaterials* **2009**, *30*, 1473–1481. [CrossRef] [PubMed]

29. Mohmmad Abdul, H.; Butterfield, D.A. Protection against amyloid beta-peptide (1-42)-induced loss of phospholipid asymmetry in synaptosomal membranes by tricyclodecan-9-xanthogenate (D609) and ferulic acid ethyl ester: Implications for Alzheimer's disease. *Biochim. Biophys. Acta* **2005**, *1741*, 140–148. [CrossRef] [PubMed]

30. Butterfield, D.A.; Swomley, A.M.; Sultana, R. Amyloid β-peptide (1-42)-induced oxidative stress in Alzheimer disease: Importance in disease pathogenesis and progression. *Antioxid. Redox Signal.* **2013**, *19*, 823–835. [CrossRef] [PubMed]

31. Wang, Y.; Mandelkow, E. Tau in physiology and pathology. *Nat. Rev. Neurosci.* **2016**, *17*, 5–21. [CrossRef] [PubMed]

32. Bloom, G.S. Amyloid-β and tau: The trigger and bullet in Alzheimer disease pathogenesis. *JAMA Neurol.* **2014**, *71*, 505–508. [CrossRef] [PubMed]

33. Šimić, G.; Babić, L.M.; Wray, S.; Harrington, C.; Delalle, I.; Jovanov-Milošević, N.; Bažadona, D.; Buée, L.; de Silva, R.; Di Giovanni, G.; et al. Tau protein hyperphosphorylation and aggregation in Alzheimer's Disease and other tauopathies, and possible neuroprotective strategies. *Biomolecules* **2016**, *6*, 6. [CrossRef] [PubMed]

34. Leroy, K.; Ando, K.; Laporte, V.; Dedecker, R.; Suain, V.; Authelet, M.; Héraud, C.; Pierrot, N.; Yilmaz, Z.; Octave, J.N.; et al. Lack of tau proteins rescues neuronal cell death and decreases amyloidogenic processing of APP in APP/PS1 mice. *Am. J. Pathol.* **2012**, *181*, 1928–1940. [CrossRef] [PubMed]

35. Behl, C. Apoptosis and Alzheimer's disease. *J. Neural. Transm.* **2000**, *107*, 1325–1344. [CrossRef] [PubMed]

36. Niikura, T.; Tajima, H.; Kita, Y. Neuronal cell death in Alzheimer's disease and a neuroprotective factor, humanin. *Curr. Neuropharmacol.* **2006**, *4*, 139–147. [CrossRef] [PubMed]

37. Cummings, J.; Aisen, P.S.; DuBois, B.; Frölich, L.; Jack, C.R., Jr.; Jones, R.W.; Morris, J.C.; Raskin, J.; Dowsett, S.A.; Scheltens, P. Drug development in Alzheimer's disease: The path to 2025. *Alzheimer's Res. Ther.* **2016**, *8*, 39. [CrossRef] [PubMed]

38. Perović, S.; Schleger, C.; Pergande, G.; Iskric, S.; Ushijima, H.; Rytik, P.; Müller, W.E.G. The triaminopyridine Flupirtine prevents cell death in rat cortical cells induced by *N*-methyl-D-aspartate and gp120 of HIV-1. *Eur. J. Pharmacol.* **1994**, *288*, 27–33. [CrossRef]

39. Kornhuber, J.; Bleich, S.; Wiltfang, J.; Maler, M.; Parsons, C.G. Flupirtine shows functional NMDA receptor antagonism by enhancing Mg^{2+} block via activation of voltage independent potassium channels. Rapid communication. *J. Neural. Transm.* **1999**, *106*, 857–867. [CrossRef] [PubMed]

40. Lipton, S.A. The molecular basis of memantine action in Alzheimer's disease and other neurologic disorders: Low-affinity, uncompetitive antagonism. *Curr. Alzheimer Res.* **2005**, *2*, 155–165. [CrossRef] [PubMed]

41. Dickey, C.A.; Kamal, A.; Lundgren, K.; Klosak, N.; Bailey, R.M.; Dunmore, J.; Ash, P.; Shoraka, S.; Zlatkovic, J.; Eckman, C.B.; et al. The high-affinity HSP90-CHIP complex recognizes and selectively degrades phosphorylated tau client proteins. *J. Clin. Investig.* **2007**, *117*, 648–658. [CrossRef] [PubMed]

42. Wu, Y.; Cao, Z.; Klein, W.L.; Luo, Y. Heat shock treatment reduces beta amyloid toxicity in vivo by diminishing oligomers. *Neurobiol. Aging* **2010**, *31*, 1055–1058. [CrossRef] [PubMed]

43. Mallouk, Y.; Vayssier-Taussat, M.; Bonventre, J.V.; Polla, B.S. Heat shock protein 70 and ATP as partners in cell homeostasis (Review). *Int. J. Mol. Med.* **1999**, *4*, 463–474. [CrossRef] [PubMed]

44. De Maio, A.; Vazquez, D. Extracellular heat shock proteins: A new location, a new function. *Shock* **2013**, *40*, 239–246. [CrossRef] [PubMed]

45. Yalak, G.; Ehrlich, Y.H.; Olsen, B.R. Ecto-protein kinases and phosphatases: An emerging field for translational medicine. *J. Transl. Med.* **2014**, *12*, 165. [CrossRef] [PubMed]

46. Müller, W.E.G.; Tolba, E.; Schröder, H.C.; Wang, S.; Glaßer, G.; Muñoz-Espí, R.; Link, T.; Wang, X.H. A new polyphosphate calcium material with morphogenetic activity. *Mater. Lett.* **2015**, *148*, 163–166. [CrossRef]

47. Gabel, N.W.; Thomas, V. Evidence for the occurrence and distribution of inorganic polyphosphates in vertebrate tissues. *J. Neurochem.* **1971**, *18*, 1229–1242. [CrossRef] [PubMed]

48. Angelova, P.R.; Baev, A.Y.; Berezhnov, A.V.; Abramov, A.Y. Role of inorganic polyphosphate in mammalian cells: From signal transduction and mitochondrial metabolism to cell death. *Biochem. Soc. Trans.* **2016**, *44*, 40–45. [CrossRef] [PubMed]

49. Moreira, P.I.; Carvalho, C.; Zhu, X.; Smith, M.A.; Perry, G. Mitochondrial dysfunction is a trigger of Alzheimer's disease pathophysiology. *Biochim. Biophys. Acta* **2010**, *1802*, 2–10. [CrossRef] [PubMed]

50. Weiner, S.; Mahamid, J.; Politi, Y.; Ma, Y.; Addadi, L. Overview of the amorphous precursor phase strategy in biomineralization. *Front. Mater. Sci. China* **2009**, *3*, 104–108. [CrossRef]

51. Wang, X.H.; Schröder, H.C.; Müller, W.E.G. Enzyme-based biosilica and biocalcite: Biomaterials for the future in regenerative medicine. *Trends Biotechnol.* **2014**, *32*, 441–447. [CrossRef] [PubMed]

52. Müller, W.E.G.; Neufurth, M.; Schlossmacher, U.; Schröder, H.C.; Pisignano, D.; Wang, X.H. The sponge silicatein-interacting protein silintaphin-2 blocks calcite formation of calcareous sponge spicules at the vaterite stage. *RSC Adv.* **2014**, *4*, 2577–2585. [CrossRef]

53. Butterworth, P.J. Alkaline phosphatase. Biochemistry of mammalian alkaline phosphatases. *Cell Biochem. Funct.* **1983**, *1*, 66–70. [CrossRef] [PubMed]

54. Müller, W.E.G.; Wang, X.H.; Diehl-Seifert, B.; Kropf, K.; Schloßmacher, U.; Lieberwirth, I.; Glasser, G.; Wiens, M.; Schröder, H.C. Inorganic polymeric phosphate/polyphosphate as an inducer of alkaline phosphatase and a modulator of intracellular Ca^{2+} level in osteoblasts (SaOS-2 cells) in vitro. *Acta Biomater.* **2011**, *7*, 2661–2671. [CrossRef] [PubMed]

55. Tarozzi, A.; Morroni, F.; Merlicco, A.; Bolondi, C.; Teti, G.; Falconi, M.; Cantelli-Forti, G.; Hrelia, P. Neuroprotective effects of cyanidin 3-O-glucopyranoside on amyloid beta (25–35) oligomer-induced toxicity. *Neurosci. Lett.* **2010**, *473*, 72–76. [CrossRef] [PubMed]

56. Baev, A.Y.; Negoda, A.; Abramov, A.Y. Modulation of mitochondrial ion transport by inorganic polyphosphate—Essential role in mitochondrial permeability transition pore. *J. Bioenerg. Biomembr.* **2017**, *49*, 49–55. [CrossRef] [PubMed]

57. Müller, W.E.G.; Tolba, E.; Feng, Q.; Schröder, H.C.; Markl, J.S.; Kokkinopoulou, M.; Wang, X.H. Amorphous Ca^{2+} polyphosphate nanoparticles regulate the ATP level in bone-like SaOS-2 cells. *J. Cell Sci.* **2015**, *128*, 2202–2207. [CrossRef] [PubMed]

58. Müller, W.E.G.; Wang, S.; Neufurth, M.; Kokkinopoulou, M.; Feng, Q.; Schröder, H.C.; Wang, X.H. Polyphosphate as donor of high-energy phosphate for the synthesis of ADP and ATP. *J. Cell Sci.* **2017**, *130*, 2747–2756. [CrossRef] [PubMed]

59. Kurokawa, Y.; Takenaka, H.; Sumida, M.; Oka, K.; Hamada, M.; Kuby, S.A. Multiforms of mammalian adenylate kinase and its monoclonal antibody against AK1. *Enzyme* **1990**, *43*, 57–71. [CrossRef] [PubMed]

60. Muñoz-Espí, R.; Mastai, Y.; Gross, S.; Landfester, K. Colloidal systems for crystallization processes from liquid phase. *CrystEngComm* **2013**, *15*, 2175–2191. [CrossRef]

61. Woo, Y.I.; Park, B.J.; Kim, H.L.; Lee, M.H.; Kim, J.; Yang, Y.I.; Kim, J.K.; Tsubaki, K.; Han, D.W.; Park, J.C. The biological activities of (1,3)-(1,6)-β-D-glucan and porous electrospun PLGA membranes containing β-glucan in human dermal fibroblasts and adipose tissue-derived stem cells. *Biomed. Mater.* **2010**, *5*. [CrossRef] [PubMed]

62. Hogins, J.; Crawford, D.C.; Zorumski, C.F.; Mennerick, S. Excitotoxicity triggered by Neurobasal culture medium. *PLoS ONE* **2011**, *6*, e25633. [CrossRef] [PubMed]

63. Wang, X.; Mori, T.; Sumii, T.; Lo, E.H. Hemoglobin-induced cytotoxicity in rat cerebral cortical neurons: Caspase activation and oxidative stress. *Stroke* **2002**, *33*, 1882–1888. [CrossRef] [PubMed]

64. Stanley, P.E. Extraction of adenosine triphosphate from microbial and somatic cells. *Methods Enzymol.* **1986**, *133*, 14–22. [PubMed]

65. Marcaida, G.; Miñana, M.D.; Grisolía, S.; Felipo, V. Determination of intracellular ATP in primary cultures of neurons. *Brain Res. Brain Res. Protoc.* **1997**, *1*, 75–78. [CrossRef]

66. Moriwaki, T.; Kato, S.; Kato, Y.; Hosoki, A.; Zhang-Akiyama, Q.M. Extension of lifespan and protection against oxidative stress by an antioxidant herb mixture complex (KPG-7) in *Caenorhabditis elegans*. *J. Clin. Biochem. Nutr.* **2013**, *53*, 81–88. [CrossRef] [PubMed]

67. Sylvester, P.W. Optimization of the tetrazolium dye (MTT) colorimetric assay for cellular growth and viability. *Methods Mol. Biol.* **2011**, *716*, 157–168. [PubMed]

68. Petrie, A.; Watson, P. *Statistics for Veterinary and Animal Science*; Wiley-Blackwell: Oxford, UK, 2013; pp. 85–99.

69. Granata, D.; Baftizadeh, F.; Habchi, J.; Galvagnion, C.; De Simone, A.; Camilloni, C.; Laio, A.; Vendruscolo, M. The inverted free energy landscape of an intrinsically disordered peptide by simulations and experiments. *Sci. Rep.* **2015**, *5*, 15449. [CrossRef] [PubMed]

70. Tsuruta, J.K.; Wong, K.; Fritz, I.B.; Griswold, M.D. Structural analysis of sulphated glycoprotein 2 from amino acid sequence. Relationship to clusterin and serum protein 40,40. *Biochem. J.* **1990**, *268*, 571–578. [CrossRef] [PubMed]

71. Saraiva, C.; Praça, C.; Ferreira, R.; Santos, T.; Ferreira, L.; Bernardino, L. Nanoparticle-mediated brain drug delivery: Overcoming blood-brain barrier to treat neurodegenerative diseases. *J. Control. Release* **2016**, *235*, 34–47. [CrossRef] [PubMed]

72. Grabrucker, A.M.; Ruozi, B.; Belletti, D.; Pederzoli, F.; Forni, F.; Vandelli, M.A.; Tosi, G. Nanoparticle transport across the blood brain barrier. *Tissue Barriers* **2016**, *4*, e1153568. [CrossRef] [PubMed]

73. Gowert, N.S.; Donner, L.; Chatterjee, M.; Eisele, Y.S.; Towhid, S.T.; Münzer, P.; Walker, B.; Ogorek, I.; Borst, O.; Grandoch, M.; et al. Blood platelets in the progression of Alzheimer's disease. *PLoS ONE* **2014**, *9*, e90523. [CrossRef] [PubMed]

74. Zenaro, E.; Piacentino, G.; Constantin, G. The blood-brain barrier in Alzheimer's disease. *Neurobiol. Dis.* **2017**, *107*, 41–56. [CrossRef] [PubMed]

75. Sowade, R.F.; Jahn, T.R. Seed-induced acceleration of amyloid-β mediated neurotoxicity in vivo. *Nat. Commun.* **2017**. [CrossRef] [PubMed]

Therapeutic Effect of Cilostazol Ophthalmic Nanodispersions on Retinal Dysfunction in Streptozotocin-Induced Diabetic Rats

Noriaki Nagai [1,*], Saori Deguchi [1], Hiroko Otake [1], Noriko Hiramatsu [2] and Naoki Yamamoto [2]

[1] Faculty of Pharmacy, Kindai University, 3-4-1 Kowakae, Higashi-Osaka, Osaka 577-8502, Japan; 1111610121m@kindai.ac.jp (S.D.); hotake@phar.kindai.ac.jp (H.O.)

[2] Laboratory of Molecular Biology and Histochemistry Joint Research Support Promotion Facility Center for Research Promotion and Support Fujita Health University, 1-98 Dengakugakubo, Kutsukake, Toyoake, Aichi 470-1192, Japan; norikoh@fujita-hu.ac.jp (N.H.); naokiy@fujita-hu.ac.jp (N.Y.)

* Correspondence: nagai_n@phar.kindai.ac.jp; Tel.: +81-6-4307-3638

Abstract: We previously prepared ophthalmic formulations containing cilostazol (CLZ) nanoparticles by bead mill methods (CLZ_{nano}), and found that instillation of CLZ_{nano} into rat eyes supplies CLZ into the retina. In this study, we investigated changes in the electroretinograms (ERG) of streptozotocin-induced diabetic rats (STZ rats), a model of diabetes mellitus. In addition, we demonstrated that dispersions containing CLZ nanoparticles attenuate changes in the ERG of STZ rats. The instillation of CLZ_{nano} had no effect on body weight or plasma glucose and insulin levels. Furthermore, no corneal toxicity was observed in the in vivo study using STZ rats. The a-wave and b-wave levels in addition to oscillatory potentials (OP) amplitude decreased in STZ rats two weeks after the injection of streptozotocin, with the instillation of CLZ_{nano} attenuating these decreases. In addition, the level of vascular endothelial growth factor (VEGF) in the retinas of STZ rats was 9.26-fold higher than in in normal rats, with this increase also prevented by the instillation of CLZ_{nano} Thus, we have found that a-wave and b-wave levels in addition to OP amplitude are decreased in rats following the injection of excessive streptozotocin. Furthermore, the retinal disorders associated with diabetes mellitus are attenuated by the instillation of CLZ_{nano}. These findings provide significant information that can be used to design further studies aimed at developing anti-diabetic retinopathy drugs.

Keywords: nanoparticle; cilostazol; diabetic retinopathy; electroretinogram; streptozotocin-induced diabetic rat

1. Introduction

Diabetes mellitus is a chronic disease that affects a large proportion of people worldwide. Diabetic retinopathy (DR) is one of the more common complications associated with diabetes mellitus [1–3]. DR is characterized by a progressive alteration in retinal microvasculature [1], which leads to capillary closure and areas of non-perfusion. This eventually results in retinal hypoxia. The non-perfused tissues enhance the production of vascular endothelial growth factor (VEGF) from the retina and causes a subsequent loss of vision and pathologic neovascularization [1]. Previous studies indicate that the changes in electroretinograms (ERG) were observed in the patients with diabetes, even when they have no symptoms of retinopathy [4–6]. Moreover, recent studies have found that microstructural changes in the intracranial optic nerve can be observed in the eye of early experimental diabetes before substantial morphological alterations [7–9]. In the clinical setting, the development of therapies for retinal dysfunction caused by diabetes mellitus is expected.

Cilostazol (CLZ) has antiplatelet, antithrombotic, and vasodilatory properties [10]. The main pharmacological effect of CLZ is to increase the level of intracellular cyclic AMP through the inhibition of phosphodiesterase 3A [10,11]. CLZ appears to have a favorable effect in preventing the progression of carotid atherosclerosis and intracranial arterial stenosis [12,13]. Hotta et al. [14] reported that treatment with CLZ leads to a vasodilatory effect on retinal arterioles and improved blood supply in animal models of diabetes. Therefore, the reduction in the vascular resistance and increased blood supply to the retina by CLZ may be useful for the treatment of DR.

In developing CLZ as a therapy for DR, it is important to design an ophthalmic formulation that can deliver the drug to the posterior segment. Recently, it has been reported that the formulation containing nanoparticles significantly improved the ability of drugs with regard to corneal penetration [15–20]. Furthermore, the formulation may lead an alternative strategy for enhancing ocular drug penetration [21–23]. We have also prepared the dispersions containing solid nanoparticles, which can provide high-quantity dispersions containing drug nanoparticles by a simple procedure [24–30]. Moreover, our previous reports show that dispersions containing CLZ nanoparticles prepared by a bead mill method supply CLZ into the retina through instillation, which can suppress retinal vasoconstriction in 1×10^{-5} M endothelin (ET-1)-injected rats (15 μL) [31].

In this study, we investigated changes in ERG of streptozotocin-induced diabetic rat (STZ rat), which is a model of diabetes mellitus. In addition, we studied whether dispersions containing CLZ nanoparticles can attenuate the changes in ERG of STZ rats.

2. Results

2.1. Changes in Retinal Function in STZ Rats

Figure 1 shows the changes in body weight, plasma glucose and insulin levels in STZ rats. The body weight of STZ rats was significantly lower than that of normal rats, while insulin levels were below the level of detection in STZ rat plasma. In addition, glucose levels were enhanced by the injection of streptozotocin, with the plasma glucose levels in STZ rats two weeks after the injection of streptozotocin being 2.8-fold higher than in normal rats. Figure 2 shows the changes in ERG of STZ rats. The levels of a-wave, b-wave, and oscillatory potentials (OPs) amplitude in STZ rats were lower than in normal rats. These retinal disorders were observed at 2–6 weeks after the injection of streptozotocin.
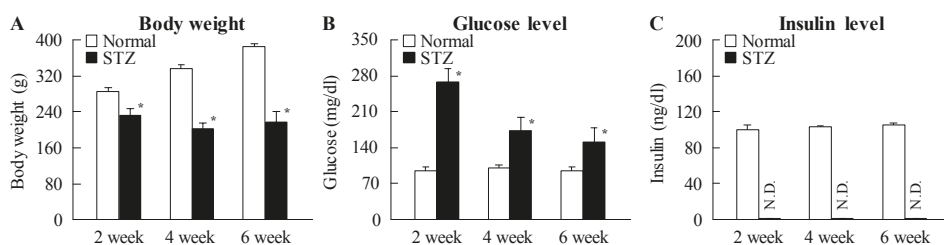

Figure 1. (**A**) Body weight; (**B**) plasma glucose; and (**C**) insulin levels in rats at two, four, and six weeks after the injection of streptozotocin. Samples were collected at 10:00 a.m. Open columns: normal rat; closed columns: streptozotocin-induced diabetic rats (STZ rats) with *n* = 6–8. N.D.: not detectable. * *p* < 0.05, vs. normal rat for each category.
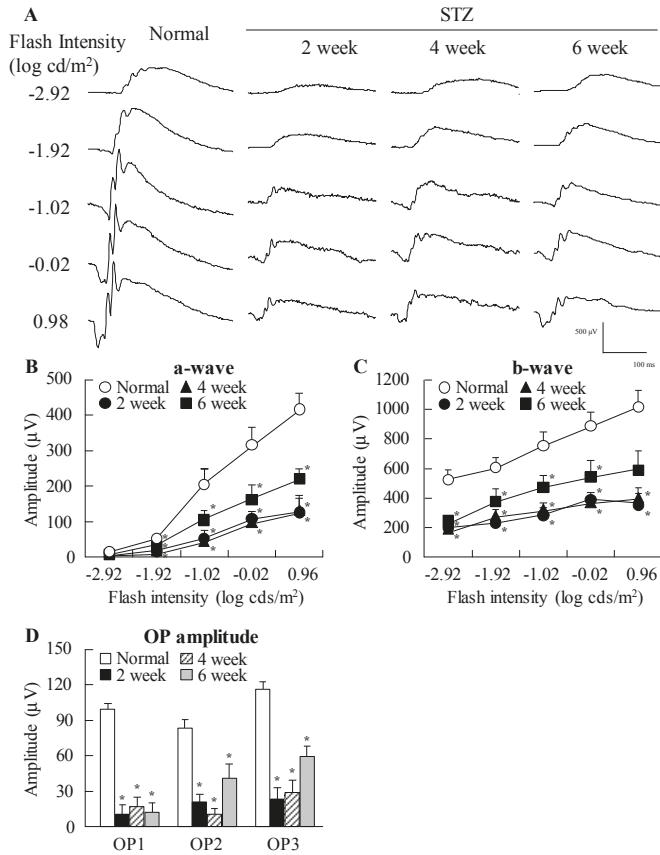
Figure 2. Typical traces of (**A**) electroretinograms (ERG); (**B**) a-wave; (**C**) b-wave; and (**D**) oscillatory potential (OP) amplitude in rat retina at two, four, and six weeks after the injection of streptozotocin. Dark-adapted ERG responses were measured at 2:00 p.m. and stimulus flashes were used from -2.92 log cds/m^2. $n = 6$–8. * $p < 0.05$, vs. normal rat for each category.

2.2. Preventive Effect of CLZ$_{nano}$ Instillation on Retinal Disorders in STZ Rats

Table 1 shows the changes in body weight in addition to plasma glucose and insulin levels in STZ rats instilled with or without CLZ$_{nano}$. The instillation of CLZ$_{nano}$ had no effect on body weight or on plasma glucose and insulin levels. Figure 3 shows the changes in CLZ levels in the blood and retina of STZ rats after the instillation of CLZ$_{nano}$. A low concentration of CLZ was found in the blood of rats after CLZ$_{nano}$ instillation, while CLZ was also detected in the left eye of instilled rats. On the other hand, the CLZ content in the right eye of rats instilled with CLZ$_{nano}$ was significantly higher than in the left eye. Figure 4A–D show the effect of CLZ$_{nano}$ instillation on ERG of STZ rats. The instillation of CLZ$_{nano}$ attenuated the decrease in the a-wave and b-wave levels, as well as in OP amplitude. Figure 4E shows the changes in VEGF in the retina of STZ rats instilled with CLZ$_{nano}$. The VEGF levels were enhanced by the injection of streptozotocin, with the VEGF levels in STZ rats being 9.26-fold that in normal rats (3.66 $\pm$ 0.48, means $\pm$ S.E., $n = 6$). The instillation of CLZ$_{nano}$ also prevented the increase in VEGF levels in STZ rats. Figure 5 shows histopathological alterations in the retina of STZ rats detected using a hematoxylin and eosin (H.E.) staining method. The distance between cells was increased in the inner plexiform layer, as well as the outer- and inner-nuclear layer (neural layer) in

retinas of STZ rats, while the distance in neural layer was normalized by the instillation of CLZ_{nano} (Figure 5). The distance between cells in the neural layer in STZ rats instilled with CLZ_{nano} was similar to that in normal rats (normal rat 74.1 ± 5.67 µm, STZ rat 116.2 ± 9.90 µm, CLZ_{nano}-instilled STZ rat 81.8 ± 7.57 µm, $n = 5$).
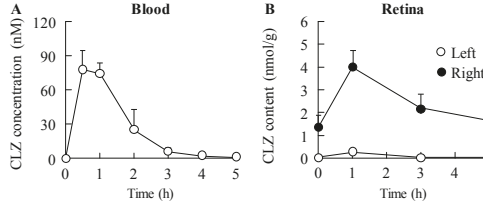
Figure 3. Cilostazol (CLZ) levels in the (**A**) blood and (**B**) retina of rats following the instillation of CLZ_{nano}. The streptozotocin was injected on two consecutive days (100 mg/kg × 2, i.p.), after that the instillation of 1% CLZ_{nano} in the right eye of STZ rats were started for two weeks (twice a day, 9:00 a.m. and 7:00 p.m.). The blood and retina were collected at 0–5 h after the last-instillation of CLZ_{nano} (9:00 a.m.–2:00 p.m.); $n = 7$; * $p < 0.05$, vs. vehicle for each category.
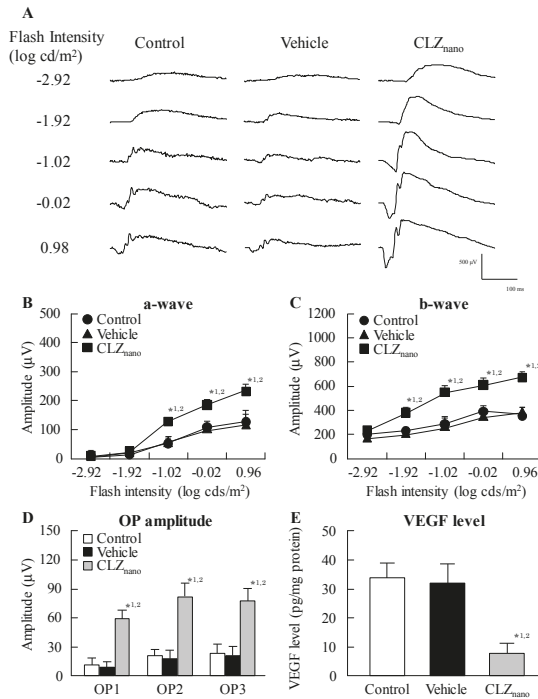
Figure 4. Typical traces of (**A**) electroretinogram (ERG), (**B**) a-wave, (**C**) b-wave, and (**D**) OP amplitude and (**E**) VEGF level in STZ rats after the instillation of CLZ_{nano}. The streptozotocin was injected on two consecutive days (100 mg/kg × 2, i.p.), after that the instillation of 1% CLZ_{nano} in the right eye of STZ rats were started for two weeks (twice a day, 9:00 a.m. and 7:00 p.m.). Dark-adapted ERG responses and vascular endothelial growth factor (VEGF) were measured at 5 h after the instillation (2:00 p.m.), and the stimulus flashes in ERG were used from −2.92 log cds/m². Control: non-instilled STZ rat; Vehicle: vehicle-instilled STZ rats; CLZ_{nano} = CLZ_{nano}-instilled STZ rats. $n = 5–7$; [*1] $p < 0.05$, vs. control for each category; [*2] $p < 0.05$, vs. vehicle for each category.

Table 1. Body weight and plasma glucose and insulin levels in STZ rats after the instillation of ophthalmic formulations containing cilostazol nanoparticles (CLZ_{nano}).

Treatment	Body Weight (g)	Glucose (mg/dL)	Insulin (ng/dL)
Vehicle	301.1 ± 8.68	273.2 ± 30.7	N.D.
CLZ_{nano}	299.5 ± 9.10	269.7 ± 29.8	N.D.

One percent CLZ_{nano} was instilled into the right eyes of STZ rats twice a day (9:00 a.m. and 7:00 p.m.) for two weeks. The samples were collected 1 h after the instillation (10:00 a.m.), $n = 7$, and N.D.: not detectable.
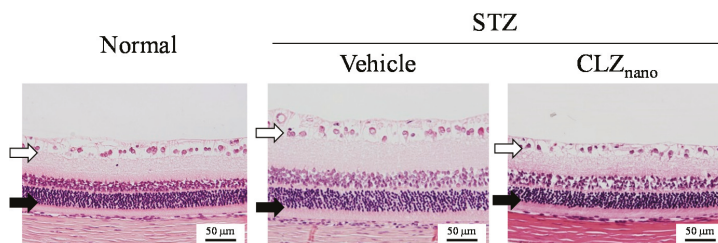
Figure 5. Hematoxylin and eosin (H.E.) staining of retina in normal and STZ rats. The streptozotocin was injected on two consecutive days (100 mg/kg × 2, i.p.), after that the instillation of 1% CLZ_{nano} in the right eye of STZ rats were started for two weeks (twice a day, 9:00 a.m. and 7:00 p.m.). Bars indicate 50 μm. Open arrows: retinal ganglion cells; Normal: normal rat; Vehicle: vehicle-instilled STZ rats; CLZ_{nano}: CLZ_{nano}-instilled STZ rats; and closed arrows: outer granule layer.

2.3. Corneal Stimulation by CLZ_{nano} Instillation

Figure 6 shows the effect of CLZ_{nano} instillation on the viability of HCE-T cells. The viability of non-treated human corneal epithelial cell line (HCE cells, the cells' viability without anything added, including both CLZ and vehicle) did not differ for 0–120 s, and there were no significant differences in viability between vehicle- and CLZ_{nano}-treated cells. In addition, the corneal stimulation was also evaluated using an STZ rat instilled with CLZ_{nano} for six weeks. Neither the vehicle nor CLZ_{nano} induced corneal epithelium damage (in vivo study).
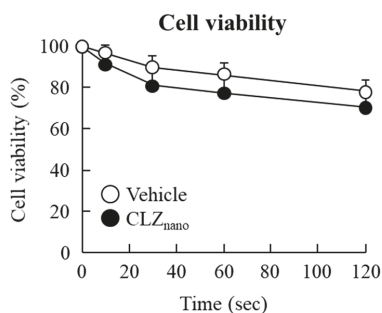
Figure 6. Corneal toxicity of CLZ_{nano} in a human corneal epithelial cell line (HCE-T cells). HCE-T cells in 96-well microplates were treated with vehicle or CLZ_{nano} for 0–120 s and the cell viability was calculated using Tetra-Color One. Vehicle: vehicle-treated HCE-T cells; CLZ_{nano}: CLZ_{nano}-treated HCE-T cells, $n = 9$.

3. Discussion

We previously designed novel ophthalmic formulations containing CLZ nanoparticles (CLZ$_{nano}$), and found that CLZ$_{nano}$ instillation can deliver CLZ into the retina [31]. In this study, we demonstrate the therapeutic effects of CLZ$_{nano}$ on retinal disorders caused by diabetes mellitus in STZ rats.

In both patient and animal models of diabetes, there is a loss of retinal neurons early in the disease progression [32], with this neuronal dysfunction being reflected in alterations in the ERG [33,34]. Moreover, patients with diabetes show altered visually-evoked potentials or ERG even when there is no observed retinopathy [4–6]. First, we investigated the changes in retinal function in rats after the injection of streptozotocin by measuring ERG. We show that the a-wave and b-wave levels in addition to the OP amplitude are decreased in rats two weeks after the injection of streptozotocin (Figure 2). There are some previous reports related to measuring the ERG of STZ rats. Li et al. [35] reported that the a-wave and b-wave amplitudes in STZ rats decreased two weeks after the injection of 60 mg/kg streptozotocin. On the other hand, Kohzaki et al. [36] showed that a-wave and b-wave responses were not significantly reduced while OPs were significantly reduced at eight weeks after the injection of 50 mg/kg streptozotocin. Thus, the onset of retinal dysfunction in STZ rats differs depending on the amount of streptozotocin injected and the data suggest that the difference is caused by the severity of diabetes mellitus via the injection of streptozotocin. In this study, plasma insulin was undetectable, while the plasma glucose levels in rats fasted for 12 h was high (STZ rat at two weeks after streptozotocin, 267.6 mg/dL). These results show that the severity of diabetes mellitus in our STZ rats was higher than in previous reports [35,36]. Early changes in ERG may determine the severity of diabetes mellitus via a high-dose injection of streptozotocin (100 mg/kg × 2). It is known that a-waves reflect the function of photoreceptors, b-waves reflect bipolar cell and Müller cell function and OPs are dependent on the hemodynamics in the central retinal artery. Taken together, our findings suggest that the retinas in STZ rats are injured and the retinal dysfunction arose at about two weeks after the injection of streptozotocin.

In treating the posterior segments, it is important to improve the effectiveness of ocular drugs by enhancing their bioavailability [37]. We previously designed a novel ophthalmic formulation called CLZ$_{nano}$ and reported that the state of the CLZ$_{nano}$ does not affect the antimicrobial activity of benzalkonium chloride against *Escherichia coli*. In addition, the instillation of the CLZ$_{nano}$ can deliver CLZ in a therapeutic range into the retina [31] where it suppresses retinal vasoconstriction in 1×10^{-5} M ET-1-injected rats (15 μL) [31]. The CLZ$_{nano}$ may lead to their new usage as therapies in the ophthalmologic field. Therefore, we demonstrated the therapeutic effect of CLZ$_{nano}$ instillation on retinal dysfunction in STZ rats. The instillation of CLZ$_{nano}$ had no effect on body weight or on plasma glucose or insulin levels (Table 1). Furthermore, no corneal toxicity was observed in the in vitro and in vivo studies using HCE-T cells or STZ rats (Figure 6). On the other hand, the CLZ content in the retina of the right eye (with instillation) was significantly higher than that of the left eye (without instillation) in rats instilled with CLZ$_{nano}$ (Figure 3). These results support our previous study and it was suggested the C_{max} in 1% CLZ$_{nano}$ instillation did not show any systemic effects, such as changes in blood pressure and flow in the carotid artery [38]. Following this, we measured the changes in ERG for STZ rats instilled with CLZ$_{nano}$. The instillation of CLZ$_{nano}$ attenuated the decrease in the levels of the a-wave and b-wave, as well as the OP amplitude in STZ rats (Figure 4). This shows that the instillation of CLZ$_{nano}$ may be useful as a therapy for retinal dysfunction via hyperglycemia.

The measurement of factors associated with the onset of DR in STZ rats, instilled with or without CLZ$_{nano}$, is important with regard to certifying the therapeutic effect. The Müller cells of the retina are activated and upregulate proangiogenic and vascular permeability factors, such as VEGF [39,40], at the onset of DR via retinal hypoxia. These VEGFs contribute to the development of clinical symptoms of retinopathy. In addition, many recent studies have identified the central role of VEGF as a main focus for developing treatments for the vascular lesions observed in DR. Blocking the action of VEGF is a main focus for developing a treatment for this debilitating disease. Therefore, we investigated changes in VEGF levels in the retinas of STZ rats instilled with or without CLZ$_{nano}$. We found that VEGF levels

in the retinas of rats are enhanced by the injection of streptozotocin, with the instillation of CLZ$_{nano}$ found to suppress these enhanced VEGF levels in STZ rats (Figure 4E). In addition, we previously reported that retinal hypoxia increases the distance between cells in the inner plexiform layer, the outer- and inner- nuclear layers (neural layer) in the retinas of STZ rats. The enhanced retinal thickening caused by the injection of excessive STZ may lead to retinal dysfunction, resulting in a decrease in ERG [41]. The enhanced retinal thickening was also reversed by the instillation of CLZ$_{nano}$ (Figure 5). These results show that CLZ$_{nano}$ may prevent retinal hypoxia through vasodilatory effects, resulting in a decrease in VEGF production and reversal of the changes in ERG and retinal thickening.

Further studies are needed to determine the mechanism for the ERG and histopathological alterations of rats injected with high-dose streptozotocin. In addition, it is important to clarify the precise mechanism for the preventive effect of CLZ$_{nano}$ on retinal dysfunction. Therefore, we are now investigating the effect of CLZ$_{nano}$ on retinal blood flow in STZ rats using laser Doppler velocimetry and will demonstrate the changes in cyclic adenosine 3′,5′-monophosphate (cAMP) levels in retina after the instillation of CLZ$_{nano}$. On the other hand, the enhanced retinal thickening was not observed in a lower-dose STZ model or a genetic model of diabetic retinopathy, and thus reversal effects of CLZ$_{nano}$ may not necessarily work on diabetic complications. Therefore, it is also important to investigate the effect of CLZ$_{nano}$ on retinal disorders in the genetic model of diabetic retinopathy in future study.

4. Materials and Methods

4.1. Reagents and Animals

Original CLZ (powder type) and methylcellulose (MC) were kindly donated by Otsuka Pharmaceutical Co., Ltd. (Tokyo, Japan) and Shin-Etsu Chemical Co., Ltd. (Tokyo, Japan), respectively. All other chemicals used were purchased and of the highest purity commercially available. Male Wistar rats (normal rat) were obtained from Kiwa Laboratory Animals Co., Ltd. (Wakayama, Japan). Diabetes mellitus was induced in 6-week old Wistar rats by injecting them with streptozotocin on two consecutive days (100 mg/kg × 2, i.p., STZ rat) and housing them for 0–6 weeks under standard conditions (7:00 a.m.–7:00 p.m. (fluorescent light), 25 °C). All procedures were performed in accordance with the Association for Research in Vision and Ophthalmology resolution on the use of animals in research and the Kindai University Faculty of Pharmacy Committee Guidelines for the Care and Use of Laboratory Animals (identification code: KAPS-25-003, From 1 May 2013).

4.2. Preparation of Ophthalmic CLZ Nanodispersions

CLZ solid nanodispersions were prepared using zirconia balls, Pulverisette 7 (a planetary ball mill, Fritsch Japan Co., Ltd., Tokyo, Japan) and Bead Smash 12 (a bead mill, Wakenyaku Co. Ltd., Kyoto, Japan) according to our previous study [31]. CLZ powder, 2-hydroxypropyl-β-cyclodextrin (HPβCD, Nihon Shokuhin Kako Co., Ltd., Tokyo, Japan), benzalkonium chloride (BAC, Kanto Chemical Co., Inc., Tokyo, Japan), mannitol (D-mannitol, Wako Pure Chemical Industries, Ltd., Osaka, Japan) and MC were used to prepare the CLZ nanoparticles. The compositions of the dispersions containing CLZ solid nanoparticles (CLZ$_{nano}$) were as follows: 1% CLZ, 0.001% BAC, 0.1% mannitol, 1% MC, and 5% HPβCD (a pH of 6.5). The solubility of CLZ in saline containing 0.001% BAC, 0.1% mannitol, 1% MC and 5% HPβCD was 0.037% (the solubility of CLZ in saline is 0.0005%). The vehicle in this study used a solution containing these various additives (0.001% BAC, 0.1% mannitol, 1% MC and 5% HPβCD), while the concentration of CLZ used in this study was detected according to our previous study [31]. In the course of preparation, the solvent containing additives was filtered through a Minisart CE (pore size of 0.20 μm, Costar, Cambridge, MA, USA) under aseptic conditions. Images and particle sizes were obtained using an SPM-9700 scanning probe microscope (Shimadzu Corp., Kyoto, Japan) and a SALD-7100 nanoparticle size analyzer (Shimadzu Corp., Kyoto, Japan; refractive index 1.60–0.10 imaginary unit), respectively (Figure 7).
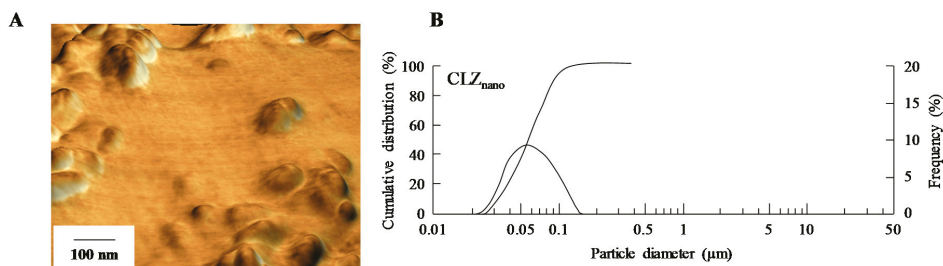
Figure 7. (**A**) Image, in addition to (**B**) the cumulative size distribution and frequency of 1% CLZ_{nano}. The image of CLZ_{nano} was obtained on an SPM-9700 and particle size was determined using a SALD-7100 nanoparticle size analyzer (refractive index 1.60–0.10 imaginary unit). Dashed line: the cumulative size distribution; solid line: the cumulative size frequency and mean particle size of CLZ_{nano} is 59 nm.

4.3. Measurement of CLZ by HPLC

CLZ levels in the samples were determined according to our previous report using a Shimadzu LC-20AT system [31]. Benzophenone was selected as the internal standard, while an Inertsil® ODS-3 column (GL Science Co., Inc., Tokyo, Japan) was used. The mobile phase consisted of acetonitrile/methanol/water (35/15/50, $v/v/v$) at a flow rate of 0.25 mL/min, the column temperature was 35 °C and the wavelength for detection was 254 nm. The peak of CLZ was detected at 3.7 min (retention time).

4.4. Measurement of Plasma Glucose and Insulin

Glucose and insulin (parameters for diabetes mellitus) were measured for normal and STZ rats according to our previous methods [42]. Blood was taken without anesthesia from the tail vein of each rat fasted for 12 h (10:00 a.m.). The plasma glucose and insulin levels were measured by an Accutrend GCT (Roche Diagnostics, Mannheim, Germany) and an ELISA Insulin Kit (Morinaga Institute of Biological Science Inc., Kanagawa, Japan), respectively.

4.5. Measurement of CLZ Content in Blood and Retina

Thirty microliters of 1% CLZ_{nano} was instilled into the right eye of the STZ rats twice a day (9:00 a.m. and 7:00 p.m.), before the blood and retina were collected at 0–5 h after the morning instillation (9:00 a.m.–2:00 p.m.). The samples were homogenized in methanol on ice and centrifuged at 10,000 rpm for 15 min at 4 °C. CLZ in the supernatant was analyzed by the HPLC method described above.

4.6. Measurement of VEGF

Retinas were collected (2:00 p.m.) and homogenized in 50 mM of Tris buffer on ice, before being centrifuged at 15,000 rpm for 20 min at 4 °C. The supernatants were used for the measurement of VEGF using a rat VEGF immunoassay Quantikine ELISA kit according to the manufacturer's instructions (R and D Systems, Inc., Minneapolis, MN, USA). VEGF levels are expressed as pg/mg protein. Protein levels in the samples used to determine the VEGF levels were assessed using a Bio-Rad Protein Assay Kit (Bio-Rad Laboratories, Hercules, CA, USA).

4.7. Measurement of ERG

ERG readings were recorded by PuREC (Mayo, Aichi, Japan) zero, two, four, and six weeks after the injection of streptozotocin. The rats were maintained in a completely dark room for 24 h, after which they were anesthetized with isoflurane. The pupils were dilated with 0.5% tropicamide

and 0.5% phenylephrine (Santen, Osaka, Japan). Flash ERG was recorded in the right eyes of the dark-adapted rats by placing a golden-ring electrode (Mayo, Aichi, Japan) in contact with the cornea and a reference electrode (Mayo, Aichi, Japan) through the tongue. A neutral electrode (Mayo, Aichi, Japan) was inserted subcutaneously near the tail. All procedures were performed under dim red light. The amplitude of the a-wave was measured from the baseline to the maximum a-wave peak, while the b-wave was measured from the maximum a-wave peak to the maximum b-wave peak. The a-wave shows the function of the photoreceptors, while the b-wave reflects bipolar cell and Müller cell function. To analyze the oscillatory potentials (OPs), the OP amplitudes were measured in the time between the a- and b-wave peaks. The relevant factors were OP number (OP1, OP2, and OP3) and flash intensity (0.98 (log cds/m^2)). OPs were isolated by the band pass filter and OP amplitudes were measured using ERG with all frequencies (0.3–500 Hz). The OPs were dependent on the hemodynamics in the central retinal artery.

4.8. Morphology of Rat Retina

Whole rat eyes were fixed in SUPER FIX™ rapid fixative solution (Kurabo Industries, Osaka, Japan) and 3-μm paraffin sections were prepared from the fixed whole rat eyeballs in the usual manner [43]. The rat retinal tissue was observed in detail by hematoxylin and eosin (H.E.) staining. A microscope (Power BX-51, Olympus, Tokyo, Japan) was used for observation. The distance from the retinal ganglion cell to the outer granule layer (neural layer: inner plexiform layer, outer- and inner-nuclear (granule) layer) was calculated using Image J (NIH, MD, USA). The photographed area has a position of about 4–5 o'clock or 7–8 o'clock when the center of the cornea is at the 12 o'clock position in the sagittal section of the eyeball at approximately the middle part of the optic nerve and the peripheral part of the retinal nerve.

4.9. Measurement of In Vitro Corneal Epithelial Stimulation by CLZ$_{nano}$

The experiment was performed according to our previous study using the immortalized human corneal epithelial cell line, HCE-T [27]. HCE-T cells (1×10^4 cells) were seeded in 96-well microplates (IWAKI, Chiba, Japan) and one day after seeding, the cell cultures were stimulated by 1% CLZ$_{nano}$ for 0–120 s. The time was determined according to a previous report as the components of eye drops are excreted though the nasolacrimal duct into the mouth at approximately 120 s after instillation [44]. Following stimulation, a culture medium containing TetraColor One (SEIKAGAKU Co., Tokyo, Japan) was added and incubated for 1 h. After that, the absorbance (Abs) at 490 nm was measured and cell viability was calculated according to the manufacturer's instructions, as represented by Equation (1):

$$\text{Cell viability (\%)} = \text{Abs}_{\text{treatment for each group}} / \text{Abs}_{\text{non-treatment for each group}} \times 100 \tag{1}$$

The wash-off and medium change was done in the non-treatment groups, and the Abs in non-treatment groups were similar.

4.10. Measurement of In Vivo Corneal Toxicity by CLZ$_{nano}$

Thirty microliters of 1% CLZ$_{nano}$ was instilled into the right eyes of STZ rats twice a day (9:00 a.m. and 7:00 p.m.) for six weeks (repetitive instillation). The eyes were kept open for about 1 min after instillation to prevent the 1% CLZ$_{nano}$ from being washed out. The wound area (corneal epithelial damage) was stained with 1% fluorescein (Alcon Japan, Tokyo, Japan) and measured using a TRC-50X fundus camera (Topcon, Tokyo, Japan) equipped with a digital camera (the instillation of fluorescein can stain the corneal epithelium damage). The image was obtained 5 h after the instillation (2:00 p.m.).

4.11. Statistical Analysis

Unpaired Student's *t*-test, Aspin-Welch's *t*-test or Dunnett's multiple comparison was used, with $p < 0.05$ considered significant. All data are expressed as means ± S.E.

5. Conclusions

We found that a-wave and b-wave levels, in addition to OP amplitude, were decreased in rats following the injection of excessive streptozotocin, while retinal disorders associated with diabetes mellitus were attenuated by the instillation of CLZ_{nano}. These findings provide significant information that can be used to design further studies aimed at developing anti-diabetic retinopathy drugs.

Author Contributions: Noriaki Nagai created the concept and design of the study, and wrote the manuscript; Saori Deguchi performed the experiments for ERG and analyzed the data; Hiroko Otake performed the experiments for preparation of nanoparticles; and Noriko Hiramatsu and Naoki Yamamoto performed the experiments for H.E. staining. All authors significantly contributed to the conception and design of the study, and to the interpretation of the data.

Conflicts of Interest: The authors report no conflicts of interest.

Abbreviations

Abs	Absorbance
BAC	Benzalkonium Chloride
CLZ	Cilostazol
DR	Diabetic Retinopathy
ERG	Electroretinogram
ET	Endotheline
HCE-T	Human Corneal Epithelial Cell Line
H.E.	Hematoxylin and Eosin
HPβCD	2-Hydroxypropyl-β-Cyclodextrin
OPs	Oscillatory Potentials
MC	Methylcellulose
STZ rat	Streptozotocin-Induced Diabetic Rat
VEGF	Vascular Endothelial Growth Factor

References

1. Miller, J.W.; Adamis, A.P.; Aiello, L.P. Vascular endothelial growth factor in ocular neovascularization and proliferative diabetic retinopathy. *Diabetes Metab. Rev.* **1997**, *13*, 37–50. [CrossRef]
2. Cheung, N.; Wong, T.Y. Diabetic retinopathy and systemic vascular complications. *Prog. Retin. Eye Res.* **2008**, *27*, 161–176. [CrossRef] [PubMed]
3. Cheung, N.; Mitchell, P.; Wong, T.Y. Diabetic retinopathy. *Lancet* **2010**, *376*, 124–136. [CrossRef]
4. Trick, G.L.; Burde, R.M.; Gordon, M.O.; Kilo, C.; Santiago, J.V. Retinocortical conduction time in diabetics with abnormal pattern reversal electroretinograms and visual evoked potentials. *Doc. Ophthalmol.* **1988**, *70*, 19–28. [CrossRef] [PubMed]
5. Wolff, B.E.; Bearse, M.A., Jr.; Schneck, M.E.; Barez, S.; Adams, A.J. Multifocal VEP (mfVEP) reveals abnormal neuronal delays in diabetes. *Doc. Ophthalmol.* **2010**, *121*, 189–196. [CrossRef] [PubMed]
6. Falsini, B.; Porciatti, V.; Scalia, G.; Caputo, S.; Minnella, A.; di Leo, M.A.; Ghirlanda, G. Steady-state pattern electroretinogram in insulin-dependent diabetics with no or minimal retinopathy. *Doc. Ophthalmol.* **1989**, *73*, 193–200. [CrossRef] [PubMed]
7. Dorfman, D.; Aranda, M.L.; Rosenstein, R.E. Enriched environment protects the optic nerve from early diabetes-induced damage in adult rats. *PLoS ONE* **2015**, *10*, e0136637. [CrossRef] [PubMed]
8. Fernandez, D.C.; Pasquini, L.A.; Dorfman, D.; Aldana Marcos, H.J.; Rosenstein, R.E. Early distal axonopathy of the visual pathway in experimental diabetes. *Am. J. Pathol.* **2012**, *180*, 303–313. [CrossRef] [PubMed]
9. Fernandez, D.C.; Pasquini, L.A.; Dorfman, D.; Aldana Marcos, H.J.; Rosenstein, R.E. Ischemic conditioning protects from axoglial alterations of the optic pathway induced by experimental diabetes in rats. *PLoS ONE* **2012**, *7*, e51966. [CrossRef] [PubMed]

10. Chapman, T.M.; Goa, K.L. Cilostazol: A review of its use in intermittent claudication. *Am. J. Cardiovasc. Drugs* **2003**, *3*, 117–138. [CrossRef] [PubMed]

11. Tanaka, K.; Gotoh, F.; Fukuuchi, Y.; Amano, T.; Uematsu, D.; Kawamura, J.; Yamawaki, T.; Itoh, N.; Obara, K.; Muramatsu, K. Effects of a selective inhibitor of cyclic AMP phosphodiesterase on the pial microcirculation in feline cerebral ischemia. *Stroke* **1989**, *20*, 668–673. [CrossRef] [PubMed]

12. Kwon, S.U.; Cho, Y.J.; Koo, J.S.; Bae, H.J.; Lee, Y.S.; Hong, K.S.; Lee, J.H.; Kim, J.S. Cilostazol prevents the progression of the symptomatic intracranial arterial stenosis: The multicenter double-blind placebo-controlled trial of cilostazol in symptomatic intracranial arterial stenosis. *Stroke* **2005**, *36*, 782–786. [CrossRef] [PubMed]

13. Katakami, N.; Kim, Y.S.; Kawamori, R.; Yamasaki, Y. The phosphodiesterase inhibitor cilostazol induces regression of carotid atherosclerosis in subjects with type 2 diabetes mellitus. *Circulation* **2010**, *121*, 2584–2591. [CrossRef] [PubMed]

14. Hotta, H.; Ito, H.; Kagitani, F.; Sato, A. Cilostazol, a selective cAMP phosphodiesterase inhibitor, dilates retinal arterioles and increases retinal and choroidal blood flow in rats. *Eur. J. Pharmacol.* **1998**, *344*, 49–52. [CrossRef]

15. Asasutjarit, R.; Thanasanchokpibull, S.; Fuongfuchat, A.; Veeranodha, S. Optimization and evaluation of thermoresponsive diclofenac sodium ophthalmic in situ gels. *Int. J. Pharm.* **2011**, *411*, 128–135. [CrossRef] [PubMed]

16. Rafie, F.; Javadzadeh, Y.; Javadzadeh, A.R.; Ghavidel, L.A.; Jafari, B.; Moogooee, M.; Davaran, S. In vivo evaluation of novel nanoparticles containing dexa-methasone for ocular drug delivery on rabbit eye. *Curr. Eye Res.* **2010**, *35*, 1081–1089. [CrossRef] [PubMed]

17. Diebold, Y.; Jarrín, M.; Sáez, V.; Carvalho, E.L.; Orea, M.; Calonge, M.; Seijo, B.; Alonso, M.J. Ocular drug delivery by liposome-chitosan nanoparticle complexes (LCS-NP). *Biomaterials* **2007**, *28*, 1553–1564. [CrossRef] [PubMed]

18. Zhou, H.Y.; Hao, J.L.; Wang, S.; Zheng, Y.; Zhang, W.S. Nanoparticles in the ocular drug delivery. *Int. J. Ophthalmol.* **2013**, *6*, 390–396. [PubMed]

19. Rahul, M.; Mohita, U.; Sanat, M. Design considerations for chemotherapeutic drug nanocarriers. *Pharm. Anal. Acta* **2014**, *5*, 279.

20. Gupta, H.; Aqil, M.; Khar, R.K.; Ali, A.; Bhatnagar, A.; Mittal, G. Biodegradable levofloxacin nanoparticles for sustained ocular drug delivery. *J. Drug Target* **2011**, *19*, 409–417. [CrossRef] [PubMed]

21. Tomoda, K.; Watanabe, A.; Suzuki, K.; Inagi, T.; Terada, H.; Makino, K. Enhanced transdermal permeability of estradiol using combination of PLGA nanoparticles system and iontophoresis. *Colloids Surf. B Biointerfaces* **2012**, *97*, 84–89. [CrossRef] [PubMed]

22. Tomoda, K.; Terashima, H.; Suzuki, K.; Inagi, T.; Terada, H.; Makino, K. Enhanced transdermal delivery of indomethacin-loaded PLGA nanoparticles by iontophoresis. *Colloids Surf. B Biointerfaces* **2011**, *88*, 706–710. [CrossRef] [PubMed]

23. Tomoda, K.; Terashima, H.; Suzuki, K.; Inagi, T.; Terada, H.; Makino, K. Enhanced transdermal delivery of indomethacin using combination of PLGA nanoparticles and iontophoresis in vivo. *Colloids Surf. B Biointerfaces* **2012**, *92*, 50–54. [CrossRef] [PubMed]

24. Nagai, N.; Ito, Y. Effect of solid nanoparticle of indomethacin on therapy for rheumatoid arthritis in adjuvant-induced arthritis rat. *Biol. Pharm. Bull.* **2014**, *37*, 1109–1118. [CrossRef] [PubMed]

25. Nagai, N.; Ito, Y. A new preparation method for ophthalmic drug nanoparticles. *Pharm. Anal. Acta* **2014**, *5*, 6.

26. Nagai, N.; Ono, H.; Hashino, M.; Ito, Y.; Okamoto, N.; Shimomura, Y. Improved corneal toxicity and permeability of tranilast by the preparation of ophthalmic formulations containing its nanoparticles. *J. Oleo Sci.* **2014**, *63*, 177–186. [CrossRef] [PubMed]

27. Nagai, N.; Ito, Y.; Okamoto, N.; Shimomura, Y. A nanoparticle formulation reduces the corneal toxicity of indomethacin eye drops and enhances its corneal permeability. *Toxicology* **2014**, *319*, 53–62. [CrossRef] [PubMed]

28. Nagai, N.; Ito, Y. Therapeutic effects of gel ointments containing tranilast nanoparticles on paw edema in adjuvant-induced arthritis rats. *Biol. Pharm. Bull.* **2014**, *37*, 96–104. [CrossRef] [PubMed]

29. Nagai, N.; Yoshioka, C.; Mano, Y.; Tanabe, W.; Ito, Y.; Okamoto, N.; Shimomura, Y. A nanoparticle formulation of disulfiram prolongs corneal residence time of the drug and reduces intraocular pressure. *Exp. Eye Res.* **2015**, *132*, 115–123. [CrossRef] [PubMed]

30. Nagai, N.; Yoshioka, C.; Ito, Y. Topical Therapies for rheumatoid arthritis by gel ointments containing indomethacin nanoparticles in adjuvant-induced arthritis rat. *J. Oleo Sci.* **2015**, *64*, 337–346. [CrossRef] [PubMed]

31. Nagai, N.; Yoshioka, C.; Tanabe, W.; Tanino, T.; Ito, Y.; Okamoto, N.; Shimomura, Y. Effects of ophthalmic formulations containing cilostazol nanoparticles on retinal vasoconstriction in rats injected with endothelin-1. *Pharm. Anal. Acta* **2015**, *6*, 4.

32. Barber, A.J.; Lieth, E.; Khin, S.A.; Antonetti, D.A.; Buchanan, A.G.; Gardner, T.W. Neural apoptosis in the retina during experimental and human diabetes. Early onset and effect of insulin. *J. Clin. Investig.* **1998**, *102*, 783–791. [CrossRef] [PubMed]

33. Lecleire-Collet, A.; Audo, I.; Aout, M.; Girmens, J.F.; Sofroni, R.; Erginay, A.; Gargasson, J.F.; Mohand-Saïd, S.; Meas, T.; Guillausseau, P.J.; et al. Evaluation of retinal function and flicker light-induced retinal vascular response in normotensive patients with diabetes without retinopathy. *Investig. Ophthalmol. Vis. Sci.* **2011**, *52*, 2861–2867. [CrossRef] [PubMed]

34. Hancock, H.A.; Kraft, T.W. Oscillatory potential analysis and ERGs of normal and diabetic rats. *Investig. Ophthalmol. Vis. Sci.* **2004**, *45*, 1002–1008. [CrossRef]

35. Li, Q.; Zemel, E.; Miller, B.; Perlman, I. Early retinal damage in experimental diabetes: Electroretinographical and morphological observations. *Exp. Eye Res.* **2002**, *74*, 615–625. [CrossRef] [PubMed]

36. Kohzaki, K.; Vingrys, A.J.; Bui, B.V. Early inner retinal dysfunction in streptozotocin-induced diabetic rats. *Investig. Ophthalmol. Vis. Sci.* **2008**, *49*, 3595–3604. [CrossRef] [PubMed]

37. Ammar, H.O.; Salama, H.A.; Ghorab, M.; Mahmoud, A.A. Nanoemulsions as potential ophthalmic delivery systems for orzolamide hydrochloride. *Pharm. Sci. Tech.* **2009**, *10*, 808–819. [CrossRef] [PubMed]

38. Nagai, N.; Yoshioka, C.; Ito, Y.; Funakami, Y.; Nishikawa, H.; Kawabata, A. Intravenous administration of cilostazol nanoparticles ameliorates acute ischemic stroke in a cerebral ischemia/reperfusion-induced injury model. *Int. J. Mol. Sci.* **2015**, *16*, 29329–29344. [CrossRef] [PubMed]

39. Fletcher, E.L.; Phipps, J.A.; Wilkinson-Berka, J.L. Dysfunction of retinal neurons and glia during diabetes. *Clin. Exp. Optom.* **2005**, *88*, 132–145. [CrossRef] [PubMed]

40. Amin, R.H.; Frank, R.N.; Kennedy, A.; Eliott, D.; Puklin, J.E.; Abrams, G.W. Vascular endothelial growth factor is present in glial cells of the retina and optic nerve of human subjects with nonproliferative diabetic retinopathy. *Investig. Ophthalmol. Vis. Sci.* **1997**, *38*, 36–47.

41. Hiramatsu, N.; Deguchi, S.; Yoshioka, C.; Otake, H.; Yamamoto, N.; Nagai, N. Evaluation of retinal function in streptozotocin-induced diabetic rats by using the electroretinography and immunohistochemistry methods. *Yakugaku Zasshi* **2017**, in press. [CrossRef] [PubMed]

42. Nagai, N.; Ito, Y.; Sasaki, S. Hyperglycemia enhances the production of amyloid β1–42 in the lenses of otsuka long-evans tokushima fatty rats, a model of human type 2 diabetes. *Investig. Ophthalmol. Vis. Sci.* **2016**, *57*, 1408–1417. [CrossRef] [PubMed]

43. Yamamoto, N.; Majima, K.; Marunouchi, T. A study of the proliferating activity in lens epithelium and the identification of tissue-type stem cells. *Med. Mol. Morphol.* **2008**, *41*, 83–91. [CrossRef] [PubMed]

44. Goto, H.; Yamada, M.; Yoshikawa, K.; Iino, M. *Presented at the Ganka-Kaigyoui notameno Gimon·nanmon Kaiketusaku*; Shindan to Chiryosha Co.: Tokyo, Japan, 2006; pp. 216–217. (In Japanese)

Article

Copper-Free *'Click'* Chemistry-Based Synthesis and Characterization of Carbonic Anhydrase-IX Anchored Albumin-Paclitaxel Nanoparticles for Targeting Tumor Hypoxia

Katyayani Tatiparti [1,†]**, Samaresh Sau** [1,*,†]**, Kaustubh A. Gawde** [1] **and Arun K. Iyer** [1,2,*]

[1] Use-Inspired Biomaterials & Integrated Nano Delivery (U-BiND) Systems Laboratory, Department of Pharmaceutical Sciences, Eugene Applebaum College of Pharmacy and Health Sciences, Wayne State University, Detroit, MI 48201, USA; katyayani.tatiparti@wayne.edu (K.T.); kaustubhagawde@gmail.com (K.A.G.)

[2] Molecular Imaging Program, Barbara Ann Karmanos Cancer Institute, Wayne State University School of Medicine, Detroit, MI 48201, USA

* Correspondence: samaresh.sau@wayne.edu (S.S.); arun.iyer@wayne.edu (A.K.I.); Tel.: +1-313-577-3220 (S.S.); +1-313-577-5875 (A.K.I.)

† These authors contributed equally to this work.

Abstract: Triple negative breast cancer (TNBC) is a difficult to treat disease due to the absence of the three unique receptors estrogen, progesterone and herceptin-2 (HER-2). To improve the current therapy and overcome the resistance of TNBC, there is unmet need to develop an effective targeted therapy. In this regard, one of the logical and economical approaches is to develop a tumor hypoxia-targeting drug formulation platform for selective delivery of payload to the drug-resistant and invasive cell population of TNBC tumors. Toward this, we developed a Carbonic Anhydrase IX (CA IX) receptor targeting human serum albumin (HSA) carriers to deliver the potent anticancer drug, Paclitaxel (PTX). We used Acetazolamide (ATZ), a small molecule ligand of CA IX to selectively deliver HSA-PTX in TNBC cells. A novel method of synthesis involving copper free '*click*' chemistry (Dibenzocyclooctyl, DBCO) moiety with an azide-labeled reaction partner, known as Strain-Promoted Alkyne Azide Cycloaddition (SPAAC) along with a desolvation method for PTX loading were used in the present study to arrive at the CA IX selective nano-carriers, HSA-PTX-ATZ. The anticancer effect of HSA-PTX-ATZ is higher compared to HSA, PTX and non-targeted HSA-PTX in MDA-MB-231 and MDA-MB-468 cells. The cell killing effect is associated with induction of early and late phases of apoptosis. Overall, our proof-of-concept study shows a promising avenue for hypoxia-targeted drug delivery that can be adapted to several types of cancers.

Keywords: carbonic anhydrase IX; tumor hypoxia targeting; paclitaxel; copper free '*click*' chemistry; triple negative breast cancer; albumin nanoparticles; human serum albumin

1. Introduction

Cancer is a one the major causes of death in the U.S.A., annually claiming more than half a million lives and an estimated 1.5 million new cases [1]. Thus, there is an urgent need to improve diagnostic tools for early detection and to develop more selective drug delivery agents for therapy of cancer with least toxic side effects. Nanomedicines have been shown to be multitasking drug delivery vehicles that can passively accumulate within tumor tissue and have been clinically approved for conventional cancer therapy. Accumulated evidence indicates that current drug delivery agents failed in clinical trials due to lack of targeting ability, poor tumor penetration, tumor heterogeneity, and

complex association of tumor associated immune cells and stroma [2]. Thus, targeted drug delivery that utilizes various ligands to recognize specific biomarkers expressed on tumor components has become extremely important in selective delivery of drugs and enhancing therapeutic efficacy [3–16]. The targeted cancer treatment approach differentiates between healthy and cancer tissues [17,18]. One smart way of designing a successful approach for tumor targeting can be the development of tumor multi-component targeting ligand library, and formulations with various types of biocompatible drug-carriers. This library of ligands could be surface decorated with drug-carrier systems using a combinatorial reagent-free organic synthesis approach for improving tumor early diagnosis and therapy. Modern research methods have the potential to transform personalized cancer treatment with improved quality of life, while providing the opportunity to integrate chemistry, drug delivery, cancer research elements and discoveries into multidisciplinary research experiences. The research presented in this study is based on a similar idea, i.e.,

(i) self-assembling of polymer, lipid, metallic-based nanosized drug-carrier, and bio-manufacturing of endogenous cell- (red blood cell, exosome) and protein (serum albumin, transferrin)-based cargo carrier [3,6,8,19–33];

(ii) functionalization of targeting ligands with the cargo carriers using a reagent-free synthesis approach, such as copper free cyclic Alkyne-Azide click reaction, "Thiol-Ene" Michael-type, and strain-promoted "Alkyne-Nitrone" cycloadditions [34–43].

The beauty of all these reactions is that they do not require any harmful chemicals, reagents, or any special condition, and they yield highly specific coupled products. The new knowledge gained through this interdisciplinary effort will provide a unique repertoire of advancement in drug delivery with rational design of targeting ligand-customized cargo carriers to exert distinct functions in the tumor microenvironment. The present study is an attempt to apply this simple strategy to develop a formulation of human serum albumin (HSA) via the copper-free cyclic Alkyne-Azide click reaction that targets tumor hypoxia.

Furthermore, nanoparticles have been broadly utilized as drug delivery systems for targeted delivery of anticancer drugs [44–64] in the pharmaceutical industry. They can enhance the delivery of hydrophobic drugs, decrease metabolic degradation of these drugs, target their delivery to malignant cancer cells just by the alteration of the surface of the delivery system with the addition of a ligand, and show controlled, extended or sustained delivery of drugs [7,8,13,25,53,58,65–81]. Alongside the capacity to improve the solubility of hydrophobic drugs, nanomicelles additionally can target cancer cells by two different strategies: passive and active targeting. The passive targeting delivery systems rely on the capacity of nanomicelles to exploit the Enhanced Permeability and Retention (EPR) effect [61,82–88]. The EPR phenomenon proposes that the multiplication of cancer cells brings about the improvement of profoundly disordered and flawed veins. Hence, nanoparticles including nanomicelles can extravasate and gather at the tumor site [89,90]. Hence, the nanomicelles are commonly conjugated with a targeting moiety in the targeted delivery system, thus, encouraging the specific aggregation of the drugs in target tissues, singular cancer cells, or intracellular organelles that are related to specific targeting biomarkers in cancer cells [83,84]. However, the presence of the EPR effect is not common to all cancer cells and, in some, may not be as effective as in others [86,91]. Further, in those cancer cells that do show the EPR effect, angiogenesis is not uniform across the tumor depth which can cause unequal distribution of the drugs. This gives a reason to develop targeted delivery systems that function via active uptake by the cancer cells via receptor-mediated cell uptake [92]. The present study is one such attempt.

Albumin is the most inexhaustible plasma protein in the human body. Its anti-immunogenic properties make albumin a favored component as a sole carrier or a component of a carrier system for an assortment of cancer medications. Like the vast majority of plasma proteins, albumin is produced in the liver where it is created at a rate of around 0.7 mg/h for each gram of liver (i.e., 10–15 g daily). The normal half-life of albumin is 19 days. Its high take-up in inflamed and tumor cells makes it

a perfect carrier for medications to target malignant cells. Numerous research- and industry-based techniques have been mentioned for in the literature, which conjugate or encapsulate different medications to albumin. Human serum albumin protein has a total set of 585 amino acids. A solitary polypeptide chain comprises 17 disulfide bonds, one free thiol and one tryptophan functional groups which make it an effective binding protein [93]. The advantages of the human serum albumin (HSA) include the presence of several drug binding sites like the amino and carboxylic groups that provide opportunities for covalent modifications and drug or protein attachment of the drugs or targeting ligands [94–96]. It has low-cost, non-immunogenic and naturally biodegradable properties that have been applied as a matrix for nanoparticles-based drug delivery systems [97–99]. The most important property that makes it preferable as a drug delivery carrier may be the fact that it is not susceptible to opsonization by serum proteins [100,101]. HSA conjugation could provide nanoparticles that are a promising delivery system for biopharmaceutically challenging medications, for example Paclitaxel (PTX), and they enhance the medication delivery and bioavailability for such drugs [102,103].

Carbonic Anhydrase (CA) is a zinc metalloenzyme that converts CO_2 to bicarbonate reversibly generating a proton in the process. There are about 15 varieties of CAs in mammals each of which exhibit different properties, but all of them are involved in ion exchange and pH balance [104]. Of all of them, CA IX is the most efficient and is available on the surface of cancer cells. The enzyme's active site is exposed outside the cell membrane. It is not expressed in normal healthy cells but is overexpressed in cancer cells under the influence of hypoxia [80,105], that is in turn produced by the extensively and fast-growing tumor cells which outgrow the oxygen supply creating a scenario of hypoxia. Thus, it has become the primary target for cancer therapy [106–108]. Sulfonamides are a group of anti-bacterial agents that have been recently proven to have antitumor activity too [109,110]. Acetazolamide (ATZ) is an aromatic member of the family of sulfonamides that is different from the other members of the group in that it does not have antibacterial properties. It was used for glaucoma and epilepsy but has also been proven to have carbonic anhydrase inhibitory activity. It has been used as an antitumor agent for 40 years. Other aromatic sulfonamides have also been found to have antitumor activities [111,112].

Paclitaxel is an effective anticancer drug used for chemotherapy. It has a unique chemical structure and results in polymerization of tubulin to stabilize microtubules and, furthermore, associates specifically with microtubules, making them stable against depolymerization in the presence of calcium and at cold temperatures, which otherwise promptly depolymerize ordinary microtubules. It is also known to act against mitochondria and inhibit apoptosis inhibitor protein B-cell Leukemia 2 (Bcl-2) [113–117]. However, it is highly hydrophobic and needs to be delivered via a delivery system that improves its solubility and delivers it at the target sites [16].

The research described in this article is one such attempt to design a targeted delivery system to deliver Paclitaxel to triple negative breast cancer (TNBC) cancer cell lines and test its efficacy in vitro. The results show a promising avenue for targeted delivery that can be adapted to several types of cancers.

2. Results

2.1. Synthesis of the Hypoxia Targeting Drug Delivery System

The product was prepared as described in Section 4.1. The final formulation was dialyzed and lyophilized to form a powder. The resultant product was then analyzed by FTIR (Fourier-transform infrared spectroscopy) to confirm the presence of the components used and the formation of the product from click reaction. The results of FTIR (Figure S1) showed characteristic peaks between 1700–2100 cm^{-1} corresponding to the $^{-}N{=}{=}\,{^{+}N}{=}{=}\,{^{-}N}$ (azide) stretching and there is an observable shift in the peaks that indicates that the reaction has occurred. It also shows peaks for –N–H, –C=O, and –C–H bond stretching at 3300–3500, 1670–1820, and 1050–1350 cm^{-1} respectively. These results were further confirmed by ^{1}H NMR spectrum (Figure S2) that show peaks between 6.8–7.4 ppm that

correspond to the hydrogens of the Dibenzocyclooctyl (DBCO) and between 2.2–3.6 ppm indicating the hydrogens of the azide apart from the peaks for the sulfonamides between 7.8–8.0 ppm.

2.2. Drug Loading

The process of drug loading was performed at room temperature as described in the synthesis in Section 4.1. The extent of drug loading was computed utilizing High performance liquid chromatography (HPLC) and UV Spectrophotometry at 227 nm for absorbance of PTX. The concentration of drug loaded was computed by utilizing a standard graph previously established. The drug loading was observed to be around 11.3% *w/w* for PTX in this hypoxia-targeting drug delivery system.

2.3. Particle Size Analysis

The investigations for measurement of the particle size of the formulation of this study were performed by the Dynamic light scattering (DLS) and Transmission electron microscopy (TEM). The outcomes demonstrated that the particle size (Figure 1a) on average was 294.0 nm and the polydispersity index (PDI) was around 0.139 demonstrating that the vast majority of the particles were inside the scope of this normal size. Further, the molecule size and morphology were considered utilizing TEM which indicated particles (Figure 1b) of the size between 105 and 130 nm. Both these outcomes affirm that the particle size is within the nanoscale.
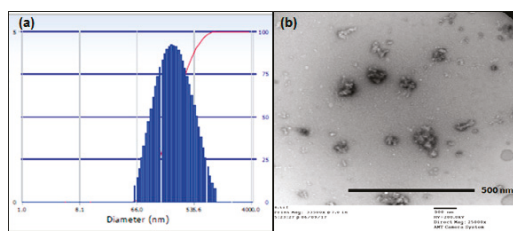

Figure 1. (**a**) Particle size by Dynamic light scattering (DLS) of the hypoxia targeting drug delivery system HSA-PTX-ATZ; (**b**) Particle size and morphology by Transmission electron microscopy (TEM) of the hypoxia targeting drug delivery system HSA-PTX-ATZ.

2.4. Drug Release Studies

Drug release studies were carried out as described in Section 4.4. The drug release studies were carried out at the physiological pH of 7 because it corresponds to that of the blood. The drug released after the albumin nanoparticles were broken down was calculated using both UV and HPLC and the results were consistent. The release was found to be steady over a period of 72 h with a release of about 29.75% at 24 h and 42.62% at 72 h (Figure 2). This shows that the product under study can be considered as a sustained release formulation.
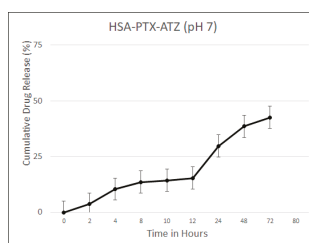

Figure 2. Drug release studies at pH 7 for the hypoxia targeting drug delivery system HSA-PTX-ATZ.

2.5. Stability Studies

Stability studies are preformed to test the resistance of the formulation to drug loss over a period of time and to the aggregation of nanoparticles. Thus, these studies have been done in three aspects of particle size, PDI and the drug loss over a period of 12 weeks or three months and the results are shown in Figure 3. As can be seen, the particle size seems to very slightly fluctuate but after a slight amount of agitation, the particle size seemed to be more or less the same; 292.5 nm at room temperature. The particle size was found to be more stable when frozen over that time than at the other two conditions. Similarly, there have been fluctuations in the PDI and at the end of the 12 weeks it was around 0.136. As for the drug loss, the loss was at 3.0% at room temperature after 12 weeks but was lesser in the frozen conditions which was of the order of 1.4%.
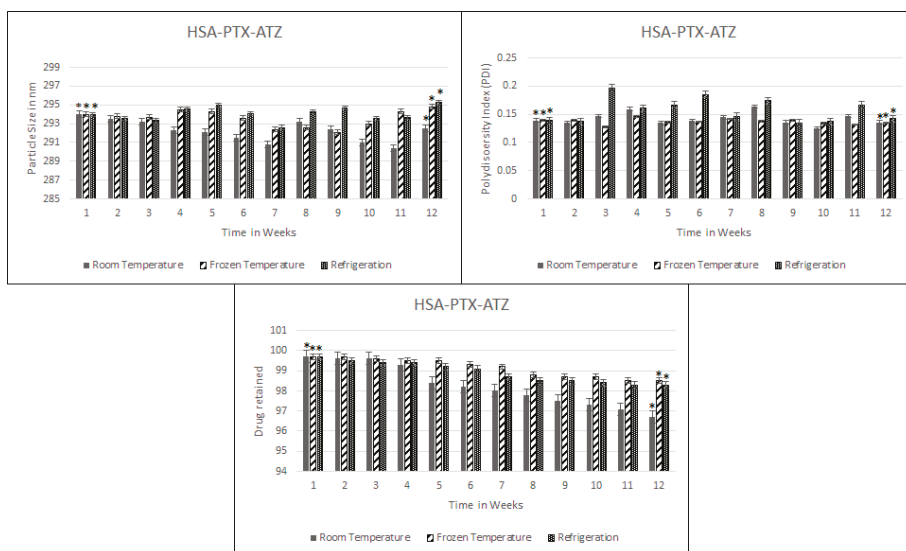

Figure 3. Stability studies over a period of 12 weeks for the hypoxia targeting drug delivery system HSA-PTX-ATZ. * Statistically not significant.

2.6. In Vitro Cytotoxicity Studies

These studies were performed on two different cell lines each expressing the CA IX receptor to a different extent [111,112]. In this direction, the results (Figure 4) of the in vitro cytotoxicity studies have shown that the MDA-MB-231 shows an IC_{50} at around 1 μm of the drug in the formulation as well as 1 μm in the MDA-MB-468 cell line as calculated via graphical and mathematical calculations from both MS Excel and GraphPad Prism 7. The results showed a dose-dependent killing and also a cell viability much lower than the non-targeted preparation and free drug in both cell lines at each concentration. The higher viability of the cells of the order of 80–90% for the carrier ligand combination additionally shows that the carrier along with ligand are safe for use. Statistical analysis was performed to calculate the significance of difference between free PTX and HAS-PTX-ATZ formulation in the two cell lines.
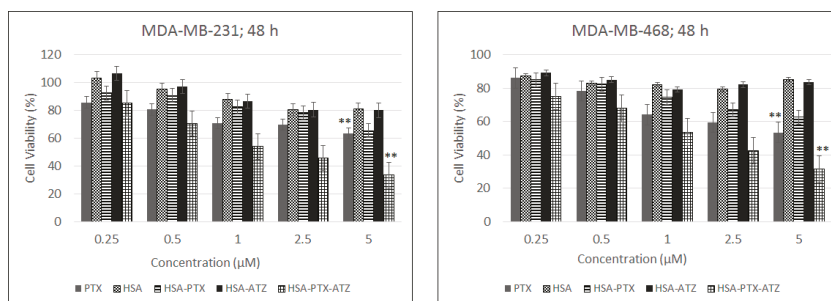
Figure 4. In vitro cytotoxicity studies in MDA-MB-231 and MDA-MB-468 cell lines respectively for the hypoxia targeting drug delivery system HSA-PTX-ATZ. ** Statistically significant.

2.7. Comparative In Vitro Cytotoxicity Studies for Normoxic and Hypoxic Conditions

This test proves that the presence of the ligand results in a higher uptake of the formulation in the hypoxic conditions and also that the CA IX receptor expression in normoxic conditions is much lower than the hypoxic conditions which results in the difference in uptake of the formulation in hypoxic conditions. The hypoxic condition was induced by the use of CoCl$_2$ [118,119]. The normoxic condition was achieved by the absence of treatment of the cells with CoCl$_2$. This was carried out at the IC$_{50}$ concentration for the formulation in both cell lines calculated from the in vitro cytotoxicity studies. The results from Figure 5 show that the cytotoxicity of the formulation in the hypoxic conditions is much less than in the hypoxic conditions with the values of the cell viability being about 92% in normoxic conditions and around 51% in the hypoxic condition in both cell lines. This also proves that the formulation is quite safe in normal cells.
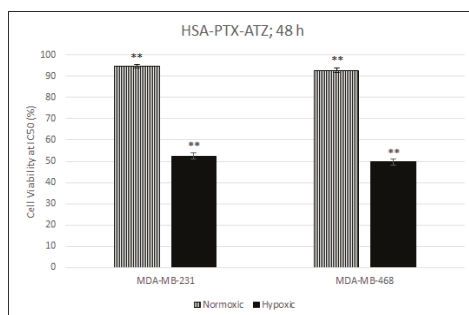

Figure 5. Comparative in vitro cytotoxicity studies for normoxic and hypoxic conditions in MDA-MB-231 and MDA-MB-468 cell lines respectively for the hypoxia targeting drug delivery system HSA-PTX-ATZ. ** Statistically significant.

2.8. Fluorescence Spectroscopic Studies

The fluorescence spectroscopic assay determines quantitatively the amount of drug entering the cells. The conjugation of rhodamine B to the drug and the nanomicelles and its subsequent detection in the spectrometer is time- and drug-concentration-dependent. The more rhodamine concentration detected with time means the more of the formulation along with the encapsulated drug might be entering the cells. The results of this assay show that the uptake of the formulation in the cells of both the cell lines increases with time taken at the time intervals of 4, 8, 16 h (Figure 6). The results have been presented in terms of fluorescence emission intensity as well as the concentration of rhodamine B that

is conjugated to the formulation. The graph also depicts that the uptake of the targeted formulation in both the cell lines is more than the non-targeted formulation.
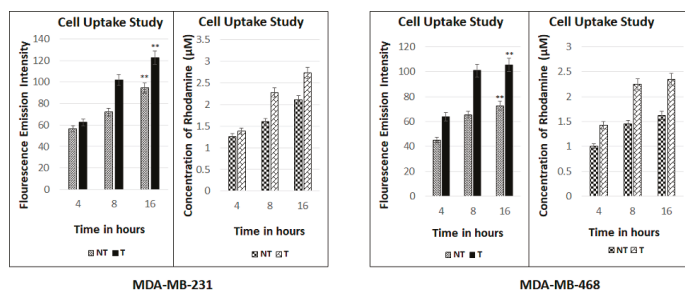

Figure 6. Fluorescence spectroscopic studies in MDA-MB-231 and MDA-MB-468 cell lines respectively for the hypoxia targeting drug delivery system HSA-PTX-ATZ. ** Statistically significant.

2.9. Apoptosis Assay by Flow Cytometry

Apoptosis is induced in both the cell lines because of the treatment with the formulations as was analyzed by flow cytometry with Annexin V/7-AAD dual staining [20,120]. The levels of Annexin V+/7-AAD+ (R3), Annexin V−/7-AAD+ (R4), Annexin V−/7-AAD− (R5), and Annexin V+/7-AAD− (R6) were utilized to illustrate the percentage of live cells, early apoptotic, late apoptotic and necrotic cells. The percentage of apoptotic cells was observed to be significantly higher in both the cell lines treated with the targeted formulation when compared to free drug non-targeted formulations. The percentage of early and late apoptotic cells in the MDA-MB-231 cell line was observed to be around 50.7% and 23.5%, respectively, in targeted formulation treated cells and 42.9% and 3.4%, respectively, in the non-targeted formulation-treated cells (Figure 7a). The percentage of early and late apoptotic cells in MDA-MB-468 cells was observed to be around 39.3% and 35.2%, respectively, in targeted formulation treated cells and 45.9% and 3.3%, respectively, in the non-targeted formulation-treated cells (Figure 7b). The outcomes present a superior apoptosis-inducing capacity of the targeted formulation. The graphical representation of these results has been demonstrated in Figure 8a,b. These results were consistent with cytotoxicity studies, cell uptake studies and the confocal microscopic studies. Additionally, the blank formulation displayed generally low apoptosis in the cell line, demonstrating the safety of the carrier system when utilized for treatment.
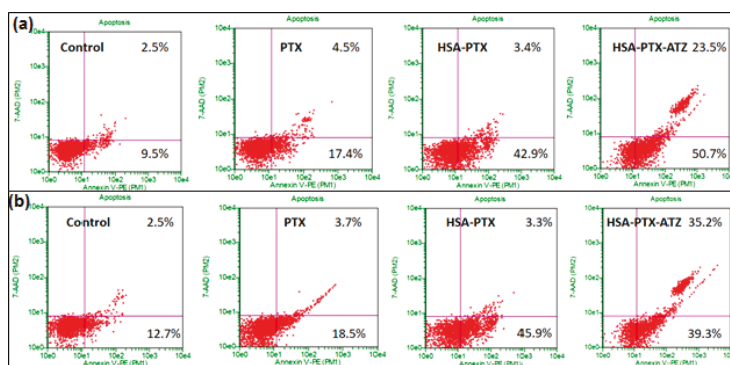

Figure 7. Apoptosis assay studies in (**a**) MDA-MB-231 and (**b**) MDA-MB-468 for the hypoxia targeting drug delivery system HSA-PTX-ATZ (The results are presented in terms of percentage of apoptotic cells similar to the previous literature [5,6,23,24,28,121]).
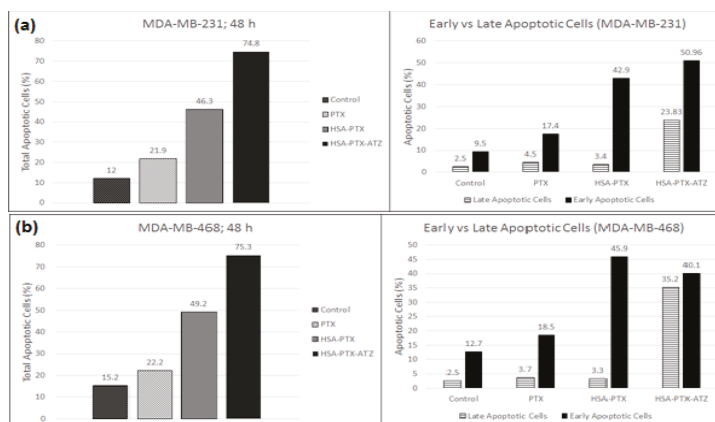
Figure 8. (**a**) Graphical representation of the apoptosis assay studies in MDA-MB-231; (**b**) Graphical representation of the apoptosis assay studies in MDA-MB-468 for the hypoxia targeting drug delivery system HSA-PTX-ATZ.

3. Discussion

It is the objective of each targeted drug delivery system to develop a framework for the nano-delivery formulations to address the difficulties discussed so far by building up a reagent-free click chemistry process. There have been a few studies conducted and strategies created to set up such click chemical reactions as of late that are anything but difficult to be performed, are brisk and yield high amounts of these products with non-poisonous results. A few analysts now consider that click chemistry is a carefully engineered approach towards the development of new molecular delivery systems. This unique yet simple technique depends basically upon the development of carbon heteroatom bonds utilizing spring-loaded reactants. The increasing extent of utilization of these reactions in delivery systems is found in about all specializations of current pharmaceutical sciences from drug delivery to material sciences [121]. These sorts of click chemistry reactions extensively incorporate cycloaddition of unsaturated species: 1,3-dipolar cycloaddition, cycloaddition of unsaturated species: [4+2]-cycloaddition (Diels-Alder), nucleophilic substitution/ring-opening responses, carbonyl responses of the non-aldol sort, expansion to carbon-carbon numerous securities [122]. Because of the undeniable favorable circumstances of such simple chemical reactions, the click chemistry has been picking up in drug discovery, drug delivery, and bioconjugation reactions [40]. Its application is utilized as a strategy for creating libraries of such targeted drug delivery systems.

The formulation thus synthesized is a result of such a simple chemical process involving three steps only, thus creating a feasibility of formulating such delivery systems for a combination of ligands and carriers for several hydrophobic drugs of different categories and not just limited to the anti-cancer drugs. The safety of the carrier system thus developed is the key for the success of this formulation. Both the targeted and non-targeted formulations were prepared so that they can be compared to each other for their anti-cancer efficiency. The drug loading is suspected to be less in the formulation due to the long duration of the reaction and due to the size of the carrier molecule. However, the same spatial reasons can be given for the prolonged and sustained release of the drug into the tumor microenvironment.

The nanoparticles thus formed are found to be in the nanoscale of the particle size and the TEM results further confirm these results. The PDI was found to be quite low indicating that the size distribution is quite narrow in the particles which means that most of the nanoparticles were about the same size as the average particle size. The particles being in the nano size also promote the entry of the

formulation into the tumor cells through the leaky vasculature by the EPR effect [61,88]. Furthermore, the particle size below 300 nm also helps prevent opsonization of the proteins via macrophages in the body that untimely leads to elimination of the formulation from the targeted tumor site. The results of the DLS and TEM are corroborative and form the basis for the results of the cytotoxicity studies.

The formulation further tested for the stability shows that the nature of the formulation is maintained close to the nature at the point of its synthesis. Thus, the formulation is found to be robust with little drug loss. This is an indication towards the long shelf-life possible by this formulation strategy. The storage conditions may also well be described from the results of this study as being stored at freezing temperatures for the longest shelf-life with the best possible stability and minimal drug loss during storage.

The cytotoxic studies were then performed to check the efficiency of the formulation in vitro. The formulation was found to have a little bit more efficacy in the MDA-MB-468 cell lines which have an overexpression of the extracellular CA IX receptor under hypoxic conditions and, hence, show good response to treatment. This effect is more or less the same in MDA-MB-231 cells [123]. Hence, the formulation does show a reasonable efficiency in this cell line also showing that it is a promising strategy to treat this more aggressive cell line [124]. Hence, based on the literature [124], we established a proof of concept that this formulation is effective in hypoxic conditions equally in both cell lines. The hypoxic conditions are found to have more of an effect because of the lowering of the pH in the swiftly proliferating cancer cells that results in the overexpression of this receptor and, thus, the formulation being taken up more effectively. The difference in cell viability between the targeted and non-targeted formulations is an indication of the fact that the formulation is being taken up not only by EPR effect but also by the targeted entry via the extracellular CA IX receptor; i.e., receptor mediated cell uptake [14]. The high cell viability in the blank formulation is proof of the safety of the carrier-ligand system. Furthermore, the difference in the response to this formulation in the normoxic (higher cell viability) and hypoxic conditions (lower cell viability) has led us to demonstrate that the uptake mechanism was CA IX receptor-mediated in TNBC cells. These studies establish the proof of concept of concept to show that this formulation is an efficient way to deliver drugs via targeting the hypoxia marker, CA IX.

The in vitro cytotoxicity studies were followed up by fluorescence spectroscopic studies that illustrated the extent of uptake of the formulation in the cells. The comparative results between the non-targeted and targeted formulations show that the targeted formulation has a more preferential uptake in hypoxic conditions and the results show that the uptake is time-dependent. Thus, it corroborates the results of the cytotoxicity studies showing receptor-mediated uptake [13,31,106,125–127] of the formulation in addition to the EPR effect. The uptake of the non-targeted formulation may be explained as being purely a response to the EPR effect. Acetazolamide is a very established ligand of CA IX [112,128–133]. Our data of high cell killing effects of HSA-PTX-ATZ in hypoxic condition compared to normoxia and higher uptake of Rhodamine-labelled HSA-PTX-ATZ indicate the CA IX-mediated drug delivery effect of HSA-PTX-ATZ.

The findings of the cytotoxic studies and the fluorescence spectroscopic studies are further strengthened by the percentage of early and late apoptotic cells in both cell lines. The higher percentage of apoptotic cells proves the efficiency of the targeted formulation in both cell lines; this demonstrates the advantage of the targeting ligand. The low percentage of total apoptotic cells in the cell with the carrier system shows that the system is safe for normal cells.

4. Materials and Methods

4.1. Synthesis of the Hypoxia Targeting Drug Delivery System

The synthesis of the drug delivery system developed in this study that targets hypoxia in the tumor cells is a simple four step utilizing click chemistry. As mentioned earlier, click chemistry is a quick process of conjugating two molecules that have complimentary functional groups that just '*click*'

with each other in minimal conditions of the reaction. The specific form of click reaction used in this study is the copper free cyclic Alkyne-Azide click reaction. The convenience of this reaction process allows the development of a library of ligands and carrier molecules that have these complimentary molecules which can take part in click reaction that can be made on a need-basis. The scheme of this reaction is presented in the Figure 9.
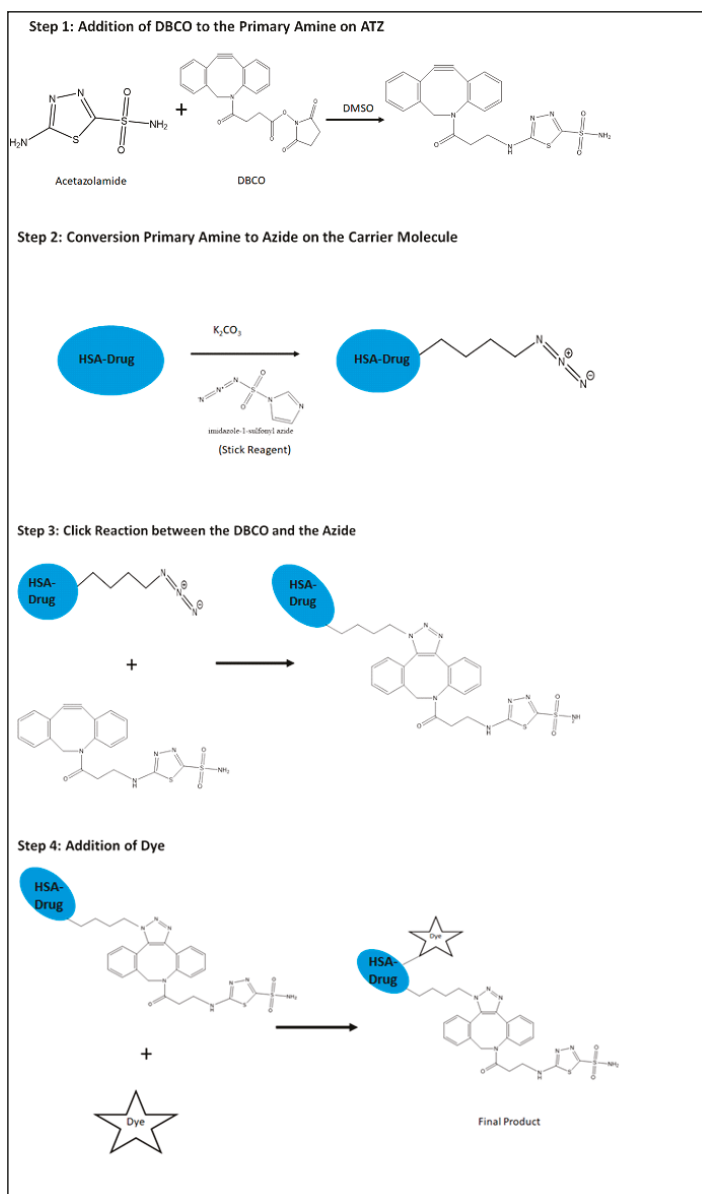

Figure 9. Schematic representation of the synthesis of the hypoxia targeting drug delivery system HSA-PTX-ATZ.

The description of this process is as follows:

4.1.1. Preparation of the Targeting Ligand

The first step is to prepare the ligand on the HSA molecule. The starting material is the Acetazolamide. The amide group of the acetazolamide is first converted to primary amine by acid hydrolysis using 1 M HCl. The primary amine group thus activated is then used to be attached to one of the complimentary molecule, DBCO with a —-C≡≡C—- group that further participates in the click reaction. The acetazolamide with the primary amine group and the DBCO are dissolved in DMSO and then allowed to react for overnight at room temperature while stirring continuously. The product is then dialyzed in a 12 kD dialysis bag (Spectrapor, Spectrum Research facilities, SD) for 4–8 h and kept ready for further conjugation.

4.1.2. Preparation of the Carrier Molecule

Preparation of the carrier molecule is the next step. This involves conversion of the amine group of the amino acids comprised in the HSA protein to azide group. This involves two steps. First, the amine groups are converted to azide groups, $^-N== \, ^+N== \, ^-N$, using the Stick Reagent (imidazole-1-sulfonyl azide) in the presence of K_2CO_3 overnight at room temperature and continuous stirring. The addition of these two components of the reaction is carried out in ice because they are highly exothermic reactions. After the conversion, the azide product is dialyzed in a 12 kD dialysis bag (Spectrapor, Spectrum Research facilities, SD) for 4–8 h and the drug is loaded onto it.

4.1.3. Drug Loading on the Carrier Molecule Comprising the Azide Group

The drug loading is performed by desolvation method that is derived from the coacervation process using previously described method in the literature [28,69,134,135]. Paclitaxel is a hydrophobic drug that is dissolved in ethanol. HSA was at first completely dissolved in phosphate buffer made in deionized water (50 mg/mL) and placed on a stirrer at a speed of around 600 rpm. The pH of the buffer is maintained at 8. The ethanolic solution of the PTX is then added to the HSA solution at the rate of 1 mL/min. The pH is again maintained at 8 using the same buffer. After half an hour of stirring, 8% glutaraldehyde is added to the reaction mixture to promote crosslinking in the HSA for encapsulating the drug effectively. The reaction is continued overnight while stirring at room temperature. The product is then dialyzed in a 12 kD dialysis bag (Spectrapor, Spectrum Research facilities, SD) for 4–8 h. This drug loaded carrier molecule with the azide group contributes the other complimentary molecule of the click reaction.

4.1.4. Conjugation of the Ligand to the Carrier Molecule

This is the final step of the process of synthesis of the hypoxia targeting drug delivery system. It involves the conjugation of the alkyne group on DBCO and the azide group on the carrier molecule click conjugate with each other. This is the simplest step of the process where in the ligand containing the DBCO and the carrier molecule with the azide are combined together in a reaction under pH condition of 8 and at room temperature while continuously stirring at 600 rpm. The reaction is carried out for 4–6 h. The final product is dialyzed in a 12 kD dialysis bag (Spectrapor, Spectrum Research facilities, SD) for 2 h and lyophilized. The final product is water soluble. The product can also be attached further with an NIR dye by the similar click reaction to produce a theranostic product. This is further taken up for characterization studies using FTIR and NMR studies to confirm the reaction.

4.2. Drug Loading

The process of drug loading was performed at room temperature as described earlier in the synthesis section. The calculation of percentage of drug loading was performed in HPLC and UV Spectrophotometer and the amount of drug encapsulated was found out using the standard graph

previously developed by the methods specified in literature for PTX in both the HPLC and UV Spectrophotometer. A series of dilutions were made for the pure PTX and the absorbance for each was taken at 227 nm. A standard graph was plotted according to the readings. Later, a specified amount of the product has been taken and tested for absorbance. The amount of drug encapsulated from the line equation obtained from the standard graph.

4.3. Particle Size Analysis

The nanoparticles were further taken for particle size studies using a Beckman Coulter Delsa Nano-C DLS Particle analyzer (Beckman Coulter, Inc., Fullerton, CA, USA) that involved a 658 nm He–Ne laser as reported earlier by our lab. Tests were also examined by JEOL Transmission Electron Magnifying Instrument outfitted with LaB6 filament gun (JEM 2010, Tokyo, Japan) at an accelerating voltage of 200 kV for studying the particle morphology [6,8,53]. The nanoparticles were also depicted for surface morphology by Transmission Electron Microscopy (TEM). Tests were set up as described in the previous literature. Determined measure of each sample (4 µL) was applied to a Formvar-coated, carbon stabilized copper matrix (400 work). The copper matrix was air-dried, stained negatively with 5% aqueous uranyl acetate, and allowed to dry.

4.4. Drug Release Studies

Drug release studies were performed with the formulation to assess the extent to which the drug has been released out from the formulation. Ideally, this is done in the physiological conditions. For this study, the studies were carried out at pH 7. The analysis was carried out at room temperature. A fixed volume of the formulation was placed in a dialysis bag under sink condition and continuous stirring. Specific volumes of samples were extracted at 2, 4, 8, 10, 12, 24, 48, 72 h from the dialysis bag. The nanoparticles were subjected to high shear in a sonicator for about 15–30 min to disrupt the nanoparticle formation so that the entire drug is released out and then the mixture was centrifuged at high speed of 15,000 rpm for 15 min. This forms a pellet of the disrupted HSA (being a heavy molecule in comparison to the drug) at the bottom and the supernatant contains the drug. The supernatant was extracted, diluted and then analyzed for drug content in UV and HPLC. The amount of was calculated from the line equation obtained from the standard graph and subtracted from the amount in the sample first taken to get the amount of drug released.

4.5. Stability Studies

The stability studies were performed to check for the stability of the formulation over a period of time in terms of particle size, polydispersity index (PDI), and drug loss. The formulation prepared was stored at three different conditions of temperatures, i.e., at room temperature (25 °C), under refrigeration (4 °C), and under frozen conditions (−20 °C) for 12 weeks [5,98]. The samples were retrieved every week and analyzed for the particle size, and PDI in DLS and drug content was analyzed in HPLC and UV.

4.6. Cell Culture

The cell lines chosen for this study are the MDA-MB-231 and MDA-MB-468 both of which correspond to the Triple Negative Breast Cancer (TNBC) [136,137]. These were the choice of cell lines because they are known to express the hypoxia marker Carbonic Anhydrase IX (CA IX) receptor on the surface of the cell lines. The MDA-MB-468 is found have a higher expression of the receptor compared to the MDA-MB-231 according to literature. The MDA-MB-231 is also found to be a more aggressive cell line that presents a greater difficulty for treatment. MDA-MB-231 is a stellate shaped cell and the MDA-MB-468 is a grape-like cluster of cells. Both the cell lines were cultured in Dulbecco's Modified Eagle's Medium (DMEM; Fisher Scientific, Waltham, MA, USA). The media was added with 10% fetal bovine serum (FBS) and streptomycin sulfate (10 mg/L). All cell lines were incubated at 37 °C in a 5% CO_2 air humidified atmosphere.

4.7. In Vitro Cytotoxicity Studies

The in vitro cytotoxicity studies were performed after the cells were induced with hypoxia using $CoCl_2$. This treatment enhances the overexpression of the CA IX receptor on the surface of the cells. The assay was performed using the MTT reagent solution in PBS (1 mg/mL) at pH 7.4. The treatments included free drug (positive control), free carrier (negative control), carrier-drug (positive control), carrier-ligand (negative control), and the formulation comprising carrier-ligand-drug. The cells were seeded in 96-well plates with a normal of 5000 cells in each well. After incubating these cells for 24 h, they were treated with different concentrations of the formulations within a range of 0.25–5 μm. The treated cells were further incubated in the presence of the formulations for 48 h at 37 °C, after which the MTT reagent solution was added. The cells were incubated furthermore at 37 °C for 2 h. Following this, the media was supplanted by DMSO and the plates were put on a shaker for 10 min. The absorbance was measured at 590 nm utilizing a high-performance multi-mode plate reader (Synergy 2, BioTek, Winooski, VT, USA). The extent of surviving cells was calculated in terms of percentage by contrasting the absorbance of the treated cells and proper controls cells. This was performed on both the cell lines individually. Statistical analysis was done to calculate the significance of difference between the responses to the formulation in both cell lines.

4.8. Comparative In Vitro Cytotoxicity Studies for Normoxic and Hypoxic Conditions

Healthy cells and cancer cells show a difference in terms of development of hypoxia and acidic conditions in the microenvironment. The healthy cells do not overexpress the CA IX receptor and do not exhibit hypoxia while the cancer cells do. Thus, this study was performed to understand the difference in the uptake of specifically the formulation in the normoxic conditions as well as the hypoxic conditions in the said cell lines. This study is believed to give an assessment of the effect of the formulation on the normal and the tumor cells. The study was done similar to the in vitro cytotoxicity studies described above in two groups of treatments; the cells that are treated with $CoCl_2$ to induce hypoxia and CA IX expression and the cells that are not treated with $CoCl_2$ for normoxia. The assay was performed using MTT reagent solution (1 mg/mL) in both the cell lines. The assay was performed at the IC_{50} concentration of specifically the formulation to prove its efficiency in the hypoxic conditions comparatively.

4.9. Fluorescence Spectroscopic Studies

This assay is a quantitative measure of the amount of formulation encapsulating the drug entering into the cells using fluorescence spectroscopy. Both the targeted and non-targeted formulations were conjugated with Rhodamine B according to a previously established method. The cell-lines MDA-MB-231 and MDA-MB-468 were treated with $CoCl_2$ first, then cultured in two separate 6 well-plates with each well comprising of about 100,000 cells in 2 mL of the media. These cells were then treated with the rhodamine conjugated formulations at their IC_{50} concentrations and incubated. Samples were collected every 4 h from the start of the treatment. Each sample collection procedure consisted of removing the formulation, washing it with PBS, and finally streaking the cells to collect the proteins and then further protein collection using lysis buffer. During the measurement of florescence, a control was also used that contained a mixture of methanol and the lysis buffer.

4.10. Apoptosis Assay by Flow Cytometry

Apoptosis assay was performed on the MDA-MB-231 and MDA-MB-468 cell lines separately according to the prior literature. The cells were induced with hypoxia by treating them with $CoCl_2$, then the cells were cultured in 6-well plates at the rate of 100,000 cells per well. The cells were incubated for 24 h at 37 °C under 5% CO_2, followed by the treatment of the cells with free drug, non-targeted formulation and the targeted formulation and incubating further for 48 h to induce apoptosis. The concentrations of the formulations were the IC_{50} concentrations of the respective

formulations obtained from the in vitro cytotoxicity assay. After a 48-h incubation, the cells were gathered, and the test was set up as indicated by the procedure described for Guava Nexin Annexin V assay (EMD Millipore, Billerica, MA, USA). Then, the media before trypsinization and the treated trypsinized cells were gathered in 15 mL tubes for each sample and centrifuged at 800 for 5 min. Cell pellets formed thus were dispersed in PBS at pH 7.4 containing 1% FBS so that the quantity of cells of the order of 2×10^5 to 1×10^6 cells/mL. 100 μL of these cell dispersions of each sample was mixed with 100 μL of the Guava Nexin Reagent and was incubated for 20 min at room temperature in the absence of sunlight. The resultant final samples were analyzed by Guava Easycyte Flow Cytometer (EMD Millipore).

5. Conclusions

Hypoxia is a target that is ubiquitously present in almost all cancers and is mostly found in the oxygen-deprived core of the tumor. It is a challenge to target it because of its location. However, the fast-growing cancer cells produce a lack of oxygen and a lowering of pH in the cancer cells which result in the overexpression of the surface receptor CA IX. This is a convenient cancer cell marker that allows the penetration of the nanocarrier to the core and, thus, effectively delivers the drug to the targeted site. This study is an attempt to establish the proof-of-concept that this can be achieved via the use of CA IX-targeting ligands like Acetazolamide and a bio-safe carrier like the human serum albumin which is abundant in the body and, hence, is non-immunogenic. This study succeeded in proving the usefulness of the formulation synthesized herein and characterized further. It shows that the cells selectively take up the formulation and shows a low cell viability in cancer cells with more percentage of apoptotic or dying cells. The results also show that the carrier system is safe and hence can be used for drug delivery. The delivery system, therefore, helps in the delivery of drugs to specific sites; thus, eliminating the undesired side effects on healthy cells. The nature of the formulation further allows the conjugation of a dye that can potentially make it a theranostic system. Thus, it can be safely said that the formulation can be further used for in vivo evaluations that are currently underway in our laboratory.

References

1. *CDC Expected New Cancer Cases and Deaths in 2020*; Centers for Disease Control and Prevention: Atlanta, GA, USA, 2015.
2. Sau, S.; Alsaab, H.O.; Bhise, K.; Alzhrani, R.; Nabil, G.; Iyer, A.K. Multifunctional nanoparticles for cancer immunotherapy: A groundbreaking approach for reprogramming malfunctioned tumor environment. *J. Control. Release* **2018**. [CrossRef] [PubMed]
3. Yang, X.; Iyer, A.K.; Singh, A.; Milane, L.; Choy, E.; Hornicek, F.J.; Amiji, M.M.; Duan, Z. Cluster of differentiation 44 targeted hyaluronic acid based nanoparticles for MDR1 siRNA delivery to overcome drug resistance in ovarian cancer. *Pharm. Res.* **2015**, *32*. [CrossRef] [PubMed]

4. Wickens, J.M.; Alsaab, H.O.; Kesharwani, P.; Bhise, K.; Amin, M.C.I.M.; Tekade, R.K.; Gupta, U.; Iyer, A.K. Recent advances in hyaluronic acid-decorated nanocarriers for targeted cancer therapy. *Drug Discov. Today* **2017**, *22*. [CrossRef] [PubMed]

5. Luong, D.; Sau, S.; Kesharwani, P.; Iyer, A.K. Polyvalent folate-dendrimer-coated iron oxide theranostic nanoparticles for simultaneous magnetic resonance imaging and precise cancer cell targeting. *Biomacromolecules* **2017**, *18*, 1197–1209. [CrossRef] [PubMed]

6. Luong, D.; Kesharwani, P.; Alsaab, H.O.; Sau, S.; Padhye, S.; Sarkar, F.H.; Iyer, A.K. Folic acid conjugated polymeric micelles loaded with a curcumin difluorinated analog for targeting cervical and ovarian cancers. *Colloids Surf. B Biointerfaces* **2017**, *157*, 490–502. [CrossRef] [PubMed]

7. Kesharwani, P.; Xie, L.; Mao, G.; Padhye, S.; Iyer, A.K. Hyaluronic acid-conjugated polyamidoamine dendrimers for targeted delivery of 3,4-difluorobenzylidene curcumin to CD44 overexpressing pancreatic cancer cells. *Colloids Surf. B Biointerfaces* **2015**, *136*, 413–423. [CrossRef] [PubMed]

8. Kesharwani, P.; Banerjee, S.; Padhye, S.; Sarkar, F.H.; Iyer, A.K. Hyaluronic acid engineered nanomicelles loaded with 3,4-difluorobenzylidene curcumin for targeted killing of CD44+ stem-like pancreatic cancer cells. *Biomacromolecules* **2015**, *16*, 3042–3053. [CrossRef] [PubMed]

9. Iyer, A.K.; Duan, Z.; Amiji, M.M. Nanodelivery systems for nucleic acid therapeutics in drug resistant tumors. *Mol. Pharm.* **2014**, *11*, 2511–2526. [CrossRef] [PubMed]

10. Ganesh, S.; Iyer, A.K.; Gattacceca, F.; Morrissey, D.V.; Amiji, M.M. In vivo biodistribution of siRNA and cisplatin administered using CD44-targeted hyaluronic acid nanoparticles. *J. Control. Release* **2013**, *172*, 699–706. [CrossRef] [PubMed]

11. Ganesh, S.; Iyer, A.K.; Weiler, J.; Morrissey, D.V.; Amiji, M.M. Combination of siRNA-directed gene silencing with cisplatin reverses drug resistance in human non-small cell lung cancer. *Mol. Ther. Nucleic Acids* **2013**, *2*. [CrossRef] [PubMed]

12. Choudhury, H.; Gorain, B.; Pandey, M.; Kumbhar, S.A.; Tekade, R.K.; Iyer, A.K.; Kesharwani, P. Recent advances in TPGS-based nanoparticles of docetaxel for improved chemotherapy. *Int. J. Pharm.* **2017**, *529*. [CrossRef] [PubMed]

13. Amjad, M.W.; Amin, M.C.I.M.; Katas, H.; Butt, A.M.; Kesharwani, P.; Iyer, A.K. In vivo antitumor activity of folate-conjugated cholic acid-polyethylenimine micelles for the codelivery of doxorubicin and sirna to colorectal adenocarcinomas. *Mol. Pharm.* **2015**, *12*, 4247–4258. [CrossRef] [PubMed]

14. Alsaab, H.; Alzhrani, R.; Kesharwani, P.; Sau, S.; Boddu, S.; Iyer, A. Folate decorated nanomicelles loaded with a potent curcumin analogue for targeting retinoblastoma. *Pharmaceutics* **2017**, *9*, 15. [CrossRef] [PubMed]

15. Abeylath, S.C.; Ganta, S.; Iyer, A.K.; Amiji, M. Combinatorial-designed multifunctional polymeric nanosystems for tumor-targeted therapeutic delivery. *Acc. Chem. Res.* **2011**, *44*, 1009–1017. [CrossRef] [PubMed]

16. Cheriyan, V.T.; Alsaab, H.O.; Sekhar, S.; Stieber, C.; Kesharwani, P.; Sau, S.; Muthu, M.; Polin, L.A.; Levi, E.; Iyer, A.K.; et al. A CARP-1 functional mimetic loaded vitamin E-TPGS micellar nano-formulation for inhibition of renal cell carcinoma. *Oncotarget* **2017**, *8*, 104928–104945. [CrossRef] [PubMed]

17. Almansour, A.I.; Arumugam, N.; Suresh Kumar, R.; Mahalingam, S.M.; Sau, S.; Bianchini, G.; Menéndez, J.C.; Altaf, M.; Ghabbour, H.A. Design, synthesis and antiproliferative activity of decarbonyl luotonin analogues. *Eur. J. Med. Chem.* **2017**, *138*, 932–941. [CrossRef] [PubMed]

18. Sau, S.; Agarwalla, P.; Mukherjee, S.; Bag, I.; Sreedhar, B.; Pal-Bhadra, M.; Patra, C.R.; Banerjee, R. Cancer cell-selective promoter recognition accompanies antitumor effect by glucocorticoid receptor-targeted gold nanoparticle. *Nanoscale* **2014**, *6*, 6745–6754. [CrossRef] [PubMed]

19. Susa, M.; Iyer, A.K.; Ryu, K.; Choy, E.; Hornicek, F.J.; Mankin, H.; Milane, L.; Amiji, M.M.; Duan, Z. Inhibition of ABCB1 (MDR1) expression by an siRNA nanoparticulate delivery system to overcome drug resistance in osteosarcoma. *PLoS ONE* **2010**, *5*. [CrossRef] [PubMed]

20. Sau, S.; Mondal, S.K.; Kashaw, S.K.; Iyer, A.K.; Banerjee, R. Combination of cationic dexamethasone derivative and STAT3 inhibitor (WP1066) for aggressive melanoma: A strategy for repurposing a phase I clinical trial drug. *Mol. Cell. Biochem.* **2017**, *436*. [CrossRef] [PubMed]

21. Sahu, P.; Kashaw, S.K.; Kushwah, V.; Sau, S.; Jain, S.; Iyer, A.K. pH responsive biodegradable nanogels for sustained release of bleomycin. *Bioorg. Med. Chem.* **2017**, *25*, 4595–4613. [CrossRef] [PubMed]

22. Sahu, P.; Das, D.; Kashaw, V.; Iyer, A.K.; Kashaw, S.K. *Nanogels: A New Dawn in Antimicrobial Chemotherapy*; Elsevier: Amsterdam, The Netherlands, 2017; ISBN 9780323527347.

23. Luong, D.; Kesharwani, P.; Killinger, B.A.; Moszczynska, A.; Sarkar, F.H.; Padhye, S.; Rishi, A.K.; Iyer, A.K. Solubility enhancement and targeted delivery of a potent anticancer flavonoid analogue to cancer cells using ligand decorated dendrimer nano-architectures. *J. Colloid Interface Sci.* **2016**, *484*, 33–43. [CrossRef] [PubMed]

24. Luong, D.; Kesharwani, P.; Deshmukh, R.; Mohd Amin, M.C.I.; Gupta, U.; Greish, K.; Iyer, A.K. PEGylated PAMAM dendrimers: Enhancing efficacy and mitigating toxicity for effective anticancer drug and gene delivery. *Acta Biomater.* **2016**, 1–16. [CrossRef] [PubMed]

25. Khan, I.; Gothwal, A.; Sharma, A.K.; Kesharwani, P.; Gupta, L.; Iyer, A.K.; Gupta, U. PLGA nanoparticles and their versatile role in anticancer drug delivery. *Crit. Rev. Ther. Drug Carrier Syst.* **2016**, *33*. [CrossRef] [PubMed]

26. Hadzijusufovic, E.; Rebuzzi, L.; Gleixner, K.V.; Ferenc, V.; Peter, B.; Kondo, R.; Gruze, A.; Kneidinger, M.; Krauth, M.-T.; Mayerhofer, M.; et al. Targeting of heat-shock protein 32/heme oxygenase-1 in canine mastocytoma cells is associated with reduced growth and induction of apoptosis. *Exp. Hematol.* **2008**, *36*, 1467–1476. [CrossRef] [PubMed]

27. Gleixner, K.V.; Mayerhofer, M.; Vales, A.; Gruze, A.; Hörmann, G.; Cerny-Reiterer, S.; Lackner, E.; Hadzijusufovic, E.; Herrmann, H.; Iyer, A.K.; et al. Targeting of Hsp32 in solid tumors and leukemias: A novel approach to optimize anticancer therapy. *Curr. Cancer Drug Targets* **2009**, *9*. [CrossRef]

28. Gawde, K.A.; Kesharwani, P.; Sau, S.; Sarkar, F.H.; Padhye, S.; Kashaw, S.K.; Iyer, A.K. Synthesis and characterization of folate decorated albumin bio-conjugate nanoparticles loaded with a synthetic curcumin difluorinated analogue. *J. Colloid Interface Sci.* **2017**, *496*, 290–299. [CrossRef] [PubMed]

29. Ganesh, S.; Iyer, A.K.; Morrissey, D.V.; Amiji, M.M. Hyaluronic acid based self-assembling nanosystems for CD44 target mediated siRNA delivery to solid tumors. *Biomaterials* **2013**, *34*, 3489–3502. [CrossRef] [PubMed]

30. Bhise, K.; Kashaw, S.K.; Sau, S.; Iyer, A.K. Nanostructured lipid carriers employing polyphenols as promising anticancer agents: Quality by design (QbD) approach. *Int. J. Pharm.* **2017**, *526*, 506–515. [CrossRef] [PubMed]

31. Bhise, K.; Sau, S.; Alsaab, H.; Kashaw, S.K.; Tekade, R.K.; Iyer, A.K. Nanomedicine for cancer diagnosis and therapy: Advancement, success and structure-activity relationship. *Ther. Deliv.* **2017**, *8*. [CrossRef] [PubMed]

32. Amiji, M.M.; Iyer, A.K. Multifunctional Self-Assembling Polymeric Nanosystems. United States Patent US 9,173,840, 3 November 2015.

33. Jain, S.; Doshi, A.S.; Iyer, A.K.; Amiji, M.M. Multifunctional nanoparticles for targeting cancer and inflammatory diseases. *J. Drug Target.* **2013**, *21*, 888–903. [CrossRef] [PubMed]

34. Agard, N.J.; Prescher, J.A.; Bertozzi, C.R. A strain-promoted [3 + 2] azide-alkyne cycloaddition for covalent modification of biomolecules in living systems. *J. Am. Chem. Soc.* **2004**, *126*, 15046–15047. [CrossRef] [PubMed]

35. Baskin, J.M.; Prescher, J.A.; Laughlin, S.T.; Agard, N.J.; Chang, P.V.; Miller, I.A.; Lo, A.; Codelli, J.A.; Bertozzi, C.R. Copper-free click chemistry for dynamic in vivo imaging. *Proc. Natl. Acad. Sci. USA* **2007**, *104*, 16793–16797. [CrossRef] [PubMed]

36. Best, M.D. Click chemistry and bioorthogonal reactions: Unprecedented selectivity in the labeling of biological molecules. *Biochemistry* **2009**, *48*, 6571–6584. [CrossRef] [PubMed]

37. Gundluru, M. *Custom Synthesis of Strained Cyclooctyne-Peptide Conjugates for Copper-Free Click Chemistry*; Peptides International, Inc.: Louisville, KY, USA, 2018.

38. Jewett, J.C.; Bertozzi, C.R. Cu-free click cycloaddition reactions in chemical biology. *Chem. Soc. Rev.* **2010**, *39*, 1272. [CrossRef] [PubMed]

39. Kolb, H.C.; Finn, M.G.; Sharpless, K.B. Click chemistry: Diverse chemical function from a few good reactions. *Angew. Chem. Int. Ed.* **2001**, *40*, 2004–2021. [CrossRef]

40. Kolb, H.C.; Sharpless, K.B. The growing impact of click chemistry on drug discovery. *Drug Discov. Today* **2003**, *8*, 1128–1137. [CrossRef]

41. Nandivada, H.; Jiang, X.; Lahann, J. Click chemistry: Versatility and control in the hands of materials scientists. *Adv. Mater.* **2007**, *19*, 2197–2208. [CrossRef]

42. Thirumurugan, P.; Matosiuk, D.; Jozwiak, K. Click chemistry for drug development and diverse chemical-biology applications. *Chem. Rev.* **2013**, *113*, 4905–4979. [CrossRef] [PubMed]

43. Totobenazara, J.; Burke, A.J. New click-chemistry methods for 1,2,3-triazoles synthesis: Recent advances and applications. *Tetrahedron Lett.* **2015**, *56*, 2853–2859. [CrossRef]

44. Sahu, P.; Kashaw, S.K.; Jain, S.; Sau, S.; Iyer, A.K. Assessment of penetration potential of pH responsive double walled biodegradable nanogels coated with eucalyptus oil for the controlled delivery of 5-fluorouracil: In vitro and ex vivo studies. *J. Control. Release* **2017**, *253*, 122–136. [CrossRef] [PubMed]

45. Iyer, A.K.; Su, Y.; Feng, J.; Lan, X.; Zhu, X.; Liu, Y.; Gao, D.; Seo, Y.; VanBrocklin, H.F.; Courtney Broaddus, V.; et al. The effect of internalizing human single chain antibody fragment on liposome targeting to epithelioid and sarcomatoid mesothelioma. *Biomaterials* **2011**, *32*. [CrossRef] [PubMed]

46. Jain, A.; Kesharwani, P.; Garg, N.K.; Jain, A.; Nirbhavane, P.; Dwivedi, N.; Banerjee, S.; Iyer, A.K.; Mohd Amin, M.C.I. Nano-constructed carriers loaded with antioxidant: Boon for cardiovascular system. *Curr. Pharm. Des.* **2015**, *21*, 4456–4464. [CrossRef] [PubMed]

47. Ng, K.E.; Amin, M.C.I.M.; Katas, H.; Amjad, M.W.; Butt, A.M.; Kesharwani, P.; Iyer, A.K. pH-responsive triblock copolymeric micelles decorated with a cell-penetrating peptide provide efficient doxorubicin delivery. *Nanoscale Res. Lett.* **2016**, *11*. [CrossRef] [PubMed]

48. Mahor, A.; Prajapati, S.K.; Verma, A.; Gupta, R.; Iyer, A.K.; Kesharwani, P. Moxifloxacin loaded gelatin nanoparticles for ocular delivery: Formulation and in vitro, in vivo evaluation. *J. Colloid Interface Sci.* **2016**, *483*. [CrossRef] [PubMed]

49. Daruwalla, J.; Greish, K.; Malcontenti-Wilson, C.; Muralidharan, V.; Iyer, A.; Maeda, H.; Christophi, C. Styrene maleic acid-pirarubicin disrupts tumor microcirculation and enhances the permeability of colorectal liver metastases. *J. Vasc. Res.* **2009**, *46*, 218–228. [CrossRef] [PubMed]

50. Daruwalla, J.; Greish, K.; Nikfarjam, M.; Millar, I.; Malcontenti-Wilson, C.; Iyer, A.K.; Christophi, C. Evaluation of the effect of SMA-pirarubicin micelles on colorectal cancer liver metastases and of hyperbaric oxygen in CBA mice. *J. Drug Target.* **2007**, *15*. [CrossRef] [PubMed]

51. Susa, M.; Iyer, A.K.; Ryu, K.; Hornicek, F.J.; Mankin, H.; Amiji, M.M.; Duan, Z. Doxorubicin loaded polymeric nanoparticulate delivery system to overcome drug resistance in osteosarcoma. *BMC Cancer* **2009**, *9*. [CrossRef] [PubMed]

52. Kobayashi, E.; Iyer, A.K.; Hornicek, F.J.; Amiji, M.M.; Duan, Z. Lipid-functionalized dextran nanosystems to overcome multidrug resistance in cancer: A pilot study basic research. *Clin. Orthop. Relat. Res.* **2013**, *471*. [CrossRef] [PubMed]

53. Kesharwani, P.; Banerjee, S.; Padhye, S.; Sarkar, F.H.; Iyer, A.K. Parenterally administrable nano-micelles of 3,4-difluorobenzylidene curcumin for treating pancreatic cancer. *Colloids Surf. B Biointerfaces* **2015**, *132*, 138–145. [CrossRef] [PubMed]

54. Amjad, M.W.; Kesharwani, P.; Mohd Amin, M.C.I.; Iyer, A.K. Recent advances in the design, development, and targeting mechanisms of polymeric micelles for delivery of siRNA in cancer therapy. *Prog. Polym. Sci.* **2017**, *64*, 154–181. [CrossRef]

55. Iyer, A.K.; Singh, A.; Ganta, S.; Amiji, M.M. Role of integrated cancer nanomedicine in overcoming drug resistance. *Adv. Drug Deliv. Rev.* **2013**, *65*, 1784–1802. [CrossRef] [PubMed]

56. Iyer, A.K.; He, J.; Amiji, M.M. Image-guided nanosystems for targeted delivery in cancer therapy. *Curr. Med. Chem.* **2012**, *19*, 3230–3240. [CrossRef] [PubMed]

57. Singh, A.; Iyer, A.K.; Amiji, M.; Ganta, S. *Multifunctional Nanosystems for Cancer Therapy*; Elsevier: Amsterdam, The Netherlands, 2013; ISBN 9780857096647.

58. Iyer, A.; Ganta, S.; Amiji, M. *Polymeric Nanoparticles as Target-Specific Delivery Systems*; Pan Stanford: Boca Raton, FL, USA, 2010; ISBN 9789814267557.

59. Patel, R.; Patel, M.; Kwak, J.; Iyer, A.K.; Karpoormath, R.; Desai, S.; Rarh, V. Polymeric microspheres: A delivery system for osteogenic differentiation. *Polym. Adv. Technol.* **2017**, *28*. [CrossRef]

60. Zhang, L.; Iyer, A.K.; Yang, X.; Kobayashi, E.; Guo, Y.; Mankin, H.; Hornicek, F.J.; Amiji, M.M.; Duan, Z. Polymeric nanoparticle-based delivery of microRNA-199a-3p inhibits proliferation and growth of osteosarcoma cells. *Int. J. Nanomed.* **2015**, *10*, 2913–2924.

61. Iyer, A.K.; Greish, K.; Seki, T.; Okazaki, S.; Fang, J.; Takeshita, K.; Maeda, H. Polymeric micelles of zinc protoporphyrin for tumor targeted delivery based on EPR effect and singlet oxygen generation. *J. Drug Target.* **2007**, *15*. [CrossRef] [PubMed]

62. Iyer, A.K.; Greish, K.; Fang, J.; Murakami, R.; Maeda, H. High-loading nanosized micelles of copoly(styrene-maleic acid)-zinc protoporphyrin for targeted delivery of a potent heme oxygenase inhibitor. *Biomaterials* **2007**, *28*, 1871–1881. [CrossRef] [PubMed]

63. Tatiparti, K.; Sau, S.; Kashaw, S.; Iyer, A. siRNA delivery strategies: A comprehensive review of recent developments. *Nanomaterials* **2017**, *7*, 77. [CrossRef] [PubMed]

64. Kesharwani, P.; Iyer, A.K. Recent advances in dendrimer-based nanovectors for tumor-targeted drug and gene delivery. *Drug Discov. Today* **2015**, *20*, 536–547. [CrossRef] [PubMed]

65. Iyer, A.K.; Ave, M. Rational Design of Multifunctional Nanoparticles for Targeted Cancer Imaging and Therapy. In *Post-Genomic Approaches in Cancer and Nano Medicine*; River Publishers: Gistrup, Denmark, 2016; pp. 609–656.

66. Hyung, W.; Ko, H.; Park, J.; Lim, E.; Sung, B.P.; Park, Y.J.; Ho, G.Y.; Jin, S.S.; Haam, S.; Huh, Y.M. Novel hyaluronic acid (HA) coated drug carriers (HCDCs) for human breast cancer treatment. *Biotechnol. Bioeng.* **2008**, *99*, 442–454. [CrossRef] [PubMed]

67. Huang, Y.; Mao, K.; Zhang, B.; Zhao, Y. Superparamagnetic iron oxide nanoparticles conjugated with folic acid for dual target-specific drug delivery and MRI in cancer theranostics. *Mater. Sci. Eng. C* **2017**, *70*, 763–771. [CrossRef] [PubMed]

68. Ganapathy, V.; Moghe, P.V.; Roth, C.M. Targeting tumor metastases: Drug delivery mechanisms and technologies. *J. Control. Release* **2015**, *219*, 215–223. [CrossRef] [PubMed]

69. Feng, S.S.; Mei, L.; Anitha, P.; Gan, C.W.; Zhou, W. Poly(lactide)-vitamin E derivative/montmorillonite nanoparticle formulations for the oral delivery of Docetaxel. *Biomaterials* **2009**, *30*, 3297–3306. [CrossRef] [PubMed]

70. Cui, M.; Naczynski, D.; Zevon, M.; Griffith, C.K.; Sheihet, L.; Poventud-Fuentes, I.; Chen, S.; Roth, C.M.; Moghe, P.V. Multifunctional albumin nanoparticles as combination drug carriers for intra-tumoral chemotherapy. *Adv. Healthc. Mater.* **2013**, *2*, 1236–1245. [CrossRef] [PubMed]

71. Basak, S.K.; Zinabadi, A.; Wu, A.W.; Venkatesan, N.; Duarte, V.M.; Kang, J.J.; Dalgard, C.L.; Srivastava, M.; Sarkar, F.H.; Wang, M.B.; et al. Liposome encapsulated curcumin-difluorinated (CDF) inhibits the growth of cisplatin resistant head and neck cancer stem cells. *Oncotarget* **2015**, *6*, 18504–18517. [CrossRef] [PubMed]

72. Kanapathipillai, M.; Brock, A.; Ingber, D.E. Nanoparticle targeting of anti-cancer drugs that alter intracellular signaling or influence the tumor microenvironment. *Adv. Drug Deliv. Rev.* **2014**, *79*, 107–118. [CrossRef] [PubMed]

73. Kim, T.H.; Jiang, H.H.; Youn, Y.S.; Park, C.W.; Tak, K.K.; Lee, S.; Kim, H.; Jon, S.; Chen, X.; Lee, K.C. Preparation and characterization of water-soluble albumin-bound curcumin nanoparticles with improved antitumor activity. *Int. J. Pharm.* **2011**, *403*, 285–291. [CrossRef] [PubMed]

74. Kim, W.; Thévenot, J.; Ibarboure, E.; Lecommandoux, S.; Chaikof, E.L. Self-assembly of thermally responsive amphiphilic diblock copolypeptides into spherical micellar nanoparticles. *Angew. Chem. Int. Ed.* **2010**, *49*, 4257–4260. [CrossRef] [PubMed]

75. Koide, H.; Yoshimatsu, K.; Hoshino, Y.; Lee, S.H.; Okajima, A.; Ariizumi, S.; Narita, Y.; Yonamine, Y.; Weisman, A.C.; Nishimura, Y.; et al. A polymer nanoparticle with engineered affinity for a vascular endothelial growth factor (VEGF165). *Nat. Chem.* **2017**, *9*, 715–722. [CrossRef] [PubMed]

76. Makadia, H.K.; Siegel, S.J. Poly lactic-*co*-glycolic acid (PLGA) as biodegradable controlled drug delivery carrier. *Polymers* **2011**, *3*, 1377–1397. [CrossRef] [PubMed]

77. Mohammadi, M.; Ramezani, M.; Abnous, K.; Alibolandi, M. Biocompatible polymersomes-based cancer theranostics: Towards multifunctional nanomedicine. *Int. J. Pharm.* **2017**, *519*, 287–303. [CrossRef] [PubMed]

78. Padhye, S.; Banerjee, S.; Chavan, D.; Pandye, S.; Swamy, K.V.; Ali, S.; Li, J.; Dou, Q.P.; Sarkar, F.H. Fluorocurcumins as cyclooxygenase-2 inhibitor: Molecular docking, pharmacokinetics and tissue distribution in mice. *Pharm. Res.* **2009**, *26*, 2438–2445. [CrossRef] [PubMed]

79. Roy, E.; Patra, S.; Madhuri, R.; Sharma, P.K. Stimuli-responsive poly (*N*-isopropyl acrylamide)-*co*-tyrosine@ gadolinium: Iron oxide nanoparticle-based nanotheranostic for cancer diagnosis and treatment. *Colloids Surf. B Biointerfaces* **2016**, *142*, 248–258. [CrossRef] [PubMed]

80. Song, Z.; Feng, R.; Sun, M.; Guo, C.; Gao, Y.; Li, L.; Zhai, G. Curcumin-loaded PLGA-PEG-PLGA triblock copolymeric micelles: Preparation, pharmacokinetics and distribution in vivo. *J. Colloid Interface Sci.* **2011**, *354*, 116–123. [CrossRef] [PubMed]

81. Wayua, C.; Roy, J.; Putt, K.S.; Low, P.S. Selective tumor targeting of desacetyl vinblastine hydrazide and tubulysin b via conjugation to a cholecystokinin 2 receptor (CCK2R) ligand. *Mol. Pharm.* **2015**, *12*, 2477–2483. [CrossRef] [PubMed]

82. Maeda, H. Toward a full understanding of the EPR effect in primary and metastatic tumors as well as issues related to its heterogeneity. *Adv. Drug Deliv. Rev.* **2015**, *91*, 3–6. [CrossRef] [PubMed]

83. Maeda, H. The enhanced permeability and retention (EPR) effect in tumor vasculature: The key role of tumor-selective macromolecular drug targeting. *Adv. Enzym. Regul.* **2001**, *41*, 189–207. [CrossRef]

84. Maeda, H.; Wu, J.; Sawa, T.; Matsumura, Y.; Hori, K. Tumor vascular permeability and the EPR effect in macromolecular therapeutics: A review. *J. Control. Release* **2000**, *65*, 271–284. [CrossRef]

85. Nakamura, Y.; Mochida, A.; Choyke, P.L.; Kobayashi, H. Nanodrug delivery: Is the enhanced permeability and retention effect sufficient for curing cancer? *Bioconjug. Chem.* **2016**, *27*, 2225–2238. [CrossRef] [PubMed]

86. Greish, K. Enhanced permeability and retention effect for selective targeting of anticancer nanomedicine: Are we there yet? *Drug Discov. Today Technol.* **2012**, *9*, e161–e166. [CrossRef] [PubMed]

87. Maeda, H. SMANCS and polymer-conjugated macromolecular drugs: Advantages in cancer chemotherapy. *Adv. Drug Deliv. Rev.* **2001**, *46*, 169–185. [CrossRef]

88. Iyer, A.K.; Khaled, G.; Fang, J.; Maeda, H. Exploiting the enhanced permeability and retention effect for tumor targeting. *Drug Discov. Today* **2006**, *11*, 812–818. [CrossRef] [PubMed]

89. Gatti, L.; Sevko, A.; de Cesare, M.; Arrighetti, N.; Manenti, G.; Ciusani, E.; Verderio, P.; Ciniselli, C.M.; Cominetti, D.; Carenini, N.; et al. Histone deacetylase inhibitor-temozolomide co-treatment inhibits melanoma growth through suppression of Chemokine (C-C motif) ligand 2-driven signals. *Oncotarget* **2014**, *5*, 4516–4528. [CrossRef] [PubMed]

90. Sau, S.; Banerjee, R. Cationic lipid-conjugated dexamethasone as a selective antitumor agent. *Eur. J. Med. Chem.* **2014**, *83*, 433–447. [CrossRef] [PubMed]

91. Peer, D.; Karp, J.M.; Hong, S.; Farokhzad, O.C.; Margalit, R.; Langer, R. Nanocarriers as an emerging platform for cancer therapy. *Nat. Nanotechnol.* **2007**, *2*, 751–760. [CrossRef] [PubMed]

92. Sau, S.; Alsaab, H.O.; Kashaw, S.K.; Tatiparti, K.; Iyer, A.K. Advances in antibody?drug conjugates: A new era of targeted cancer therapy. *Drug Discov. Today* **2017**. [CrossRef] [PubMed]

93. He, X.M.; Carter, D.C. Atomic structure and chemistry of human serum albumin. *Nature* **1992**, *358*, 209–215. [CrossRef] [PubMed]

94. Langer, K.; Balthasar, S.; Vogel, V.; Dinauer, N.; von Briesen, H.; Schubert, D. Optimization of the preparation process for human serum albumin (HSA) nanoparticles. *Int. J. Pharm.* **2003**, *257*, 169–180. [CrossRef]

95. Trerè, D.; Fiume, L.; De Giorgi, L.B.; Di Stefano, G.; Migaldi, M.; Derenzini, M. The asialoglycoprotein receptor in human hepatocellular carcinomas: Its expression on proliferating cells. *Br. J. Cancer* **1999**, *81*, 404–408. [CrossRef] [PubMed]

96. Weber, C.; Reiss, S.; Langer, K. Preparation of surface modified protein nanoparticles by introduction of sulfhydryl groups. *Int. J. Pharm.* **2000**, *211*, 67–78. [CrossRef]

97. Petitpas, I.; Bhattacharya, A.A.; Twine, S.; East, M.; Curry, S. Crystal structure analysis of warfarin binding to human serum albumin. Anatomy of drug site I. *J. Biol. Chem.* **2001**, *276*, 22804–22809. [CrossRef] [PubMed]

98. Elzoghby, A.O.; Samy, W.M.; Elgindy, N.A. Albumin-based nanoparticles as potential controlled release drug delivery systems. *J. Control. Release* **2012**, *157*, 168–182. [CrossRef] [PubMed]

99. Elsadek, B.; Kratz, F. Impact of albumin on drug delivery—New applications on the horizon. *J. Control. Release* **2012**, *157*, 4–28. [CrossRef] [PubMed]

100. Rhaese, S.; Von Briesen, H.; Rübsamen-Waigmann, H.; Kreuter, J.; Langer, K. Human serum albumin-polyethylenimine nanoparticles for gene delivery. *J. Control. Release* **2003**, *92*, 199–208. [CrossRef]

101. Simoes, S.; Slepushkin, V.; Pires, P.; Gaspar, R.; Pedroso de Lima, M.C.; Düzgüneş, N. Human serum albumin enhances DNA transfection by lipoplexes and confers resistance to inhibition by serum. *Biochim. Biophys. Acta* **2000**, *1463*, 459–469. [CrossRef]

102. Larsen, M.T.; Kuhlmann, M.; Hvam, M.L.; Howard, K.A. Albumin-based drug delivery: Harnessing nature to cure disease. *Mol. Cell. Ther.* **2016**, *4*, 3. [CrossRef] [PubMed]

103. Fonseca, D.P.; Khalil, N.M.; Mainardes, R.M. Bovine serum albumin-based nanoparticles containing resveratrol: Characterization and antioxidant activity. *J. Drug Deliv. Sci. Technol.* **2017**, *39*, 147–155. [CrossRef]

104. Švastová, E.; Hulíková, A.; Rafajová, M.; Zaťovičová, M.; Gibadulinová, A.; Casini, A.; Cecchi, A.; Scozzafava, A.; Supuran, C.T.; Pastorek, J.; et al. Hypoxia activates the capacity of tumor-associated carbonic anhydrase IX to acidify extracellular pH. *FEBS Lett.* **2004**, *577*, 439–445. [CrossRef] [PubMed]

105. Pastorekova, S.; Pastorek, J. *Carbonic Anhydrase, Its Inhibitors and Activators*; CRC Press: Boca Raton, FL, USA, 2004.

106. Pastorek, J.; Pastorekova, S. Hypoxia-induced carbonic anhydrase IX as a target for cancer therapy: From biology to clinical use. *Semin. Cancer Biol.* **2015**, *31*, 52–64. [CrossRef] [PubMed]

107. Sneddon, D.; Poulsen, S.A. Agents described in the Molecular Imaging and Contrast Agent Database for imaging carbonic anhydrase IX expression. *J. Enzym. Inhib. Med. Chem.* **2014**, *29*, 753–763. [CrossRef] [PubMed]

108. Tafreshi, N.K.; Lloyd, M.C.; Bui, M.M.; Gillies, R.J.; Morse, D.L. Chapter 13: Carbonic Anhydrase IX as an Imaging and Therapeutic Target for Tumors and Metastases. In *Carbonic Anhydrase: Mechanism, Regulation, Links to Disease, and Industrial Applications*; Springer: Dordrecht, The Netherlands, 2014; Volume 75, pp. 221–254, ISBN 978-94-007-7358-5.

109. Mohan, R.; Banerjee, M.; Ray, A.; Manna, T.; Wilson, L.; Owa, T.; Bhattacharyya, B.; Panda, D. Antimitotic sulfonamides inhibit microtubule assembly dynamics and cancer cell proliferation. *Biochemistry* **2006**, *45*, 5440–5449. [CrossRef] [PubMed]

110. Owa, T.; Yoshino, H.; Okauchi, T.; Yoshimatsu, K.; Ozawa, Y.; Sugi, N.H.; Nagasu, T.; Koyanagi, N.; Kitoh, K. Discovery of novel antitumor sulfonamides targeting G1 phase of the cell cycle. *J. Med. Chem.* **1999**, *42*, 3789–3799. [CrossRef] [PubMed]

111. Schrier, R.W. *Renal and Electrolyte Disorders*; Little Brown and Co.: Boston, MA, USA, 1976.

112. Chegwidden, W.R.; Spencer, I. Sulfonamide inhibitors of carbonic anhydrase inhibit the growth of human lymphoma cells in culture. *Inflammopharmacology* **1995**, *3*, 231–239. [CrossRef]

113. Gradishar, W.J. Albumin-bound paclitaxel: A next-generation taxane. *Expert Opin. Pharmacother.* **2006**, *7*, 1041–1053. [CrossRef] [PubMed]

114. Stinchcombe, T.E. Nanoparticle albumin-bound paclitaxel: A novel Cremphor-EL®-free formulation of paclitaxel. *Nanomedicine* **2007**, *2*, 415–423. [CrossRef] [PubMed]

115. Liggins, R.T.; Hunter, W.L.; Burt, H.M. Solid-state characterization of paclitaxel. *J. Pharm. Sci.* **1997**, *86*, 1458–1463. [CrossRef] [PubMed]

116. Perez, E. Paclitaxel in Breast Cancer. *Oncologist* **1998**, *3*, 373–389. [PubMed]

117. Weaver, B.A. How Taxol/paclitaxel kills cancer cells. *Mol. Biol. Cell* **2014**, *25*, 2677–2681. [CrossRef] [PubMed]

118. Ledaki, I.; McIntyre, A.; Wigfield, S.; Buffa, F.; McGowan, S.; Baban, D.; Li, J.; Harris, A.L.; Ledaki, I.; McIntyre, A.; et al. Carbonic anhydrase IX induction defines a heterogeneous cancer cell response to hypoxia and mediates stem cell-like properties and sensitivity to HDAC inhibition. *Oncotarget* **2015**, *6*, 19413–19427. [CrossRef] [PubMed]

119. Triantafyllou, A.; Liakos, P.; Tsakalof, A.; Georgatsou, E.; Simos, G.; Bonanou, S. Cobalt induces hypoxia-inducible factor-1α (HIF-1α) in HeLa cells by an iron-independent, but ROS-, PI-3K- and MAPK-dependent mechanism. *Free Radic. Res.* **2006**, *40*, 847–856. [CrossRef] [PubMed]

120. Mukherjee, S.; Sau, S.; Madhuri, D.; Bollu, V.S.; Madhusudana, K.; Sreedhar, B.; Banerjee, R.; Patra, C.R. Green synthesis and characterization of monodispersed gold nanoparticles: Toxicity study, delivery of doxorubicin and its bio-distribution in mouse model. *J. Biomed. Nanotechnol.* **2016**, *12*, 165–181. [CrossRef] [PubMed]

121. Moses, J.E.; Moorhouse, A.D. The growing applications of click chemistry. *Chem. Soc. Rev.* **2007**, *36*, 1249–1262. [CrossRef] [PubMed]

122. Lutz, J.F.; Zarafshani, Z. Efficient construction of therapeutics, bioconjugates, biomaterials and bioactive surfaces using azide-alkyne "click" chemistry. *Adv. Drug Deliv. Rev.* **2008**, *60*, 958–970. [CrossRef] [PubMed]

123. Tafreshi, N.K.; Lloyd, M.C.; Proemsey, J.B.; Bui, M.M.; Kim, J.; Gillies, R.J.; Morse, D.L. Evaluation of CAIX and CAXII expression in breast cancer at varied O2Levels: CAIX is the superior surrogate imaging biomarker of tumor hypoxia. *Mol. Imaging Biol.* **2016**, *18*, 219–231. [CrossRef] [PubMed]

124. Holliday, D.L.; Speirs, V. Choosing the right cell line for breast cancer research. *Breast Cancer Res.* **2011**, *13*, 215. [CrossRef] [PubMed]

125. Srinivasarao, M.; Galliford, C.V.; Low, P.S. Principles in the design of ligand-targeted cancer therapeutics and imaging agents. *Nat. Rev. Drug Discov.* **2015**, *14*, 203–219. [CrossRef] [PubMed]

126. Xu, S.; Olenyuk, B.Z.; Okamoto, C.T.; Hamm-Alvarez, S.F. Targeting receptor-mediated endocytotic pathways with nanoparticles: Rationale and advances. *Adv. Drug Deliv. Rev.* **2013**, *65*, 121–138. [CrossRef] [PubMed]

127. Yoo, H.S.; Park, T.G. Folate-receptor-targeted delivery of doxorubicin nano-aggregates stabilized by doxorubicin-PEG-folate conjugate. *J. Control. Release* **2004**, *100*, 247–256. [CrossRef] [PubMed]
128. Pastorekova, S.; Zatovicova, M.; Pastorek, J. Cancer-associated carbonic anhydrases and their inhibition. *Curr. Pharm. Des.* **2008**, *14*, 685–698. [CrossRef] [PubMed]
129. Winum, J.-Y.; Scozzafava, A.; Montero, J.-L.; Supuran, C.T. Inhibition of carbonic anhydrase IX: A new strategy against cancer. *Anticancer Agents Med. Chem.* **2009**, *9*, 693–702. [CrossRef] [PubMed]
130. Supuran, C.T. Carbonic anhydrase inhibitors. *Bioorg. Med. Chem. Lett.* **2010**, *20*, 3467–3474. [CrossRef] [PubMed]
131. Winum, J.Y.; Rami, M.; Scozzafava, A.; Montero, J.L.; Supuran, C. Carbonic anhydrase IX: A new druggable target for the design of antitumor agents. *Med. Res. Rev.* **2008**, *28*, 445–463. [CrossRef] [PubMed]
132. Supuran, C.; Briganti, F.; Tilli, S.; Chegwidden, W.; Scozzafava, A. Carbonic anhydrase inhibitors: Sulfonamides as antitumor agents? *Bioorg. Med. Chem.* **2001**, *9*, 703–714. [CrossRef]
133. Panda, D. Antimitotic sulfonamide inhibit microtubule assembly dynamics & anticancer. *Biochemistry* **2006**, *45*, 5440.
134. Galisteo-González, F.; Molina-Bolívar, J.A. Systematic study on the preparation of BSA nanoparticles. *Colloids Surf. B Biointerfaces* **2014**, *123*, 286–292. [CrossRef] [PubMed]
135. Jithan, A.; Madhavi, K.; Madhavi, M.; Prabhakar, K. Preparation and characterization of albumin nanoparticles encapsulating curcumin intended for the treatment of breast cancer. *Int. J. Pharm. Investig.* **2011**, *1*, 119–125. [CrossRef] [PubMed]
136. Lock, F.E.; McDonald, P.C.; Lou, Y.; Serrano, I.; Chafe, S.C.; Ostlund, C.; Aparicio, S.; Winum, J.Y.; Supuran, C.T.; Dedhar, S. Targeting carbonic anhydrase IX depletes breast cancer stem cells within the hypoxic niche. *Oncogene* **2013**, *32*, 5210–5219. [CrossRef] [PubMed]
137. Ivanova, L.; Zandberga, E.; Siliņa, K.; Kalniņa, Z.; Ābols, A.; Endzeliņš, E.; Vendina, I.; Romanchikova, N.; Hegmane, A.; Trapencieris, P.; et al. Prognostic relevance of carbonic anhydrase IX expression is distinct in various subtypes of breast cancer and its silencing suppresses self-renewal capacity of breast cancer cells. *Cancer Chemother. Pharmacol.* **2015**, *75*, 235–246. [CrossRef] [PubMed]

Article

Identification and Evaluation of Cytotoxicity of Peptide Liposome Incorporated Citron Extracts in an in Vitro System

Xiaowei Zhang [1],[†], Hee Jeong Yoon [1],[†], Min Gyeong Kang [1], Gyeong Jin Kim [1], Sun Young Shin [2], Sang Hong Baek [2], Jung Gyu Lee [3], Jingjing Bai [3], Sang Yoon Lee [3], Mi Jung Choi [3], Kwonho Hong [4] and Hojae Bae [4],*

[1] Department of Bioindustrial Technologies, College of Animal Bioscience and Technology, Konkuk University, Seoul 05029, Korea; zhangxiaowei9304@gmail.com (X.Z.); rose_0013@naver.com (H.J.Y.); vq1004pv@naver.com (M.G.K.); kkg0118@gmail.com (G.J.K.)
[2] Laboratory of Cardiovascular Regeneration, Division of Cardiology, Seoul St. Mary's Hospital, The Catholic University of Korea School of Medicine, Seoul 02841, Korea; tempast606@naver.com (S.Y.S.); whitesh@catholic.ac.kr (S.H.B.)
[3] Department of Food Science and Biotechnology of Animal Resources, Sanghuh College of Life Sciences, Konkuk University, Seoul 02841, Korea; nocturne933@gmail.com (J.G.L.); baiijing@naver.com (J.B.); dhgus4211@naver.com (S.Y.L.); choimj@konkuk.ac.kr (M.J.C.)
[4] Department of Stem Cell and Regenerative Biotechnology, KU Convergence Science and Technology Institute, Konkuk University, Seoul 05029, Korea; hongkh27@gmail.com
* Correspondence: hojaebae@konkuk.ac.kr; Tel.: +82-2-450-0525; Fax: +82-2-455-1044
† These authors equally contributed to this work.

Abstract: Citrons have been widely used for medicinal purposes for a long time, but the application of citron in the food industry is still restricted. The extensive advantages of nanotechnology in the food industry have greatly broadened the application of foods. In this study, by employing nanotechnology, we prepared citron-extract nanoparticle with an average size of 174.11 ± 3.89 nm, containing protein peptide and/or liposome. In order to evaluate the toxicity of nanoparticles and to ensure food safety, biological cytotoxicity at the cell and genomic levels was also identified to examine the toxicity of citron extracts by using an in vitro system. Our results demonstrated that the cytotoxicity of $citron_{liposome}$ was dependent on cell type in high concentrations (1 and 5 mg/mL), selectively against primary human cardiac progenitor cells (hCPCs), and human endothelial progenitor cells (hEPCs) in MTT and lactate dehydrogenase (LDH) assays. Interestingly, for the NIH-3T3 and H9C2 cell lines, cell cytotoxicity was observed with slight genotoxicity, especially from $citron_{peptide}$ extract for both cell lines. Taken together, our study provides cytotoxicity data on nanoengineered citron extracts according to different cell type as is crucial for further applications.

Keywords: citrus fruits; citron; nanotechnology; liposome; peptide; cell viability; cytotoxicity

1. Introduction

Citrus fruits have been consumed by humans for thousands of years, and are increasingly consumed worldwide for their nutritional and medicinal value [1]. Functional compounds, such as β-cryptoxanthin, β-carotene, folate, vitamin C, and quercetin are some recognized bioactive ingredients of citrus that defend against cancers [2–5]. For instance, some studies have reported that intake of citrus fruits results in reduced risk of breast and stomach cancers [6,7]. Other studies have focused on evaluating the antioxidant capacity of citrus extracts, their protective effect against oxidative damage, and other defensive responses against certain diseases such as lowering high blood-pressure

risk or preventing kidney-stone formation [8,9]. However, despite the increased demand for citrus, studies related to the potential toxicity of citrus fruits are limited and restricted. Therefore, the focal point of our study was to investigate and identify the toxicity of citrus fruits to ensure their safety for various applications.

The citron (*Citrus medica*) is one of the three original citrus species and has already developed extensive applications for medicinal purposes, such as to treat sea sickness, pulmonary troubles, and intestinal ailments. With the improvement of processing technology, various citron fruit applications that maximize its functional advantages have been developed, but are still limited because of the botanical characteristics of the citron. Unlike other citrus fruits, its thick white rind is the main content of the citron and its pulp is dry with little juice [10]. Hence, citron has had only restricted use in the food industry, mainly as candied peel. Meanwhile, few studies have provided a biological examination of citron, such as of its bioactivity, pharmacology, toxicology, or bioavailability. Therefore, experimental studies to improve use of the citron and to determine its biological properties are essential.

Nanotechnology, as a cutting-edge scientific field, has many prospects for applications in various fields, such as medicine delivery, computer electronics, materials science, and for the food industry [11]. The application of nanotechnology in food science not only significantly increases the economic benefits, but also remarkably reforms food quality and safety [12–14]. Given the special nature of nanoparticles, the changes in the properties of food products are apparent, such as the improvement of food bioavailability, solubility, stability, biological activity, and safety [14]. To broaden the application of the citron and to further elaborate its biological benefits, the citron was prepared in nanometer scale by means of nanotechnology, and experiments were performed to measure its cell viability and genotoxicity by employing diverse in vitro models. By conducting comparative studies, we evaluated the different effects of citron extracts on different cell lines at the cellular and genomic levels.

2. Results

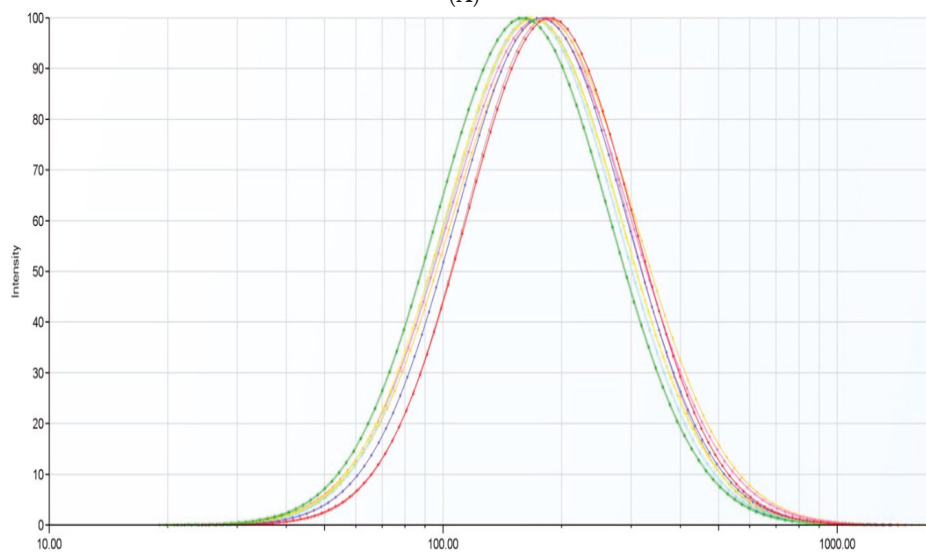### 2.1. Measurement of Nanoparticles

To evaluate the morphology and the size of citron nanoparticles, citron extracts were examined by using SEM and a Nano Size Analyzer (NanoBrook, Omni, Brookhaven Instruments Corporation, New York City, NY, USA). In our study, we labeled citron extract consisting of peptide with or without liposome as $citron_{liposome}$ and $citron_{peptide}$, respectively. The morphology of $citron_{peptide}$ and $citron_{liposome}$ is shown in Figure 1A. As can be seen from these images, typical particles within the size range of 120–150 nm were visible in both $citron_{peptide}$ and $citron_{liposome}$ test groups. In addition, Figure 1B shows the size distribution of citron extracts. $Citron_{peptide}$ cannot be analyzed by the Nano Size Analyzer. However, in the case of $citron_{liposome}$ group, nano-sized particles were detectable and exhibited a broad distribution with size, ranging from 60 to 300 nm (Figure 1B). The average size of $citron_{liposome}$ nanoparticle was 174.11 ± 3.89 nm.

2.2. Measurement of Cell Viability

In this study, three different types of citron extract samples (citron only, $citron_{peptide}$, and $citron_{liposome}$) were fabricated by using fish-skin peptide with or without liposome, as described in "Materials and Methods". Liposome, with its typical physical and chemical properties, has had broad applications, ranging from the delivery of functional flavors and nutrients, food additives, and food antimicrobials [15,16]. Protein peptide, as materials for food encapsulation, also plays an important role in various food applications and therefore we utilized nanoengineered liposome and peptide to extend citron usage in food products, and evaluate the potential biological cytotoxicity [17].
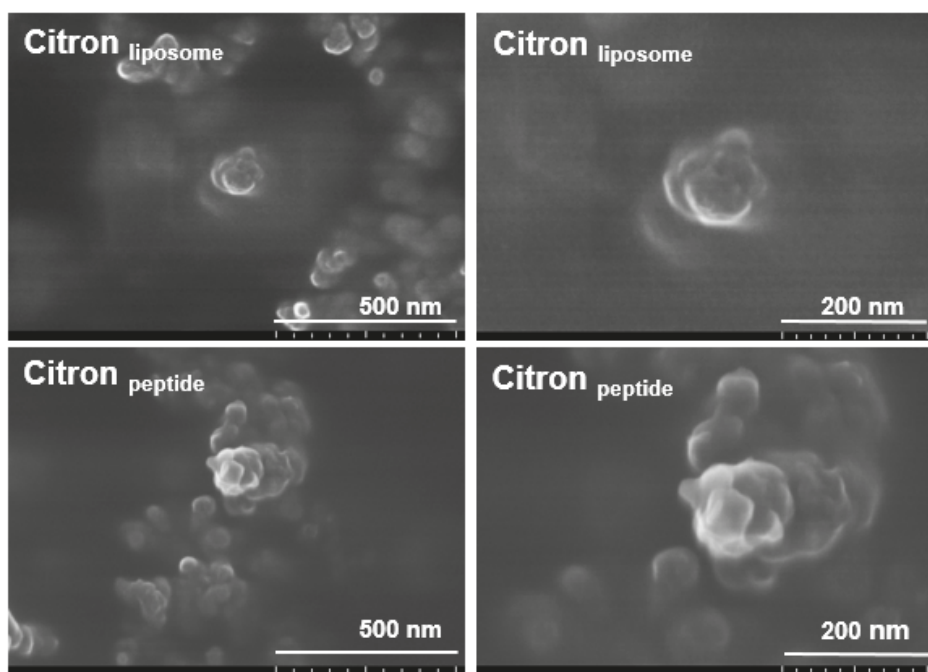
Figure 1. Nanoparticle measurements of citron, citron$_{peptide}$, and citron$_{liposome}$. (**A**) Citron extract powder was dispersed in PBS (10 mg/mL). Then 25–50 µL of dispersion was applied to a carbon tape and kept at room temperature until completely dried. After the gold coating, the morphology of the nanoparticles was analyzed by using field-emission scanning electron microscopy (FE-SEM, Hitachi SU-8010); (**B**) Citron$_{liposome}$ was dispersed in PBS at a final concentration of 10 mg/mL. Then the size of samples was measured at 640 nm by NanoBrook Omni Analyzer. The curves showed similar output from three identical samples.

Six different cell lines (HepG2, NIH-3T3, Caco-2, H9C2, primary hCPCs, and primary hEPCs) were employed to test the cell viability by the MTT method. As can be seen from Figure 2, neither citron, citron$_{peptide}$ or citron$_{liposome}$ induced any cell toxicity in the HepG2, NIH-3T3, and Caco-2 cell lines, even at the highest tested concentration of 5 mg/mL (Figure 2B,C,E). Interestingly, a dose-response pattern was apparently seen in the other three cell lines. In other words, the cell viability decreased with the increasing citron extract concentration. For instance, after treatment of citron and citron$_{peptide}$, no effect was observed on H9C2 cells (Figure 2D), but in primary hCPCs and hEPCs, the percentage of living cells was reduced to around 50% at 5 mg/mL (Figure 2B,F). In addition, citron$_{liposome}$ exhibited higher toxic effects than did citron and citron$_{peptide}$ against H9C2 (Figure 2D), hCPCs, and hEPCs, with only 4% cell survival in hCPCs at 5 mg/mL (Figure 2F). It was clear that cytotoxicity of citron extracts showed cell type selectivity.
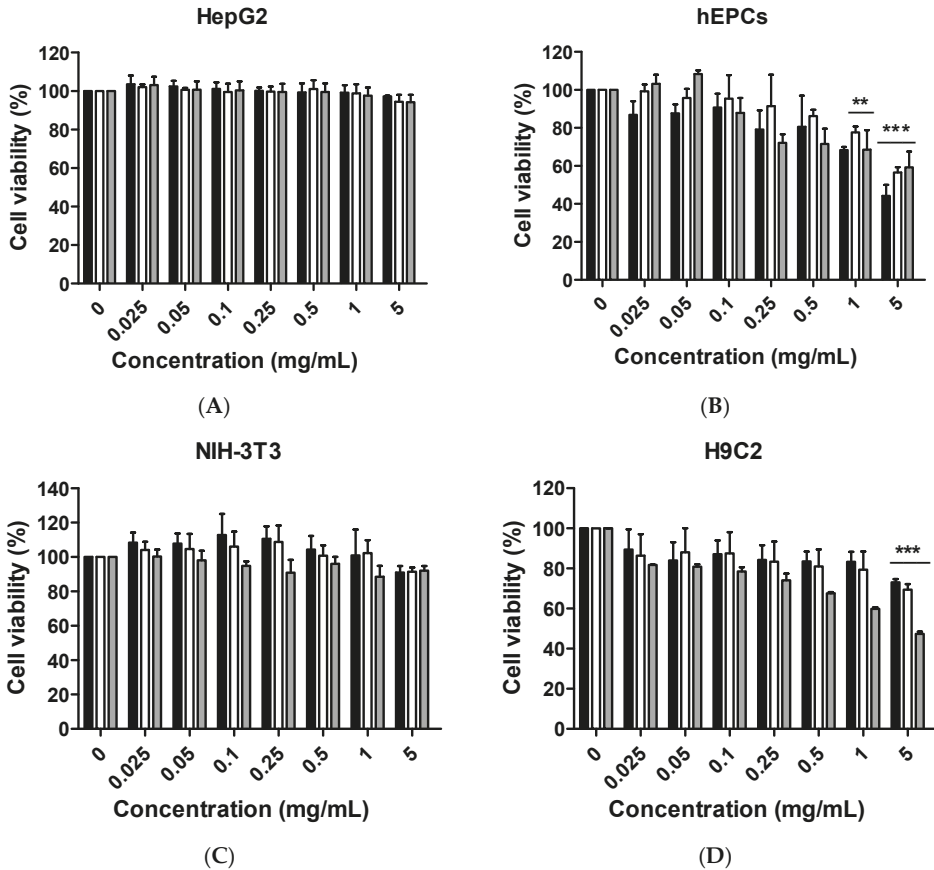

Figure 2. *Cont.*
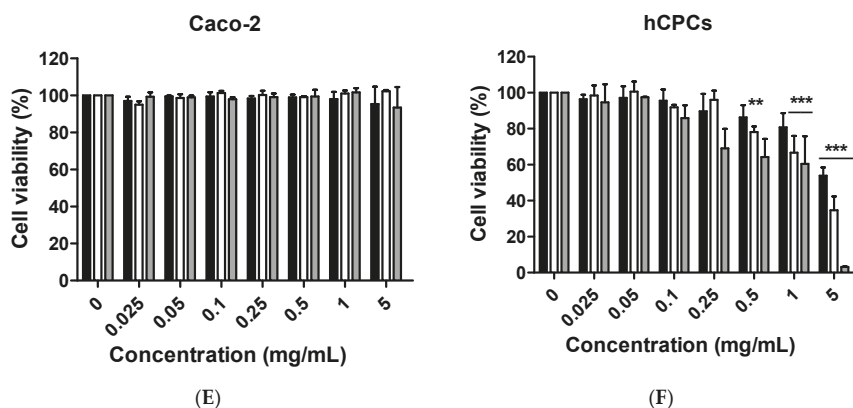
Figure 2. Cell viability measurement of citron, citron$_{peptide}$, and citron$_{liposome}$ by MTT assay. (**A**) HepG2 cells were cultured to the indicated time in 96-well plates. Then, the cells were treated with increasing concentrations of tested samples, as shown in the figure. After incubation for 24 h, cell viability was measured by MTT assay as described in "Materials and Methods"; (**B**) primary hEPC cell line; (**C**) NIH-3T3 cell line; (**D**) H9C2 cell line; (**E**) Caco-2 cell line; and, (**F**) primary hCPC cell line. The data were analyzed by using GraphPad Prism 5.0. Representative data is shown from three independent experiments with similar outcomes. Color in graph: Black, Citron; White, Citron$_{peptide}$; Gray, Citron$_{liposome}$. Significant results from the control group are calculated and marked with asterisks ** $p < 0.01$, *** $p < 0.001$).

2.3. Visualization of Cell Viability

To further observe the cell cytotoxicity, the Live/Dead assay was conducted to visualize live and dead cells (shown in merged images in Figure 3 and Figure S1). The results were consistent with Figure 1. In Figure S1, no difference can be observed between the HepG2, NIH-3T3, Caco-2, and H9C2 cell lines (data only shows 5 mg/mL concentration). As expected, in Figure 3A, the ratio of live/dead cells increased in proportion to the sample concentration for hCPCs, but no difference could be distinguished in hEPCs (Figure 3B).
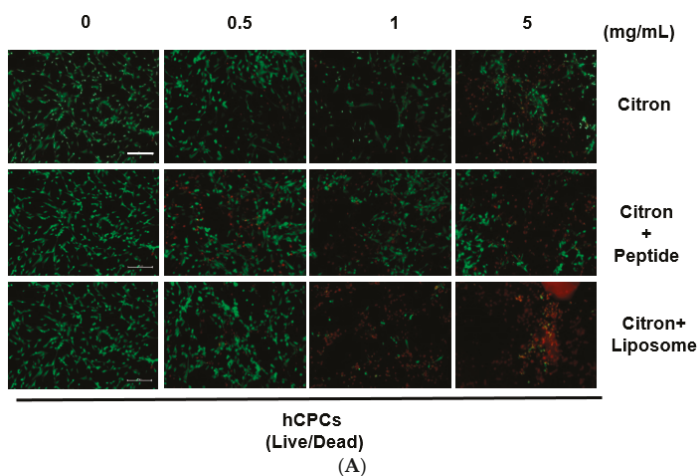

Figure 3. *Cont.*
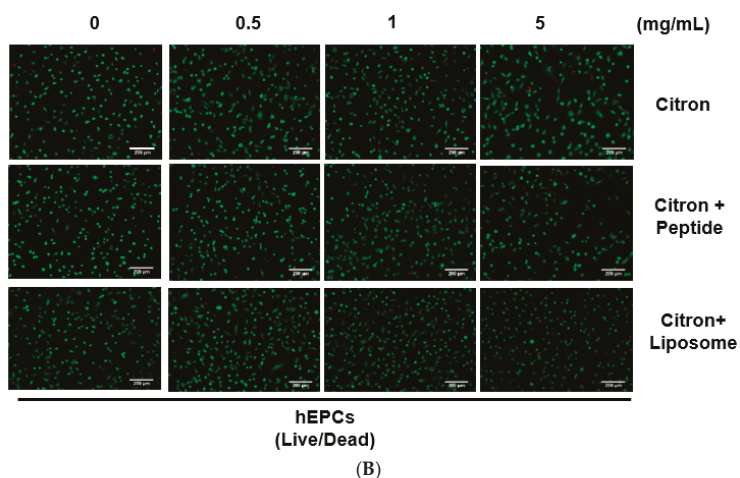
Figure 3. Visualization of Cell cytotoxicity by Live/Dead assay. (**A**) The primary hCPC cells were seeded into 48-well plates for this experiment. Following 24 h incubation after treatment of tested samples, the cells were stained by using fluorescent dyes according to the Live/Dead assay kit. The living cells are shown in green, the dead cells in red. The merged images in the figure show co-distribution of live and dead cells; (**B**) The primary hEPC cell line. Scale bar is 200 μm.

2.4. Measurement of Cytotoxicity

Figure 4 shows the effects of citron extracts on the cytotoxicity, as measured by the lactate dehydrogenase (LDH) release assay. The cytotoxicity did not significantly differ from the lowest concentration to the highest concentration, including the control group, in HepG2 and NIH-3T3 cells (Figure S2). However, both primary hCPCs and hEPCs were affected by the addition of the citron samples and showed cell death up to 50% at 5 mg/mL treatment (Figure 4A,B). Consistent with the result in Figure 1D, citron$_{liposome}$ showed a higher LDH activity than citron and citron$_{peptide}$ in H9C2 cell line (Figure 4C).
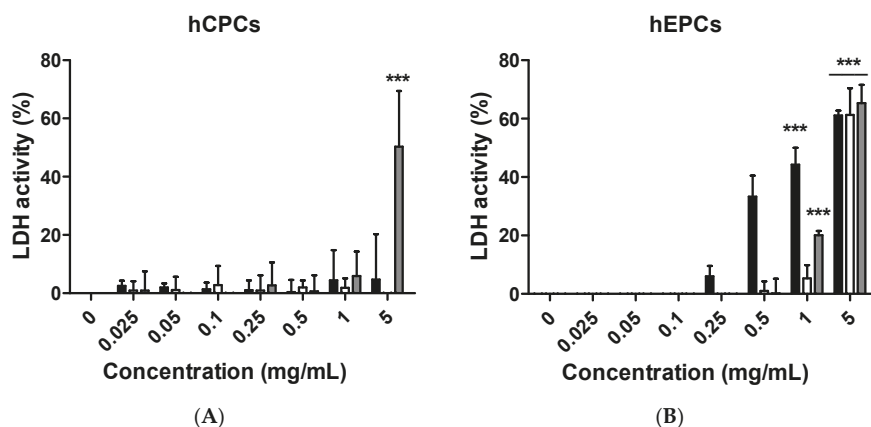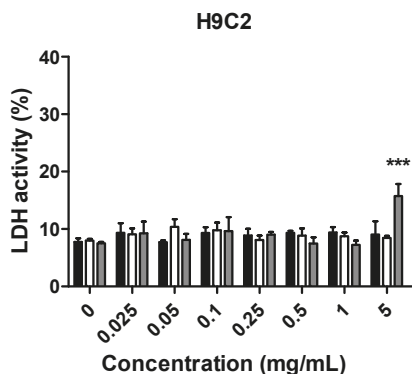

Figure 4. *Cont.*

(**C**)

Figure 4. Cytotoxicity measurement by EZ-LDH assay. (**A**) hCPC cells were cultured in 96-well plates. Then, the cells were incubated with different concentrations of citron extracts. After incubation for 24 h, cell cytotoxicity was measured by using EZ-LDH assay kits, according to the manufacturer's introduction; (**B**) primary hEPC cell line; (**C**) H9C2 cell line. GraphPad Prism 5.0 was used to analyze data and make graphs. The experiments were repeated three times with similar outcomes. Color in graph: Black, Citron; White, Citron$_{peptide}$; Gray, Citron$_{liposome}$. Significant results from the control group are calculated and marked with asterisks (*** $p < 0.001$).

2.5. Measurement of Genotoxicity

To evaluate whether the citron extracts affect genes, a single-cell gel electrophoresis assay (comet assay) was performed with the hCPCs, H9C2, and NIH-3T3 cell lines. Surprisingly, although citron extracts can cause cell cytotoxicity in hCPCs, with over 90% mortality of cells in the citron$_{liposome}$ group (Figure 2F), there was no detectable genotoxicity in the same cell line (Figure S3). In contrast, in the H9C2 and NIH-3T3 cells, as shown in Figure 5A,B, the proportion of tail DNA increased after citron$_{peptide}$ treatment, but no genotoxicity was observed in either the citron group or the citron$_{liposome}$ group. Interestingly, the genotoxicity disappeared in the presence of liposome in the citron$_{peptide}$ extract. Figure 5C displays the toxicity of citron$_{peptide}$ on genes in H9C2 and NIH-3T3 cells. It was evident that citron$_{peptide}$ selectively caused gene damage in NIH-3T3 cells. With the liposome in the citron extract to form nanoparticles, the damage to genes can be suppressed or abolished (Figure 5A,B).
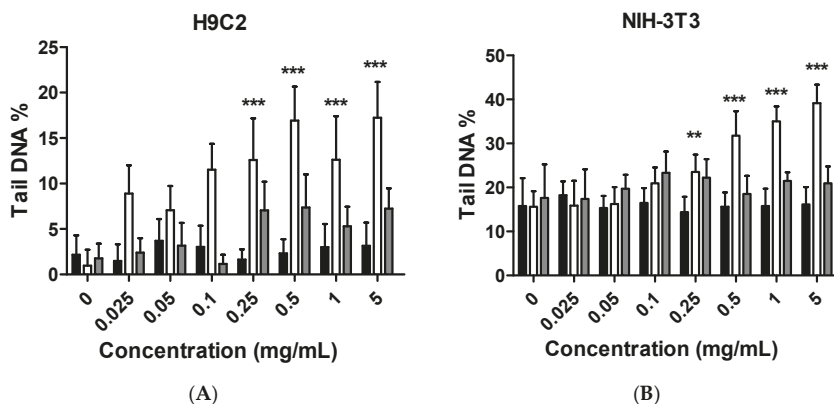

(**A**)

(**B**)

Figure 5. *Cont.*
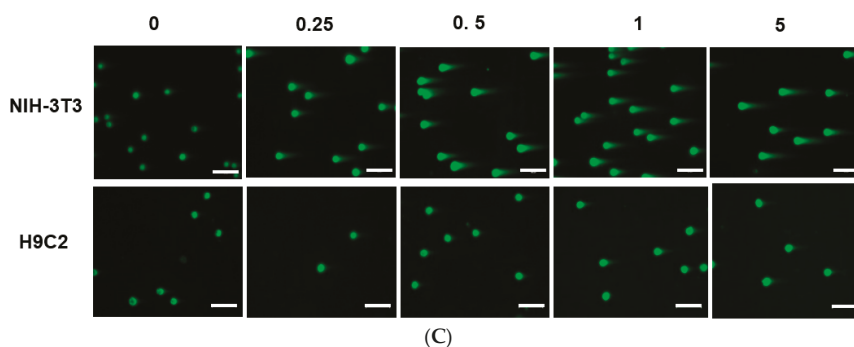
| | 0 | 0.25 | 0. 5 | 1 | 5 |

(**C**)

Figure 5. Genotoxicity measured by comet assay. (**A**) The H9C2 cells were seeded into 48-well plates to perform this experiment. Following 24 h incubation after treatment of tested samples, the assay was carried out according to the comet assay protocol as described in "Materials and Methods"; (**B**) NIH-3T3 cell line. Color in graph: Black, Citron; White, Citron$_{peptide}$; Gray, Citron$_{liposome}$. Significant results from the control group are calculated and marked with asterisks (** $p < 0.01$, *** $p < 0.001$); (**C**) The typical comet assay images in the Citron$_{peptide}$ group are shown at the concentration of 0.25, 0.5, 1, 5 mg/mL. Scale bar is 100 μm.

3. Discussion

Functional foods, as one area of the food industry, have grown a lot over the years [18]. Benefiting from the improvement of food technology, especially with the emergence of nanotechnology, it is expected that the functional foods will further advance, with promising prospects [19]. In this study, by using nanotechnology, we prepared citron extract at a nanometer scale by incorporating functional ingredients, liposome, and peptide. We employed fish oligopeptide and water-soluble liposome to formulate citron nanoparticles. With predominant properties in viscosity and foaming, oligopeptide has been widely used in food processing. Meanwhile, because of its high yield, low cost, and the beneficial effects in human body, we used fish collagen peptide to process citron$_{peptide}$ into nanoparticle, as shown in Figure 1A. The typical size of citron$_{peptide}$ nanoparticles was around 100 nm. However, because of the biological limitation of oligopeptide, such as chemical degradation, low stability, and bioavailability, physicochemical instability, and low permeability, its development in the food industry is restricted. To avoid the deficiencies of peptide, we used both liposome and oligopeptide to formulate citron nanoparticles, labeled as citron$_{liposome}$ in Figure 1A. The content ratio of three types of citron samples (Citron, Citron$_{peptide}$, and Citron$_{liposome}$) are depicted in supplementary data Table S1. Furthermore, the description of the citron extract compositions such as general composition (Table S2), amino acid (Table S3), fatty acid (Table S4), minerals (Table S5), and vitamins (Table S6) are provided in supplementary data file as well (obtained from Rural Development Administration, Korea).

Next, regarding the determination of citron nanoparticle, the morphology of citron$_{peptide}$ and citron$_{liposome}$ clearly demonstrated the formation of citron extracts nanoparticles. On the other hand, concerns remain with the significantly reduced size of particles when utilizing nanotechnology. For example, it has been reported that particles with a diameter of less than 100 nm may induce toxic effects [20]. To assess the toxicity of citron nanoparticles and provide quantitative references for various applications, we confirmed the biological toxicity, as shown in the results section.

Although citron is well-known for its medicinal usage, we know little about its application as food and its bioactivities. Here, in an in vitro test, six different cells were used to measure the toxicity of citron extracts. Embryonic fibroblasts from mice (NIH-3T3), heart myoblasts from rats (H9C2), a human liver-cancer cell line (HepG2), and human epithelial colorectal adenocarcinoma cells (Caco-2) were selected to test the different effects. In addition, we also used two human-derived primary cells,

human cardiac progenitor cells (hCPC) and human endothelial progenitor cells (hEPC), to examine the toxicity and make the results more credible. Our work showed that the cytotoxicity of citron extract had two aspects. One aspect was that the cytotoxicity was cell-type dependent (Figure 2), selectively against primary hCPCs and hEPCs, especially in the citron$_{liposome}$ group. The other was the genotoxicity (Figure 5). No cytotoxicity was observed in NIH-3T3 and H9C2 cell lines, but citron$_{peptide}$ can cause genotoxicity in those two cell lines. Interestingly, in the presence of liposome in citron$_{liposome}$, the gene damage disappeared. With the particles being in the nanometer scale, nanoparticles may penetrate biological membranes and have access to the cell. Nanoparticle can also have different biodistributions in the human body, perhaps because of different affinities with the diverse cell types or organs. In recent years, some studies have explored the nanotoxicity of nanoparticles [21,22]. In this view, we can conclude that citron extract behaved differently for different cell types. For instance, citron$_{liposome}$ may show a higher affinity with hCPCs and hEPCs than other cell lines to cause cell damage (Figure 2), and with high affinity for genes, citron$_{peptide}$ can have a genotoxic effect in the H9C2 or NIH-3T3 cell lines (Figure 5). We also discovered that citron extracts did not suppress human liver cancer cell lines or human epithelial colorectal adenocarcinoma cells, HepG2 and Caco-2.

The main purpose of this study is to identify the potential toxicity of citron nanoparticles (citron$_{peptide}$ and citron$_{liposome}$) in an in vitro system, and to provide accessible information for further industrial production and application. Many studies have shown that nanotoxicity can emerge with the decreased particle size to nanometer scale. Because the size of citron$_{peptide}$ and citron$_{liposome}$ is between 100 and 200 nm, it is essential to examine their toxicity. Our results demonstrate that cytotoxicity increased in some cell lines, like hCPCs, hEPCs, and H9C2, after treatment with citron$_{peptide}$ or citron$_{liposome}$. Meanwhile, citron$_{peptide}$ caused genotoxicity in the NIH-3T3 and H9C2 cell lines, but not cytotoxicity. These results clearly show the toxic effects of citron nanoparticles. In addition, although our studies provide information about the cytotoxicity of citron for applications in the food industry, more research is needed to reveal the mechanism before use in final food products.

4. Materials and Methods

4.1. Chemicals and Kits

Trizma base, *N*-laurylsarcosine, Triton X-100, boric acid, and 3-(4,5-Dimethylthiazol-2-yl)-2,5-diphenyltetrazolium bromide (MTT) were obtained from Sigma-Aldrich (Madison, WI, USA). The cell-culture medium and dish were acquired from Welgene (Daegu, Korea). Fetal bovine serum (FBS) was bought from Welgene (Daegu, Korea). The LIVE/DEAD® Viability/Cytotoxicity Assay Kit was purchased from Invitrogen (Carlsbad, CA, USA). The lactate dehydrogenase (LDH) Cytotoxicity Assay kit was obtained from Thermo Fisher Scientific (Waltham, MA, USA). All of the other reagents and chemicals were purchased from commercial companies.

4.2. Preparation of Samples

The method used for preparation of liposome has been described previously. Briefly, the 2% lecithin (Metarin P, Cargill Texturizing Solutions, Hamburg, Germany) was added to 0.5% peptide (Naticol 4000, Weishardt International, Graulhel, France) aqueous solution at a ratio of 1:1. Then, after homogenization for 3 min at 8000 rpm using a high-speed homogenizer (IKAT25 digital ULTRA-TURRAX®, Germany), the extracts were collected and homogenized again at 80 W for 3 min by using an ultrasonicator. The citron extract containing 50% citron and 50% sucrose was prepared by mixing with water (1:1 *w/w*) using a blender to make citron syrup for further study. The citron$_{peptide}$ was obtained by mixing with fish skin peptide. Sixty grams of peptide were used per 0.5 L of citron extract. The citron$_{liposome}$ was obtained by mixing with fish-skin peptide and liposome. The ratio was 1 g liposome and 60 g fish-skin peptide per 0.5 L of citron extract. Finally, all of the samples were dried using a spray dryer (SD-1000, EYELA, Tokyo, Japan) to obtain a powder. The morphology and size of citron extracts were detected by using scanning electron microscope (SEM) and Nano Size analyzer.

4.3. Cell Culture

NIH-3T3 (mouse), H9C2 (rat), and HepG2 (human) were purchased from Korean Cell Line Bank (KCLB, Seoul, Korea) and cultured in high glucose Dulbecco's Modified Eagle's Medium (DMEM; Welgene, Daegu, Korea) containing 10% FBS and 1% penicillin/streptomycin (P/S, Welgene). Primary human EPCs and human CPCs were provided by S.M. Kwon (IRB No. 05-2-15-133, Pusan University, Pusan, Korea). The hEPCs were cultured in EC basal medium 2 (EBM-2MV, Lonza, Walkersville, MD, USA) containing 5% FBS, EGM-2-MV Bullet Kit, and 1% penicillin/streptomycin. The hCPCs were cultured in Ham's F12 medium (Hyclone, Logan, UT, USA) containing 10% FBS, 1% penicillin/streptomycin, 0.005 U/mL human erythropoietin (hEPO, R & D system, Minneapolis, MN, USA), 5 ng/mL human basic fibroblast growth factor (hbFGF, PeproTech, Rocky Hill, NJ, USA), and 0.2 mM L-glutathione reduced (Sigma-Aldrich, St. Louis, MO, USA). All cell lines were cultured at 37 °C in a humidified incubator with 5% CO_2 atmosphere. The logarithmic cells were harvested before performing each experiment.

4.4. MTT Assay

The cell viability was measured by employing an MTT assay as described previously [23]. The cells were seeded into 96-well plates at a density of 1×10^5 cells per well and were cultured overnight. After incubation, the medium was replaced by a starvation medium containing 1% FBS for another 24 h. Then, the cells were treated with the desired concentrations of drugs for an additional 24 h. The supernatant was removed, and an MTT solution at a final concentration of 0.25 mg/mL was added in each well to label the cells. The plates were incubated in a humidified incubator for 4 h. Then, 100 µL of dimethyl sulfoxide (DMSO) was used to dissolve the formazan, and the cell viability was detected by measuring the optical density (OD) at the absorbance of 595 nm using BioTek Microplate Readers (Winooski, VT, USA).

4.5. Live/Dead Assay

To visualize the cell viability, the cells were labeled with calcein AM and ethidium homodimer (EthD-1) by using a Live/Dead assay kit. The cells were cultured in 48-well plates at a density of 1×10^5 cells per well for 24 h. After incubation with a starvation medium overnight, the various concentrations of drugs were added in each well and were incubated for the next 24 h. Then, the supernatant was discarded, and the cells were washed once using DPBS. A 500 µL cell-staining solution at a final concentration of 2 µM calcein AM and 4 µM EthD-1 in DPBS was added to each well, and the plates were incubated for 45 min at room temperature by blocking light. Finally, live and dead cells were visualized by using a fluorescence microscope (Nikon, ECLIPSE Ts2, Tokyo, Japan). The live cells are shown in green, the dead cells in red. The images merged by Image J software were used to show co-localization.

4.6. LDH Release Assay

Cell cytotoxicity was evaluated by measuring the enzymatic activity of released LDH from dead cells. Before the measurement, the cells were prepared, as described previously, and then incubated in various concentrations of drugs for 24 h. The plates were then centrifuged at $700 \times g$ for 5 min at room temperature using a Beckman Coulter Allegra® X-15R centrifuge. The supernatant was collected to measure the released LDH. The assay was performed according to the manufacturer's instructions. The absorbance at 450 nm was detected to calculate the cell cytotoxicity.

4.7. Single-Cell Gel Electrophoresis Assay

A single-cell gel electrophoresis assay (comet assay) was carried out to measure the deoxyribonucleic acid (DNA) damage. The method used for this assay analysis has been described previously. Briefly, cells were first seeded into 48-well plates. After incubation with different concentrations of drugs for 24 h, the cells were harvested and mixed with 100 µL 0.7% low-melting-point agarose at a

cell density of 2×10^5 per milliliter. Then, the cells were laid onto agarose-coated glass slides, which were stored at 4 °C for solidification until electrophoresis. Slides were placed in a lysis solution (2.5 M NaCl, 0.1 M EDTA, 10 mM Trizma base, 1% *N*-laurylsarcosine, 0.5% Triton X-100, and 10% DMSO, pH 10) for 1 h at 4 °C. After lysis, slides were submerged in an alkaline solution (300 mM NaOH, 1 mM EDTA, pH > 13) for 30 min at 4 °C. The slides were washed three times with electrophoresis buffer (89 Mm Trisbase, 89 mM boric acid, 2 mM EDTA, pH 8.3) and then subjected to electrophoresis at 25 V for 20 min using a RunOne™ Powder Supply. Then, slides were fixed with absolute ethanol and stained with DNA dye. The cell images were photographed using a fluorescence microscope and Casplab software was used to analysis the comet assay results.

4.8. Statistics

All data were analyzed by GraphPad Prism and shown as means ± standard deviation (SD). Comparisons between the groups were conducted by using two-way analysis of variance with Bonferroni post-tests and/or Student's *t* test. Statistical significance was considered to be a *p* value less than 0.05.

5. Conclusions

In this study, toxicity studies were conducted to determine the possible toxic effects of nano-engineered citron samples in the cellular level and to provide credible information for the future application of citron. To make the result more convincing, two human primary cell lines were employed in our study. Our findings revealed that citron$_{liposome}$ could significantly cause cell damage in primary hEPC and hCPC cells, much greater than the slight damage caused by citron or citron$_{peptide}$. However, cytotoxicity was not observed from NIH-3T3, HepG2, and Caco-2 cell lines. In the genotoxicity test, significant toxic effects were not observed from hEPCs or hCPCs, followed by the treatment with citron, citron$_{peptide}$, or citron$_{liposome}$. Minimal genotoxicity was detected from NIH-3T3 cells and in H9C2 cells after the treatment with citron$_{peptide}$, but disappeared in the presence of liposome in the citron$_{liposome}$ group. Overall, our findings provide important information for the further use of citron in the food industry. Moreover, in vitro study will be performed to further determine the toxicity in order to meet the final food products.

Author Contributions: Xiaowei Zhang performed the experiments on NIH-3T3 and H9C2 cells, arranged the data, and wrote the manuscript; Hee Jeong Yoon performed the experiments on hCPCs; Gyeong Jin Kim performed the experiments on hEPCs; Min Gyeong Kang performed the experiments on HepG2 cells; Sun Young Shin performed the experiments on in vitro analysis experiments and interpretation of data; Sang Hong Baek participated in interpretation of the data and structure of the data presentation; Jung Gyu Lee, Jingjing Bai, Sang Yoon Lee, and Mi Jung Choi participated in developing citron peptide and citron liposome; Kwonho Hong participated in interpretation of the data; Hojae Bae participated in the design of all experiments and interpretation of the experimental results as corresponding author. All authors significantly contributed to the study and to the interpretation of the data.

Conflicts of Interest: The authors declare no conflict of interest.

Abbreviations

hEPCs	Human endothelial progenitor cells
hCPCs	Human cardiac progenitor cells
LDH	Lactate dehydrogenase
FBS	Fetal bovine serum
P/S	Penicillin/Streptomycin

References

1. Tripoli, E.; la Guardia, M.; Giammanco, S.; di Majo, D.; Giammanco, M. Citrus flavonoids: Molecular structure, biological activity and nutritional properties: A review. *Food Chem.* **2007**, *104*, 466–479. [CrossRef]

2. Franceschi, S.; Bidoli, E.; Negri, E.; Zambon, P.; Talamini, R.; Ruol, A.; Parpinel, M.; Levi, F.; Simonato, L.; la Vecchia, C. Role of macronutrients, vitamins and minerals in the aetiology of squamous-cell carcinoma of the oesophagus. *Int. J. Cancer* **2000**, *86*, 626–631. [CrossRef]

3. Garcia-Closas, R.; Gonzalez, C.A.; Agudo, A.; Riboli, E. Intake of specific carotenoids and flavonoids and the risk of gastric cancer in Spain. *Cancer Causes Control* **1999**, *10*, 71–75. [CrossRef] [PubMed]

4. Larsson, S.C.; Håkansson, N.; Giovannucci, E.; Wolk, A. Folate intake and pancreatic cancer incidence: A prospective study of Swedish women and men. *J. Natl. Cancer Inst.* **2006**, *98*, 407–413. [CrossRef] [PubMed]

5. Shekelle, R.; Liu, S.; Raynor, W.; Lepper, M.; Maliza, C.; Rossof, A.; Paul, O.; Shryock, A.; Stamler, J. Dietary vitamin A and risk of cancer in the Western Electric study. *Lancet* **1981**, *318*, 1185–1190. [CrossRef]

6. Bae, J.-M.; Lee, E.J.; Guyatt, G. Citrus fruit intake and stomach cancer risk: A quantitative systematic review. *Gastric Cancer* **2008**, *11*, 23–32. [CrossRef] [PubMed]

7. Song, J.-K.; Bae, J.-M. Citrus fruit intake and breast cancer risk: A quantitative systematic review. *J. Breast Cancer* **2013**, *16*, 72–76. [CrossRef] [PubMed]

8. Murakami, A.; Nakamura, Y.; Torikai, K.; Tanaka, T.; Koshiba, T.; Koshimizu, K.; Kuwahara, S.; Takahashi, Y.; Ogawa, K.; Yano, M. Inhibitory effect of citrus nobiletin on phorbol ester-induced skin inflammation, oxidative stress, and tumor promotion in mice. *Cancer Res.* **2000**, *60*, 5059–5066. [PubMed]

9. Rekha, C.; Poornima, G.; Manasa, M.; Abhipsa, V.; Devi, P.; Kumar, V.; Kekuda, P. Ascorbic acid, total phenol content and antioxidant activity of fresh juices of four ripe and unripe citrus fruits. *Chem. Sci. Trans.* **2012**, *1*, 303–310. [CrossRef]

10. Abdul, D.A. Preparation and characterization of pectin from peel of Kabad (*Citrus medica*) fruit in Sulaimani city, Iraqi Kurdistan Region. *Int. J. Curr. Res. Chem. Pharm. Sci.* **2014**, *1*, 142–146.

11. Sanguansri, P.; Augustin, M.A. Nanoscale materials development—A food industry perspective. *Trends Food Sci. Technol.* **2006**, *17*, 547–556. [CrossRef]

12. Duncan, T.V. Applications of nanotechnology in food packaging and food safety: Barrier materials, antimicrobials and sensors. *J. Colloid Interface Sci.* **2011**, *363*, 1–24. [CrossRef] [PubMed]

13. Rashidi, L.; Khosravi-Darani, K. The applications of nanotechnology in food industry. *Crit. Rev. Food Sci. Nutr.* **2011**, *51*, 723–730. [CrossRef] [PubMed]

14. Sozer, N.; Kokini, J.L. Nanotechnology and its applications in the food sector. *Trends Biotechnol.* **2009**, *27*, 82–89. [CrossRef] [PubMed]

15. Reza Mozafari, M.; Johnson, C.; Hatziantoniou, S.; Demetzos, C. Nanoliposomes and their applications in food nanotechnology. *J. Liposome Res.* **2008**, *18*, 309–327. [CrossRef] [PubMed]

16. Taylor, T.M.; Weiss, J.; Davidson, P.M.; Bruce, B.D. Liposomal nanocapsules in food science and agriculture. *Crit. Rev. Food Sci. Nutr.* **2005**, *45*, 587–605. [CrossRef] [PubMed]

17. Mohan, A.; Rajendran, S.R.; He, Q.S.; Bazinet, L.; Udenigwe, C.C. Encapsulation of food protein hydrolysates and peptides: A review. *RSC Adv.* **2015**, *5*, 79270–79278. [CrossRef]

18. Hasler, C.M. Functional foods: Benefits, concerns and challenges—A position paper from the American Council on Science and Health. *J. Nutr.* **2002**, *132*, 3772–3781. [CrossRef] [PubMed]

19. Momin, J.K.; Jayakumar, C.; Prajapati, J.B. Potential of nanotechnology in functional foods. *Emir. J. Food Agric.* **2013**, *25*, 10. [CrossRef]

20. Fischer, H.C.; Chan, W.C. Nanotoxicity: The growing need for in vivo study. *Curr. Opin. Biotechnol.* **2007**, *18*, 565–571. [CrossRef] [PubMed]

21. Pisanic, T.R.; Blackwell, J.D.; Shubayev, V.I.; Fiñones, R.R.; Jin, S. Nanotoxicity of iron oxide nanoparticle internalization in growing neurons. *Biomaterials* **2007**, *28*, 2572–2581. [CrossRef] [PubMed]

22. Soenen, S.J.; Rivera-Gil, P.; Montenegro, J.-M.; Parak, W.J.; De Smedt, S.C.; Braeckmans, K. Cellular toxicity of inorganic nanoparticles: Common aspects and guidelines for improved nanotoxicity evaluation. *Nano Today* **2011**, *6*, 446–465. [CrossRef]

23. Van Meerloo, J.; Kaspers, G.J.; Cloos, J. Cell sensitivity assays: The MTT assay. *Methods Mol. Biol.* **2011**, *731*, 237–245. [PubMed]

Article

Cytotoxicity Evaluation of Turmeric Extract Incorporated Oil-in-Water Nanoemulsion

Hee Jeong Yoon [1,†], Xiaowei Zhang [1,†], Min Gyeong Kang [1], Gyeong Jin Kim [1], Sun Young Shin [2], Sang Hong Baek [2], Bom Nae Lee [3], Su Jung Hong [3], Jun Tae Kim [3], Kwonho Hong [4] and Hojae Bae [4,*]

[1] College of Animal Bioscience and Technology, Department of Bioindustrial Technologies, Konkuk University, Hwayang-dong, Kwangjin-gu, Seoul 05029, Korea; rose_0013@naver.com (H.J.Y.); zhangxiaowei9304@gmail.com (X.Z.); vq1004pv@naver.com (M.G.K.); kkg0118@gmail.com (G.J.K.)
[2] Laboratory of Cardiovascular Regeneration, Division of Cardiology, Seoul St. Mary's Hospital, The Catholic University of Korea School of Medicine, Seoul 02841, Korea; tempast606@naver.com (S.Y.S.); whitesh@catholic.ac.kr (S.H.B.)
[3] Department of Food Science and Technology, Keimyung University, Daegu 42601, Korea; bomnae1110@gmail.com (B.N.L.); tnwjd0799@naver.com (S.J.H.); jtkim92@kmu.ac.kr (J.T.K.)
[4] KU Convergence Science and Technology Institute, Department of Stem Cell and Regenerative Biotechnology, Konkuk University, Hwayang-dong, Kwangjin-gu, Seoul 05029, Korea; hongkh27@gmail.com
* Correspondence: hojaebae@konkuk.ac.kr; Tel.: +82-2-450-0525
† These authors contributed equally to this work.

Abstract: To overcome the drawbacks of conventional drug delivery system, nanoemulsion have been developed as an advanced form for improving the delivery of active ingredients. However, safety evaluation is crucial during the development stage before the commercialization. Therefore, the aim of this study was to evaluate the cytotoxicity of two types of newly developed nanoemulsions. Turmeric extract-loaded nanoemulsion powder-10.6 (TE-NEP-10.6, high content of artificial surfactant Tween 80), which forms the optimal nanoemulsion, and the TE-NEP-8.6 made by increasing the content of natural emulsifier (lecithin) to reduce the potential toxicity of nanoemulsion were cultured with various cells (NIH3T3, H9C2, HepG2, hCPC, and hEPC) and the changes of each cell were observed followed by nanoemulsion treatment. As a result, the two nanoemulsions (TE-NEP-10.6 and TE-NEP-8.6) did not show significant difference in cell viability. In the case of cell line (NIH3T3, H9C2, and HepG2), toxicity was not observed at an experimental concentration of less than 1 mg/mL, however, the cell survival rate decreased in a concentration dependent manner in the case of primary cultured cells. These results from our study can be used as a basic data to confirm the cell type dependent toxicity of nanoemulsion.

Keywords: turmeric; curcumin; nanoemulsion; cytotoxicity

1. Introduction

Emulsions are small-sized droplets dispersed using two immiscible solutions with appropriate surfactants and are called nanoemulsion if the size of the droplet is at nano-scale. Since nanoemulsions can be fabricated in many different forms (liquids, creams, sprays, gels, aerosols, and foams), they can be employed in a variety of applications, including food and pharmaceuticals [1,2]. For instance, bioavailability can be significantly improved through the encapsulation of poorly soluble active ingredients, thus providing improved applicability [3,4].

Turmeric extract powder (TEP) used in this study for the production of curcumin nanoemulsion, is a mixture containing a number of commercially available vegetable supplements [5]. Among them,

the pharmacological activity of curcumin, an index substance of turmeric, has been reported through many studies [6–8]. However, curcumin, a yellow hydrophobic polyphenolic component extracted from turmeric has limited applications due to poor solubility and toxicity at high concentrations [9–11]. Moreover, its low bioavailability in the body remains as a major issue. To solve these problems, curcumin nanoemulsion was prepared by using TEP to increase applicability and bioavailability of curcumin.

Although nanotechnology have emerged as a technology that could positively modify or control the functionality, stability, and usefulness of the active substances for high value-added products [12–14], the regulation of nanotechnology incorporation varies in different countries and methods as well as procedures for safety evaluation of nano-substances are also being implemented [15–19]. For example, the toxicity of the nano-sized materials cannot be completely identified in the human body, which is one of the major obstacle for commercialization (e.g., food, cosmetics or drugs) [20,21]. Therefore, the safety evaluation of the nano-materials is crucial.

In this study, the toxicity of nanoemulsion as a carrier to improve the bioavailability of bioactive substances such as curcumin (extracted from TEP), and the possibility of its application has been verified through evaluating the potential toxicity. Two types of oil-in-water nanoemulsions containing curcumin were prepared as shown in Figure 1 and Table 1. TE-NEP-8.6 was produced by lowering the ratio of synthetic emulsifier (tween 80). The toxicity of each emulsion was evaluated at the cellular level (3-(4, 5-dimethylthiazol-2-yl) 2, 5-diphenyl tetrazolium bromide (MTT) assay, lactate dehydrogenase (LDH) assay, Live/dead assay, and comet assay).
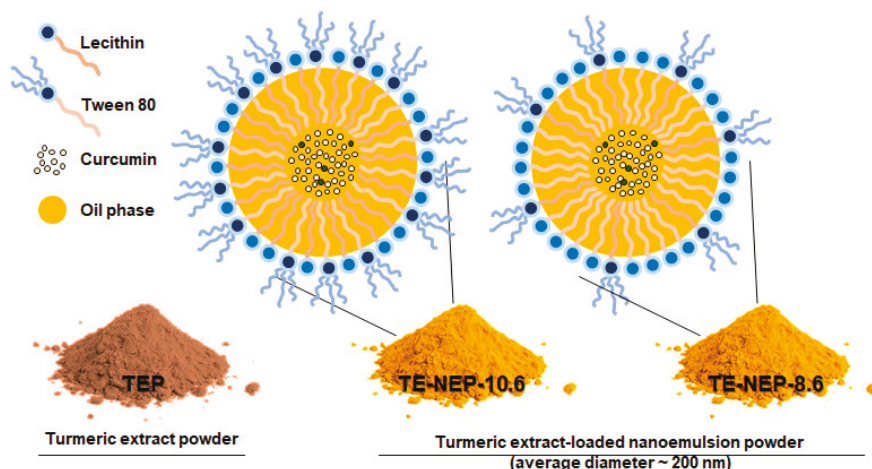

Figure 1. Schematic of o/w nanoemulsion including curcumin. Turmeric extract-loaded nanoemulsion powder (TE-NEP) was prepared using Turmeric extract powder (TEP). TE-NEP-10.6 has a HLB value of 10.6, and TE-NEP-8.6 has a HLB value of 8.6. Abbreviations: o/w, oil in water; HLB, hydrophilic lipophilic balance.

Table 1. Composition of turmeric extract-loaded nanoemulsion powder (TE-NEP).

| Sample | HLB Value | MCT Oil (g) | Surfactant (g) | | DW (mL) | TEP (g) | Dextrin (g) |
			Lecithin	Tween 80			
TE-NEP-8.6	8.6	500	400	100	9000	107.41	1107.41
TE-NEP-10.6	10.6	750	412.5	337.5	8500	161.11	1661.11

Abbreviations: HLB, hydrophile-lipophile balance; MCT, Medium-chain triglyceride; DW, distilled water; TEP, turmeric extract powder, TE-NEP-8.6, turmeric extract-loaded nanoemulsion powder with HLB value of 8.6; TE-NEP-10.6, turmeric extract-loaded nanoemulsion powder with HLB value of 10.6.

2. Results

Cytotoxicity of Turmeric Extract-Loaded Nanoemulsion

To assess the cell viability activity of turmeric extract-loaded nanoemulsion powder (TE-NEP) against various cell types (NIH3T3, H9C2, HepG2, hCPC, and hEPC, respectively), MTT assay was performed to evaluate the cell metabolic activity of living cells. Both cell lines and primary cells were incubated with different concentrations of TE-NEP, TE-NEP-10.6, and TE-NEP-8.6 (0–20 mg/mL). Cell viability was determined after 24 h of incubation. As can be seen in Figure 2, some of the extracts induced cell cytotoxicity in certain concentrations. In all cell types, TEP induced cytotoxicity in proportion to its concentration. In the case of cell lines, toxicity was not observed after the treatment with two nanoemulsions except for H9C2 at a concentration of 5 mg/mL (Figure 2a–c). The two nanoemulsion samples showed toxicity in proportion to the concentration of the sample at concentrations above 0.25 mg/mL for hCPC and above 0.5 mg/mL for hEPC (Figure 2d,e). The results of positive control are shown in Figure S2. Since the curcumin content varied between three groups (turmeric extract and two nanoemulsions), the MTT assay was performed by matching the content of curcumin to evaluate the toxicity according to its exact content. As a result, the toxicity of the TEP decreased (Figure S3). The NIH3T3 cell line showed cell viability of less than 85% at the concentrations of 3.248 and 16.24 μg/mL in TEP and two nanoemulsion samples, respectively (Figure S3a). On the other hand, the cell viability of H9C2 cells tended to decrease in proportion to the concentration of curcumin. At the concentration of 0.812 μg/mL, all of the sample groups showed cell viability below 85% (Figure S3b). In the case of human hepatocytes (HepG2), TE-NEP-10.6 and TE-NEP-8.6 showed cell viability of $66 \pm 2.7\%$ and $27 \pm 3.7\%$ at concentration of 32.48 μg/mL, respectively (Figure S3c). In contrast, human-derived primary cells showed dosage-dependent cytotoxicity in all groups (Figure S3d,e). Compared with the results obtained by adjusting the content of curcumin, the high toxicity of TEP when treated with the same concentration of powder is due to the high concentration of curcumin which is toxic to the cells.
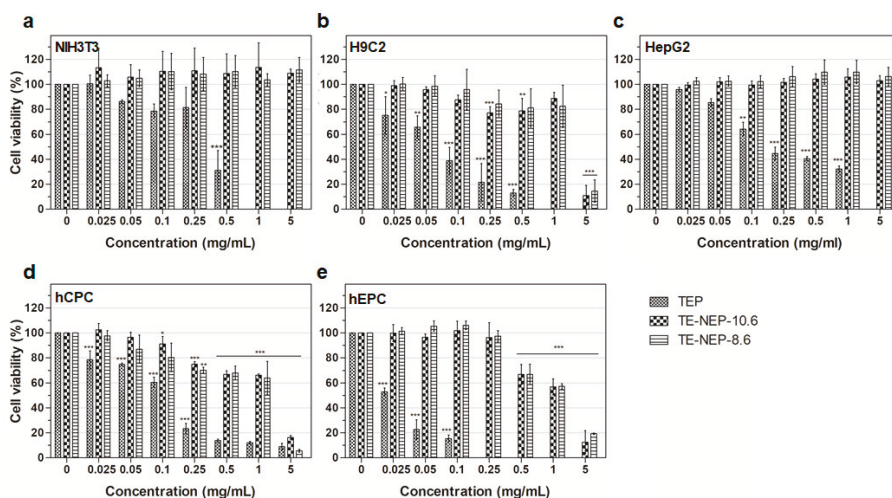

Figure 2. Evaluation of cell viability by MTT assay on (**a**) NIH3T3 cell line, (**b**) H9C2 cell line, (**c**) HepG2 cell line, (**d**) hCPC primary cell, (**e**) hEPC primary cell treated with Turmeric extract powder (TEP) and turmeric extract-loaded nanoemulsion powder with HLB values of 10.6 (TE-NEP-10.6) and 8.6 (TE-NEP-8.6), respectively. Cells were incubated with nanoemulsion samples (0.025, 0.05, 0.1, 0.25, 0.5, 1 and 5 mg/mL) for 24 h. Experiments were repeated 3 times independently. *, **, *** $p < 0.05$, compared to the control.

In addition, the cytotoxicity of the samples (TEP, TE-NEP-8.6, and TE-NEP-10.6) was assessed by LDH assay, which assessed cell damage by LDH released from damaged cells. In all cell lines, the LDH assay results of TEP and two nanoemulsion samples were similar to MTT assay results, but in HepG2, TEP showed toxicity at concentrations above 1 mg/mL (Figure 3a–c). Concentration dependent cytotoxicity was detected at hCPC treated TEP and the two nanoemulsions were toxic only at the highest concentration of 5 mg/mL (Figure 3d). On the other hand, hEPC showed high toxicity results regardless of concentration in TEP, and concentration-dependent toxicity was confirmed at higher than 0.5 mg/mL of two nanoemulsions (Figure 3d). Figure S4 shows the results of positive control according to each cell types. When the content of curcumin was matched, the LDH analysis results were similar to that of MTT assay (Figure S5). Overall, NIH3T3 and H9C2 showed high levels of cytotoxicity at 16.24 and 8.12 μg/mL, respectively (Figure S5a,b). In the case of HepG2, TEP showed a concentration-dependent cytotoxicity from 3.248 μg/mL, and the two nanoemulsions showed cytotoxicity at the highest concentration of 32.48 μg/mL (Figure S5c). For hEPC, the nanoemulsion showed concentration dependent cytotoxicity from 0.812 to 32.48 μg/mL, while for hCPC, the highest toxicity was observed at 8.12 μg/mL nanoemulsion concentration (Figure S5d,e).
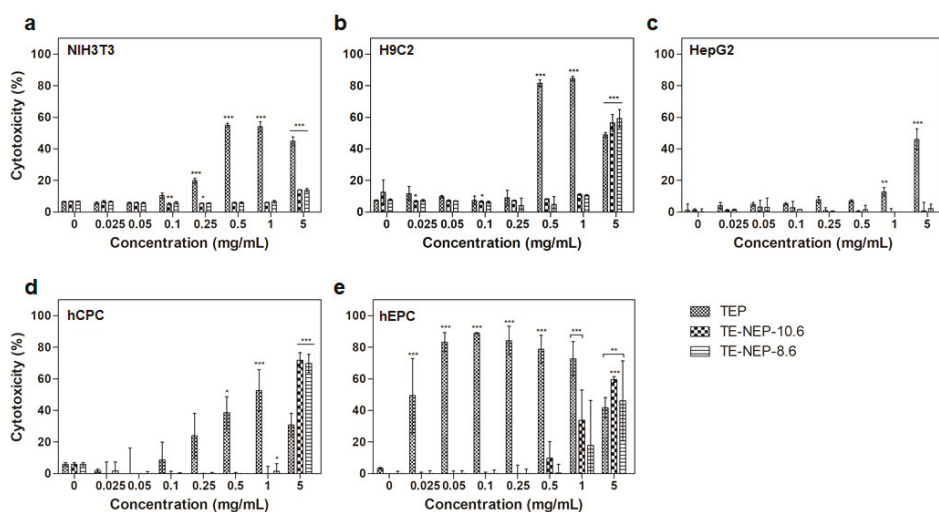

Figure 3. The cytotoxicity effects of TEP, TE-NEP-10.6 and TE-NEP-8.6 (0.025, 0.05, 0.1, 0.25, 0.5, 1 and 5 mg/mL) on (**a**) NIH3T3, (**b**) H9C3, (**c**) HepG2, (**d**) hCPC and (**e**) hEPC. Cell death was measured with the LDH assay after 24 h. Experiments were repeated 3 times independently. *, **, *** $p < 0.05$, compared to the control.

The viability of each cells was visualized by fluorescence staining (Figure 4). Live cells and dead cells were stained with calcein-AM and EthD-1, respectively. TEP was cytotoxic in a concentration-dependent manner in all cell types. The number of dead cells increased, and the viability decreased significantly at the highest concentration of 5 mg/mL. In NIH3T3 and HepG2, cells showed low toxicity against nanoemulsion. On the other hand, in the case of H9C2, it was confirmed that most of the cells were dead at 5 mg/mL. The primary cultured cells, hCPC, indicated definite concentration dependent cytotoxicity. hEPC showed significantly reduced cell density, similar to H9C2, due to the depletion of dead cells at a concentration of 5 mg/mL. Figure S6 implied quantification data for living cells. The live/dead test results for all experimental concentrations are shown in Figure S7.
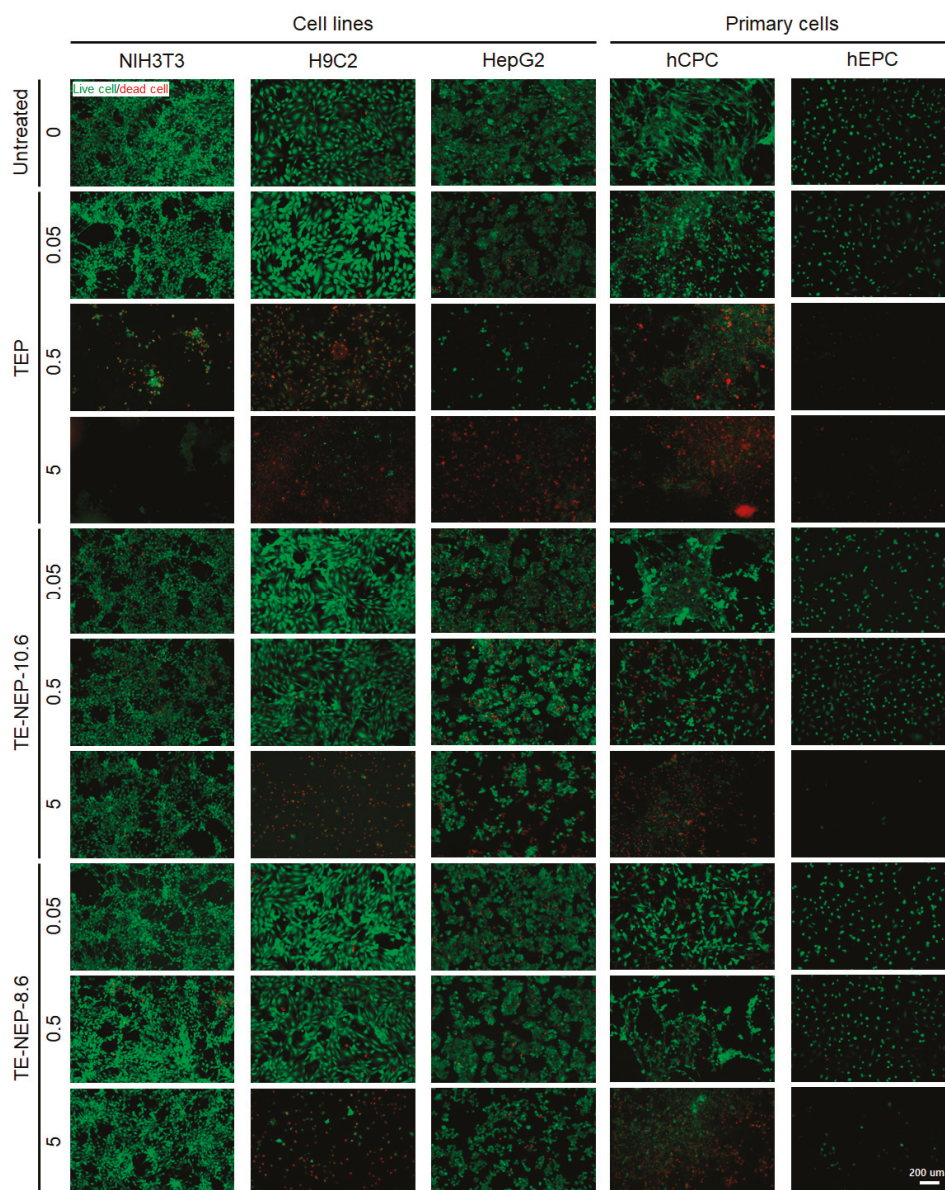
Figure 4. Representative fluorescence live/dead images of NIH3T3, H9C3, HepG2, hCPC, and hEPC. Each cell was stained with calcein-AM (green)/ethidium homodimer (red) LIVE/DEAD assay after the sample (TEP, TE-NEP10.6 and TE-NEP-8.6) treatment (24 h). Scale bar = 200 μm.

3. Discussion

Mouse fibroblasts (NIH3T3), rat heart myoblasts (H9C2) were selected as representative animal cell line. Since the liver is a detoxifying organ where bulk of nutrients are received [22], HepG2 was chosen as representative of human-derived cell lines. Once received, metabolized nutrients are

then released back into blood stream through the blood vessel, and blood is pumped throughout the body from the heart [23]. Therefore, human cardiac progenitor cells (hCPC) and human endothelial progenitor cells (hEPC) were selected as representative of primary human cells. In particular, it would be possible to evaluate more reliable toxicity towards humans by using various human-derived primary cells [24].

The TEP is a mixture containing a number of commercially available vegetable supplements [5]. Among them, the pharmacological activity of curcumin, an index substance of turmeric, has been reported through research [6–8]. Curcumin, a yellow hydrophobic polyphenolic component extracted from turmeric has limited applications due to low solubility and availability [9–11]. Moreover, its low bioavailability in the body remains as a major issue. To solve these problems, curcumin nanoemulsion was prepared by using TEP to increase applicability and bioavailability of curcumin. Nanoemulsions are widely applied in drug delivery systems and food applications due to their biocompatibility and permeability enhancing properties [25,26]. In addition, the materials used to make the nanoemulsion, water, oil (Medium-chain triglyceride (MCT) oil), and surfactant (Lecithin and Tween-80), have been approved for food use [27,28]. In particular, MCT oil is a vegetable oil, and lecithin is a component extracted from soybeans. According to the Material Safety Data Sheet (MSDS), both substances are highly safe food ingredients not classified as hazardous/hazardous substances. Tween 80 is a hydrophilic emulsifier and is the most widely used emulsifier to make oil in water nanoemulsion [29]. However, Tween 80 have been reported to be toxic in some cases and therefore the allowable amount of Tween 80 used as a food additive is 11.8 g/kg for nutritional supplement and 1 g/kg for non-standard processed food. The Tween 80 content of the nanoemulsion (TE-NEP) was 337.5 g/10 L, and after mixing with dextrin powder, the final Tween 80 contained in the dried powder (TE-NEP) was about 37 g/kg (3.7%) (Table 1).

The content of curcumin, which is a target substance contained in the nanoemulsion, was confirmed by HPLC. The curcumin content of TEP was 32.48 μg/mL, and the curcumin contents of TE-NEP-10.6 and TE-NEP-8.6 were 1.83 and 1.64 μg/mL, respectively (Table 2). TEP has about 17 times higher curcumin content than nanoemulsion. Since curcumin can induce cell death according to its concentration, as well as exhibit various pharmacological activities [30] (e.g., antioxidation [27,31,32], antiinflammation [33,34], and antitumor effects [35–37]), our results showing cytotoxicity at high TEP with a high curcumin content can be explained. Furthermore, based on the No Observed Adverse Effect Level (NOAEL) value of curcumin (250–320 mg/kg bw/day), international expert scientific committee JECFA (joint FAO/WHO Expert Committee on Food Additives) have proposed an acceptable daily intake (ADI) of 3 mg/kg bw/day for insoluble curcumin. [38].

Table 2. Content of curcumin in TE-NEP.

Sample	AVE (μg/mL)	STD
TE-NEP-8.6	1.64	0.01
TE-NEP-10.6	1.83	0.02
TEP	32.48	0.46

AVE: Average; STD: Standard deviation.

Applied nanoemulsions can potentially induce toxicity which may be caused by their small size [20]. For example, nanoparticles can penetrate the body through various pathways and remain in the system because they can escape phagocytosis through macrophages, as opposed to micro-sized particles. These residual nanoparticles with artificially created new chemical and physical properties can cause toxicity due to the ongoing body reaction and active state [39–41]. Also, due to their physico-chemical properties, such as their composition and concentration, particle size distribution, electrical properties, and interfacial properties, toxicities may change in nano-sized materials even if they were proven not to be toxic in micro- or macro-scales [20,42]. In addition, the toxicity test was performed by matching the curcumin content of TEP with the two types of nanoemulsion samples

(TE-NEP-10.6 and TE-NEP-8.6), and cytotoxicity of the nanomaterial was confirmed. The nanoemulsion (TE-NEP-10.6 and TE-NEP-8.6) used in this study showed an average diameter of 196.93 ± 4.80 nm and 202.11 ± 4.21, respectively (Figure S1). The structure of nanoemulsion was confirmed by SEM analysis. There are three reasons why emulsion sizes are observed to be smaller in representative SEM images: (1) Particle size measured using dynamic light scattering technology can be changed by the angle of light reflection or the mobility of the nanoemulsion in the solvent [43,44]. (2) The dispersed emulsion can easily aggregate with one another and the size of the emulsion can be seen to be larger when measured in the coagulated state [44–46]. Finally, (3) the sample is dried during sample preparation for SEM analysis, at which time the size of the emulsion can be reduced.

Since DNA damage is one of the important factors in tumor formation, there have been concerns regarding potential genotoxicity of the substance aimed for food or drug applications [47,48]. Previous research reports have shown that nanomaterials can cause direct or indirect DNA damage [49,50]. For instance, it has been reported that curcumin itself may cause DNA damage induced by oxidative stress at high doses (>8 μg/mL) in HepG2 cell lines [38,51]. These previous results support the genetic toxicity results induced by TE-NEP in this study. In our study, genotoxic effects were determined by comet assay to evaluate DNA damage of cells (NIH3T3, H9C2 and hCPC). This assay allows DNA damage quantification in highly efficient manner with good sensitivity. In particular, hCPC and hEPC showed higher cytotoxicity according to MTT, LDH and live/dead assay when comparing the results from the cell lines (Figure 2). Specifically, the comet assay results of hCPC showed significant differences in tail DNA% at all experimental concentrations (Figure S8b). This can be due to the fact that various cells have different characteristics such as growth environment, proliferation, and membrane properties. In general, primary cultured cells require stringent conditions such as various growth factors for cell culture and are difficult to survive in normal environments required for cell lines [24,52]. Tumor cells are also more likely to survive in harsh environments that can be caused by nanomaterials, due to their proliferative properties [53]. In addition, these cell specificities can explain relatively low cytotoxicity at several concentrations of HepG2, a tumor cell line, identified in MTT (Figure 2c) and LDH (Figure 3c) assays. Several studies also confirmed that the cytotoxicity of nanomaterials was relatively lower in the case of HepG2 compared to other cell lines [54–56]. In this study, the cellular toxicity of the prepared nanoemulsion was evaluated. Genetic toxicity assessment using comet assay was also performed. However, in the case of genotoxicity, further experiments such as micronucleus assay and gH2AX staining are required to produce more reasonable result. Ultimately, for practical applications in food and drug delivery systems, animal-level toxicity testing should be essential before the final application.

4. Materials and Methods

4.1. Sample Preparation

Turmeric extract powder (TEP) was provided by Ottogi Co., Ltd. (Anyang, Gyeonggi-do, Korea). Two types of turmeric extract-loaded nanoemulsion powder (TE-NEP-8.6 and TE-NEP-10.6) were provided by J.T. Kim (Keimyung University, Daegu, Korea). Briefly, oil phase was prepared by dissolving 20% (*w/w* based on MCT) TEP in MCT oil containing soy lecithin. The aqueous phase was prepared by mixing tween 80 and distilled water. The amount of soy lecithin and tween 80 were adjusted to the hydrophilic lipophilic balance (HLB) values of 10.6 and 8.6. The coarse emulsion was prepared by magnetic stirring under ambient temperature for 2 h. Then, nanoemulsions were prepared by further homogenizing the coarse emulsion through high speed homogenization (HSH) (HG-15D, Daihan Scientific Co., Ltd., Wonju, Korea) at 5000 rpm for 10 min, ultrasonication (US) with a Vibra Cell (VCX-750, Sonics & Materials, Inc., Sandy Hook, CT, USA) for 15 min, and high-pressure homogenization under 10,000 psi for 3 cycles. TE-NEP-10.6 and TE-NEP-8.6 indicate the turmeric extract-loaded nanoemulsion with HLB values of 10.6 and 8.6, respectively. Control NE was prepared by using the same method without turmeric extract powder. TE-NEP was prepared by spray drying

(KL-8, Seo Gang Engineering Co., Ltd., Cheonan, Korea) with TE-NE solution and dextrin. The spray drying conditions were as follows: inlet temperature at 120 °C, flow rate at 50 mL/min, and outlet temperature at 180 °C.

4.2. Cell Culture

4.2.1. Cell Lines

Mouse fibroblasts (NIH3T3), rat heart myoblasts (H9C2), and human hepatoblastoma (HepG2) cells were purchased from Korean Cell Line Bank (KCLB, Seoul, Korea). Cells were cultured in high-glucose Dulbecco's Modified Eagle's Medium (DMEM; Welgene, Daegu, Korea) supplemented with 10% fetal bovine serum (FBS, Welgene) and 1X penicillin/streptomycin (P/S, Welgene). Cells were routinely incubated under humidified atmosphere containing 5% CO_2 at 37 °C and subcultured when 85% confluent.

4.2.2. Primary Cells

Human endothelial progenitor cells (hEPCs) and Human cardiac progenitor cells (hCPCs) were kindly provided by S.M. Kwon (Pusan University, Pusan, Korea, IRB number: 05-2015-133). The hEPCs were cultured on 1% gelatin coated dishes in EC basal medium 2 (EBM-2MV, Lonza, Walkersville, MD, USA) supplemented with 5% FBS, EGM-2-MV BulletKit and 1X P/S. The hCPCs were cultured in Ham's F12 medium (Hyclone, Logan, UT, USA) containing 10% FBS, 1X P/S, 0.005 U/mL human erythropoietin (hEPO, R&D system, Minneapolis, MN, USA), 5 ng/mL human basic fibroblast growth factor (hbFGF, PeproTech, Rocky Hill, NJ, USA) and 0.2 mM L-glutathione reduced (Sigma-Aldrich, St. Louis, MO, USA). All of the cells were cultured under standard cell culture condition using 5% CO_2 incubator at 37 °C and subcultured when 85% confluent.

4.3. Cytotoxicity Assay

4.3.1. MTT Assay

The cytotoxicity of cells was observed by using 3-(4,5-Dimethylthiazol-2-yl)-2,5-diphenyltetrazoliumbromide (MTT, Duchefa, Haarlem, The Netherlands) assay. Briefly, cells were seeded on a 96-well plate and cultivated for 24 h at 37 °C (5% CO_2). The appropriate cell density was selected according to the cell type. HepG2 at a cell density of 2×10^4 cells, all other cells at 1×10^4 cells per 100 μL medium were seeded into each well of the 96-well plates. Afterwards, the cells were exposed to the TEP, TE-NEP-10.6, TE-NEP-8.6 at the several concentrations (0–20 mg/mL), respectively and incubated for 1 day. Negative control was prepared by adding single-wall carbon nanotube (SWCNT) at concentrations of 0.025, 0.05, 0.1, 0.25, 0.5, 1, and 5 mg/mL. After the exposure, medium was changed followed by the addition of 5 μL of MTT reagent (5 mg/mL stock). The cells were incubated for 3 h at cell culture condition, and lysed in DMSO (100 μL per well). The development of color was measured spectrophotometrically using Epoch microplate spectrophotometer (BioTek Instruments, Winooski, VT, USA) at 570 nm. All absorbance values were corrected against blank wells. The cell viability was calculated by the following formula (A = absorbance):

$$\text{Cell viability (\%)} = \frac{A_{sample} - A_{blank}}{A_{control} - A_{blank}} \times 100$$

4.3.2. Live/Dead Assay

A LIVE/DEAD Viability/Cytotoxicity Kit for mammalian cells (Thermo Fisher Scientific, Walthan, MA, USA) was used according to the manufacturer's instructions to visualize cell viability. Briefly, 20 μL of 2 mM ethidium homodimer-1 (EthD-1) stock solution and 5 μL of 4 mM calcein-AM solutions were diluted in 10 mL of sterile and prewarmed Dulbecco's Phosphate-Buffered Saline

(DPBS, Welgene). The mixture was then mixed and distributed to cells in 96-well plates, followed by incubation for 45 min at room temperature. After the staining procedure, stained cells were imaged using fluorescent microscope (Nikon, ECLIPSE Ts2, Tokyo, Japan).

4.3.3. Lactate Dehydrogenase (LDH) Assay

Lactate dehydrogenase (LDH) leakage into the culture medium from dead cells was measured using EZ-LDH Cell Cytotoxicity Assay Kit (Daeil Lab Service, Seoul, Korea). The LDH release assay was used according to the manufacturer's direction. In brief, cells were seeded in 96-well plates. Optimal cell density was selected for each cell through the cell optimization step. Cells were treated with a range of concentrations (0–20 mg/mL) of each sample (TEP, TE-NEP-8.6 and TE-NEP-10.6) for 24 h. CNT was used a positive control and group without cells were prepared as a blank. After the incubation with treated sample for 1 day, the cultures were centrifuged at 600 g for 5 min. The high control, which was the maximum amount of LDH that could be released from a cell by artificially killing the cells, was combined with the lysis buffer before the collection of the supernatant and reacted for 5 min at room temperature. Following the centrifugation, 10 μL of the supernatant was transferred to new 96-well plate and 100 μL of LDH reaction mixture was added to each well and mixed carefully. The mixture was reacted at room temperature for 30 min in dark. Absorbance was measured at 450 nm using the microplate spectrophotometer after shaking gently. The percentage of total cellular LDH released was determined using the following equation:

$$\text{Cytotoxicity} = (A - B)/(C - B) \times 100$$

where A indicates the OD value of Experimental LDH release, B is OD value of spontaneous LDH release, and C stands for OD value of maximal LDH release (high control).

4.4. Statistical Analysis

The statistical evaluations of results were analyzed by GraphPad Prism 5.0 (GraphPad Prism Software, Inc., San Diego, CA, USA). The values are expressed as mean ± standard deviation (SD). For comparison of multiple groups, one-way analysis of variance (ANOVA) with a post-hoc Bonferroni test was applied. For all analyses, $p < 0.05$ was considered as statistically significant. The significance of differences between two groups was performed by unpaired two-tailed Student t test.

5. Conclusions

Cell-level toxicity studies (MTT, LDH, Live/dead assay) were conducted for applications in food or drug delivery of nanoemulsions. Overall, the toxicity of the nanoemulsion did not significantly affect its composition and increased in a concentration-dependent manner. Results obtained from this study provide a basic knowledge of the cytotoxicity of nanoemulsion on various cell types and can be used as a basis for future animal experiments.

References

1. Singh, Y.; Meher, J.G.; Raval, K.; Khan, F.A.; Chaurasia, M.; Jain, N.K.; Chourasia, M.K. Nanoemulsion: Concepts, development and applications in drug delivery. *J. Control. Release* **2017**, *252*, 28–49. [CrossRef] [PubMed]

2. Bush, L.; Stevenson, L.; Lane, K.E. The oxidative stability of omega-3 oil-in-water nanoemulsion systems suitable for functional food enrichment: A systematic review of the literature. *Crit. Rev. Food Sci. Nutr.* **2017**, 1–15. [CrossRef] [PubMed]

3. Silva, H.D.; Cerqueira, M.Â.; Vicente, A.A. Nanoemulsions for food applications: Development and characterization. *Food Bioprocess Technol.* **2012**, *5*, 854–867. [CrossRef]

4. Ma, P.; Zeng, Q.; Tai, K.; He, X.; Yao, Y.; Hong, X.; Yuan, F. Preparation of curcumin-loaded emulsion using high pressure homogenization: Impact of oil phase and concentration on physicochemical stability. *LWT Food Sci. Technol.* **2017**, *84*, 34–46. [CrossRef]

5. Laokuldilok, N.; Thakeow, P.; Kopermsub, P.; Utama-ang, N. Optimisation of microencapsulation of turmeric extract for masking flavour. *Food Chem.* **2016**, *194*, 695–704. [CrossRef] [PubMed]

6. Devaraj, S.D.; Neelakantan, P. Curcumin-pharmacological actions and its role in dentistry. *Asian J. Pharm. Res. Health Care* **2014**, *6*, 19–22.

7. Ferrari, E.; Benassi, R.; Saladini, M.; Orteca, G.; Gazova, Z.; Siposova, K. In vitro study on potential pharmacological activity of curcumin analogues and their copper complexes. *Chem. Biol. Drug Des.* **2017**, *89*, 411–419. [CrossRef] [PubMed]

8. Adiwidjaja, J.; McLachlan, A.J.; Boddy, A.V. Curcumin as a clinically-promising anti-cancer agent: Pharmacokinetics and drug interactions. *Expert Opin. Drug Metab. Toxicol.* **2017**, *13*, 953–972. [CrossRef] [PubMed]

9. Martins, R.M.; Pereira, S.V.; Siqueira, S.; Salomão, W.F.; Freitas, L.A.P. Curcuminoid content and antioxidant activity in spray dried microparticles containing turmeric extract. *Food Res. Int.* **2013**, *50*, 657–663. [CrossRef]

10. Yu, H.; Nguyen, M.-H.; Cheow, W.S.; Hadinoto, K. A new bioavailability enhancement strategy of curcumin via self-assembly nano-complexation of curcumin and bovine serum albumin. *Mater. Sci. Eng. C* **2017**, *75*, 25–33. [CrossRef] [PubMed]

11. Hartono, S.B.; Hadisoewignyo, L.; Yang, Y.; Meka, A.K.; Yu, C. Amine functionalized cubic mesoporous silica nanoparticles as an oral delivery system for curcumin bioavailability enhancement. *Nanotechnology* **2016**, *27*, 505605. [CrossRef] [PubMed]

12. Rashidi, L.; Khosravi-Darani, K. The applications of nanotechnology in food industry. *Crit. Rev. Food Sci. Nutr.* **2011**, *51*, 723–730. [CrossRef] [PubMed]

13. Cushen, M.; Kerry, J.; Morris, M.; Cruz-Romero, M.; Cummins, E. Nanotechnologies in the food industry–Recent developments, risks and regulation. *Trends Food Sci. Technol.* **2012**, *24*, 30–46. [CrossRef]

14. Pulizzi, F. Nanotechnology and food: What people think. *Nat. Nanotechnol.* **2016**. [CrossRef]

15. Commission, E. Commission Recommendation of 18 October 2011 on the definition of nanomaterial (2011/696/EU). Official Journal of the European Union. 2011. Available online: https://ec.europa.eu/research/industrial_technologies/pdf/policy/commission-recommendation-on-the-definition-of-nanomater-18102011_en.pdf (accessed on 20 October 2011).

16. Committee, E.S. Guidance on the risk assessment of the application of nanoscience and nanotechnologies in the food and feed chain. *EFSA J.* **2011**, *9*. [CrossRef]

17. OFFICE, G.P. *An Act to Authorize Appropriations for Nanoscience, Nanoengineering, and Nanotechnology Research, and for Other Purposes*; U.S. Government Publishing Office: Washington, DC, USA, 2003; Volume 149, pp. 1923–1932.

18. Health, U.D.O.; Services, H. *Guidance for Industry: Considering Whether an FDA-Regulated Product Involves the Application of Nanotechnology*; FDA Center for Drug Evaluation and Research (CDER): Silver Spring, MD, USA, 2014; pp. 1–14.

19. Department, I.A. *Management System of Nanotechnology Applied Food*; National Food Safety Information Service: Seoul, Korea, 2017.

20. McClements, D.J.; Rao, J. Food-grade nanoemulsions: Formulation, fabrication, properties, performance, biological fate, and potential toxicity. *Crit. Rev. Food Sci. Nutr.* **2011**, *51*, 285–330. [CrossRef] [PubMed]

21. McClements, D.J. Edible lipid nanoparticles: Digestion, absorption, and potential toxicity. *Prog. Lipid Res.* **2013**, *52*, 409–423. [CrossRef] [PubMed]

22. Mitzner, S.R.; Stange, J.; Klammt, S.; Peszynski, P.; Schmidt, R.; NÖLDGE-SCHOMBURG, G. Extracorporeal detoxification using the molecular adsorbent recirculating system for critically ill patients with liver failure. *J. Am. Soc. Nephrol.* **2001**, *12*, S75–S82. [PubMed]

23. Lakatta, E.G. Cardiovascular System. In *Comprehensive Physiology*; John Wiley & Sons, Inc.: Hoboken, NJ, USA, 2011. [CrossRef]

24. Ekwall, B.; Silano, V.; Paganuzzi-Stammati, A.; Zucco, F. *Toxicity Tests with Mammalian Cell Cultures*; John Wiley & Sons Ltd.: Hoboken, NJ, USA, 1990; pp. 75–99.

25. Bhushani, J.A.; Karthik, P.; Anandharamakrishnan, C. Nanoemulsion-based delivery system for improved bioaccessibility and Caco-2 cell monolayer permeability of green tea catechins. *Food Hydrocoll.* **2016**, *56*, 372–382. [CrossRef]

26. Gonçalves, A.; Nikmaram, N.; Roohinejad, S.; Estevinho, B.N.; Rocha, F.; Greiner, R.; McClements, D.J. Production, properties, and applications of solid self-emulsifying delivery systems (S-SEDS) in the food and pharmaceutical industries. *Colloids Surf. A Physicochem. Eng. Asp.* **2017**, *538*, 108–126. [CrossRef]

27. Joung, H.J.; Choi, M.J.; Kim, J.T.; Park, S.H.; Park, H.J.; Shin, G.H. Development of Food-Grade Curcumin Nanoemulsion and its Potential Application to Food Beverage System: Antioxidant Property and In Vitro Digestion. *J. Food Sci.* **2016**, *81*. [CrossRef] [PubMed]

28. Lin, C.-C.; Lin, H.-Y.; Chi, M.-H.; Shen, C.-M.; Chen, H.-W.; Yang, W.-J.; Lee, M.-H. Preparation of curcumin microemulsions with food-grade soybean oil/lecithin and their cytotoxicity on the HepG2 cell line. *Food Chem.* **2014**, *154*, 282–290. [CrossRef] [PubMed]

29. Prabhakar, K.; Afzal, S.M.; Surender, G.; Kishan, V. Tween 80 containing lipid nanoemulsions for delivery of indinavir to brain. *Acta Pharm. Sin. B* **2013**, *3*, 345–353. [CrossRef]

30. Hussain, Z.; Thu, H.E.; Amjad, M.W.; Ahmed, T.A.; Khan, S. Exploring recent developments to improve antioxidant, anti-inflammatory and antimicrobial efficacy of curcumin: A review of new trends and future perspectives. *Mater. Sci. Eng. C* **2017**, *77*, 1316–1326. [CrossRef] [PubMed]

31. Malik, P.; Singh, M. Study of curcumin antioxidant activities in robust oil–water nanoemulsions. *New J. Chem.* **2017**, *41*, 12506–12519. [CrossRef]

32. Gómez-Estaca, J.; Balaguer, M.; López-Carballo, G.; Gavara, R.; Hernández-Muñoz, P. Improving antioxidant and antimicrobial properties of curcumin by means of encapsulation in gelatin through electrohydrodynamic atomization. *Food Hydrocoll.* **2017**, *70*, 313–320. [CrossRef]

33. Edwards, R.L.; Luis, P.B.; Varuzza, P.V.; Joseph, A.I.; Presley, S.H.; Chaturvedi, R.; Schneider, C. The anti-inflammatory activity of curcumin is mediated by its oxidative metabolites. *J. Biol. Chem.* **2017**, *292*, 21243–21252. [CrossRef] [PubMed]

34. Yang, H.; Du, Z.; Wang, W.; Sanidad, K.; Zhang, G. Structure and activity relationship of curucmin: Role of methoxy group in anti-inflammatory and anti-colitis effects of curcumin. *FASEB J.* **2017**, *31*, 972.24.

35. Wang, X.-P.; Wang, Q.-X.; Lin, H.-P.; Chang, N. Anti-tumor bioactivities of curcumin on mice loaded with gastric carcinoma. *Food Funct.* **2017**, *8*, 3319–3326. [CrossRef] [PubMed]

36. Sirohi, V.K.; Popli, P.; Sankhwar, P.; Kaushal, J.B.; Gupta, K.; Manohar, M.; Dwivedi, A. Curcumin exhibits anti-tumor effect and attenuates cellular migration via Slit-2 mediated down-regulation of SDF-1 and CXCR4 in endometrial adenocarcinoma cells. *J. Nutr. Biochem.* **2017**, *44*, 60–70. [CrossRef] [PubMed]

37. Mock, C.D.; Jordan, B.C.; Selvam, C. Recent advances of curcumin and its analogues in breast cancer prevention and treatment. *RSC Adv.* **2015**, *5*, 75575–75588. [CrossRef] [PubMed]

38. EFSA. Scientific Opinion on the reevaluation of curcumin (E 100) as a food additive. *EFSA J.* **2010**, *8*, 46.

39. Karakoti, A.; Hench, L.; Seal, S. The potential toxicity of nanomaterials—The role of surfaces. *JOM J. Miner. Met. Mater. Soc.* **2006**, *58*, 77–82. [CrossRef]

40. Oberdörster, G.; Oberdörster, E.; Oberdörster, J. Nanotoxicology: An emerging discipline evolving from studies of ultrafine particles. *Environ. Health Perspect.* **2005**, *113*, 823–839. [CrossRef] [PubMed]

41. Borm, P.J.; Robbins, D.; Haubold, S.; Kuhlbusch, T.; Fissan, H.; Donaldson, K.; Schins, R.; Stone, V.; Kreyling, W.; Lademann, J. The potential risks of nanomaterials: A review carried out for ECETOC. *Part. Fibre Toxicol.* **2006**, *3*, 11. [CrossRef] [PubMed]

42. Nel, A.; Xia, T.; Mädler, L.; Li, N. Toxic potential of materials at the nanolevel. *Science* **2006**, *311*, 622–627. [CrossRef] [PubMed]

43. Beliciu, C.; Moraru, C. Effect of solvent and temperature on the size distribution of casein micelles measured by dynamic light scattering. *J. Dairy Sci.* **2009**, *92*, 1829–1839. [CrossRef] [PubMed]

44. Teng, T.-P.; Hung, Y.-H.; Teng, T.-C.; Chen, J.-H. Performance evaluation on an air-cooled heat exchanger for alumina nanofluid under laminar flow. *Nanoscale Res. Lett.* **2011**, *6*, 488. [CrossRef] [PubMed]

45. Ogawa, S.; Decker, E.A.; McClements, D.J. Influence of environmental conditions on the stability of oil in water emulsions containing droplets stabilized by lecithin−chitosan membranes. *J. Agric. Food Chem.* **2003**, *51*, 5522–5527. [CrossRef] [PubMed]

46. Klang, V.; Matsko, N.B.; Valenta, C.; Hofer, F. Electron microscopy of nanoemulsions: An essential tool for characterisation and stability assessment. *Micron* **2012**, *43*, 85–103. [CrossRef] [PubMed]

47. Roos, W.P.; Thomas, A.D.; Kaina, B. DNA damage and the balance between survival and death in cancer biology. *Nat. Rev. Cancer* **2016**, *16*, 20–33. [CrossRef] [PubMed]

48. Ohnishi, S.; Ma, N.; Thanan, R.; Pinlaor, S.; Hammam, O.; Murata, M.; Kawanishi, S. DNA damage in inflammation-related carcinogenesis and cancer stem cells. *Oxidative Med. Cell. Longev.* **2013**, *2013*, 387014. [CrossRef] [PubMed]

49. Kumar, A.; Dhawan, A. Genotoxic and carcinogenic potential of engineered nanoparticles: An update. *Arch. Toxicol.* **2013**, *87*, 1883–1900. [CrossRef] [PubMed]

50. Landsiedel, R.; Kapp, M.D.; Schulz, M.; Wiench, K.; Oesch, F. Genotoxicity investigations on nanomaterials: Methods, preparation and characterization of test material, potential artifacts and limitations—Many questions, some answers. *Mutat. Res.* **2009**, *681*, 241–258. [CrossRef] [PubMed]

51. Cao, J.; Jiang, L.-P.; Liu, Y.; Yang, G.; Yao, X.-F.; Zhong, L.-F. Curcumin-induced genotoxicity and antigenotoxicity in HepG2 cells. *Toxicon* **2007**, *49*, 1219–1222. [CrossRef] [PubMed]

52. Zorn-Kruppa, M.; Tykhonova, S.; Belge, G.; Diehl, H.A.; Engelke, M. Comparison of human corneal cell cultures in cytotoxicity testing. *Altex* **2004**, *21*, 129–134. [PubMed]

53. Kong, B.; Seog, J.H.; Graham, L.M.; Lee, S.B. Experimental considerations on the cytotoxicity of nanoparticles. *Nanomedicine* **2011**, *6*, 929–941. [CrossRef] [PubMed]

54. Kim, I.-Y.; Joachim, E.; Choi, H.; Kim, K. Toxicity of silica nanoparticles depends on size, dose, and cell type. *Nanomed. Nanotechnol. Biol. Med.* **2015**, *11*, 1407–1416. [CrossRef] [PubMed]

55. Das, G.K.; Chan, P.P.; Teo, A.; Loo, J.S.C.; Anderson, J.M.; Tan, T.T.Y. In vitro cytotoxicity evaluation of biomedical nanoparticles and their extracts. *J. Biomed. Mater. Res. Part A* **2010**, *93*, 337–346.

56. Sambale, F.; Wagner, S.; Stahl, F.; Khaydarov, R.; Scheper, T.; Bahnemann, D. Investigations of the toxic effect of silver nanoparticles on mammalian cell lines. *J. Nanomater.* **2015**, *16*, 6. [CrossRef]

Article

Fabrication of In Vitro Cancer Microtissue Array on Fibroblast-Layered Nanofibrous Membrane by Inkjet Printing

Tae-Min Park [1],[†], Donggu Kang [2],[†], Ilho Jang [3], Won-Soo Yun [4],[5], Jin-Hyung Shim [5], Young Hun Jeong [6], Jong-Young Kwak [7], Sik Yoon [8] and Songwan Jin [5],*

[1]   Research Institute, Femtobiomed Co., Ltd., 700, Pangyo-ro, Seongnam-si, Gyeonggi-do 13516, Korea; taemin333@gmail.com
[2]   Department of Mechanical System Engineering, Korea Polytechnic Univsersity, 237 Sangidaehak-ro, Siheung-si, Gyoenggi-do 15073, Korea; kdgplant@naver.com
[3]   Department of Advanced Convergence Technology, Korea Polytechnic Univsersity, 237 Sangidaehak-ro, Siheung-si, Gyoenggi-do 15073, Korea; bluenadsky@gmail.com
[4]   Research Institute, T&R Biofab Co., Ltd., 237 Sangidaehak-ro, Siheung-si, Gyoenggi-do 15073, Korea; wsyun@tnrbiofab.com
[5]   Department of Mechanical Engineering, Korea Polytechnic Univsersity, 237 Sangidaehak-ro, Siheung-si, Gyoenggi-do 15073, Korea; happyshim@kpu.ac.kr
[6]   School of Mechanical Engineering, Kyungpook National University, 80 Daehak-ro, Buk-gu, Daegu 702-701, Korea; yhjeong@knu.ac.kr
[7]   Department of Pharmacology, Ajou University School of Medicine, Suwon 442-721, Korea; jykwak@ajou.ac.kr
[8]   Department of Anatomy, Pusan National University School of Medicine, Yangsan 626-770, Korea; sikyoon@pusan.ac.kr
*   Correspondence: songwan@kpu.ac.kr; Tel.: +82-31-8041-1819
†   These authors contributed equally to this work.

Abstract: In general, a drug candidate is evaluated using 2D-cultured cancer cells followed by an animal model. Despite successful preclinical testing, however, most drugs that enter human clinical trials fail. The high failure rates are mainly caused by incompatibility between the responses of the current models and humans. Here, we fabricated a cancer microtissue array in a multi-well format that exhibits heterogeneous and batch-to-batch structure by continuous deposition of collagen-suspended Hela cells on a fibroblast-layered nanofibrous membrane via inkjet printing. Expression of both Matrix Metalloproteinase 2 (MMP2) and Matrix Metalloproteinase 9 (MMP9) was higher in cancer microtissues than in fibroblast-free microtissues. The fabricated microtissues were treated with an anticancer drug, and high drug resistance to doxorubicin occurred in cancer microtissues but not in fibroblast-free microtissues. These results introduce an inkjet printing fabrication method for cancer microtissue arrays, which can be used for various applications such as early drug screening and gradual 3D cancer studies.

Keywords: in vitro cancer model; inkjet cell printing; microtissue array; cancer drug discovery; electrospinning; nanofibrous membrane

1. Introduction

Animal models are limited in their ability to mimic extremely complex carcinogenic and physiological processes in humans and more than 90% of drugs that pass animal trials fail in the clinical trials [1,2]. Various researchers have developed biomimetic models that can produce results similar to

actual responses in humans, and three-dimensionally (3D) cultured cells have been found to better represent human tissue than two-dimensionally (2D) cultured cells [3–9]. Most cells in tissues are surrounded by an extracellular matrix (ECM), which provides a structural chemical environment for cells and interacts with cells/ECM to regulate diverse functions including proliferation, differentiation, and migration [10]. Therefore, we employed an electrospun nanofibrous membrane (NF) whose structure is similar to that of the extracellular matrix. The cell-laden NF has various morphologies, in contrast to two-dimensionally cultured cells, and the cells interact more actively based on the surface characteristics of this membrane.

In the drug discovery process, multiple tests are required to verify various factors such as efficacy, safety, and dose of the drug [11]. Current 3D culture models have various difficulties such as limited control over cell positioning and multiply arrayed cells and batch-to-batch variability. To this end, this study developed and evaluated a patterned cancer microtissue array with controlled size and shape as well as batch-to-batch structures using an inkjet printer. Multiple tests can be simultaneously performed on the developed microtissue array (Figure 1). The inkjet printer enabled precise adjustment of the spatial placement of the tissue formed on the NF with microscale resolution, and quantitative cell seeding was possible, thus improving the repeatability and reproducibility of the model.

The tumor microenvironment is constantly evolving owing to tissue remodeling and changes in the recruitment of stromal cells including a diversity of immune cells with angiogenesis. As the tumor becomes larger, the phenotype of cancer cells changes to aggressive, and in the tumor microenvironment, the extracellular matrix also changes [12]. In addition, fibroblasts, which are cancer stromal cells, play an important role in tumor progression, growth, and metastasis [13]. Therefore, developing functional and gradational cancer models that mimic the tumor microenvironment, including stromal cells, are required for testing drugs and investigating mechanisms of tumor progression as well as cancer metastasis.

This study used cervical cancer cells, which are invasive and aggressive and closely associated with matrix metalloproteinases (MMPs). In particular, MMP2 and MMP9 have been found to be the most important in the degradation of the basement membrane and extracellular matrix needed for cells to acquire invasive capabilities [14]. In this study, MMP2 and MMP9 levels were measured through enzyme-linked immunosorbent assay (ELISA) to verify the effect of co-culturing with fibroblasts. The 3D structure of the fabricated cancer microtissue was examined using histological analysis, scanning electron microscopy (SEM), and confocal microscopy by staining for human papillomavirus 18 (HPV18), which is specifically found in cervical cancer cells. Finally, we treated the model with an anticancer drug for assessment of the drug response.
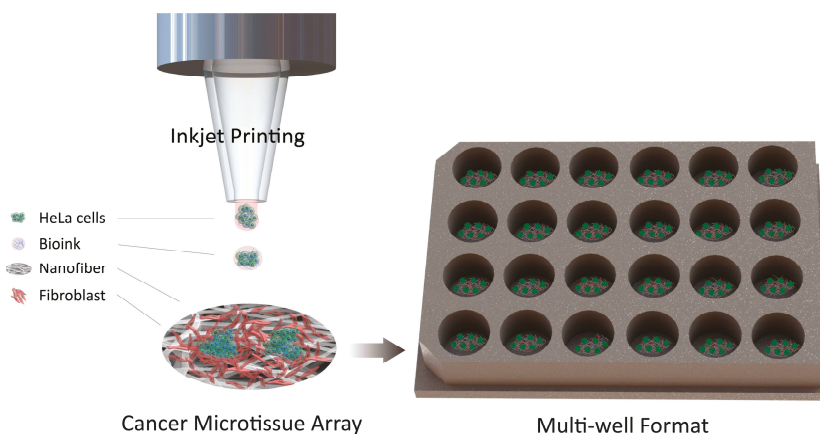

Figure 1. Schematic illustration of cancer microtissue array.

2. Results

2.1. Concept of the Cancer Microtissue Array

2.1.1. Electrospinning and Nanofibrous Membrane

The diameter distribution of the nanofibers characterized by SEM imaging (Figure 2a) is shown in Figure 2b; the nanofiber diameter ranged from 150 to 1200 nm, and the peak frequency of the diameter was 350 to 500 nm.
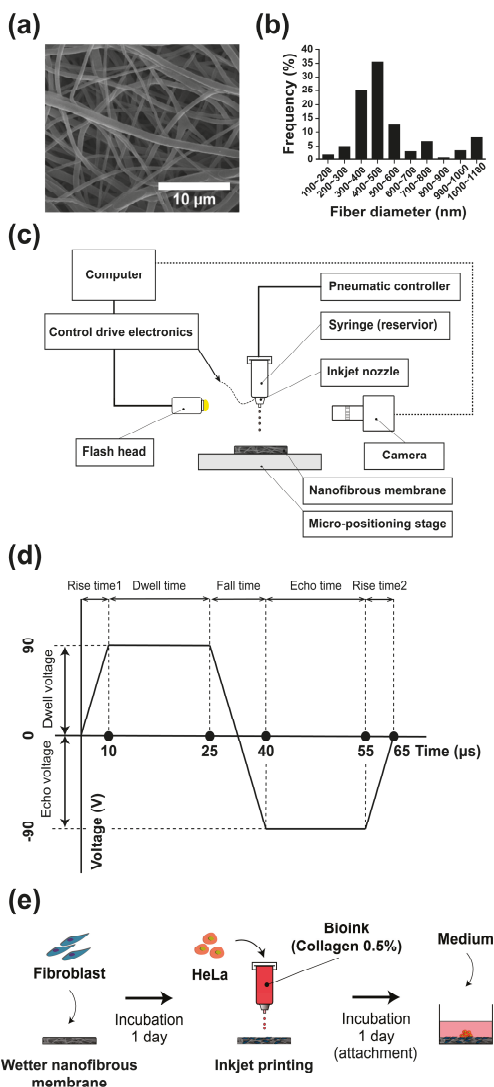

Figure 2. Scanning electron microscopy (SEM) image of the electrospun nanofibrous membrane (NF) (**a**); diameter distribution of the nanofibers (**b**); schematic representation of the inkjet printer (**c**); bipolar waveform for piezo actuation (**d**); and schematic representation of the cancer microtissue fabrication process (**e**).

2.1.2. Inkjet Printer Setup

Figure 2c presents a schematic representation of the inkjet printer setup. The piezoelectric drop-on-demand print-head had an inner diameter of 80 μm (MJ-AL-01-80-8MX, Microfab, Inc., Plano, TX, USA), and an electronic control drive (CT-M3-04, Microfab, Inc.) and a pressure controller (Super EX-V7, Musashi Engineering, Inc., Tokyo, Japan) were coupled. The pressure controller applied negative pressure to prevent leakage of bioink from the nozzle.

The printing droplet frequency was set at 10 Hz, and the distance between the printer head and NF was maintained at 2 mm or less to minimize physical damage to the cells during printing. The piezo actuation of the inkjet printing was as shown in Figure 2d. The droplet pattern could be printed by directly moving the NF using a triaxial microstage.

2.1.3. Schematic Illustration of Cancer Microtissue Array Process

To fabricate cancer microtissue samples, droplets of the 0.5% collagen bioink containing cancer cells were dropped 150 times using an inkjet printer on a NF as shown in Figure 2e. Three different conditions for the NF were tested: the first was bare membrane, and the others were fibroblast-layered NF with different cell seeding densities.

2.2. Cell Viability and Diameter

2.2.1. Cell Viability on Glass and Nanofibrous Membrane

In this study, we aimed to pattern four cancer microtissue arrays (diameter of each cancer microtissue, approximately 500 μm) within a diameter of 10 mm. In order to insure the consistency in size of each microtissue, the same number of cells needs to be seeded at one point in designed positions. Inkjet cell printing technology was used for microtissue array fabrication since it enables high resolution patterning of specific cells with soluble biomaterials, providing an ideal environment for fabricating the biomimetic samples. The viability of printed cells compared with that of cells suspended only in medium (bioink) or medium containing 0.5% collagen (collagen-containing bioink) was evaluated through a Live/Dead assay (Figure 3a,b). The cell viability on the NF was approximately 100%, whereas that on glass was approximately 0% owing to drying out of bioink, as shown in Figure 3c. Therefore, it was confirmed that the NF provided a sufficient niche for cells in terms of a medium-infiltrated substrate, owing to its large surface-to-volume ratio.

2.2.2. Cell Aggregate Formation on Glass and NF

As shown in Figure 3c, the droplet of collagen-containing bioink printed on the glass had smaller diameter and a narrower cell distribution area than that of the bioink only, indicating that the cancer cells were more strongly distributed at the central area of the droplets. Similarly, the cell-distributed area of collagen-containing bioink on the NF was smaller than that of the bioink. Consequently, the cell-distributed area of collagen-containing bioink on the NF was the narrowest (Figure 3d), owing to the robust structure of randomly intertwined interstitial fibers and viscous collagen. Therefore, printing on a non-porous two-dimensional substrate such as a glass was unsuitable for fabricating cell aggregates, and the NF was a rather suitable alternative. Inkjet printing with collagen-containing bioink on an NF was optimal for fabricating cancer cell aggregates.

2.3. Diameter of Cancer Microtissue

We next compared mono-cultured cancer microtissue and co-cultured (i.e., fibroblast-layered NF; 1×10^4 cells/mL) cancer microtissue. Figure 4 shows the remodeling and diameter of the printed microtissue over time. On days 3, 5, and 7, the printed microtissue on fibroblast-layered NF (Figure 4d–f) maintained its size better than the mono-cultured microtissue (Figure 4a–c). The diameter of the fibroblast-layered microtissue increased by approximately 14% from day 3 to day 5, but the

shape was almost identical on days 5 and 7, as shown in Figure 4g. In contrast, the diameter of the mono-cultured microtissue increased by 30% between day 3 and day 5 and by approximately 40% between day 5 and day 7. Therefore, the fibroblast-layered microtissue is more appropriate as a cancer model because it maintains the cancer-aggregate formation over time and hence does not have temporal constraints in drug screening applications.
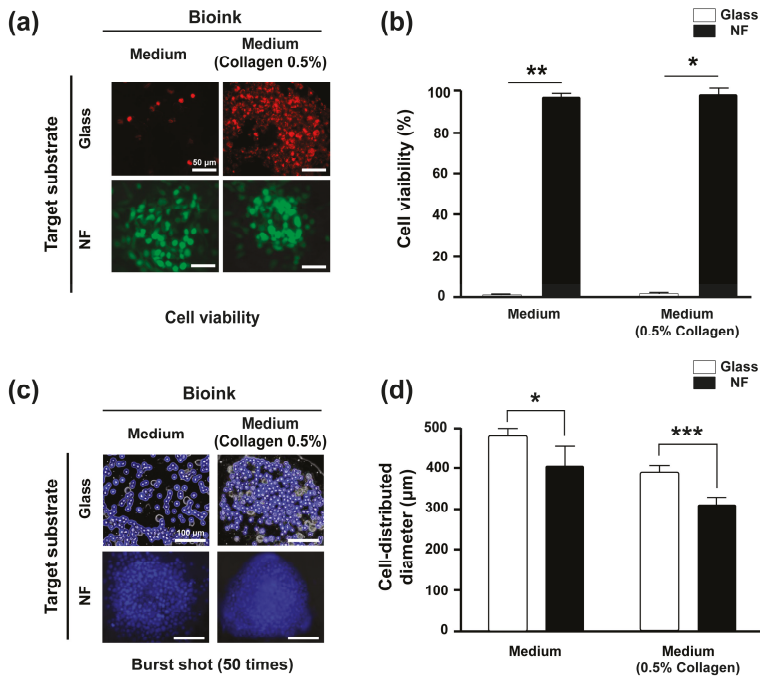

Figure 3. Cell viability and aggregate formation of cancer cells printed on glass and NF; Live/Dead assays of HeLa cells printed on the NF and glass. Cells were suspended in culture medium and culture medium containing 0.5% collagen. The live and dead cells are denoted in green and red, respectively (**a**). Viability of the printed cancer cells (**b**). Shapes of droplets printed on glass and NF (**c**); white arrows show protruding cells. Cells were suspended in culture medium and culture medium containing 0.5% collagen. Cell-distributed diameter according to the number of printed droplets (burst shot; 50 times) on glass and the NF (**d**). All experimental samples were $n > 3$. $* p < 0.01$, $** p < 0.005$, $*** p < 0.001$. Unmarked scale bars in Figure 3a and 3c, 50 µm and 100 µm, respectively.
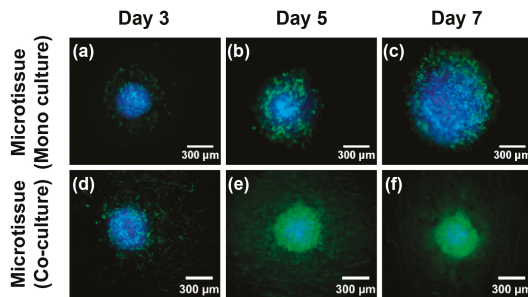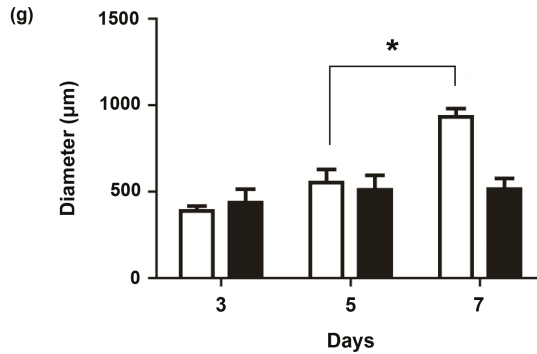

Figure 4. *Cont.*

Figure 4. Immunofluorescence staining images of the mono-cultured cancer microtissue (**a**–**c**) and fibroblast-layered microtissue (**d**–**f**). Change in diameter of cancer microtissues with time (**g**). Blue, cell nucleus; green, F-actin staining. All experimental samples were $n > 3$. (* $p < 0.01$).

2.4. Cancer Microtissue Formation on Fibroblast Layer

To verify the effect of the interstitial fibroblast layer on the NF for generation of an in vitro cancer microtissue array, the mono-cultured microtissue and the fibroblast-layered microtissues (1×10^4 cells/mL) were examined using immunofluorescent staining on day 7 (Figure 5a–f). The cancer cells in monoculture models were spread widely without forming cell aggregates, whereas the fibroblast layer stabilized the forms of the cell aggregates.

The expression of MMP2 and MMP9 was measured by ELISA using the monocultured and fibroblast-layered microtissue (1×10^4 cells/mL), respectively. As shown in Figure 5g,h, MMP2 and MMP9 were upregulated in the fibroblast-layered microtissue rather than in the mono-cultured microtissue. Especially on day 7, the MMP2 and MMP9 expression of the fibroblast-layered microtissue was approximately 1.5-fold and 2-fold higher than that of the monocultured microtissue. The high levels of MMP2 and MMP9, which are important factors in extracellular matrix remodeling [14], are evidence of good biomimicry, and we can conclude that the fibroblast-layered microtissue better represents cancer tissues than the monocultured microtissue.
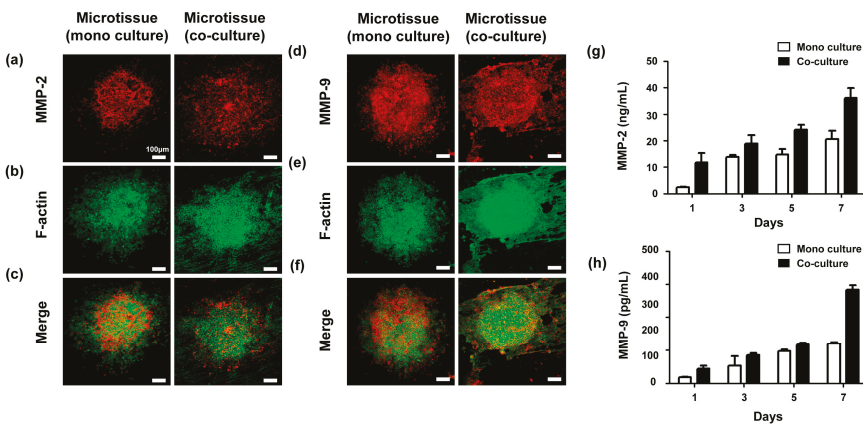

Figure 5. Cancer microtissues (**a**–**f**); monocultured microtissue and fibroblast-layered microtissue (1×10^4 cell/mL) on day 7. Red, MMP2 (**a**) and MMP9 (**d**); green, F-actin (**b**,**e**). MMP2 (**g**) and MMP9 (**h**) expression in the mono-cultured and fibroblast-layered microtissues was quantified using ELISA. All experimental samples were $n > 3$. Unmarked Scale bars, 100 μm.

2.5. 3D Formation and Shape of The Cancer Microtissue

3D characteristics of the fabricated microtissue are shown in Figure 6. Confocal imaging showed that the HeLa cells cultured on the fibroblast-layered NF formed a 3D, disk-like structure with a thickness of approximately 50 μm. Furthermore, fluorescence staining showed that HPV18, which is specifically associated with cervical cancer, was strongly expressed by the patterned cancer tissues, and the cancer tissues were easily identified in the fibroblast-layered microtissue (Figure 6b). As shown in Figure 6b, we were able to prepare four individual cancer microtissues within one well of a 96-well plate, and those tissues were maintained for up to seven days. SEM (Figure 6c) showed that the surrounding fibroblasts (Figure 6c; white arrow) and the formed cancer tissue (Figure 6c; red arrow) were clearly distinguished. This shows that the cancer tissue has a three-dimensional structure, in contrast to the fibroblasts that grow with no layering on the surface of the NF. Histological analysis revealed that the mono-cultured microtissue was thinner than fibroblast-layered microtissue (Figure 6d), whereas the HeLa cells in the fibroblast-layered microtissue were thicker (Figure 6e). Interestingly, some of the HeLa cells penetrated into the NF through the interstitial fibroblast layer (Figure 6 d,e; white dotted lines). In fact, most carcinomas begin in a tissue that lines the inner or outer surfaces with flat and circular structures and then gradually spread and invade into adjacent layers. The fabricated microtissues also adopted flat and circular structures. However, the fibroblast-layered microtissue progressively developed the real tissue-like structure of invasive carcinoma as shown in Figure 6e.
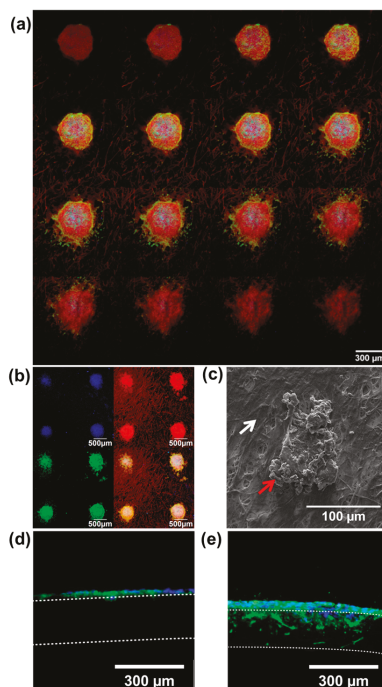

Figure 6. Three-dimensional shapes of cancer microtissues. (**a**,**b**) Confocal microscope images of the cancer microtissues. (**a**) Confocal stacking image (3 μm step; 16 layers) and (**b**) patterned cancer microtissue. (**a**,**b**) Green indicates HPV18, and red indicates F-actin. (**c**) SEM image (white arrow: fibroblast, red arrow: cancer tissue). (**d**,**e**) Frozen section images, (**d**) mono-cultured sample, and (**e**) co-cultured sample. Blue indicates Hoechst 33342 (**d**,**e**); only cancer cells are stained. Green indicates F-actin; both fibroblast and cancer cells are stained. All experimental samples were *n* > 3.

2.6. Reaction of the Drug-Treated Cancer Microtissue

Doxorubicin (0.1, 1.0, and 2.0 µM) was added to the cancer microtissues at day 7, and the resistance of the cells to the anticancer drug was examined by screening through the Live/Dead staining method (Figure 7a–h). Moreover, the expression of MMP2 and MMP9 was verified through ELISA (Figure 7i). Live/Dead staining two days after doxorubicin treatment revealed that the fibroblast-layered microtissue had higher drug resistance than the mono-cultured microtissue, especially for 0.1 and 1.0 µM doxorubicin (Figure 7b,c,f,g). This result verifies that the fibroblast-layered samples had less reduction of viability (Figure 7i) than mono-cultured microtissue, in which many cancer cells were killed by increasing concentrations of doxorubicin. Thus, the interstitial fibroblast layer conjugated with cancer micro tissue had stronger resistance to anticancer drugs with increasing concentration.
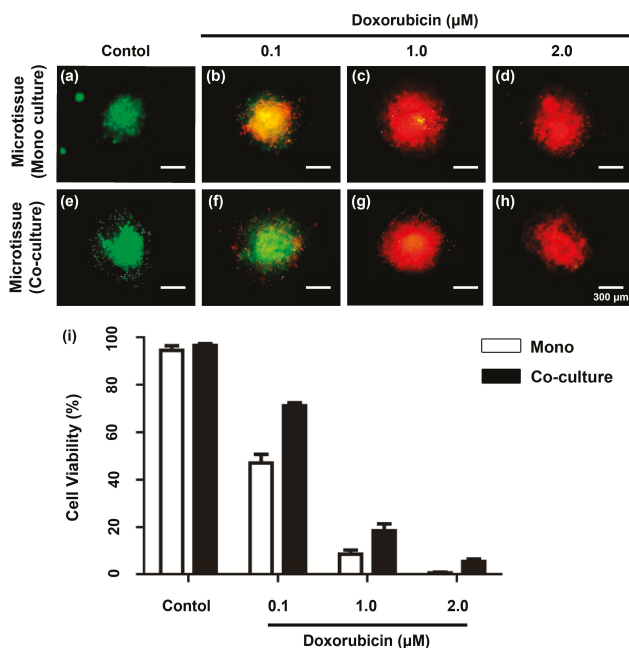

Figure 7. Drug test on day-7 cancer microtissue. (**a**–**h**) Cancer microtissues with Live/Dead staining; (**a**–**d**) mono-cultured sample, (**e**–**h**), co-cultured sample. (**a**,**e**) Standard samples with no doxorubicin treatment. (**b**–**d**,**f**–**h**) Samples with doxorubicin treatment, (**b**,**f**) 0.1, (**c**,**g**) 1.0, and (**d**,**h**) 2.0 µm doxorubicin. (**i**) Graph of viability of cancer micro tissue models after two days of treatment with doxorubicin. All experimental samples were $n > 3$. Unmarked Scale bars, 300 µm.

3. Discussion

Environmental factors have significant biochemical influences on cells [15]. A two-dimensional culture is advantageous in terms of manipulation to observe cells and extract proteins and mRNA. However, most of these cells are flat, in contrast to their actual shapes in the human body, and in many cases, the experimental results are different from the actual in vivo situations. In contrast, a three-dimensional culture model is more complex and difficult to manipulate and evaluate than a two-dimensional culture model, but it can accurately mimic the 3D structures of cells in the human body, and their behaviors and the expression of proteins and mRNA in actual in vivo situations [16]. Thus, in this study, fibroblasts were cultured with NF to provide a sufficient niche for cancer cells, and the co-cultured microtissue showed a different tissue-like structure and drug resistance compared to the monoculture.

The complex test processes and high throughput of each cell are the greatest obstacles to quantitative and in-depth molecular analysis of single cells or cell populations. The distribution of cells can be quantified by patterning cells to aid in the study of cell processes, such as reactions between individual tissues and cells. The advantage of patterning technology is the exposure of tissues to the same conditions owing to the arrangement of tissues. This study exploited inkjet printing to arrange cancer microtissues on nanofibrous membranes and analyzed the viability, size changes, and other characteristics of the patterned microtissues. The analysis showed that the viability of the cells was close to 100% when they were printed on a nanofibrous membrane using an inkjet printer, and the cancer microtissues produced and patterned using inkjet printing maintained their initial patterns even after culturing for one week. Such patterned cancer microtissues can be multi-screened, thus enabling simultaneous verification of the changes in the size of multiple cancer microtissues and observation of various tissues.

The rapid evaporation of droplets is one of the greatest drawbacks of the inkjet cell printer. The easy evaporation of droplets in micro units makes it difficult to culture cells, and many researchers have addressed this problem by printing hydrogels in wells containing a crosslinking agent [17–19]. In contrast, in this study, a nanofibrous membrane soaked in medium was used as the substrate, and printing on this wetted nanofibrous membrane prevented the rapid evaporation of droplets. The nanofibrous membrane provided an appropriate niche for inkjet printing without the use of a crosslinking agent when culturing the printed cells and also provided structural and biochemical elements of the extracellular matrix when culturing the cells together with fibroblasts. We also showed that inkjet printing on nanofibrous membrane is advantageous in terms of shaping and maintaining cell aggregates.

In future studies, the immunity network based on the interaction between immune cells and the fabricated cancer microtissues will be simulated, and drug tests with a sample with such an immunity network are expected to produce results that are closer to the results obtained from the human body. The significance of this study is the simulation of in vitro cancer tissues in drug tests and the production of highly reliable samples. The failure rates of clinical trials are expected to decrease as the reactions to drugs would better replicate those in the human body, and this will have positive effects on pharmaceutical discovery processes with low success rates.

4. Materials and Methods

4.1. Fabrication of NFs by Electrospinning

NF was fabricated by a previously reported electrospinning method [20,21]. Briefly, nanofibers were produced by diluting high molecular weight (80,000 MW) polycaprolactone (Sigma-Aldrich, St. Louis, MO, USA) at a concentration of 17% in a 1:1 mixture of chloroform (99.5%, Samchun Pure Chemical Co., Ltd., Seoul, Korea) and dimethylformamide (Sigma-Aldrich). During electrospinning, the temperature and humidity were maintained at 20–21 °C and 50–55%, respectively. The voltage, tip-to-collector distance, and flow rate of the solution were maintained at 15 kV, 18 cm, and 0.5 mL/h, respectively. The fabricated NF was dried for 24 h to evaporate the remaining solvent, and the dried membrane was then baked in an oven at 60 °C for 10 s to improve the interconnectivity of interstitial fibers before they were cut to a diameter of 10 mm. The fabricated NF was soaked in 70% ethanol and sterilized under an ultraviolet lamp overnight. Then, the sample was washed out three times with phosphate-buffered saline (PBS; pH 7.4, Gibco, Rockvile, MD, USA) and soaked in Dulbecco's modified Eagle's medium (DMEM, GenDEPOT) containing 10% fetal bovine serum (FBS, GenDEPOT) and 1% penicillin-streptomycin (Pen Strep, Gibco). The diameter distribution of the nanofibers characterized by an SEM image (Figure 2a) is shown in Figure 2b; the diameter of the nanofibers was estimated to be 400–500 nm.

4.2. Cell and Bioink Preparation

Fibroblasts (CCD-1112SK, ATCC, Manassas, VA, USA) and HPV18-positive cervical cancer cells (HeLa; KCLB, Seoul, Korea) were cultured with a medium containing 10% FBS and 1% Pen Strep in a 100-mm Petri dish (Nunclon Delta Surface, Thermo Fisher Scientific, Waltham, MA, USA). When cell confluency reached 80%, the cells were washed three times with PBS and treated with 2 mL of trypsin-EDTA (0.25%; Gibco) to produce single-cell units before culturing in 5% CO_2 at 37 °C for 2 min. After culturing, the detached cells were collected in a 15-mL conical tube into which culture medium was added, diluted 10 times to neutralize the trypsin, and centrifuged for 3 min at 1200 rpm. The cells obtained after removal of the supernatant were mixed with the culture medium and then used in the experiment.

The fibroblasts (1×10^4, 1×10^5 cells/mL) were seeded on NF with a diameter of 10 mm. After culturing in an incubator overnight, fibroblast-layered NF or bare NF was used as a substrate for inkjet cell printing.

For the cell-laden bioink, cell suspensions (3×10^7 cells/mL) were produced containing 0.5% collagen (collagen type I, Thermo Fisher Scientific) or cell suspension alone.

4.3. Inkjet Cell Printing

Inkjet printing technology that improves cell aggregation is essential for fabricating cancer microtissues. Therefore, the formation of the printed droplets on different substrates (glass and NF) and bioink was verified. To examine the effects of the bioink on the droplets, the culture medium with or without 0.5% collagen was mixed with HeLa cells (4×10^7 cells/mL) stained with Hoechst 33342 (Thermo Fisher Scientific), and this mixture was then used as the bioink for printing. To examine the effect of the substrate, the droplets were printed on a glass and the NF wetted in the medium.

To fabricate cancer microtissue samples, droplets of the 0.5% collagen bioink containing cancer cells were dropped 150 times using an inkjet printer on a NF as shown in Figure 2e. Three different conditions of NF were tested: the first was bare membrane, and the others ware fibroblast-layered membranes (1×10^4 cells/mL). An array of a maximum of four microtissues was patterned on the membrane (⌀10 mm). Immediately afterwards, the microtissues were cultured for 2 h in 5% CO_2 at 37 °C to enable the cancer cells to positively adhere. A sufficient amount of culture medium was added after adhesion of the cancer cells to the sample. Furthermore, for the co-cultured sample, fibroblasts were seeded on the NF and then soaked in the medium. The cells were then cultured in 5% CO_2 at 37 °C for one day before the cancer cells were printed as described above (Figure 2d).

4.4. Cell Viability

To verify the viability of the printed cells, a Live/Dead kit (Invitrogen) was used in this experiment according to the manufacturer's recommended procedure. In brief, 20 μL of 2 mM EthD-1 stock solution enclosed in the product was added to 10 mL of PBS and mixed by vortexing. Then, 5 μL of 4 mM calcein AM stock solution was added to the mixed solution, which was vortexed again to produce a live/dead solution. The samples were washed out three times with PBS and treated with the live/dead solution on the NF. Then, the specimen was cultured at room temperature, i.e., 20 °C, for 40 min.

Specifically, to compare the viability of printed cells on dried glass and wetted nanofibrous membrane (Figure 3), the printed cells were gently subjected to the live/dead assay immediately after the printing. Thereafter, the sample was cultured in situ at 25 °C for 30 min.

4.5. Immunocytochemistry/Immunofluorescence

The sample was fixed by treatment with 4% paraformaldehyde for 20 min at room temperature and then washed three times with PBS to remove the paraformaldehyde. The washed sample was treated with 0.1% Triton X-100 for 15 min at room temperature to ensure permeability and then washed

out with PBS three times. BSA buffer (1%) was used as the blocking buffer, and after treatment for 1 h at room temperature, the sample was washed with PBS three times. Then, the specific antibodies (MMP-2, MMP-9, and HPV18) were diluted in PBS at a ratio of 1:500. The primary and secondary antibodies were applied to the sample for 1 h at room temperature without light exposure.

4.6. Enzyme-Linked Immunosorbent Assay (ELISA)

Human MMP2 (ab100606, Abcam, Cambridge, UK) and MMP9 (ab100610, Abcam, Cambridge, UK) ELISA kits were used to measure the level of MMP2 and MMP9. The procedure was followed the manufacturer's instructions. To summarize, 100 μL of the standard sample, which was the benchmark, and 100 μL of the specific experimental sample to be measured in this experiment were added to the well plates and cultured for 150 min at room temperature. Then, the solution was removed and the plates were washed with distilled water and PBS-Triton. Then, 100 μL of biotinylated (MMP2, MMP9) detection antibody was added to the well plates and mixed carefully for 1 h at room temperature. The solution was removed and the well plates were washed again with distilled water and PBS-Triton. Then, 100 μL of HRP–streptavidin solution was added to each well plate and carefully mixed for 45 min at room temperature. The well plates were washed with distilled water and PBS-Triton again, and 100 μL of TMB one-step substrate reagent was added to each well plate and carefully mixed for 30 min at room temperature without light exposure. Finally, 50 μL of the stop solution was added to each well plate and the absorbance at 450 nm was measured using a microreader. The amount of MMP in the cancer microtissue sample was compared with that in the standard sample.

4.7. Drug Testing

Doxorubicin (1 mg, Sigma Aldrich) was used to verify the drug resistance of the fabricated samples. The doxorubicin was diluted to 0.1, 1.0, and 2.0 μM in cell culture medium and added to the day-7 co-cultured samples, after which further culture was performed in 5% CO_2 at 37 °C. Then, the amounts of MMP2 and MMP9 expressed after one and two days of administration were measured with ELISA, and a Live/Dead assay was used to examine the drug resistance of the fabricated cancer tissues.

4.8. Statistical Analysis

All of the data were presented as the mean ± standard deviation (SD). Statistical significance was defined as * $p < 0.01$, ** $p < 0.005$, *** $p < 0.001$.

5. Conclusions

This study fabricated a cancer microtissue array by inkjet printing cancer cells on NF on which fibroblasts were cultured. The cancer microtissues fabricated by printing cells on NF with a bioink containing 0.5% collagen showed the highest performance. The shapes of the cell aggregates were maintained well when the printed cancer cells were co-cultured with fibroblasts, and the tissues maintained their shapes and sizes with no significant variations until day 7 after production. The patterned cancer microtissues could be distinguished by staining of HPV18 in the fibroblast-layered microtissue, and their three-dimensional structures were verified using frozen sections, SEM, and confocal microscopy. The fibroblast-layered microtissue showed higher expression of MMP2 and MMP9 compared with the monocultured microtissue and higher resistance to doxorubicin.

Author Contributions: This report was completed by the following group of authors: Tae-Min Park, Donggu Kang, Ilho Jang, Won-Soo Yun, Jin-Hyung Shim, Young Hun Jeong, Jong-Young Kwak, Sik Yoon, and Songwan Jin. All authors contributed significantly to this work. Tae-Min Park, Donggu Kang and Songwan Jin performed the experiments; Donggu Kang supported the nanofibrous material work; Ilho Jang supported the inkjet printing

20. Jin, S.; Park, T.; Kim, C.; Kim, J.; Le, B.; Jeong, Y.; Kwak, J.; Yoon, S. Three-dimensional migration of neutrophils through an electrospun NF. *Biotechniques* **2015**, *58*, 285–292. [CrossRef] [PubMed]
21. Kang, D.; Kim, J.H.; Jeong, Y.H.; Kwak, J.-Y.; Yoon, S.; Jin, S. Endothelial monolayers on collagen-coated NFs: Cell–cell and cell–ecm interactions. *Biofabrication* **2016**, *8*, 25008. [CrossRef] [PubMed]

Review

Current Approaches Including Novel Nano/Microtechniques to Reduce Silicone Implant-Induced Contracture with Adverse Immune Responses

Shin Hyuk Kang [1], Chanutchamon Sutthiwanjampa [2], Chan Yeong Heo [3], Woo Seob Kim [1], Soo-Hong Lee [4,5,*] and Hansoo Park [2,*]

[1] Department of Plastic and Reconstructive Surgery, Chung-Ang University Graduate School of Medicine, Seoul 06974, Korea; kangshinhyeok@hotmail.com (S.H.K.); kimws@cau.ac.kr (W.S.K.)
[2] School of Integrative Engineering, Chung-Ang University, Seoul 06974, Korea; pupura_chan@hotmail.com
[3] Department of Plastic and Reconstructive Surgery, Seoul National University Bundang Hospital, Seongnam 13620, Korea; lionheo@gmail.com
[4] Department of Biomedical Science, CHA University, Seongnam-si 13488, Korea
[5] Department of Medical Biotechnology, Dongguk University, Gyeonggi-do 10326, Korea
* Correspondence: soohong@dongguk.edu (S.-H.L.); heyshoo@cau.ac.kr (H.P.); Tel.: +82-31-961-5153 (S.-H.L.); +82-2-820-5940 (H.P.)

Abstract: Capsular contracture, which is the pathologic development of fibrous capsules around implants, is a major complication of reconstructive and aesthetic breast surgeries. Capsular contracture can cause implant failure with breast hardening, deformity, and severe pain. The exact mechanisms underlying this complication remain unclear. In addition, anaplastic large cell lymphoma is now widely recognized as a very rare disease associated with breast implants. Foreign body reactions are an inevitable common denominator of capsular contracture. A number of studies have focused on the associated immune responses and their regulation. The present article provides an overview of the currently available techniques, including novel nano/microtechniques, to reduce silicone implant-induced contracture and associated foreign body responses.

1. Introduction

Silicone has been used widely in medicine for the last 70 years, with the first implant placed in humans in 1946 for duct repair during biliary surgery [1]. Since then, silicone-based materials have been used extensively in implants in humans, including pacemakers, cardiac valves, hydrocephalic shunts, aesthetic implants, orthopedic implants, nerve conduits, and dental implants. The aesthetic application of silicone is mainly in plastic and reconstructive surgery; it has also been used to correct congenital deformities or defects after reconstructive surgeries following trauma or cancer.

The most frequent use of this material is in silicone breast implants. Since 1961, when Dow Corning along with the Houston-based cosmetic surgeons Tom Cronin and Frank Gerow developed the first silicone breast implants, which were rubber sacs filled with viscous silicone gels, silicone mammary implants have been associated with a number of risks and complications, which has significantly limited their application. The formation of a constrictive fibrotic capsule around the implant with a concurrent foreign body reaction post-implantation, known as capsular contracture, is experienced by up to 50 percent of patients after breast augmentation and reconstruction [2–5]. Clinically, significant

breast capsular contracture is characterized by excessive constrictive fibrotic capsule formation that leads to firmness, distortion, and displacement of the breast implant [6]. Baker et al. developed a clinical classifcation system of capsular contracture after breast inplant surgery, specifically: grade I capsular contracure of the augmented breast feels as soft as an unoperated breast. Grade II capsular contracture is minimal; the breast is less soft than an unoperated breast; the implant can be palpated but is not visible. Grade III capsular contracture is moderate; the breast is firmer; the implant can be palpated easily and may be distorted or visible. Grade IV capsular contracture is severe; the breast is hard, tender, and painful, with significant distortion. The capsule thickness is not directly proportional to the palpable firmness, although some relationship may exist [7].

Capsular contracture remains the major reason underlying patient dissatisfaction and additional subsequent surgeries [8,9]. Additional surgeries are required in severe cases, but these procedures are complex, challenging, and unpredictable. Therefore, secondary procedures cannot guarantee a successful outcome without recurrence. The surface type and biomaterial are very important in regulating the inflammatory foreign body reaction in the surrounding tissue. The foreign body reaction is a natural tissue reaction that occurs after inserting an implant. There is no clear conclusive theory to date, but the consensus is that the immune system plays a very important role in the development of capsular contracture. The current understanding of capsular contracture is that it involves a complex combination of bacterial contamination in pockets and other related factors that stimulate inflammation around the implant, leading to a proliferation of fibroblasts along with collagen deposition and contracture [10,11]. However, the detailed mechanisms underlying capsular contracture remain unclear.

2. Anaplastic Large Cell Lymphoma (ALCL)

Anaplastic large cell lymphoma (ALCL) is a very rare breast implant-associated T-cell lymphoma that is $CD30^+$ and anaplastic lymphoma kinase (ALK) negative [12–14]. This disease is now widely recognized and there is an increased public awareness of the association between breast implants and the development of ALCL, a rare form of non-Hodgkin's lymphoma after warnings were released from the U.S. Food and Drug Administration on 26 January 2011 [15]. ALCL $CD30^+$ occurs due to the activation and abnormal proliferation of T lymphocytes [15,16]. ALCL is classified into cutaneous and systemic forms and the expression of the *ALK* gene characterizes the ALCL into subtypes and determines the prognosis. The morphology and cytology of breast implant-associated ALCL (BIA-ALCL) are similar to those of ALK-negative systemic ALCL. However, ALK-negative systemic ALCL has a poor prognosis, while breast implant-associated ALK-negative ALCL typically has a benign course with better prognosis [17]. These cases present as late-onset seroma with the swelling or mass of the unilateral breast [15,18]. These clinical symptoms are not consistent with the clinical symptoms of both cutaneous and systemic ALCL. Therefore, there is agreement that breast implant-related ALCL should be classified as a separate clinical entity [14,19–21].

To date, there has been no population-based estimation of the incidence of ALCL in women with breast implants in the United States. De Jong et al. reported an epidemiological study of ALCL in women with breast implants in the Netherlands [12]. They calculated an incidence of ALCL of 0.1 to 0.3 per 100,000 women per year based on an estimate of 100,000 to 300,000 Dutch women with breast implants [12]. Antonella et al. reported that the estimated incidence of the Italian BIA-ALCL cases reported to 2015 as 2.8 per 100,000 patients [22]. Recent studies have found the incidence of breast implant-associated ALCLs has increased with the clinical use of implants with larger textured surface areas [23], which induce an excessive inflammatory response and chronic antigenic stimulation due to bacterial infection (Figure 1) [24,25]. Most confirmed cases of breast implant-associated ALCLs have occurred in women with textured breast implants. However, cases of BIA-ALCLs in patients with smooth type breast implants have also been reported [26–28]. According to the global adverse event reports of breast implant-associated ALCL published by Srinivasa et al. in 2017, the textured type

was significantly more prevalent than the smooth type (50% versus 4.2%; $p = 0.0001$), but its use was unknown or not reported in 44.6% cases [29].
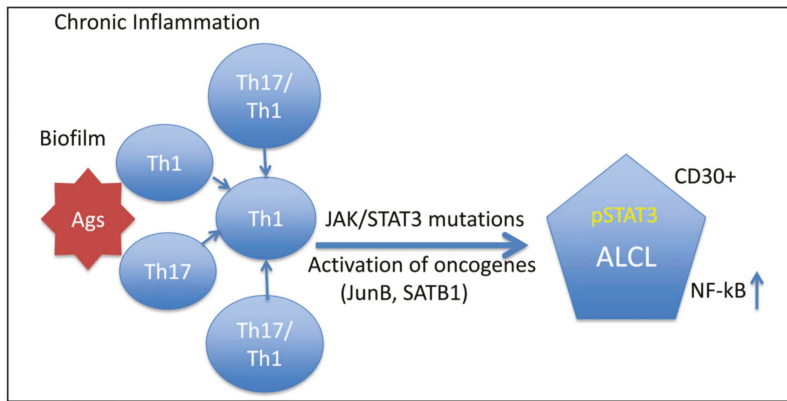
Figure 1. Hypothesis: Breast implant-associated anaplastic large cell lymphoma (ALCL) is caused by persistent T-cell immune reactions to chronic stimulation from bacterial antigens (Ags) and subsequent genetic events. Arrow means progression of immune responding T lymphocytes to BIA-ALCL [25].

Silicone implants induce a specific local immune reaction involving activated T-helper (Th1/Th17) cells that results in fibrosis, which is facilitated by the increased production of profibrotic cytokines due to the decrease in local T regulatory cell functions [24,30]. Miler and Anderson [31] reported that interleukin (IL)-1 is generated by macrophages following exposure to silicone. IL-1 acts as an immunochemical message to T-lymphocytes that a foreign substance has appeared and initiates immune activation. There have been many reports of specific T-lymphocyte proliferation in silicone implant capsules of augmented women [30,32,33]. Intracapsular T cells predominantly produce IL-17, IL-6, IL-8, transforming growth factor-beta1 (TGF-β1), and interferon-gamma, suggesting a Th1/Th17-weighted local immune response [30]. Promising novel therapies for preventing inappropriate stimulation of T cell responses and complications are being studied. In this review, we provide an overview of the current techniques aimed at reducing silicone implant-induced contracture with concurrent foreign body responses, including novel nano/microtechniques.

3. Approaches to Reducing Adverse Immune Responses

3.1. Drugs

3.1.1. Systemic Drugs

Breast infections following implant-based breast reconstructive surgery can form persistent biofilms and develop capsular contracture [34]. Furthermore, delaying the postoperative prophylactic use of antibiotics following implant-based breast reconstruction increases the risk of surgical-site infection, reoperation, and reconstructive failure [35]. There is no global consensus on the duration of antibiotic prophylaxis after breast reconstruction. Standardized definitions of antibiotic regimens are needed. The use of leukotriene antagonists (LTAs) to treat capsular contracture was reported in 2002 [36,37] and many studies have since demonstrated the benefits of these LTAs, including softening of breasts and reduction in severity of capsular contracture, using either montelukast (Singulair) [38] or zafirlukast (Accolate) [39,40]. The protective role of LTAs is based on their antagonist effect on TGF-β1 [41]. The pharmacological action of LTAs involves competitive binding with cysteinyl-leukotrienes receptor type 1 (Cys-LT1) [41]. The cysteinyl-leukotrienes facilitate TGF-β1

production, which results in fibroblast proliferation and fibrosis, suggesting that these Cys-LT1 receptor antagonists reverse fibroblast remodeling and fibrosis [42]. Treatment with Cys-LT1 receptor antagonists can decrease IL-6, IL-10, IL-13, and TGF-β1 levels, all of which are elevated in fibrotic lungs [43]. However, some studies indicate the effects of leukotriene receptor antagonists are anecdotal [39,44]. In 2007, the angiotensin-converting-enzyme inhibitor Enalapril was reported to decrease the expression of fibrotic mediators, TGF-β1, inflammatory markers, monoclonal antibodies to ED1 (CD68) and collagen III, and the periprosthetic fibrosis process [45].

In 2008, a short-term study on the use of Pirfenidone (PFD) to prevent capsular contracture after the installation of silicone implants in rats reported that PFD clearly reduced the capsular thickness of the surrounding submammary tissue, fibroblast-like cell proliferation, and recruitment of inflammatory cells [46]. PFD is a wide spectrum anti-fibrotic agent that modulates various inflammatory cytokines and has promising effects in the prevention and regression of many fibrotic diseases [47–49]. In the 2008 study, the total collagen content in the PFD-treated group was 50% lower and fibroblasts had a 45% less activated phenotype than in the control group. Furthermore, expression of the *TGF-β* and *collagen 1* genes was also reduced by 85% and 60%, respectively, in rats after oral administration of PFD compared to the control group [46]. A controlled clinical trial published in 2013 reported the effectiveness of oral PFD in breast capsular contracture [50]. This open, controlled, prospective, pilot clinical trial was conducted to assess the efficacy of 1800 mg oral PFD per day for 6 months. However, side effects, such as photosensitivity, rash, and itching sensation, nausea, diarrhea, and abdominal discomfort, have been reported [46].

Oral colchicine, a drug commonly used in the treatment of gout, appears to decrease the severity of capsular contracture in an animal model [51]. Colchicine is a well-known drug that inhibits inflammation. It inhibits cell migration and proliferation through disruption of microtubule polymerization by binding to a cytoskeletal protein [52]. The most common side effect of colchicine is gastrointestinal distress, such as diarrhea and vomiting, which limits its use and can lead to stoppage of therapy [53].

Baker et al. found that alpha-tocopherol (vitamin E) reduces the incidence of spherical constriction that occurs around breast implants [54]. Vitamin E is the main lipid-soluble antioxidant that inhibits the accumulation of peroxides, protects cells from damage by free radicals, and contributes to the stability and integrity of biological membranes. Vitamin E shows beneficial effects on various inflammatory diseases [55–57]. Based on this, the early administration of vitamin E reportedly aided in reducing fibrous capsule contracture following breast augmentation [54]. In addition, the prophylactic use of vitamin E is effective for capsule contracture in patients who receive adjuvant radiotherapy after reconstructive surgery with implants [58].

Recently, Kang et al. reported that oral administration of a synthetic tryptophan metabolite, Tranilast, reduced capsule formation in a rabbit model [59]. Tranilast inhibits the release of chemical mediators from inflammatory cells such as monocytes/macrophages [60], neutrophils [61], and lymphocytes [62,63] that are involved in capsule formation. It also inhibits the release of related cytokines that regulate T-cell immunity; it also inhibits TGF-β1 release, as well as collagen synthesis [59].

3.1.2. Topical Application

The incidence of capsular contracture is decreased by the use of povidone-iodine [64,65] and antibiotic irrigants [66] during breast implant surgery. In addition, because a significant increase in both infections and seromas, which lead to capsular contracture, was observed in patients not treated with topical antibiotics, some studies also support the use of topical antibiotics during cosmetic breast surgeries [67]. The use of povidone-iodine irrigation reduces Baker class III/IV capsular contracture and is not associated with implant rupture or increased deflation of saline breast implants [64,65]. However, due to the low methodologic quality of related studies, recommendations for perioperative povidone-iodine irrigation as standard procedure are limited [64,65].

Topical use of botulinum toxin type A prevents capsule formation around silicone implants, possibly by blocking TGF-β1 signaling and interrupting differentiation of fibroblasts into myofibroblasts. In 2016, botulinum toxin type A was reported to reduce capsule formation around silicone implants and inhibit differentiation of fibroblasts into myofibroblasts through the TGF-β/Smad signaling pathway in vivo [68,69]. The occurrence of hematoma is one of the various causes of capsular contracture. Spyropoulou et al. showed that hyaluronidase, which causes reabsorption of bleeding, can reduce capsular contracture in a rabbit model [70]. In addition, clinical use of hyaluronidase in subglandular or submuscular pockets before implant placement was reported to reduce capsule formation [71]. However, the authors did not perform a histological and statistical analysis. Primarily used as a cytotoxic chemotherapeutic, 5-fluorouracil only decreases cellular metabolism and blocks protein synthesis at lower concentrations. Therefore, it may be used to prevent capsule formation around silicone breast implants if it is loaded onto slow-releasing carriers, such as gelatin block [72]. Along with 5-fluorouracil, mitomycin C, which is used as an antitumor agent and antibiotic, can inhibit DNA synthesis through functional alkylation of double helix crosslinking, as well as inhibiting RNA and protein synthesis. Therefore, the topical application of mitomycin C may prevent fibroblast proliferation and collagen synthesis [73].

Xiaflex, a collagenase from the bacterium *Clostridium histolyticum*, can degrade human capsular contracture tissue ex vivo. However, skin perforation and adequate drug distribution within the implant pocket are issues with Xiaflex that need to be addressed prior to clinical use [74,75]. Short-term in vitro studies have demonstrated a dose-dependent decrease in capsule thickness from skin injections of Xiaflex. Reductions in collagen subtypes 1, 2, and 3 concentrations, as well as an up-regulation of profibrotic and inflammatory markers, were observed following Xiaflex treatment [76]. In 2016, Fischer et al. [74] described a dose-dependent reduction in human capsule contracture tissue ex vivo in a Xiaflex-treated group. Only collagen type 4 remained after degradation, which can act as a neo-capsule/acellular tissue matrix. In 2017, Fischer et al. [75] reported significant reductions in capsule thickness and collagen density following Xiaflex treatment in a study of the long-term effects of using this collagenase to treat capsular fibrosis in vivo. Low expression of collagen subtypes, as well as significant down-regulation of TGF-β3, was also detected in the group injected with Xiaflex. Anti-adhesion agents can reduce capsule thickness and the myofibroblast ratio [77]. Moreover, leukotriene receptor antagonists reduce silicone-induced peri-implant capsule formation in both white rabbit and rat models [78,79].

In 2015, Park et al. reported the acute suppression of TGF-β with the local and sustained release of synthetic tryptophan metabolite (Tranilast) in the formation of fibrous capsules around silicone implants in a rat model [80]. Finally, the slow distribution of prednisolone by liposome localization reportedly decreases fibrous capsule thickness around textured silicone implants [81] and the introduction of triamcinolone acetonide into implant pockets influences early capsule formation and reduces capsular contracture in a rabbit model [81,82].

In 2011, Sconfienza et al. reported that ultrasound-guided topical application of triamcinolone acetonide 40 mg to peri-implant capsules in patients undergoing breast implant surgery reduced capsule thickness and patient discomfort [83]. Zeplin et al. reported the potential of topical halofuginone application in decreasing the foreign body response [84]. Halofuginone is an alkaloid derived from *Dichroa febrifuga*, a flowering plant in the family Hydrangeaceae. It inhibits Smad3 phosphorylation in the TGF-β signaling pathway, which results in a marked inhibition of *collagen α I* gene expression [85]. Halofuginone has been used to inhibit various fibrotic disorders in vivo [86–88]. Submuscular implantation of implants applied with halofuginone in animal models can decrease CD68$^+$, histocytes, TGF-β, fibroblasts, collagen type I and type III, and capsular thickness [84].

Systemic uses and the topical use of colchicine and vitamin E have also been reported [89,90]. In an in vivo study, insertion of silicone implants applied with colchicine resulted in less inflammatory infiltrate, no myofibroblasts, and random and disorganized collagen fibers around the implants compared to the control group, which might result in prevention of capsule formation [89].

Topical application of vitamin E and croton oil to reduce pseudocapsules around the prosthesis has also been studied [90]. Individuals with topically applied vitamin E and croton oil showed thicker pseudocapsules and more marked cellular infiltrate than individuals who received an intramuscular injection of vitamin E [90].

Ng et al. [91] had studied the effect of local delivery of nicotine from the implant surface on the reduction of capsular contracture formation. There was no significant difference in capsular thickness between the nicotine-treated group and the control group. However, significant differences in angiogenesis were observed, which may potentially be useful for the fabrication of other biomaterials [91]. Li et al. [92] demonstrated the ability of medical chitosan to reduce capsule formation around breast implants by blocking the signaling pathway of tissue inhibitor of metalloproteinases (TIMPs) in vivo. At 4, 8, and 12 weeks following surgery, both capsular thickness and the expression of TIMP-1 and TIMP-2 were significantly lower in the medical chitosan-treated group than in the control group [92].

3.2. Materials

3.2.1. Combined with Autologous Tissues (Fat Grafts)

Autologous fat grafting has drawn increasing attention and gained widespread acceptance for improving the outcomes of breast reconstruction. Fat grafting to the breast has been widely used since 2008 when the 1987 moratorium imposed by the American Society of Plastic Surgeons was reversed [93]. However, fat grafting has natural limitations in the breast due to its soft nature. Therefore, "composite breast surgery", a combination of the classic implant technique and simultaneous management of overlying soft tissue with fat grafting, was introduced as a new paradigm. Breast augmentation that simultaneously uses implants and fat is a more powerful and versatile approach and achieves a synergistic outcome [94]. Moreover, multiple clinical studies have demonstrated that autologous fat grafts reduce the incidence of postoperative complications, including capsular contracture [95,96]. Additionally, an animal study suggested autologous fat transfer could be used to treat capsular contracture by neovascularization of the tissue around the implant [97]. However, this technique remains controversial for use in aesthetic breast surgery.

3.2.2. Combined with Acellular Dermal Matrix

The acellular dermal matrix (ADM) has recently emerged as a potential tool for surgical prevention of capsular contracture. ADMs are immunologically inert materials that minimize capsule formation in animal models and clinically. Animal studies have shown that implants completely wrapped in the allograft display decreased inflammation, myofibroblast cell proliferation, and capsule thickness [98]. Moreover, ADM envelopes can decrease radiation-induced inflammatory changes and pseudoepithelium formation in an irradiated rat model. These findings suggest a slower progression to capsular contracture [99]. In a 13-year long-term study, Salzberg et al. [100] reported the low cumulative incidence of capsular contracture with ADM-assisted direct-to-implant reconstruction, even in irradiated breasts. In this study, capsular contracture was considered an early event occurring within the first 2 years after reconstruction because longer follow-up durations found no increase in incidence. These findings suggest that ADM may truly prevent the development of capsular contracture. Since then, surgeons have modified the ADMs with strategically placed fenestrations to increase support to the implant within a rapidly expanding pocket and ultimately improve the aesthetic result. Despite these manipulations, fenestrated ADMs decrease capsular contracture rates in a manner similar to non-fenestrated matrixes [101]. In addition to its prevention of capsular contracture, ADMs have also been useful for the treatment of capsular contracture. Cheng et al. [102] reported a novel technique using complete coverage of implants with ADM to treat capsular contracture.

3.3. Surface Type

3.3.1. Smooth and Textured Surfaces

Implant surface texture, which acts as the interface between the device and the body tissue, has a dramatic influence. Therefore, much attention has been given to implant surface textures, i.e., smooth versus textured, and their impact on the development of capsular contracture [103]. Ersek [104] reported that texture can alter the host interface and induce a multiplanar conformation of collagen fibers, which results in thinner and more pliable capsules that are more resilient and less likely to contract. Liu et al. [105] studied the formation of capsular contracture after implantation of smooth or textured silicone breast prostheses in a meta-analysis. Smooth breast implants were significantly more associated with capsular contracture than were textured implants. Other long-term studies and meta-analyses have reported significantly more capsular contracture in primary subglandular breast augmentations using smooth implants than ones using textured implants [3,106,107]. In a pig model, Minami et al. [108] found that the thickness of the capsular contracture in the group with the smooth implants was thicker than the group with the textured implants (mean capsule thickness around smooth vs. textured implants measured 270 days post-implantation was 2040 μm vs. 1281 μm, respectively). Abramo et al. applied the parallelogram law to linear vectors drawn within concavities in the textured surface to achieve their resultant contraction vector [109]. In this study, the pore diameter and depth of the texture displayed significant effects on fibrous capsule formation. Textured implants with large open-pore diameters (250–350 μm, and 600–800 μm) and depth (40–100 μm) resulted in normal breast firmness. In contrast, textured implants with a small open-pore diameter (70–150 μm) and depth (10–760 μm, 150–200 μm) resulted in very long resultant vectors over the fibrous capsule and increased breast firmness. The implants with a macrotextured surface (open-pore diameter 600–800 μm; depth 150–200 μm) led to the formation of vectors of different lengths and directions, which significantly reduced the risk of fibrous capsular contraction. Capsular contracture can be reduced, although not eliminated, with textured implants. However, other complications have appeared with the use of textured breast implants. Double capsules and late seromas have not been observed for smooth saline or smooth silicone gel breast implants, but have been observed for aggressively textured implants [110]. Mechanical shear stress applied to an immature periprosthetic capsule has been linked to the formation of capsules [111]. Moreover, implants with larger textured surface areas have a significantly higher risk of breast implant-associated ALCL [23]. Therefore, to overcome complications related to the texture of implant surfaces, nano/microtechnologies were recently introduced. These innovations have brought enormous changes to breast surgery.

3.3.2. Surface Modification Using Nano/Microtechnology

The geometries of nano/microtopographies in the extracellular matrix (ECM) contribute to cell interactions and signaling [112]. Surface nano/microtopographies influence cell polarization, alignment, migration, attachment, adhesion, proliferation, and morphology naturally at the nano/micro level as the cells react naturally to surrounding structures [112–114]. T-cell migration, which is considered to play an important role in capsular contracture and ALCL, is also highly dependent on interactions between cells and the implant in the ECM [115]. The latest nano/micro-engineering techniques have enabled the analysis and fabrication of native tissue topography. There are three basic nanotopography geometries: nanogratings, nanoposts, and nanopits (Figure 2) [114].

The reactions of various cells to substrates fabricated using this technique have been studied with human fibroblasts (FCs), endothelial cells (ECs), smooth muscle cells (SMCs), and Schwann cells (Figures 3–6) [114,116–118].

Biela et al. [116] studied the effect of surface structures on the shape and alignment of FCs, ECs, and SMCs after seeding them on polydimethylsiloxane (PDMS) substrates for 24 h. Most cells aligned

along the grooves on substrates with 2-μm-wide grooves with a depth of 200 nm (Figure 3A,C,E); cell alignment was much lesser on substrates with 10-μm-wide grooves (Figure 3B,D,F) [116].
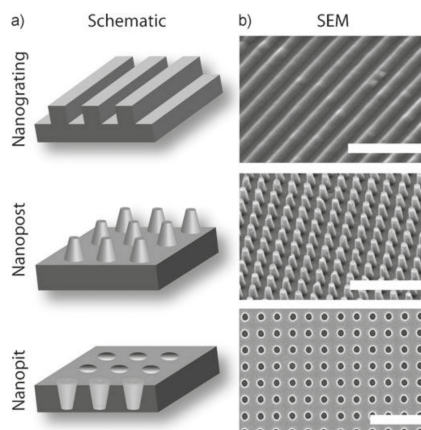
Figure 2. Schematic illustrations (**a**) and SEM images (**b**) of representative nanotopography geometries. Nanograting (scale bar = 5 μm), nanopost (scale bar = 5 μm), and nanopit array (scale bar = 1 μm) [114].
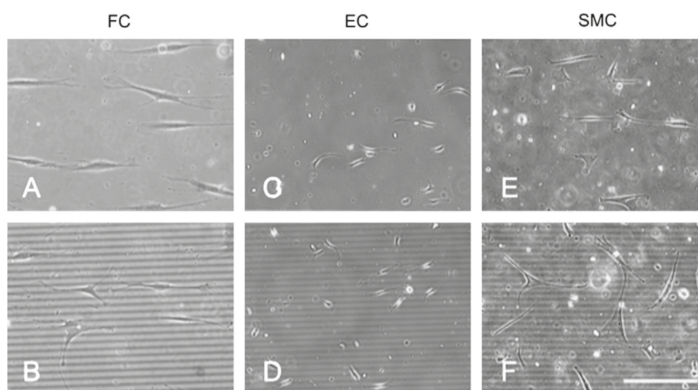
Figure 3. Human fibroblasts (FCs), endothelial cells (ECs), and smooth muscle cells (SMCs). (**A,C,E**) The grooves on substrates with 2-μm-wide grooves with a depth of 200 nm; (**B,D,F**) The grooves on substrates with 10-μm-wide grooves.Deep (200 nm) grooves with 2 and 10 μm wide grooved substrates are evident in phase-contrast images taken 24 h after seeding on polydimethylsiloxane (PDMS) substrates (scale bar = 150 μm) [116].

Dalby et al. [117] observed filopodia of FCs cultured on a substrate with 10-nm-high islands. Figure 4 shows low-magnification SEM images of cells on control (planar) and 10-nm-high island substrates. FCs with clear, well-spread lamellae were observed on both the control and island substrates. However, a greater number of filopodia were observed on the substrate with 10-nm-high islands than on the control substrate [117].

Bettinger et al. [114] reported that the impact on cell geometry was the most noticeable effect of nanotopography on cell function. The response of various types of cells, such as FCs, ECs, SMC, stem cells, epithelial cells, and Schwann cells, upon seeding on nanogratings was to commonly align and elongate in the direction of the grating axis [114]. Figure 5 demonstrates the alignment and elongation

of epithelial cells [114]; Figure 6 shows the same response by Schwann cells [118]. Hsu et al. [118] studied the alignment of Schwann cells on microgrooves and found that their width/spacing was also important for determining cellular alignment (Figure 6). When the grooves were narrower than 1.5 μm, Schwan cells were attached to the spaces between the grooves rather than aligning within the grooves themselves. This response was observed most prominently on 10/10 μm, 10/20 μm, and 20/10 substrates and least on the 20/20 μm substrate (Figure 6) [118].
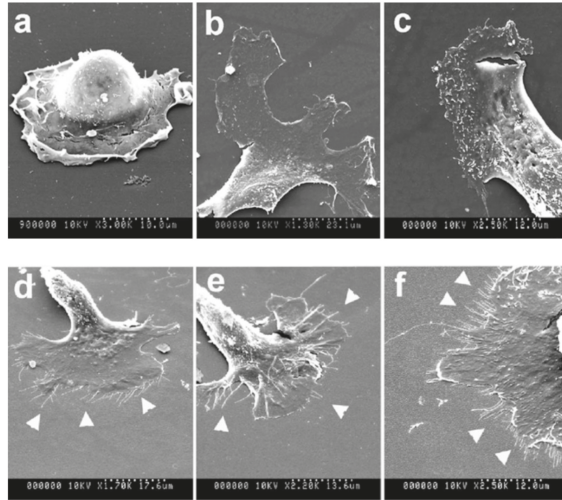
Figure 4. Flat (**a–c**) and 10-nm-high island (**d–f**) substrates. Fibroblasts on the latter substrate display fringed lamella with numerous filopodia (arrowheads) [117].
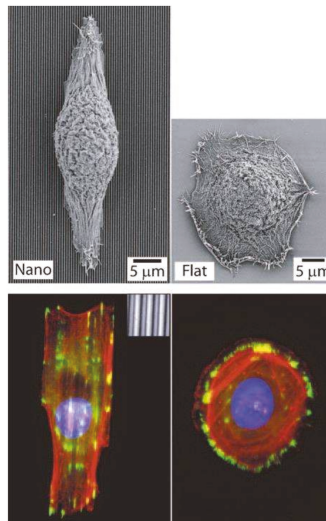
Figure 5. Epithelial cell response to nanograting. Fluorescence (**bottom**) and SEM (**top**) images. Arrangement and alignment along the grid axis. Reproduced with permission from the Company of Biologists [114].
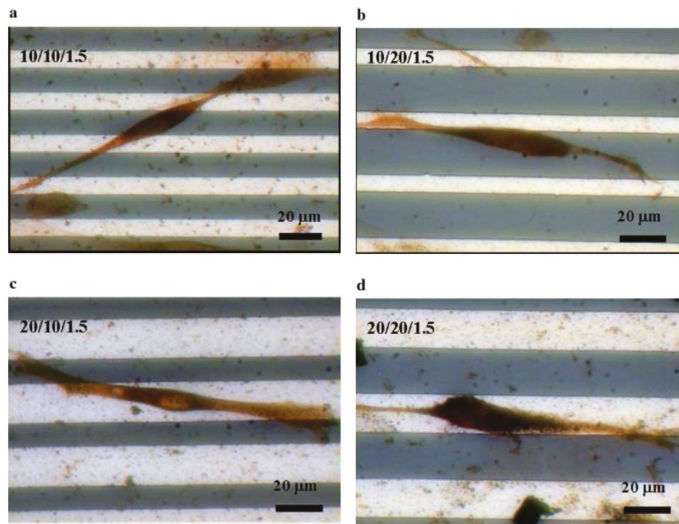
Figure 6. Schwann cells on a patterned silicon substrate (anti-S-100 stain, observed using optical microscopy). (**a**) 10/10/1.5 μm; (**b**) 10/20/1.5 μm; (**c**) 20/10/1.5 μm; and (**d**) 20/20/1.5 μm [118].

The development, fabrication, and functional evaluation of new biocompatible polydimethylsiloxane (PDMS) surfaces with various nano/microtopographical features enable favorable foreign body reactions. Kyle et al. [119] reported that the nano/microscale features of ADM can be successfully replicated with PDMS using a new three-dimensional grayscale fabrication technique (Figures 7 and 8).
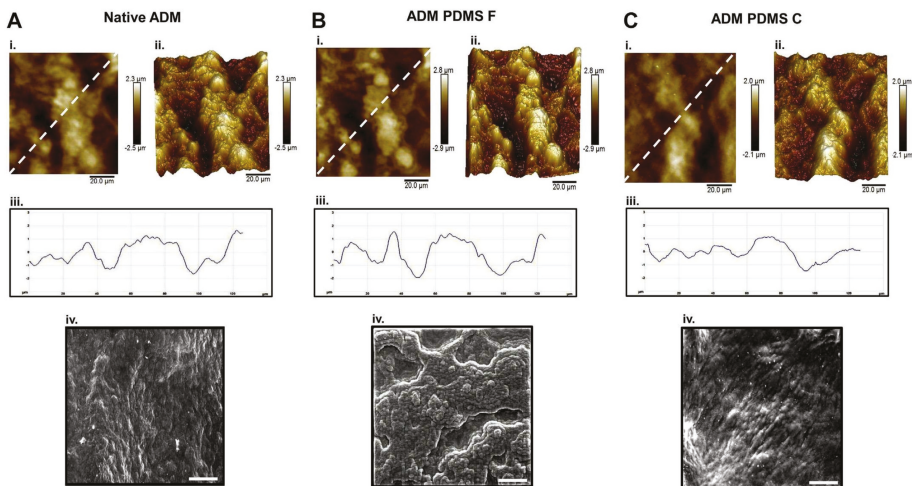
Figure 7. (**A**) Native acellular dermal matrix (ADM); (**B**) ADM PDMS fabricated surface (ADM PDMS F); and (**C**) ADM PDMS cast surface (ADM PDMS C) (i) Two-dimensional atomic force microscopy and (ii) three-dimensional images. (iii) Section profiles of two-dimensional and (iv) SEM image (scale bars (iv) = ×1000 magnification) [119].
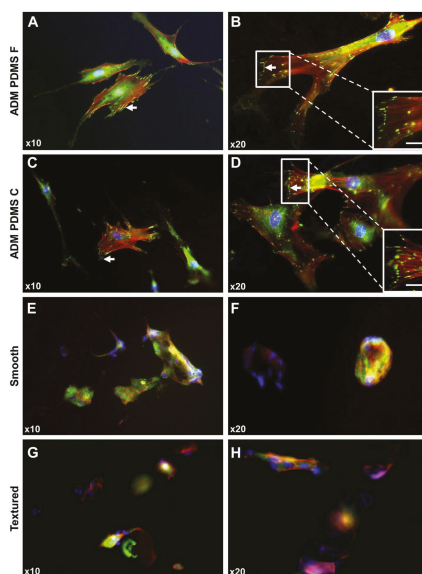
Figure 8. Immunofluorescence images of breast-derived fibroblasts (BDFs) on various PDMS surfaces. (**B**,**D**) BDFs on ADM PDMS formed focal contacts (white arrows) with substrates (white scale bars = ×40 magnification); (**A**,**D**) Fibroblasts on ADM PDMS F and C surfaces attached and spread. The representative "spindle-like" morphology is shown; (**E**,**F**) Conversely, BDFs on smooth silicone implant surfaces had a poor cell-substrate attachment; (**G**,**H**) BDFs on textured implant surfaces also had poor cell attachment with some focal contact formation. Moreover, cells appeared got trapped in the deep troughs between the steep nodules [119].

Figure 7A–C shows that both the PDMS fabricated surface (ADM PDMS F) and the ADM PDMS cast surface (ADM PDMS C) techniques were able to reproduce ADM topography and roughness of PDMS accurately. However, the ADM PDMS C technique reproduced the surface features most reliably (Figure 7C(i–iv)) [119]. Figure 7A(iv),B(iv) show SEM images, which demonstrate that both techniques were able to elucidate features down to 10 s of nanometers in scale [119].

Figure 8A–D shows immunofluorescence images with focal staining of vinculin in breast-derived fibroblasts (BDFs) on ADM PDMS surfaces [119]. Kyle et al. [119] have reported that the formation of focal contacts at the tips of F-actin filaments is characteristic of focal adhesions, indicating that BDFs on ADM PDMS surfaces are able to form a stable attachment with the underlying biomimetic topography, and subsequently spread to develop typical fibroblast "spindle-like" morphology. Figure 8E, F shows immunofluorescence staining of BDFs on smooth implant surfaces [119]. The cells showed a round morphology containing diffuse and non-specific vinculin staining with no focal contact formation. BDFs aggregated on the smooth implant surfaces and were often seen to bind to each other rather than forming focal contacts with the underlying implant surface topography [119]. On the other hand, BDFs on textured implant surfaces showed mostly diffuse and non-specific staining of vinculin and minimal focal contact formation, with a significant number of cells appearing to be trapped in deep troughs between the nodules (Figure 8G,H) [119].

Barr et al. [120] created biomimetic breast tissue-derived implant surfaces through three-dimensional grayscale photolithographic and oxygen plasma-etching techniques (Figure 9). Pro-inflammatory genes, such as those encoding *IL-β1*, *TNF-α*, and *IL-6*, were down-regulated and anti-inflammatory gene *IL-10* was up-regulated on the novel surfaces. Immunocytochemistry and

SEM show the fibroblasts were well spread and spindle-shaped, and that macrophages had favorable responses to these novel surfaces (Figure 10).
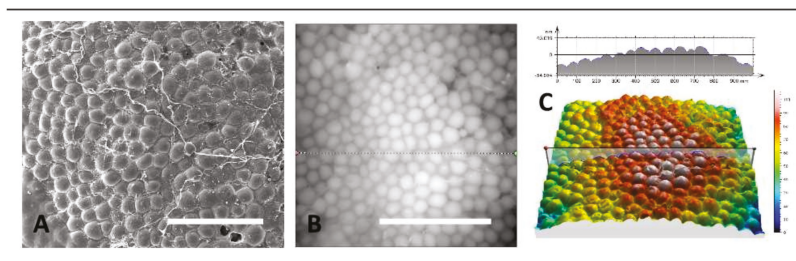
Figure 9. (**A**) Native breast adipose tissue surface (SEM image, scale bars = 500 µm); (**B**) grayscale laser confocal height images; and (**C**) three-dimensional projection of image B cross-sectional profile [120].
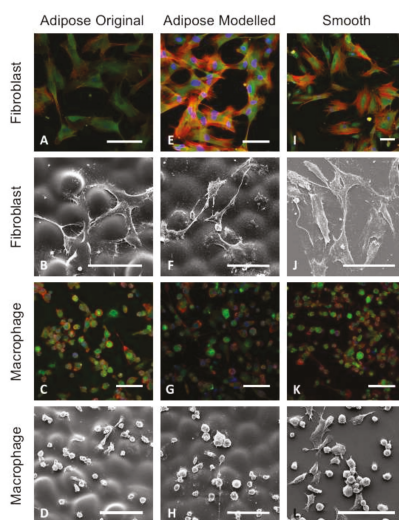
Figure 10. Immunocytochemistry and SEM images (scale bars = 100 µm). Fibroblasts and macrophages were grown in culture on (**A–D**) the original adipose; (**E–H**) modeled adipose; and (**I–L**) smooth control surfaces; (**A,E,I**) Few differences were observed in focal contacts and cells were well spread and had a classical spindle shape; (**B**) Fibroblasts on the original adipose surface aligned with valleys between the hemispherical shapes; (**F**) while cells on the modeled surface spread across the surface and their secondary texture masked the primary hemispherical nature; (**D,H**) Macrophages did not align with the underlying primary topography and adhered to the uppermost surfaces of the original and modeled adipose surfaces; (**D,H,L**) Macrophages cultured on the modeled adipose surfaces spread less than those on the original adipose and smooth surfaces [120].

Sforza et al. [121] performed a preliminary 3-year evaluation of nano/microtextured silicone breast implants. In this study, the nano/microtextured breast implants were constructed with a uniform topography using three-dimensional imprinting of PDMS to create optimized biocompatible outer shells. Fabrication was particle-free and did not use extrusion of foreign material to create the surface geometry, thus enabling a uniform and controlled shell thickness (Figure 11) [121]. The physical characteristics of the nano/microtextured surfaces are presented in Table 1. The rate of complications,

e.g., early seromas, infections, hematomas, wound dehiscence, ruptures, and implant malpositions, with nanotextured surface implants, was 0.36% (95% CI: 0.19 to 0.68%) compared to 1.06% (95% CI: 0.76 to 1.47%) with microtextured surface implants. However, the short-term nature of the study limits comparisons of capsular contracture formation and ALCL occurrence. Long-term studies are required.
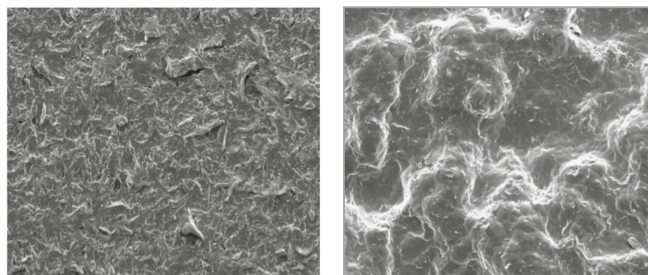
Figure 11. Nano- and microtextured surfaces visualized by SEM [121].

Table 1. Physical characteristics of nano/microtextured surfaces.

Characteristics	Nanotextured	Microtextured
Consistent surface roughness	4000 nanometers on average (Ra)	17 ± 3 μm
Median profile height (μm)	13 ± 2	57 ± 15
Kurtosis	3.1 ± 0.4	2.6 ± 0.3
Skewness	0.4 ± 0.2	0.1 ± 0.2
Contact angle *	$131° \pm 4°$	$119° \pm 3°$
Contact points per cm^2	49,000	1800–2200

* Contact angle reveals how the topography increases hydrophobicity compared to a smooth PDMS (surface contact angle of less than $110° \pm 4°$) [121].

4. Future Directions

Application of novel approaches from the fields of micro- and nanotechnology for the development of breast implants, such as micro- and nanotopography, could improve biointegration and enhance biocompatibility of implants. Surface modification of the nano/microtopographies by integrating reservoirs for controlled release of antimicrobial or anti-inflammatory agents into them could potentially reduce capsular contracture. Thus, the nanoscale architecture of the breast implants could be modified to alter the body's immune response to them, minimize biofilm formation, and affect the subsequent degree of capsular contracture. This could lead to the development of permanently implantable materials with immunologically inactive nano-engineered surfaces. Furthermore, in the near future, nano/microelectromechanical devices and breast cancer cell-specific proteins integrated within newer implants could be used to detect cancer cells, cancer recurrence, and treat pathologic cells.

5. Conclusions

To date, a wide variety of studies has investigated the reduction of capsular contracture caused by silicone implants. Table 2 shows an overview of techniques for reducing implant-inducted contracture and associated foreign body responses. However, complications caused by silicone implants remain unresolved. Researchers are attempting to reduce these complications. Studies focusing on developing implant surfaces similar to human tissues are of particular importance. A physiological ECM-like surface reduces inflammatory foreign body reactions and modulates the immune response. The plastic and reconstructive surgery fields have significantly benefited from nano/microtechnology in cosmetic dermatological applications, wound healing, implant and prosthesis development, tissue engineering and regenerative medicine, and drug delivery materials. In particular, the development of materials

has evolved due to nano/microtechnology that enables the analysis of material surface topography. Recently, a novel implant technology utilizing various nano-/micro-engineering techniques has emerged. Development of implants using these new technologies would allow increasingly natural interactions between the implants and surrounding tissues, which would reduce the peri-implant inflammatory response in the clinic and the induction of chronic inflammation in cells and tissues. Although no clinical long-term follow-up results on these implants have been reported, novel implant surfaces with improved interactions with surrounding tissues may reduce the risk of capsular contracture and should improve the results in anaplastic large cell lymphoma. In the field of plastic and reconstructive surgery, the nano/microtechnology that develops a more advanced biocompatible implant will continue to grow and expand, and continued research is needed on new biomaterials that mimic human tissues.

Table 2. Overview of techniques for reducing implant-induced contracture and associated foreign body responses.

Type of Method	Subtype	References
Systemic drugs	Antibiotics	[34,35]
	Leukotriene antagonists	[36–44]
	Angiotensin-converting enzyme inhibitors	[45]
	Anti-fibrotics	[46,50]
	Colchicine	[51]
	Vitamin E	[54,58]
	Synthetic tryptophan metabolite	[59]
Topical application	Anti-adhesion agents	[77,78]
	Antibiotics	[66,67]
	Leukotriene antagonists	[78,79]
	Steroids	[81–83]
	Povidone-iodine	[64,65]
	5-Fluorouracil	[72]
	Type A Botulinum toxin	[68,69]
	Hyaluronidase	[70,71]
	Mitomycin C	[73]
	Collagenase	[76]
	Synthetic tryptophan metabolite	[80]
	Halofuginone	[84]
	Colchicine	[89]
	Vitamin E	[90]
	Croton oil	[90]
	Nicotine	[91]
	Medical chitosan	[92]
Materials	Combined with autologous tissue	[93–97]
	Combined with acellular dermal matrix	[98,100–102]
Surface types	Smooth and textured surfaces	[3,23,103–108,110,111]
	Nano-micro modifications	[112–121]

Conflicts of Interest: The authors declare no conflict of interest.

Abbreviations

ALCL	Anaplastic large cell lymphoma
IL-17	Interleukin-17
IL-6	Interleukin-6
IL-8	Interleukin-8
TGF-β1	Transforming growth factor-β1
IFN-γ	Interferon-gamma
LTAs	Leukotriene antagonists
Cys-LT1	Cysteinyl leukotrienes receptors type 1
PFD	Pirfenidone
ADM	Acellular dermal matrix
ECM	Extracellular matrix
FCs	Human fibroblasts
ECs	Human endothelial cells
SMCs	Human smooth muscle cells
PDMS	Polydimethylsiloxane
SEM	Scanning electron microscopy
ADM PDMS F	Acellular dermal matrix polydimethylsiloxane fabricated surface
ADM PDMS C	Acellular dermal matrix polydimethylsiloxane cast surface
BDFs	Breast-derived fibroblasts
TNF-α	Tumor necrosis factor-alpha

References

1. Pearse, H.E. Results from using Vitallium tubes in biliary surgery. *Ann. Surg.* **1946**, *124*, 1020–1029. [CrossRef] [PubMed]
2. Cunningham, B.; McCue, J. Safety and effectiveness of Mentor's Memorygel implants at 6 years. *Aesthet. Plast. Surg.* **2009**, *33*, 440–444. [CrossRef] [PubMed]
3. Spear, S.L.; Murphy, D.K.; Slicton, A.; Walker, P.S. Inamed silicone breast implant, U.S.S.G. Inamed silicone breast implant core study results at 6 years. *Plast. Reconstr. Surg.* **2007**, *120*, 8S–16S. [CrossRef] [PubMed]
4. Cunningham, B. The Mentor study on contour profile gel silicone MemoryGel breast implants. *Plast. Reconstr. Surg.* **2007**, *120*, 33S–39S. [CrossRef] [PubMed]
5. Araco, A.; Gravante, G.; Araco, F.; Delogu, D.; Cervelli, V. Capsular contracture: Results of 3002 patients with aesthetic breast augmentation. *Plast. Reconstr. Surg.* **2006**, *118*, 1499–1500. [CrossRef] [PubMed]
6. Walker, P.S.; Walls, B.; Murphy, D.K. Natrelle saline-filled breast implants: A prospective 10-year study. *Aesthet. Surg. J.* **2009**, *29*, 19–25. [CrossRef] [PubMed]
7. Spear, S.L.; Baker, J.L., Jr. Classification of capsular contracture after prosthetic breast reconstruction. *Plast. Reconstr. Surg.* **1995**, *96*, 1119–1123. [CrossRef] [PubMed]
8. Forster, N.A.; Kunzi, W.; Giovanoli, P. The reoperation cascade after breast augmentation with implants: What the patient needs to know. *J. Plast. Reconstr. Aesthet. Surg.* **2013**, *66*, 313–322. [CrossRef] [PubMed]
9. Handel, N.; Cordray, T.; Gutierrez, J.; Jensen, J.A. A long-term study of outcomes, complications, and patient satisfaction with breast implants. *Plast. Reconstr. Surg.* **2006**, *117*, 757–767. [CrossRef] [PubMed]
10. Kamel, M.; Protzner, K.; Fornasier, V.; Peters, W.; Smith, D.; Ibanez, D. The PERI-implant breast capsule: An immunophenotypic study of capsules taken at explantation surgery. *J. Biomed. Mater. Res.* **2001**, *58*, 88–96. [CrossRef]
11. Adams, W.P., Jr.; Haydon, M.S.; Raniere, J., Jr.; Trott, S.; Marques, M.; Feliciano, M.; Robinson, J.B., Jr.; Tang, L.; Brown, S.A. A rabbit model for capsular contracture: Development and clinical implications. *Plast. Reconstr. Surg.* **2006**, *117*, 1214–1219. [CrossRef] [PubMed]
12. De Jong, D.; Vasmel, W.L.; de Boer, J.P.; Verhave, G.; Casparie, M.K.; van Leeuwen, F.E. Anaplastic large-cell lymphoma in women with breast implants. *JAMA* **2008**, *300*, 2030–2035. [CrossRef] [PubMed]
13. Duvic, M.; Moore, D.; Menter, A.; Vonderheid, E.C. Cutaneous T-cell lymphoma in association with silicone breast implants. *J. Am. Acad. Dermatol.* **1995**, *32*, 939–942. [CrossRef]

14. Roden, A.C.; Macon, W.R.; Keeney, G.L.; Myers, J.L.; Feldman, A.L.; Dogan, A. Seroma-associated primary anaplastic large-cell lymphoma adjacent to breast implants: An indolent T-cell lymphoproliferative disorder. *Mod. Pathol.* **2008**, *21*, 455–463. [CrossRef] [PubMed]

15. Kim, B.; Roth, C.; Chung, K.C.; Young, V.L.; van Busum, K.; Schnyer, C.; Mattke, S. Anaplastic large cell lymphoma and breast implants: A systematic review. *Plast. Reconstr. Surg.* **2011**, *127*, 2141–2150. [CrossRef] [PubMed]

16. Smith, C.A.; Gruss, H.J.; Davis, T.; Anderson, D.; Farrah, T.; Baker, E.; Sutherland, G.R.; Brannan, C.I.; Copeland, N.G.; Jenkins, N.A.; et al. Cd30 antigen, a marker for Hodgkin's lymphoma, is a receptor whose ligand defines an emerging family of cytokines with homology to TNF. *Cell* **1993**, *73*, 1349–1360. [CrossRef]

17. Falini, B.; Martelli, M.P. Anaplastic large cell lymphoma: Changes in the world health organization classification and perspectives for targeted therapy. *Haematologica* **2009**, *94*, 897–900. [CrossRef] [PubMed]

18. Brody, G.S. Anaplastic large cell lymphoma occurring in women with breast implants: Analysis of 173 cases. *Plast. Reconstr. Surg.* **2015**, *136*, 553e–554e. [CrossRef] [PubMed]

19. Kim, B.; Roth, C.; Young, V.L.; Chung, K.C.; van Busum, K.; Schnyer, C.; Mattke, S. Anaplastic large cell lymphoma and breast implants: Results from a structured expert consultation process. *Plast. Reconstr. Surg.* **2011**, *128*, 629–639. [CrossRef] [PubMed]

20. Jewell, M.; Spear, S.L.; Largent, J.; Oefelein, M.G.; Adams, W.P., Jr. Anaplastic large T-cell lymphoma and breast implants: A review of the literature. *Plast. Reconstr. Surg.* **2011**, *128*, 651–661. [CrossRef] [PubMed]

21. Thompson, P.A.; Lade, S.; Webster, H.; Ryan, G.; Prince, H.M. Effusion-associated anaplastic large cell lymphoma of the breast: Time for it to be defined as a distinct clinico-pathological entity. *Haematologica* **2010**, *95*, 1977–1979. [CrossRef] [PubMed]

22. Antonella, C.; Rosaria, B.; Marcella, M. 22 cases of BIA-ALCL: Awareness and outcome tracking from the Italian ministry of health. *Plast. Reconstr. Surg.* **2018**, *141*, 11e–19e.

23. Loch-Wilkinson, A.; Beath, K.J.; Knight, R.J.W.; Wessels, W.L.F.; Magnusson, M.; Papadopoulos, T.; Connell, T.; Lofts, J.; Locke, M.; Hopper, I.; et al. Breast implant-associated anaplastic large cell lymphoma in Australia and New Zealand: High-surface-area textured implants are associated with increased risk. *Plast. Reconstr. Surg.* **2017**, *140*, 645–654. [CrossRef] [PubMed]

24. Hu, H.; Johani, K.; Almatroudi, A.; Vickery, K.; van Natta, B.; Kadin, M.E.; Brody, G.; Clemens, M.; Cheah, C.Y.; Lade, S.; et al. Bacterial biofilm infection detected in breast implant-associated anaplastic large-cell lymphoma. *Plast. Reconstr. Surg.* **2016**, *137*, 1659–1669. [CrossRef] [PubMed]

25. Kadin, M.E.; Deva, A.; Xu, H.; Morgan, J.; Khare, P.; MacLeod, R.A.; van Natta, B.W.; Adams, W.P., Jr.; Brody, G.S.; Epstein, A.L. Biomarkers provide clues to early events in the pathogenesis of breast implant-associated anaplastic large cell lymphoma. *Aesthet Surg. J.* **2016**, *36*, 773–781. [CrossRef] [PubMed]

26. Aladily, T.N.; Medeiros, L.J.; Amin, M.B.; Haideri, N.; Ye, D.; Azevedo, S.J.; Jorgensen, J.L.; de Peralta-Venturina, M.; Mustafa, E.B.; Young, K.H.; et al. Anaplastic large cell lymphoma associated with breast implants: A report of 13 cases. *Am. J. Surg. Pathol.* **2012**, *36*, 1000–1008. [CrossRef] [PubMed]

27. Gidengil, C.A.; Predmore, Z.; Mattke, S.; van Busum, K.; Kim, B. Breast implant-associated anaplastic large cell lymphoma: A systematic review. *Plast. Reconstr. Surg.* **2015**, *135*, 713–720. [CrossRef] [PubMed]

28. Thompson, P.A.; Prince, H.M. Breast implant-associated anaplastic large cell lymphoma: A systematic review of the literature and mini-meta analysis. *Curr. Hematol. Malig. Rep.* **2013**, *8*, 196–210. [CrossRef] [PubMed]

29. Srinivasa, D.R.; Miranda, R.N.; Kaura, A.; Francis, A.M.; Campanale, A.; Boldrini, R.; Alexander, J.; Deva, A.K.; Gravina, P.R.; Medeiros, L.J.; et al. Global adverse event reports of breast implant-associated ALCL: An international review of 40 government authority databases. *Plast. Reconstr. Surg.* **2017**, *139*, 1029–1039. [CrossRef] [PubMed]

30. Wolfram, D.; Rabensteiner, E.; Grundtman, C.; Bock, G.; Mayerl, C.; Parson, W.; Almanzar, G.; Hasenohrl, C.; Piza-Katzer, H.; Wick, G. T regulatory cells and TH17 cells in peri-silicone implant capsular fibrosis. *Plast. Reconstr. Surg.* **2012**, *129*, 327e–337e. [CrossRef] [PubMed]

31. Miller, K.M.; Anderson, J.M. Human monocyte/macrophage activation and interleukin 1 generation by biomedical polymers. *J. Biomed. Mater. Res.* **1988**, *22*, 713–731. [CrossRef] [PubMed]

32. O'Hanlon, T.P.; Okada, S.; Love, L.A.; Dick, G.; Young, V.L.; Miller, F.W. Immunohistopathology and T cell receptor gene expression in capsules surrounding silicone breast implants. *Curr. Top. Microbiol. Immunol.* **1996**, *210*, 237–242. [PubMed]

33. Wolfram, D.; Rainer, C.; Niederegger, H.; Piza, H.; Wick, G. Cellular and molecular composition of fibrous capsules formed around silicone breast implants with special focus on local immune reactions. *J. Autoimmun.* **2004**, *23*, 81–91. [PubMed]

34. Ooi, A.; Song, D.H. Reducing infection risk in implant-based breast-reconstruction surgery: Challenges and solutions. *Breast Cancer* **2016**, *8*, 161–172. [PubMed]

35. Clayton, J.L.; Bazakas, A.; Lee, C.N.; Hultman, C.S.; Halvorson, E.G. Once is not enough: Withholding postoperative prophylactic antibiotics in prosthetic breast reconstruction is associated with an increased risk of infection. *Plast. Reconstr. Surg.* **2012**, *130*, 495–502. [CrossRef] [PubMed]

36. Schlesinger, S.L.; Ellenbogen, R.; Desvigne, M.N.; Svehlak, S.; Heck, R. Zafirlukast (Accolate): A new treatment for capsular contracture. *Aesthet. Surg. J.* **2002**, *22*, 329–336. [CrossRef] [PubMed]

37. Schlesinger, S.L.; Desvigne, M.N.; Ellenbogen, R.; Svehlak, S.; Heck, R. Results of using zafirlukast (Accolate) and montelukast (Singulair) for treatment of capsular contracture. *Aesthet. Surg. J.* **2003**, *23*, 101–102. [CrossRef] [PubMed]

38. Huang, C.K.; Handel, N. Effects of singulair (Montelukast) treatment for capsular contracture. *Aesthet. Surg. J.* **2010**, *30*, 404–408. [CrossRef] [PubMed]

39. Scuderi, N.; Mazzocchi, M.; Fioramonti, P.; Bistoni, G. The effects of Zafirlukast on capsular contracture: Preliminary report. *Aesthet. Plast. Surg.* **2006**, *30*, 513–520. [CrossRef] [PubMed]

40. Mazzocchi, M.; Dessy, L.A.; Alfano, C.; Scuderi, N. Effects of Zafirlukast on capsular contracture: Long-term results. *Int. J. Immunopathol. Pharmacol.* **2012**, *25*, 935–944. [CrossRef] [PubMed]

41. Sapountzis, S.; Kim, J.H.; Francescato Veiga, D.; Masako Ferreira, L. The effect of Zafirlukast on capsule formation in post-radiation silicone implants. *Med. Hypotheses* **2012**, *78*, 787–789. [CrossRef] [PubMed]

42. Perng, D.W.; Wu, Y.C.; Chang, K.T.; Wu, M.T.; Chiou, Y.C.; Su, K.C.; Perng, R.P.; Lee, Y.C. Leukotriene C_4 induces TGF-β_1 production in airway epithelium via P38 kinase pathway. *Am. J. Respir. Cell Mol. Biol.* **2006**, *34*, 101–107. [CrossRef] [PubMed]

43. Shimbori, C.; Shiota, N.; Okunishi, H. Effects of montelukast, a cysteinyl-leukotriene type 1 receptor antagonist, on the pathogenesis of bleomycin-induced pulmonary fibrosis in mice. *Eur. J. Pharmacol.* **2011**, *650*, 424–430. [CrossRef] [PubMed]

44. Spano, A.; Palmieri, B.; Taidelli, T.P.; Nava, M.B. Reduction of capsular thickness around silicone breast implants by Zafirlukast in rats. *Eur. Surg. Res.* **2008**, *41*, 8–14. [CrossRef] [PubMed]

45. Zimman, O.A.; Toblli, J.; Stella, I.; Ferder, M.; Ferder, L.; Inserra, F. The effects of angiotensin-converting-enzyme inhibitors on the fibrous envelope around mammary implants. *Plast. Reconstr. Surg.* **2007**, *120*, 2025–2033. [CrossRef] [PubMed]

46. Gancedo, M.; Ruiz-Corro, L.; Salazar-Montes, A.; Rincon, A.R.; Armendariz-Borunda, J. Pirfenidone prevents capsular contracture after mammary implantation. *Aesthet. Plast. Surg.* **2008**, *32*, 32–40. [CrossRef] [PubMed]

47. Iyer, S.N.; Wild, J.S.; Schiedt, M.J.; Hyde, D.M.; Margolin, S.B.; Giri, S.N. Dietary intake of pirfenidone ameliorates bleomycin-induced lung fibrosis in hamsters. *J. Lab. Clin. Med.* **1995**, *125*, 779–785. [PubMed]

48. Garcia, L.; Hernandez, I.; Sandoval, A.; Salazar, A.; Garcia, J.; Vera, J.; Grijalva, G.; Muriel, P.; Margolin, S.; Armendariz-Borunda, J. Pirfenidone effectively reverses experimental liver fibrosis. *J. Hepatol.* **2002**, *37*, 797–805. [CrossRef]

49. Shimizu, T.; Kuroda, T.; Hata, S.; Fukagawa, M.; Margolin, S.B.; Kurokawa, K. Pirfenidone improves renal function and fibrosis in the post-obstructed kidney. *Kidney Int.* **1998**, *54*, 99–109. [CrossRef] [PubMed]

50. Veras-Castillo, E.R.; Cardenas-Camarena, L.; Lyra-Gonzalez, I.; Munoz-Valle, J.F.; Lucano-Landeros, S.; Guerrerosantos, J.; Gonzalez-Ulloa, B.; Mercado-Barajas, J.L.; Sanchez-Parada, M.G.; Azabache-Wennceslao, R.; et al. Controlled clinical trial with pirfenidone in the treatment of breast capsular contracture: Association of TGF-β polymorphisms. *Ann. Plast. Surg.* **2013**, *70*, 16–22. [CrossRef] [PubMed]

51. Hawtof, D.B.; Kelly, C.B. Colchicine and capsular contracture around breast prostheses. *Eur. J. Plast. Surg.* **1996**, *19*, 81–83. [CrossRef]

52. Borisy, G.G.; Taylor, E.W. The mechanism of action of colchicine. Binding of colchincine-3H to cellular protein. *J. Cell Biol.* **1967**, *34*, 525–533. [CrossRef] [PubMed]

53. Cocco, G.; Chu, D.C.; Pandolfi, S. Colchicine in clinical medicine. A guide for internists. *Eur. J. Intern. Med.* **2010**, *21*, 503–508. [CrossRef] [PubMed]

54. Baker, J.L., Jr. The effectiveness of α-tocopherol (vitamin E) in reducing the incidence of spherical contracture around breast implants. *Plast. Reconstr. Surg.* **1981**, *68*, 696–699. [CrossRef] [PubMed]

55. Cook-Mills, J.M. Isoforms of Vitamin E differentially regulate PKC α and inflammation: A review. *J. Clin. Cell. Immunol.* **2013**, *4*, 1000137. [CrossRef] [PubMed]

56. Ascherio, A.; Weisskopf, M.G.; O'Reilly E, J.; Jacobs, E.J.; McCullough, M.L.; Calle, E.E.; Cudkowicz, M.; Thun, M.J. Vitamin E intake and risk of amyotrophic lateral sclerosis. *Ann. Neurol.* **2005**, *57*, 104–110. [CrossRef] [PubMed]

57. Rossato, M.F.; Hoffmeister, C.; Tonello, R.; de Oliveira Ferreira, A.P.; Ferreira, J. Anti-inflammatory effects of Vitamin E on adjuvant-induced arthritis in rats. *Inflammation* **2015**, *38*, 606–615. [CrossRef] [PubMed]

58. Cook, M.; Johnson, N.; Zegzula, H.D.; Schray, M.; Glissmeyer, M.; Sorenson, L. Prophylactic use of Pentoxifylline (Trental) and Vitamin E to prevent capsular contracture after implant reconstruction in patients requiring adjuvant radiation. *Am. J. Surg.* **2016**, *211*, 854–859. [CrossRef] [PubMed]

59. Kang, S.H.; Jang, S.Y.; Ryou, J.H.; Kim, W.S.; Kim, H.K.; Bae, T.H.; Kim, M.K. Preventive effect of synthetic tryptophan metabolite on silicone breast implant-induced capsule formation. *Ann. Plast. Surg.* **2018**, *80*, 565–571. [CrossRef] [PubMed]

60. Chikaraishi, A.; Hirahashi, J.; Takase, O.; Marumo, T.; Hishikawa, K.; Hayashi, M.; Saruta, T. Tranilast inhibits interleukin-1β-induced monocyte chemoattractant protein-1 expression in rat mesangial cells. *Eur. J. Pharmacol.* **2001**, *427*, 151–158. [CrossRef]

61. Shimizu, T.; Kanai, K.; Kyo, Y.; Asano, K.; Hisamitsu, T.; Suzaki, H. Effect of tranilast on matrix metalloproteinase production from neutrophils in-vitro. *J. Pharm. Pharmacol.* **2006**, *58*, 91–99. [CrossRef] [PubMed]

62. Frumento, G.; Rotondo, R.; Tonetti, M.; Damonte, G.; Benatti, U.; Ferrara, G.B. Tryptophan-derived catabolites are responsible for inhibition of t and natural killer cell proliferation induced by indoleamine 2,3-dioxygenase. *J. Exp. Med.* **2002**, *196*, 459–468. [CrossRef] [PubMed]

63. Inglis, J.J.; Criado, G.; Andrews, M.; Feldmann, M.; Williams, R.O.; Selley, M.L. The anti-allergic drug, *N*-(3′,4′-dimethoxycinnamonyl) anthranilic acid, exhibits potent anti-inflammatory and analgesic properties in arthritis. *Rheumatology* **2007**, *46*, 1428–1432. [CrossRef] [PubMed]

64. Yalanis, G.C.; Liu, E.W.; Cheng, H.T. Efficacy and safety of povidone-iodine irrigation in reducing the risk of capsular contracture in aesthetic breast augmentation: A systematic review and meta-analysis. *Plast. Reconstr. Surg.* **2015**, *136*, 687–698. [CrossRef] [PubMed]

65. Wiener, T.C. The role of betadine irrigation in breast augmentation. *Plast. Reconstr. Surg.* **2007**, *119*, 12–15. [CrossRef] [PubMed]

66. Adams, W.P., Jr.; Rios, J.L.; Smith, S.J. Enhancing patient outcomes in aesthetic and reconstructive breast surgery using triple antibiotic breast irrigation: Six-year prospective clinical study. *Plast. Reconstr. Surg.* **2006**, *118*, 46S–52S. [CrossRef] [PubMed]

67. Pfeiffer, P.; Jorgensen, S.; Kristiansen, T.B.; Jorgensen, A.; Holmich, L.R. Protective effect of topical antibiotics in breast augmentation. *Plast. Reconstr. Surg.* **2009**, *124*, 629–634. [CrossRef] [PubMed]

68. Kim, S.; Ahn, M.; Piao, Y.; Ha, Y.; Choi, D.K.; Yi, M.H.; Shin, N.; Kim, D.W.; Oh, S.H. Effect of botulinum toxin type a on TGF-β/SMAD pathway signaling: Implications for silicone-induced capsule formation. *Plast. Reconstr. Surg.* **2016**, *138*, 821e–829e. [CrossRef] [PubMed]

69. Lee, S.D.; Yi, M.H.; Kim, D.W.; Lee, Y.; Choi, Y.; Oh, S.H. The effect of botulinum neurotoxin type A on capsule formation around silicone implants: The in vivo and in vitro study. *Int. Wound J.* **2016**, *13*, 65–71. [CrossRef] [PubMed]

70. Spyropoulou, G.A.; Papalois, A.; Batistatou, A.; Doukas, M.; Tsoutsos, D. Can the use of hyaluronidase reduce capsule formation? *Aesthet. Plast. Surg.* **2011**, *35*, 782–788. [CrossRef] [PubMed]

71. Cachay-Velasquez, H.; Ale, A. Lateral approach in mammary implants. *Ann. Plast. Surg.* **1990**, *25*, 258–262. [CrossRef] [PubMed]

72. Ibrahim Canter, H.; Konas, E.; Bozdogan, O.; Vargel, I.; Ozbatir, B.; Oner, F.; Erk, Y. Effect of slow-release 5-fluorouracil on capsule formation around silicone breast implants: An experimental study with mice. *Aesthet. Plast. Surg.* **2007**, *31*, 674–679. [CrossRef] [PubMed]

73. Nava, M.B.; Rocco, N.; Catanuto, G.; Frangou, J.; Rispoli, C.; Ottolenghi, J.; Bruno, N.; Spano, A. Role of Mitomycin C in preventing capsular contracture in implant-based reconstructive breast surgery: A randomized controlled trial. *Plast. Reconstr. Surg.* **2017**, *139*, 819–826. [CrossRef] [PubMed]

74. Fischer, S.; Hirche, C.; Diehm, Y.; Nuutila, K.; Kiefer, J.; Gazyakan, E.; Bueno, E.M.; Kremer, T.; Kneser, U.; Pomahac, B. Efficacy and safety of the collagenase of the bacterium clostridium histolyticum for the treatment of capsular contracture after silicone implants: Ex-vivo study on human tissue. *PLoS ONE* **2016**, *11*, e0156428. [CrossRef] [PubMed]

75. Fischer, S.; Diehm, Y.; Henzler, T.; Berger, M.R.; Kolbenschlag, J.; Latz, A.; Bueno, E.M.; Hirche, C.; Kneser, U.; Pomahac, B. Long-term effects of the collagenase of the bacterium clostridium histolyticum for the treatment of capsular fibrosis after silicone implants. *Aesthet. Plast. Surg.* **2017**, *41*, 211–220. [CrossRef] [PubMed]

76. Fischer, S.; Hirsch, T.; Diehm, Y.; Kiefer, J.; Bueno, E.M.; Kueckelhaus, M.; Kremer, T.; Hirche, C.; Kneser, U.; Pomahac, B. The collagenase of the bacterium clostridium histolyticum for the treatment of capsular fibrosis after silicone implants. *Plast. Reconstr. Surg.* **2015**, *136*, 981–989. [CrossRef] [PubMed]

77. Shin, K.C.; Chung, K.I.; Park, B.Y.; Kim, H.K.; Kim, W.S.; Bae, T.H.; Kim, M.K. The effect of antiadhesion agent on peri-implant capsular formation in rabbits. *Ann. Plast. Surg.* **2013**, *71*, 600–604. [CrossRef] [PubMed]

78. Yang, J.D.; Kwon, O.H.; Lee, J.W.; Chung, H.Y.; Cho, B.C.; Park, H.Y.; Kim, T.G. The effect of montelukast and antiadhesion barrier solution on the capsule formation after insertion of silicone implants in a white rat model. *Eur. Surg. Res.* **2013**, *51*, 146–155. [CrossRef] [PubMed]

79. Kang, S.H.; Shin, K.C.; Kim, W.S.; Bae, T.H.; Kim, H.K.; Kim, M.K. The preventive effect of topical Zafirlukast instillation for peri-implant capsule formation in rabbits. *Arch. Plast. Surg.* **2015**, *42*, 179–185. [CrossRef] [PubMed]

80. Park, S.; Park, M.; Kim, B.H.; Lee, J.E.; Park, H.J.; Lee, S.H.; Park, C.G.; Kim, M.H.; Kim, R.; Kim, E.H.; et al. Acute suppression of TGF-SS with local, sustained release of Tranilast against the formation of fibrous capsules around silicone implants. *J. Control. Release* **2015**, *200*, 125–137. [CrossRef] [PubMed]

81. Moreira, M.; Fagundes, D.J.; de Jesus Simoes, M.; Taha, M.O.; Perez, L.M.; Bazotte, R.B. The effect of liposome-delivered prednisolone on collagen density, myofibroblasts, and fibrous capsule thickness around silicone breast implants in rats. *Wound Repair Regener.* **2010**, *18*, 417–425. [CrossRef] [PubMed]

82. Marques, M.; Brown, S.; Correia-Sa, I.; Rodrigues-Pereira, P.; Goncalves-Rodrigues, A.; Amarante, J. The impact of triamcinolone acetonide in early breast capsule formation in a rabbit model. *Aesthet. Plast. Surg.* **2012**, *36*, 986–994. [CrossRef] [PubMed]

83. Sconfienza, L.M.; Murolo, C.; Callegari, S.; Calabrese, M.; Savarino, E.; Santi, P.; Sardanelli, F. Ultrasound-guided percutaneous injection of triamcinolone acetonide for treating capsular contracture in patients with augmented and reconstructed breast. *Eur. Radiol.* **2011**, *21*, 575–581. [CrossRef] [PubMed]

84. Zeplin, P.H.; Larena-Avellaneda, A.; Schmidt, K. Surface modification of silicone breast implants by binding the Antifibrotic drug Halofuginone reduces capsular fibrosis. *Plast. Reconstr. Surg.* **2010**, *126*, 266–274. [CrossRef] [PubMed]

85. McGaha, T.L.; Phelps, R.G.; Spiera, H.; Bona, C. Halofuginone, an inhibitor of type-I collagen synthesis and skin sclerosis, blocks transforming-growth-factor-β-mediated SMAD3 activation in fibroblasts. *J. Investig. Dermatol.* **2002**, *118*, 461–470. [CrossRef] [PubMed]

86. Spira, G.; Mawasi, N.; Paizi, M.; Anbinder, N.; Genina, O.; Alexiev, R.; Pines, M. Halofuginone, a collagen type I inhibitor improves liver regeneration in cirrhotic rats. *J. Hepatol.* **2002**, *37*, 331–339. [CrossRef]

87. Pines, M.; Domb, A.; Ohana, M.; Inbar, J.; Genina, O.; Alexiev, R.; Nagler, A. Reduction in dermal fibrosis in the tight-skin (TSK) mouse after local application of Halofuginone. *Biochem. Pharmacol.* **2001**, *62*, 1221–1227. [CrossRef]

88. Pines, M.; Snyder, D.; Yarkoni, S.; Nagler, A. Halofuginone to treat fibrosis in chronic graft-versus-host disease and scleroderma. *Biol. Blood Marrow Transplant.* **2003**, *9*, 417–425. [CrossRef]

89. Acuner, B.; Baser, N.T.; Aslan, G.; Terzioglu, A.; Caydere, M.; Ustun, H.; Gorgu, M. The effects of colchicine-impregnated oxidized regenerated cellulose on capsular contracture. *Surg. Innov.* **2017**, *24*, 417–422. [CrossRef] [PubMed]

90. Peters, C.R.; Shaw, T.E.; Raju, D.R. The influence of Vitamin E on capsule formation and contracture around silicone implants. *Ann. Plast. Surg.* **1980**, *5*, 347–352. [CrossRef] [PubMed]

91. Kenneth, K.N.; Neven, A.; Michael, A.B.; Alison, C.H.; Heather, S. Local delivery of nicotine does not mitigate fibrosis but may lead to angiogenesis. *J. Biomater. Appl.* **2010**, *26*, 349–358.

92. Li, S.; Ren, L.; Xu, H.; Jia, D.; Luo, S.; Hao, L.; Yang, D. Effects of medical chitosan on capsular formation following silicone implant insertion in a rabbit model. *Aesthet. Plast. Surg.* **2016**, *40*, 613–624. [CrossRef] [PubMed]

93. Oshitani, N.; Takeda, S.; Matsumoto, H.; Minamino, H.; Hayakawa, T.; Aomatsu, K. Possible antistenotic effect of tranilast in a patient with small bowel tuberculosis to prevent intestinal obstruction due to stenosis progression by antituberculous chemotherapy. *Dig. Endosc.* **2013**, *25*, 333–335. [CrossRef] [PubMed]

94. Auclair, E.; Blondeel, P.; Del Vecchio, D.A. Composite breast augmentation: Soft-tissue planning using implants and fat. *Plast. Reconstr. Surg.* **2013**, *132*, 558–568. [CrossRef] [PubMed]

95. Salgarello, M.; Visconti, G.; Farallo, E. Autologous fat graft in radiated tissue prior to alloplastic reconstruction of the breast: Report of two cases. *Aesthet. Plast. Surg.* **2010**, *34*, 5–10. [CrossRef] [PubMed]

96. Sarfati, I.; Ihrai, T.; Kaufman, G.; Nos, C.; Clough, K.B. Adipose-tissue grafting to the post-mastectomy irradiated chest wall: Preparing the ground for implant reconstruction. *J. Plast. Reconstr. Aesthet. Surg.* **2011**, *64*, 1161–1166. [CrossRef] [PubMed]

97. Roca, G.B.; Graf, R.; da Silva Freitas, R.; Salles, G., Jr.; Francisco, J.C.; Noronha, L.; Maluf, I., Jr. Autologous fat grafting for treatment of breast implant capsular contracture: A study in pigs. *Aesthet. Surg. J.* **2014**, *34*, 769–775. [CrossRef] [PubMed]

98. Schmitz, M.; Bertram, M.; Kneser, U.; Keller, A.K.; Horch, R.E. Experimental total wrapping of breast implants with Acellular dermal matrix: A preventive tool against capsular contracture in breast surgery? *J. Plast. Reconstr. Aesthet. Surg.* **2013**, *66*, 1382–1389. [CrossRef] [PubMed]

99. Komorowska-Timek, E.; Oberg, K.C.; Timek, T.A.; Gridley, D.S.; Miles, D.A. The effect of Alloderm envelopes on Periprosthetic capsule formation with and without radiation. *Plast. Reconstr. Surg.* **2009**, *123*, 807–816. [CrossRef] [PubMed]

100. Salzberg, C.A.; Ashikari, A.Y.; Berry, C.; Hunsicker, L.M. Acellular dermal matrix-assisted direct-to-implant breast reconstruction and capsular contracture: A 13-year experience. *Plast. Reconstr. Surg.* **2016**, *138*, 329–337. [CrossRef] [PubMed]

101. Mowlds, D.S.; Salibian, A.A.; Scholz, T.; Paydar, K.Z.; Wirth, G.A. Capsular contracture in implant-based breast reconstruction: Examining the role of acellular dermal matrix fenestrations. *Plast. Reconstr. Surg.* **2015**, *136*, 629–635. [CrossRef] [PubMed]

102. Cheng, A.; Lakhiani, C.; Saint-Cyr, M. Treatment of capsular contracture using complete implant coverage by acellular dermal matrix: A novel technique. *Plast. Reconstr. Surg.* **2013**, *132*, 519–529. [CrossRef] [PubMed]

103. Embrey, M.; Adams, E.E.; Cunningham, B.; Peters, W.; Young, V.L.; Carlo, G.L. A review of the literature on the etiology of capsular contracture and a pilot study to determine the outcome of capsular contracture interventions. *Aesthet. Plast. Surg.* **1999**, *23*, 197–206. [CrossRef]

104. Ersek, R.A. Molecular impact surface textured implants (MISTI) alter beneficially breast capsule formation at 36 months. *J. Long Term Eff. Med. Implants* **1991**, *1*, 155–169. [PubMed]

105. Liu, X.; Zhou, L.; Pan, F.; Gao, Y.; Yuan, X.; Fan, D. Comparison of the postoperative incidence rate of capsular contracture among different breast implants: A cumulative meta-analysis. *PLoS ONE* **2015**, *10*, e0116071. [CrossRef] [PubMed]

106. Wong, C.H.; Samuel, M.; Tan, B.K.; Song, C. Capsular contracture in subglandular breast augmentation with textured versus smooth breast implants: A systematic review. *Plast. Reconstr. Surg.* **2006**, *118*, 1224–1236. [CrossRef] [PubMed]

107. Barnsley, G.P.; Sigurdson, L.J.; Barnsley, S.E. Textured surface breast implants in the prevention of capsular contracture among breast augmentation patients: A meta-analysis of randomized controlled trials. *Plast. Reconstr. Surg.* **2006**, *117*, 2182–2190. [CrossRef] [PubMed]

108. Minami, E.; Koh, I.H.; Ferreira, J.C.; Waitzberg, A.F.; Chifferi, V.; Rosewick, T.F.; Pereira, M.D.; Saldiva, P.H.; de Figueiredo, L.F. The composition and behavior of capsules around smooth and textured breast implants in pigs. *Plast. Reconstr. Surg.* **2006**, *118*, 874–884. [CrossRef] [PubMed]

109. Abramo, A.C.; de Oliveira, V.R.; Ledo-Silva, M.C.; de Oliveira, E.L. How texture-inducing contraction vectors affect the fibrous capsule shrinkage around breasts implants? *Aesthet. Plast. Surg.* **2010**, *34*, 555–560. [CrossRef] [PubMed]

110. Hall-Findlay, E.J. Breast implant complication review: Double capsules and late seromas. *Plast. Reconstr. Surg.* **2011**, *127*, 56–66. [CrossRef] [PubMed]

111. Danino, M.A.; Nizard, N.; Paek, L.S.; Govshievich, A.; Giot, J.P. Do bacteria and biofilm play a role in double-capsule formation around macrotextured implants? *Plast. Reconstr. Surg.* **2017**, *140*, 878–883. [CrossRef] [PubMed]

112. Pamula, E.; de Cupere, V.; Dufrene, Y.F.; Rouxhet, P.G. Nanoscale organization of adsorbed collagen: Influence of substrate hydrophobicity and adsorption time. *J. Colloid Interface Sci.* **2004**, *271*, 80–91. [CrossRef] [PubMed]

113. Bozec, L.; van der Heijden, G.; Horton, M. Collagen fibrils: Nanoscale ropes. *Biophys. J.* **2007**, *92*, 70–75. [CrossRef] [PubMed]

114. Bettinger, C.J.; Langer, R.; Borenstein, J.T. Engineering substrate topography at the micro- and nanoscale to control cell function. *Angew. Chem.* **2009**, *48*, 5406–5415. [CrossRef] [PubMed]

115. Friedl, P.; Brocker, E.B. T cell migration in three-dimensional extracellular matrix: Guidance by polarity and sensations. *Dev. Immunol* **2000**, *7*, 249–266. [CrossRef] [PubMed]

116. Biela, S.A.; Su, Y.; Spatz, J.P.; Kemkemer, R. Different sensitivity of human endothelial cells, smooth muscle cells and fibroblasts to topography in the nano-micro range. *Acta Biomater.* **2009**, *5*, 2460–2466. [CrossRef] [PubMed]

117. Dalby, M.J.; Riehle, M.O.; Johnstone, H.; Affrossman, S.; Curtis, A.S. Investigating the limits of filopodial sensing: A brief report using SEM to image the interaction between 10 nm high Nano-topography and fibroblast Filopodia. *Cell Biol. Int.* **2004**, *28*, 229–236. [CrossRef] [PubMed]

118. Hsu, S.H.; Chen, C.Y.; Lu, P.S.; Lai, C.S.; Chen, C.J. Oriented Schwann cell growth on microgrooved surfaces. *Biotechnol. Bioeng.* **2005**, *92*, 579–588. [CrossRef] [PubMed]

119. Kyle, D.J.; Oikonomou, A.; Hill, E.; Bayat, A. Development and functional evaluation of biomimetic silicone surfaces with hierarchical micro/nano-topographical features demonstrates favourable in vitro foreign body response of breast-derived fibroblasts. *Biomaterials* **2015**, *52*, 88–102. [CrossRef] [PubMed]

120. Barr, S.; Hill, E.W.; Bayat, A. Development, fabrication and evaluation of a novel biomimetic human breast tissue derived breast implant surface. *Acta Biomater.* **2017**, *49*, 260–271. [CrossRef] [PubMed]

121. Sforza, M.; Zaccheddu, R.; Alleruzzo, A.; Seno, A.; Mileto, D.; Paganelli, A.; Sulaiman, H.; Payne, M.; Maurovich-Horvat, L. Preliminary 3-year evaluation of experience with Silksurface and Velvetsurface motiva silicone breast implants: A single-center experience with 5813 consecutive breast augmentation cases. *Aesthet. Surg. J.* **2017**. [CrossRef] [PubMed]

Review

Temporomandibular Joint Regenerative Medicine

Xavier Van Bellinghen [1,2,3,†], **Ysia Idoux-Gillet** [1,2,†], **Marion Pugliano** [1,2,†], **Marion Strub** [1,2,3],
Fabien Bornert [1,2,3], **Francois Clauss** [1,2,3], **Pascale Schwinté** [1,2], **Laetitia Keller** [1,2],
Nadia Benkirane-Jessel [1], **Sabine Kuchler-Bopp** [1], **Jean Christophe Lutz** [1,3,4] and
Florence Fioretti [1,2,3,*]

1 INSERM (French National Institute of Health and Medical Research), UMR 1260, Regenerative Nanomedicine (RNM), FMTS, 11 rue Humann, 67000 Strasbourg, France; dr.xvb@laposte.net (X.V.B.); ysiaidouxgillet@free.fr (Y.I.-G.); marion.pugliano@gmail.com (M.P.); strub.marion@orange.fr (M.S.); bornertfabien@gmail.com (F.B.); francois_clauss@hotmail.com (F.C.); pschwinte@unistra.fr (P.S.); lkeller@unistra.fr (L.K.); nadia.jessel@inserm.fr (N.B.-J.); kuchler@unistra.fr (S.K.-B.); Jean-Christophe.LUTZ@chru-strasbourg.fr (J.C.L.)
2 Faculté de Chirurgie Dentaire, Université de Strasbourg, 8 rue Ste Elisabeth, 67000 Strasbourg, France
3 Médecine et Chirurgie Bucco-Dentaires & Chirurgie Maxillo-Facial, Hôpitaux Universitaires de Strasbourg (HUS), 1 place de l'Hôpital, 67000 Strasbourg, France
4 Faculté de Médecine, Université de Strasbourg, 11 rue Humann, 67000 Strasbourg, France
* Correspondence: f.fioretti@unistra.fr; Tel.: +33-3-68-85-33-76
† These authors contributed equally to this work.

Abstract: The temporomandibular joint (TMJ) is an articulation formed between the temporal bone and the mandibular condyle which is commonly affected. These affections are often so painful during fundamental oral activities that patients have lower quality of life. Limitations of therapeutics for severe TMJ diseases have led to increased interest in regenerative strategies combining stem cells, implantable scaffolds and well-targeting bioactive molecules. To succeed in functional and structural regeneration of TMJ is very challenging. Innovative strategies and biomaterials are absolutely crucial because TMJ can be considered as one of the most difficult tissues to regenerate due to its limited healing capacity, its unique histological and structural properties and the necessity for long-term prevention of its ossified or fibrous adhesions. The ideal approach for TMJ regeneration is a unique scaffold functionalized with an osteochondral molecular gradient containing a single stem cell population able to undergo osteogenic and chondrogenic differentiation such as BMSCs, ADSCs or DPSCs. The key for this complex regeneration is the functionalization with active molecules such as IGF-1, TGF-β1 or bFGF. This regeneration can be optimized by nano/micro-assisted functionalization and by spatiotemporal drug delivery systems orchestrating the 3D formation of TMJ tissues.

Keywords: temporomandibular joint; regenerative medicine; stem cells; scaffolds; growth factors; functionalization; drug delivery systems; nanotechnology; osteochondral regeneration

1. Introduction

1.1. Temporomandibular Joint (TMJ)

The temporomandibular joint (TMJ) is an articulation covered by dense fibrocartilage formed between the mandibular condyle and the temporal bone. The temporal articular surface is large and consists of the mandibular fossa and the articular tubercle. Along this large articular temporal surface, each mandibular condyle has a wide motion range, consisting of both rotation and translation.

Fibrocartilaginous disc cushions mechanical stresses that exist between the temporal and mandibular articular surfaces. The high collagen content of this disc provides great rigidity and

durability. The TMJ disc has no direct vascularization or innervation by itself. However, its posterior attachment, known as retrodiscal tissue, features many vessels and nerves which are crucial during physio-pathological processes.

1.2. Temporomandibular Joint Disorders (TMJD)

TMJD (temporomandibular joint disorders) are very common, their prevalence being around 52% [1]. TMJD is a general term actually covering a large number of clinical occurrences affecting the TMJ and masticatory-related structures. They cover in various etiologies: traumatic, inflammatory, and congenital. TMJD are also characterized by deficient wound healing and fibrosis caused by continuous and irreversible injuries.

Pain, malocclusion, limited range of motion, deviation, joint clicking and clenching are most of time associated with TMJD. These disorders are often so painful during basic oral activities (eating and speaking) that quality of life of patients is greatly impacted [2]. Pain is the primary symptom and the main reason why patients are referred to practitioners to seek treatment.

Osteoarthritis-like degenerative joint disease belonging to TMJD is a destruction of bone and cartilage with a consecutive inflammation which enhances tissue destruction [3]. TMJ degeneration features are: displacement, thickening and/or disc perforation, whole destruction of articular fibrocartilage and crucial modifications of bone remodeling such as sclerosis or periarticular osteophyte formation [4,5]. The ultimate stage of degeneration can even result in the replacement of TMJ by a block of fibrous and bony tissue, namely, ankylosis [6] (Figure 1).
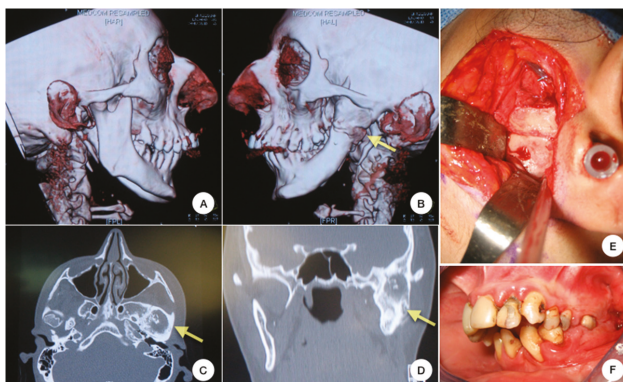
Figure 1. Invasive treatment of a patient suffering from TMJ (temporomandibular joint) ankylosis: Right lateral view of a 3D CT scan reconstruction of the head: the right TMJ is affected by joint space narrowing (**A**) and the left TMJ space has completely disappeared and been replaced by an osseous block (**B**). This replacement of the left TMJ by an osseous block of ankylosis is seen on transversal (**C**), and on coronal (**D**) CT scan sections. Intraoperative view of invasive treatment: the osseous bloc of ankylosis replacing the left TMJ space is approached through a pre-auricular incision (**E**). Preoperative intraoral photograph showing the absence of mouth opening (**F**).

2. Current Status of Temporomandibular Treatments

2.1. Current Therapies

Once the primary factors of TMJD have been identified and eliminated, the treatment can vary according to the severity of the disorder: non-invasive, minimally invasive and invasive procedures. However, permanent recovery is rarely obtained and therefore, follow-up therapies are required [7].

Occlusal orthodontics, medications, physical therapy and acupuncture are the most common non-invasive treatments. Although occlusal orthodontics are widely used, their effectiveness remains

questionable [8,9]. Non-invasive medications consist anxiolytics, muscle relaxants, non-steroidal anti-inflammatory drugs and opioids [4,10]. Similarly, there is no consensus regarding the long-term effectiveness of such oral or topical medications [11].

Minimally invasive treatments can target either extrinsic masticatory muscles or TMJ itself. Masticatory muscles (masseter, temporalis and lateral pterygoid) have been injected with botulinum toxin type A (Botox) for thirty years [12,13]. The findings of a literature review conducted using The Cochrane Controlled Trials Register between 1980 and 2012 suggest that there is level 1 evidence supporting the efficacy of Botox in the treatment of TMJD [14].

Minimally invasive treatments of TMJ itself include intra-articular injections, arthrocentesis, and arthroscopy. Intra-articular injections of corticosteroids into either one or both joint compartments improve TMJD symptoms [15,16]. Arthrocentesis is a lavage of the superior TMJ space by a saline solution. The pressure generated by irrigation may remove adhesions. Some authors proposed morphine irrigation after arthrocentesis [17]. The short and long term efficacy of this minimally invasive treatment is well-documented [17–19]. The miniaturization of endoscopes allowed TMJ arthroscopy. It provides adequate visualization and manipulation of pathological intra-articular tissues [20]. Small-diameter instruments permit their direct removal with a high rate of success [20,21].

Invasive treatment is the only option for patients suffering from ankylosis, neoplasia, dislocation, and developmental disorders [22,23]. It consists of open joint surgery, namely arthrotomy, which aims at either restoring joint tissues or completely replacing the TMJ with autogenous or alloplastic material (Figure 1).

Regarding invasive treatment of the TMJ disc, both its surgical repositioning and the removal of affected tissues have short-term efficacy [24]. The surgical removal of the entire affected TMJ disc (discectomy) is most of the time prescribed [25]. Although discectomy has a significant long-term efficacy, it does not prevent from osteoarthrosis [26]. Along with poor remodeling of the mandibular condyle, destruction of its articular surface or osteophyte formation can occur [26]. It has been shown in vivo also that a functional disc is crucial for mandibular condyle regeneration [27].

The many options proposed for disc replacement have not shown satisfactory clinical outcomes: teflon-proplast or silicone synthetic implants [28,29], sear cartilage, autologous dermal graft [26], full-thickness skin graft, or pedicled temporalis muscle flap [23,30,31]. For instance, the clinically tested TMJ disc implants did not provide any significant advantage over discectomy, except for the reduction of clicking [4].

For severe TMJ degeneration, the total surgical joint replacement is currently prescribed. The first experiments on regeneration using alloplastic TMJ implants showed a tendency for premature failure. Subsequent immune reactions were triggered, therefore resulting in catastrophic joint damage [32,33]. Thus, TMJ regeneration strategies have been reconsidered with more caution. At the moment, the consensual strategy seems to recommend reconstruction of the TMJ using autologous tissues for young patients, and TMJ replacement using metallic prostheses for adults. With conventional alloplastic strategies, the articular surfaces can be affected by erosion or heterotopic bone formation [34]. Therefore, two-piece 3D custom-made prostheses include an ultra-high molecular weight polyethylene (UHMWPE) implant for the replacement of the temporal articular surface (mandibular fossa). Such prostheses seem to currently be the most satisfying solution available for total surgical joint replacement [35,36].

Tissue engineering of TMJ has been a primary concern in scientific discussion and practice. The limitations of current therapeutics for TMJD have led to an increased interest in regenerative strategies combining cells, implantable scaffolds and well-targeting bioactive molecules. The recent advances of regenerative medicine for orthopedics may contribute to meet the challenge of this specific complex regeneration.

2.2. Challenging Regeneration

Meeting the demands for anatomic, structural, and functional regeneration of TMJ is very challenging. Innovative strategies and biomaterials are absolutely crucial because TMJ can be considered as one of the most difficult tissues to regenerate.

The TMJ is an anatomic zone so narrow and dense that surgical access is not easy. Its limited blood supply and hence its very limited healing capacity do not facilitate regenerative strategies either.

The mechanical and structural (three-dimensional) properties of the mandibular condyle implant must match that of anatomic condyle for human clinical applications. Also, the implanted tissue-engineered mandibular condyle must have rapid and adequate remodeling potential allowing oral functions.

Histologically, the TMJ cartilage differs a lot from the other hyaline articular cartilages. Thus, regenerating this unique articular cartilage with its complex structure and organization is very tricky. TMJ regeneration means to be able to engineer a mandibular condyle implant with its unique cartilage and its underlying bone in a single osteochondral construct. The challenge in TMJ regeneration is to promote matrix synthesis and tissue maturation of chondrogenic and osteogenic cells in suitable scaffolds containing active molecules which are able to separately orchestrate osteogenesis and chondrogenesis (Figure 2).
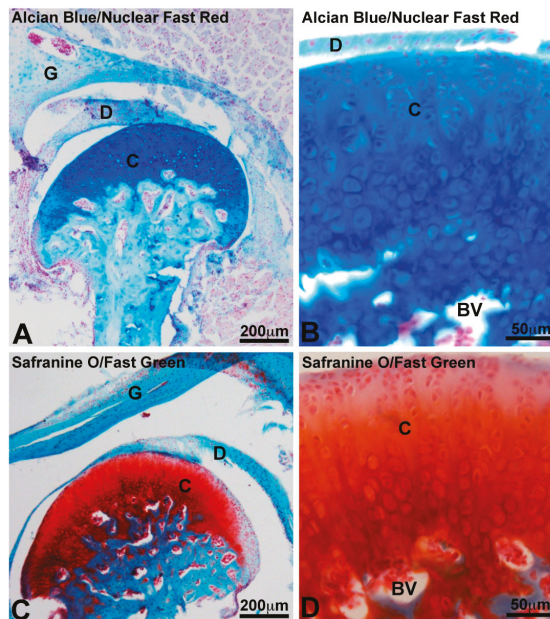
Figure 2. Histological organization of murine TMJ. TMJ is an articulation between the glenoid fossa of temporal bone (G) and mandibular condyle (C). TMJ disc cushioning articular mechanical stresses is fibrocartilaginous (D). TMJ condyle is made of a specific articular cartilage and a underlying bone containing blood vessels in medullar spaces (BV). Alcian Blue/Nuclear Fast Red specifically staining of mucopolysaccharides in blue (**A**,**B**) and Safranine O/Fast Green staining of cartilaginous proteoglycans in orange/red (**C**,**D**) highlight the osteochondral interface.

The success of TMJ regenerative strategy is not only measured by the restoration of function but also by the long-term prevention of ossified or fibrous adhesions which are the main complications of

engineered TMJ replacements [37]. Thus, pro-regenerative active molecules incorporated in scaffolds of engineered TMJ must also prevent any ossifications and any adhesions.

3. Histology and Macromolecular Biology of the TMJ

There is a continuous debate about the embryonic origin of mandibular articulating surface: blastemal or periosteal origin [38,39]. The thickness of condylar fibrocartilage in humans can reach 0.48 mm as a maximum and is subject to variations caused by age and functional conditions [40,41]. The articular surface of most synovial joints is covered by hyaline cartilage. It is not the case of the TMJ which has an articular surface covered by a layer of fibrous tissue [42]. This fibrous zone contains abundant type I collagen, while collagen type II is minimally present. Underlying this superficial fibrous zone, a fibrocartilage layer is described which can be subdivided schematically into proliferative and hypertrophic zones [42,43]. The proliferative zone functioning as a cell reservoir [44] is rich in type I collagen. In the fibrous and proliferative zones, the orientation of collagen fibers was revealed as anisotropic with initiation of antero-posterior alignment of the fibers [43,45]. A chondroitin sulfate-based proteoglycan resembling versican predominates in both of these zones [46,47]. The hypertrophic zone is rich in chondrocytes, in aggrecan and in collagen type II. Collagen types I and X are also detected [47]. TMJ condylar fibrocartilage contains less glycosaminoglycans (GAGs) than hyaline articular cartilage [48] (Figures 3 and 4).

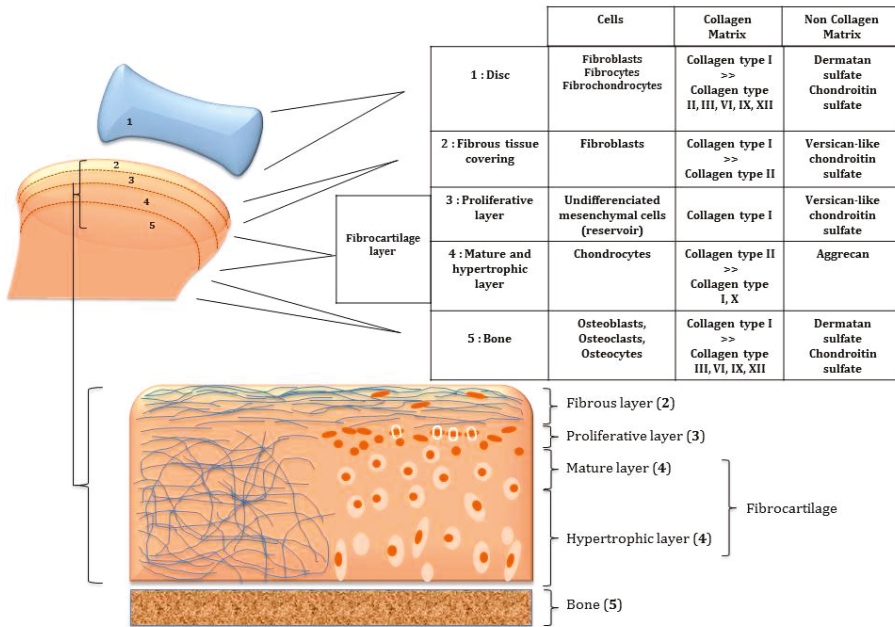|	Cells	Collagen Matrix	Non Collagen Matrix
1 : Disc	Fibroblasts Fibrocytes Fibrochondrocytes	Collagen type I >> Collagen type II, III, VI, IX, XII	Dermatan sulfate Chondroitin sulfate
2 : Fibrous tissue covering	Fibroblasts	Collagen type I >> Collagen type II	Versican-like chondroitin sulfate
3 : Proliferative layer	Undifferenciated mesenchymal cells (reservoir)	Collagen type I	Versican-like chondroitin sulfate
4 : Mature and hypertrophic layer	Chondrocytes	Collagen type II >> Collagen type I, X	Aggrecan
5 : Bone	Osteoblasts, Osteoclasts, Osteocytes	Collagen type I >> Collagen type III, VI, IX, XII	Dermatan sulfate Chondroitin sulfate

Figure 3. Scheme of the composition of the five compartments of TMJ to regenerate. Their cellular and macromolecular compositions differ of lot. An osteochondral molecular gradient of functionalization able to orchestrate the 3D formation of different TMJ tissues is the key of its regeneration.
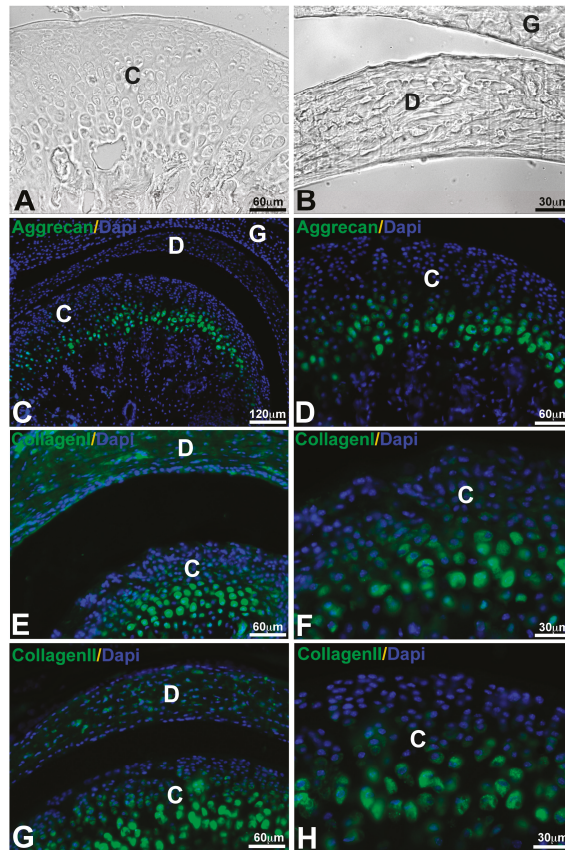
Figure 4. Expression of different conjunctive macromolecules in murine TMJ detected by immunofluorescence. TMJ observed by phase contrast microscope (**A,B**), Aggrecan expressed by chondrocytes in hypertrophic layer of mandibular condyle (**C,D**), type I collagen in the disc and in the fibrocartilage layer of mandibular condyle (**E,F**) and type II collagen in the fibrocartilage layer of mandibular condyle (**G,H**). Nuclei were stained with 4′,6-diamidino-2-phenylindole (DAPI). Condyle (**C**); Disc (**D**); Glenoid fossa (**G**).

The TMJ disc attached to the condyle and temporal bone by fibrous connective tissue measures 14 mm antero-posteriorly and 23 mm medico-laterally in humans [49]. Its periphery is thicker than the center, consequently its shape is biconcave. Populations of cells found in the TMJ disc differ from those of hyaline cartilage and are heterogeneous: fibroblasts, fibrocytes and fibrochondrocytes [50]. The periphery and attachments of the disc are well-vascularized but its central heart is avascular [51]. Type I collagen predominates but other collagens are found: types II, III, VI, IX, and XII [52]. Collagens in the disc are mostly anisotropic [53]. Orientation of fibers is antero-posterior in the center and more circumferential in the peripheral area [53]. Human disc mechanical tensile properties in anteroposterior and mediolateral directions reflect this anisotropy of the collagen fiber arrangement [49]. The particularity of these collagen fibers is to be crimped. It may improve the mechanical properties of the disc, in particular under tension [54]. TMJ disc contains less glycosaminoglycans (GAGS) than hyaline articular cartilage [55]: fraction of GAGS ranges from 1 to 10% by dry weight. Dermatan sulfate and chondroitin sulfate are the most abundant GAGS [56] (Figures 3 and 4).

4. TMJ Tissue Engineering

4.1. Cell Strategies

Two methods are possible in cartilage and bone engineering: (1) in situ tissue engineering, which involves an incorporation of an acellular scaffold matrix attracting local cells (cell homing) guiding the process of regeneration; (2) ex vivo cell seeding on the scaffold, which provides enough competent cells to orchestrate the regenerative mechanism [57]. The second strategy appears better for TMJ regeneration because of its limited capacities of self-repair and the rapid regeneration expected. Whatever the cell origin, low-intensity pulsing ultrasound on mandibular condyle enhances its regeneration [58]. In the same way, culture in spinner flasks, increases matrix production of TMJ disc cells as compared to static conditions [59].

Autogenic cells are the ideal cell source for tissue regeneration. Fibrochondrocytes from mandibular condyle seeded on polyglycolic acid (PGA) scaffolds showed weaker regenerative capacities than chondrocytes from ankle joint. Notably, they produced less GAGS and collagens [44]. In the same way, TMJ disc cells as compared to costal chondrocytes have inferior biochemical qualities and so produce less GAGs and collagens [60–62]. These limited capacities of TMJ fibrochondrocytes and the fact that it would be very difficult to have enough competent cells from the diseased TMJ, lead to find another sources of competent cells [63].

To regenerate TMJ condylar cartilage, primary costal-chondrocytes or hyaline cartilage cells from all cartilages in the body can be used [44,62]. Stem cells from the synovial capsule surrounding the joint can be extracted to generate new cartilage but their properties are reduced compared with other stem cells [64]. Human umbilical cord-derived mesenchymal-like stem cells (HUCM) are also proposed for TMJ regeneration [63]. Compared with the fibrochondrocytes from mandibular condyle, they promoted higher collagen types I and II, GAGs and cell colonization inside PGA scaffolds [63].

Bone marrow mesenchymal stem cells (BMSCs) provide a high rate of cell growth and division. Their advantage is the important volume of cells available and the numerous kind of possible differentiation. They can promote bone and cartilage regeneration of TMJ. Their disadvantage is their tendency to endochondral ossification [64–67].

Adipose stem cells (ADSCs) could be a potential cell source for TMJ engineering [65]. They are pluripotent mesenchymal stem cells that present multilineage differentiation [68]. These stem cells reaped from adipose tissue are easily obtainable whatever the quantity needed [67]. The implantation site of TMJ having a low vascularization, the capacity of ADSCs to undergo a low oxygen environment is very interesting. They can replicate the extracellular matrix environment of the implantation site, with the different types of collagen [65].

Different tooth-derived stem cells are also potential competent cells for TMJ regeneration. periodontal ligament stem cells (PDLSCs) and stem cells from apical papilla (SCAPs) similar to mesenchymal stem cells (MSCs) [69,70] are able to differentiate into chondrocytes and osteoblasts [71,72]. Dental follicle progenitor cells (DFPCs) which are stem cells from dental follicles involved in early tooth formation phases [73] can also differentiate into chondrocytes and osteoblasts [69,74].

Dental pulp stem cells (DPSCs) mesenchymal stem cells from dental pulp [75] are known to differentiate into different kinds of cells, such as osteoblasts and chondrogenic cells [69]. They are particularly adequate for regeneration of mineralized tissue [76]. Their multipotency, proliferation rate and availability appear better than those of BMSCs.

The capacity of osteogenic differentiation of DPSCs is well-documented [77–79]. DPSCs and collagen sponges showed excellent results inside human mandibular defects [71]. In a rabbit model of alveolar bone defects, it has shown high expression of BMP-2 by DPSCs as well as a high amount of bone formation [80]. This high expression of BMP-2 is the key for the differentiation of DPSCs [81–83]. The simple immobilization of DPSCs in scaffolds activates their osteogenic differentiation [84].

For regeneration of discal fibrocartilage, dermal fibroblasts are promising. Easily available, these autologous cells seeded in quantity and treated with IGF-1 showed a high chondrogenic potential [85]. For disc regeneration, seeding density must be carefully controlled in order to not decrease biomechanical properties. Increasing the cell number up to 1.2×10^8 cells/mL of scaffold volume enhanced fibrocartilaginous deposition but modified mechanical properties. The lowest seeding density that promotes functional properties close to in vivo conditions must be identified for each cell source to regenerate TMJ disc [85].

These stem cells able to undergo both chondrogenic and osteogenic differentiation are crucial for TMJ regeneration. The best strategy should be to use a unique stem cell type able to support in a unique scaffold biphasic osteochondral regeneration orchestrated by active pro-chondrogenic and pro-osteogenic molecules.

4.2. Scaffolds for TMJ Cartilage Regeneration

Hyaluronic acid (HA) is a polysaccharide abundant in cartilaginous matrices, which constitutes an ideal chondrogenic microenvironment, ideal for cartilage regeneration [86]. HA hydrogels promote the differentiation of stem cells into chondrocytes and their synthesis of cartilaginous matrix [87] and support a level of chondrogenic protein expression required for cartilage regeneration [88]. Incorporation of other molecules improves mechanical properties of HA scaffolds to support cartilage tissue regeneration.

Agarose is a polysaccharide extracted from seaweed, used as agar for cell culture. Its advantage is its adaptable stiffness, which allows an easy variation of mechanical features of the scaffold [89]. Agarose scaffolds promote differentiation of different stem cells, such as MSCs and ADSCs into chondrocytes [90–92].

Poly-vinyl alcohol (PVA) is a hydrophilic polymer which is also very appropriate for cartilage regeneration due to its high water content and its elastic properties [93]. Its capacity to promote repair of articular cartilage is well-documented [94–96]. Modifications of parameters in PVA hydrogel synthesis allow suitable tensile strength [97] and elastic modulus [98] to sustain cartilage regeneration. PVA scaffolds retain long enough their chondrogenic and mechanical properties in vivo. Indeed, the rate of degradation of PVA is enough low enough to give time for cartilage to regenerate [99].

Poly-L-lactic-coglycolic acid (PLGA) is a synthetic polymer approved by the FDA for clinical applications which is greatly interesting for cartilage regeneration. The versatility of its structure allows also a modulation of mechanical properties of the scaffold. PLGA scaffolds promote colonization and differentiation of MSCs in vivo [100]. PLGA interacts positively with chondrocytes and other resident cells of the TMJ disc to regenerate. Nevertheless, it does not interact well with native collagens of the TMJ disc [101]. Incorporation of other polymers in PLGA scaffolds improves theirs chondrogenesis capacity and reduces the process of degeneration [102].

4.3. Scaffold for Fibrocartilage Regeneration

For the specific regeneration of TMJ disc, a variety of scaffolds have shown their efficacy in vitro and in vivo [103,104]. An aporous scaffold of polyglycerol sebacate (PGS), an elastomer, was used for regeneration of the TMJ disc. PGS scaffolds revealed to be favorable for culture of goat fibrochondrocytes and therefore for TMJ disc regeneration [105]. Poly-glycolique acid (PGA) is a biodegradable polyester. An engineered disc was proposed, made by PGA mesh scaffold-included cells [106]. Scaffolds of PGA have shown their capacity to support the culture of stem cells from human umbilical cord, their chondrogenic differentiation and expansion [63]. Poly-L-Lactic acid (PLLA) is interesting for its slow degradation rate. PLLA scaffolds seeded with porcine TMJ cells and treated with TGF β-1 improved mechanicals properties and showed higher collagen and GAGS deposition as compared to PGA scaffolds [4,107]. A mixed scaffold made by polytetrafluorethylene monofilaments, PLA monofilaments, polyamide monofilaments, and natural bone has been shown to support human and porcine disc cells culture and expansion [108]. An acellular regenerative template

for reconstruction of TMJ disc made of porcine-derived extracellular matrix was studied. Implantation of this scaffold after six months showed attractive results [109].

4.4. Scaffold for Osteochondral Regeneration

Collagens are natural polymers very convenient for osteochondral regeneration and also for total TMJ disc reconstruction [110]. Collagens can be used as a gel which gives the opportunity to be injected into the narrow space of TMJ. Rigidity must be weak enough to allow intra-articular injection and important enough to allow cell adhesion and proliferation. Composite scaffolds incorporating collagens optimize the mechanical properties of osteochondral regenerative implants [111]. A collagen scaffold associated with GAGs increased chondrogenic differentiation of mesenchymal stem cells in a rat model [112]. Collagen scaffolds with hydroxyapatite and platelet-rich plasma promoted regeneration of entire TMJ condyles in children and adolescents suffering of TMJ ankyloses. Other clinical investigations are required to evidence the long-term efficiency of these scaffolds [113].

Gelatin, derived from the lysis of collagen is also appropriate for osteochondral regeneration. Gelatin extracellular environment is favorable to the adhesion and colonization of chondrocytes [114]. Gelatin scaffolds with chitosan have shown their capacity to support chondrogenic differentiation in vitro and in vivo [115,116].

Nanofibers constitute pro-regenerative biomimetic extracellular matrices very interesting for tissue regeneration. The electrospinning technique makes it possible to obtain different matrices made of synthetic and natural polymers whose nanofiber diameter is close to the size of the collagen nanofibers (50–500 nm). The network of electrospun nanofibers as well as the micropores formed (less than 100 μm in diameter) mimics the structure of the connective tissue matrix [117,118]. Poly(ε-caprolactone) (PCL) is a biodegradable synthetic polymer, approved by the FDA for clinical applications. Electrospun matrices of PCL show favorable results for osteochondral regeneration [119–121] (Figure 5).
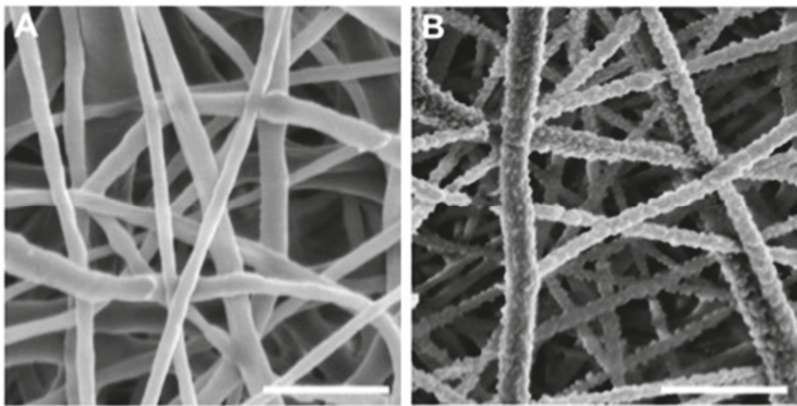

Figure 5. Scanning electron microscopy (SEM) observations of nanofibrous pro-regenerative biomimetic implants: Poly(ε-caprolactone) implant with an electrospun nanofiber network mimicking the pattern of the connective tissue matrix (**A**); Poly(ε-caprolactone) implant functionalized with nanoreservoirs of growth factors on the surface of nanofibers (**B**). Scale bar: 3 μm.

Fibrin presents a great interest for osteochondral regeneration. Most of studies deal with fibrin scaffolds for culture and differentiation of stem cells [89]. Fibrin-based scaffolds functionalized with adequate active molecules sustain differentiation of mesenchymal stem cells for cartilage [122,123] or bone [124,125] regeneration.

These scaffolds, able to support both cartilage and bone regeneration are crucial for TMJ regeneration. They give the opportunity to build an osteochondral construct in the same scaffold, i.e., a sole scaffold but biphasic due to its functionalization.

4.5. Growth Factors of Interest

Growth factors help tissue regeneration at different levels. They can promote the differentiation and proliferation of cells. They support extracellular matrix synthesis and its mineralization [126]. They can also biologically modulate the regeneration in order to be self-limited and prevent ossification and fibrous adhesion [37].

The three key growth factors for TMJ regeneration are basic fibroblast growth factor (bFGF), insulin-like growth factor 1 (IGF-1) and transforming growth factor-β1 (TGF-β1). They are able to maintain disc-like tissue in culture [127,128] and to induce BMSCs differentiation into fibroblast-like cells, synthesizing discal matrix of type I collagen and glycosaminoglycans (GAGS) [129,130].

The effect of IGF-1 on stimulating chondrogenesis is well-documented in vitro and in vivo. In particular, it increases both GAG and collagen contents of the engineered cartilage [131,132]. The fibrochondrocytes from mandibular condyle are less responsive to IGF-1 than hyaline chondrocytes [44].

TGF-β1 shows some positive effects on cellular proliferation and on the production of extracellular matrix in TMJ disc implants [133]. It induces a significant increase in the total fraction of collagen and matrix deposition inside the engineered cartilage [134]. TGF-β1 and IGF-1 promote cellular proliferation and secretion of type I collagen and GAGs in vitro on engineered mandibular condyle [130]. TGF-β1 increased collagen synthesis, Young's modulus and compressive stiffness in co-culture of articular chondrocytes and fibrochondrocytes [133].

The stimulating effect of bFGF on cell proliferation and production of collagen is well-known. GAGS synthesis is also significantly stimulated by bFGF [7]. bFGF and IGF-1 synergistically better promote the proliferation of disc cells [106] than the synthesis of the TMJ disc matrix [65]. In 2D culture, 10 ng/mL of bFGF increased the proliferation of fibrochondrocytes from mandibular condyle more than the 10 ng/mL of TGF-β1 and IGF-1 [135].

Platelet derivative growth factor (PDGF) significantly increases the proliferation rate of the TMJ-disc derived cells, collagen and hyaluronic acid synthesis in engineered TMJ disc. It upregulates RNA levels of type I and II collagens, matrix metalloproteinases (MMPs), and their specific tissue inhibitors (TIMPs) [136]. PDGF also significantly increases GAGs synthesis [7].

Over-expression of some interesting growth factors for tissue regeneration has been evidenced in malignant tumors. The debate about their oncogenic capability still hounds their clinical employment for tissue regeneration of the oral and maxillofacial region [137]. Finally, it is the drug delivery system of the active molecule, which is crucial.

5. Drug Delivery Systems

Various technologies for incorporation of growth factors into scaffolds are possible. The release of growth factors must match the rate of healing and regeneration [138,139]. The best drug delivery system can be achieved by incorporating active molecules into the scaffold. Immersion of scaffold in a solution of growth factors allows a snappy release in random distribution. Covalent binding of growth factors to the scaffold improves the control of the release. The covalent linkage may be sluggish and allows a more suitable release corresponding to cellular requests [140].

Functionalization can otherwise be accomplished by gene therapy. Gene transfer can also be conducted by viral or non-viral transduction. For tissue regeneration, the most appropriate method for gene transfer uses retroviruses, adenoviruses or adeno-associated viruses [141–143]. These functionalizations are optimized through nanotechnologies. Nanotechnologies could meet the challenge of the regeneration of ATM. To build drug delivery systems at a nanoscale level increases the quality of targeting and the control of distribution of the active molecules. It allows reduction of

their quantity, thereby their side effects and their cost. Concentration of different active molecules allowed by nanotechnologies is also very advantageous for orchestration of different stages of TMJ regeneration and for synergetic action of growth factors.

Nanofunctionalization of scaffolds made of electrospun nanofibers is possible by different techniques: plasma or wet chemical treatment, surface graft polymerization and co-axial electrospinning [144]. The co-axial technique consists of incorporating active molecules into the polymer solution to be electrospun and so of encapsulating them inside the nanofibers for a delayed action [145]. Electrospinning can be associated with electrospraying in order to functionalize nanofibers during their production [146]. The strategy of nanofibers functionalization by BMP-2 or BMP-7 nanoreservoirs is very effective for bone regeneration. This strategy also allows the differentiation of MSCs, and accelerates the tissue regeneration in vivo [147–149]. Besides, co-functionalization allowed by nanoreservoirs on nanofibers can promote regeneration but also normalization of inflammation at the implantation site [150] (Figure 5B).

Intra-articular drug delivery methods applied to the TMJ seem very attractive for both pain management and regenerative strategies. Benefits of current methods of intra-articular injection are controversial. Some alarming reports describing post-injection complications have discouraged their use for TMJ pain [151,152]. The risk of complications is correlated to the number of injections and so reduced by increasing the half-life of the drug and by promoting slow-release of intra-articular medications [151,152]. Hydrogels, polymeric microparticles and liposomes are suitable drug delivery systems. They limit rapid degradation and clearance of injected active molecules and therefore avoid frequent injections and high concentrations [153]. Intra-articular drug delivery can be convenient to modify the joint environment prior to implantation or to deliver pro-regenerative molecules in a surgically controlled fashion. It avoids systemic drug release, ectopic effects and other complications [153]. Microparticles of PLGA have been revealed to be biocompatible and suitable for intra-articular delivery to TMJ in rat and therefore can support regenerative strategies [154]. Controlled release of anti-inflammatory siRNA from biodegradable microparticles of PLGA have been proposed for intra-articular delivery to TMJ [155].

6. Osteochondral Regeneration

Bone and cartilage regeneration occur in very different competing conditions. To engineer a biphasic osteochondral implant is therefore challenging. Ideal approaches for TMJ regeneration are a single scaffold functionalized by an osteochondral molecular gradient and a unique stem cell population associated using rapid and synchronized tissue engineering techniques [156]. Understanding molecular interactions between cells of the osteochondral interface is crucial for engineering innovative osteochondral implants [157].

In large osteochondral defects of goat condyles, PLGA composite implants seeded with Nel-related protein 1 (NRP1) modified-autologous BMSCs were able to regenerate bone and cartilage tissue after transplantation. The fibrocartilage was regenerated six weeks after transplantation and the subchondral bone native articular cartilage after 24 weeks [158].

Promising results in mandibular condyle tissue regeneration were obtained after subcutaneous implantation of athymic mice with PGA and PLA scaffolds seeded with calf osteoblasts and chondrocytes in athymic mice. Analysis after 12 weeks of implantation evidenced the condylar shape of the neoformed bone and the formation of hyaline cartilage on the articular surface and of trabecular bone [159].

Hyper-hydrated collagen gels seeded with MSCs preconditioned in two different media were proposed with one osteogenic and one chondrogenic medium at each extremity. After seven days of in vitro culture, distinct bone-like and cartilage-like areas were observed which resembled to primordial joint-like structure [156].

The same strategy of gradient-based scaffolding was proposed with PLGA microspheres: implants were functionalized with TGF-β1 at the cartilaginous end and BMP-2 at the bony end. It promoted

neoformed osteochondral tissue after six weeks of implantation in mandibular condyle defects of New Zealand rabbits [158,160].

A hybrid compartmented implant was proposed with cartilage-promoting alginate/HA hydrogel at the cartilaginous end and bone-promoting nanofibrous collagen membrane at the bony end. This biphasic scaffold promoted in vitro osteogenic and chondrogenic differentiation of a single stem cell population (human MSCs). A gradient of mineralization for articular cartilage and a natural 'glue' at the osteochondral interface were obtained in vitro [161].

7. 3D Regeneration of TMJ

Whatever the strategies used, the regeneration of TMJ must match the anatomic, structural, and functional particularities of the mandibular condyle and its disc.

A bone implant of biodegradable PLGA seeded with porcine bone marrow MSCs was designed as mandibular condyle [162]. Similarly, implants of TMJ disc were engineered in the shape of TMJ discs [58,163]. Rat MSCs seeded into condyle-shaped PEG hydrogel were able to differentiate into chondrogenic and osteogenic cells [164]. Porcine derived extracellular matrix scaffolds were designed to mimic the size and shape of the TMJ. Their implantation in a canine model of TMJ discectomy led to regeneration of a functional TMJ disc [109].

The application of static uniaxial load on shape-specific TMJ disc engineered by co-culture of articular chondrocytes and meniscal fibrochondrocytes increased its functional properties. It optimized GAG synthesis and anisotropic properties resembling those of a TMJ disc [165].

Current TMJ replacement is made by prostheses. These alloplastic strategies are constantly improving in order to obtain personalized 3D prosthesis. Personalized prostheses of TMJ fabricated by 3D-printing were designed and implanted in patients. Compared with stock devices, these personalized 3D prostheses present better biomechanical and clinical outcomes. This 3D-printing technique also improves the surgery. Indeed, the positioning of an implant is easier, due to its optimal shape and to the opportunity to have an optimal 3D surgical guide [166–170].

These crucial clinical advances of personalized 3D prosthesis benefit regenerative strategies. Indeed, personalized 3D scaffolds can be considered. In that direction, the computer-designed nanofibrous and microporous scaffolds proposed by Chen et al. are very attractive and lead the way of a personalized 3D bone regenerative nanomedicine [171].

Currently, different techniques exist to produce 3D scaffolds such as phase separation, self-assembly, electrospinning and bioprinting. As seen previously, two points are necessary for the 3D scaffold to help and favor tissue regeneration: growth factors and living cells. Electrospinning can combine these three parameters. It allows 3D and porous structures constituted of nanofibers mimicking extracellular matrix. It can also be tuned to modulate biodegradability and resistance depending of the type of tissue to regenerate. Living cells can be added on the 3D scaffold for colonization of the matrix, or directly be included inside fibers using coaxial techniques [172,173]. 3D bioprinting also brings together the three parameters necessary for tissue regeneration. Compared to electrospinning, 3D bioprinting can reproduce structure and shape of tissues identical to those found in vivo [174]. This technique works in a layer-by-layer fashion, in which cells and growth factors can be included, allowing the control of the entire architecture of the tissues to be reproduced. These technologies participate to significant advances in tissue engineering and are promising for future clinical regenerative strategies.

A personalized 3D polyamide implant coated by nanoscale hydroxyapatite was rapidly designed and manufactured by computer in replacement of mandibular condyle. Its implantation into a patient showed positive clinical outcomes [175].

3D printed scaffolds were engineered with a spatiotemporal delivery of connective tissue growth factor (CTGF) and TGF-β3 encapsulated in microparticles in order to build a rabbit TMJ disc. Their implantation evidenced positive results. Significant improvement of regeneration was observed with the spatiotemporal gradient of functionalization [176]. Same approaches were developed to

engineer human 3D-printed TMJ discs. 3D-printed scaffolds mimicking anisotropic collagen alignment of the human TMJ disc were functionalized by microparticles of CTGF and TGF-β3 and then colonized by human MSCs over six weeks. Synthesis and remodeling of the matrix promoted by this 3D growth factor delivery system allow the obtainment of an implant with heterogeneous fibrocartilaginous matrix close to a human TMJ disc. This 3D reproduction of matrix heterogeneity gives to the implant viscoelastic properties which are region-dependent and so crucial for its function in future clinical applications [177].

8. Conclusions

Prevalence of affections of TMJ is important. Severe affections are preferentially concerned by regeneration. Currently, they are treated by arthrotomy and implantation of prostheses. The recent advances in regenerative medicine for orthopedics may provide solutions for TMJ regeneration. However, anatomic, structural, and functional regeneration of TMJ is very challenging and specific. The fibrocartilaginous property of the mandibular condyle and its tight link with its fibrocartilaginous disk contribute to modifying issues. The difficulty is not to obtain a pure hyaline cartilage with an underlying bone as for the other articulations. The main issue is to get a long-term fibrocartilage well-separated from its underlying bone without ossifications or fibrous adhesions which are dramatic for crucial oral functions of patients. At present, concrete progress of TMJ arthroscopy allows adequate visualization and manipulation of pathological intra-articular tissues and motivate the emergence of innovative and specific regenerative strategies of TMJ. Numerous proposals of interest have been presented focusing on suitable cells, scaffolds or active molecules for TMJ regeneration. Global strategies, able to support the entire mandibular condyle regeneration, are very attractive. So, the desired approach is a unique scaffold inducing an osteochondral molecular gradient containing a single stem cell population able to undergo osteogenic and chondrogenic differentiation such as BMSCs, ADSCs or DPSCs. The key to this complex regeneration is the functionalization by active molecules such as IGF-1, TGF-β1 or b-FGF. This regeneration can be optimized by nano/micro-assisted functionalization and by spatiotemporal drug delivery systems orchestrating the 3D formation of TMJ tissues.

References

1. Gopal, S.K.; Shankar, R.; Vardhan, B.H. Prevalence of temporo-mandibular disorders in symptomatic and asymptomatic patients: A cross-sectional study. *Int. J. Adv. Health Sci.* **2014**, *1*, 14–20.
2. Su, N.; Liu, Y.; Yang, X.; Shen, J.; Wang, H. Association of malocclusion, self-reported bruxism and chewing-side preference with oral health-related quality of life in patients with temporomandibular joint osteoarthritis. *Int. Dent. J.* **2017**. [CrossRef] [PubMed]
3. Tanaka, E.; Detamore, M.S.; Mercuri, L.G. Degenerative disorders of the temporomandibular joint: Etiology, diagnosis, and treatment. *J. Dent. Res.* **2008**, *87*, 296–307. [CrossRef] [PubMed]
4. Aryaei, A.; Vapniarsky, N.; Hu, J.C.; Athanasiou, K.A. Recent tissue engineering advances for the treatment of temporomandibular joint disorders. *Curr. Osteoporos. Rep.* **2016**, *14*, 269–279. [CrossRef] [PubMed]
5. Zarb, G.A.; Carlsson, G.E. Temporomandibular disorders: Osteoarthritis. *J. Orofac. Pain* **1999**, *13*, 295–306. [PubMed]

6. Sporniak-Tutak, K.; Janiszewska-Olszowska, J.; Kowalczyk, R. Management of temporomandibular ankylosis—Compromise or individualization—A literature review. *Med. Sci. Monit.* **2011**, *17*, RA111–RA116. [CrossRef] [PubMed]

7. Murphy, M.K.; MacBarb, R.F.; Wong, M.E.; Athanasiou, K.A. Temporomandibular disorders: A review of etiology, clinical management, and tissue engineering strategies. *Int. J. Oral Maxillofac. Implants* **2013**, *28*, e393–e414. [CrossRef] [PubMed]

8. Ingawalé, S.; Goswami, T. Temporomandibular joint: Disorders, treatments, and biomechanics. *Ann. Biomed. Eng.* **2009**, *37*, 976–996. [CrossRef] [PubMed]

9. Al-Ani, M.Z.; Davies, S.J.; Gray, R.J.; Sloan, P.; Glenny, A.M. Stabilisation splint therapy for temporomandibular pain dysfunction syndrome. *Cochrane Database Syst. Rev.* **2004**, CD002778. [CrossRef]

10. Liu, F.; Steinkeler, A. Epidemiology, diagnosis, and treatment of temporomandibular disorders. *Dent. Clin. N. Am.* **2013**, *57*, 465–479. [CrossRef] [PubMed]

11. Mujakperuo, H.R.; Watson, M.; Morrison, R.; Macfarlane, T.V. Pharmacological interventions for pain in patients with temporomandibular disorders. *Cochrane Database Syst. Rev.* **2010**, CD004715. [CrossRef] [PubMed]

12. Bakke, M.; Møller, E.; Werdelin, L.M.; Dalager, T.; Kitai, N.; Kreiborg, S. Treatment of severe temporomandibular joint clicking with botulinum toxin in the lateral pterygoid muscle in two cases of anterior disc displacement. *Oral Surg. Oral Med. Oral Pathol. Oral Radiol. Endod.* **2005**, *100*, 693–700. [CrossRef] [PubMed]

13. Sunil Dutt, C.; Ramnani, P.; Thakur, D.; Pandit, M. Botulinum toxin in the treatment of muscle specific oro-facial pain: A literature review. *J. Maxillofac. Oral Surg.* **2015**, *14*, 171–175. [CrossRef] [PubMed]

14. Persaud, R.; Garas, G.; Silva, S.; Stamatoglou, C.; Chatrath, P.; Patel, K. An evidence-based review of botulinum toxin (Botox) applications in non-cosmetic head and neck conditions. *JRSM Short Rep.* **2013**, *4*, 10. [CrossRef] [PubMed]

15. Dym, H.; Bowler, D.; Zeidan, J. Pharmacologic treatment for temporomandibular disorders. *Dent. Clin. N. Am.* **2016**, *60*, 367–379. [CrossRef] [PubMed]

16. Machado, E.; Bonotto, D.; Cunali, P.A. Intra-articular injections with corticosteroids and sodium hyaluronate for treating temporomandibular joint disorders: A systematic review. *Dent. Press J. Orthod.* **2013**, *18*, 128–133. [CrossRef]

17. Brennan, P.A.; Ilankovan, V. Arthrocentesis for temporomandibular joint pain dysfunction syndrome. *J. Oral Maxillofac. Surg.* **2006**, *64*, 949–951. [CrossRef] [PubMed]

18. Carvajal, W.A.; Laskin, D.M. Long-term evaluation of arthrocentesis for the treatment of internal derangements of the temporomandibular joint. *J. Oral Maxillofac. Surg.* **2000**, *58*, 852–855. [CrossRef] [PubMed]

19. Monje-Gil, F.; Nitzan, D.; González-Garcia, R. Temporomandibular joint arthrocentesis. Review of the literature. *Med. Oral Patol. Oral Cir. Bucal.* **2012**, *17*, e575–e581. [CrossRef] [PubMed]

20. Dym, H.; Israel, H. Diagnosis and treatment of temporomandibular disorders. *Dent. Clin. N. Am.* **2012**, *56*, 149–161. [CrossRef] [PubMed]

21. Rigon, M.; Pereira, L.M.; Bortoluzzi, M.C.; Loguercio, A.D.; Ramos, A.L.; Cardoso, J.R. Arthroscopy for temporomandibular disorders. *Cochrane Database Syst. Rev.* **2011**, CD006385. [CrossRef]

22. Elgazzar, R.F.; Abdelhady, A.I.; Saad, K.A.; Elshaal, M.A.; Hussain, M.M.; Abdelal, S.E.; Sadakah, A.A. Treatment modalities of TMJ ankylosis: Experience in Delta Nile, Egypt. *Int. J. Oral Maxillofac. Surg.* **2010**, *39*, 333–342. [CrossRef] [PubMed]

23. Dimitroulis, G. Temporomandibular joint surgery: What does it mean to the dental practitioner? *Aust. Dent. J.* **2011**, *56*, 257–264. [CrossRef] [PubMed]

24. Dolwick, M.F. Disc preservation surgery for the treatment of internal derangements of the temporomandibular joint. *J. Oral Maxillofac. Surg.* **2001**, *59*, 1047–1050. [CrossRef] [PubMed]

25. Miloro, M.; Henriksen, B. Discectomy as the primary surgical option for internal derangement of the temporomandibular joint. *J. Oral Maxillofac. Surg.* **2010**, *68*, 782–789. [CrossRef] [PubMed]

26. Dimitroulis, G. Condylar morphology after temporomandibular joint discectomy with interpositional abdominal dermis-fat graft. *J. Oral Maxillofac. Surg.* **2011**, *69*, 439–446. [CrossRef] [PubMed]

27. Hayashi, H.; Fujita, T.; Shirakura, M.; Tsuka, Y.; Fujii, E.; Terao, A.; Tanimoto, K. Role of articular disc in condylar regeneration of the mandible. *Exp. Anim.* **2014**, *63*, 395–401. [CrossRef] [PubMed]

28. Kaplan, P.A.; Ruskin, J.D.; Tu, H.K.; Knibbe, M.A. Erosive arthritis of the temporomandibular joint caused by Teflon-Proplast implants: Plain film features. *Am. J. Roentgenol.* **1988**, *151*, 337–339. [CrossRef] [PubMed]

29. Westesson, P.L.; Eriksson, L.; Lindström, C. Destructive lesions of the mandibular condyle following diskectomy with temporary silicone implant. *Oral Surg. Oral Med. Oral Pathol.* **1987**, *63*, 143–150. [CrossRef]

30. Dimitroulis, G.; Slavin, J. Histological evaluation of full thickness skin as an interpositional graft in the rabbit craniomandibular joint. *J. Oral Maxillofac. Surg.* **2006**, *64*, 1075–1080. [CrossRef] [PubMed]

31. Bradley, P.; Brockbank, J. The temporalis muscle flap in oral reconstruction. A cadaveric, animal and clinical study. *J. Maxillofac. Surg.* **1981**, *9*, 139–145. [CrossRef]

32. Detamore, M.S.; Athanasiou, K.A.; Mao, J. A call to action for bioengineers and dental professionals: Directives for the future of TMJ bioengineering. *Ann. Biomed. Eng.* **2007**, *35*, 1301–1311. [CrossRef] [PubMed]

33. Dimitroulis, G. The prevalence of osteoarthrosis in cases of advanced internal derangement of the temporomandibular joint: A clinical, surgical and histological study. *Int. J. Oral Maxillofac. Surg.* **2005**, *34*, 345–349. [CrossRef] [PubMed]

34. Mercuri, L.G. Alloplastic temporomandibular joint replacement: Rationale for the use of custom devices. *Int. J. Oral Maxillofac. Surg.* **2012**, *41*, 1033–1040. [CrossRef] [PubMed]

35. Sidebottom, A.J. Alloplastic or autogenous reconstruction of the TMJ. *J. Oral Biol. Craniofac. Res.* **2013**, *3*, 135–139. [CrossRef] [PubMed]

36. Gerbino, G.; Zavattero, E.; Bosco, G.; Berrone, S.; Ramieri, G. Temporomandibular joint reconstruction with stock and custom-made devices: Indications and results of a 14-year experience. *J. Craniomaxillofac. Surg.* **2017**, *45*, 1710–1715. [CrossRef] [PubMed]

37. Mehrotra, D. TMJ bioengineering: A review. *J. Oral Biol. Craniofac. Res.* **2013**, *3*, 140–145. [CrossRef] [PubMed]

38. Symons, N.B. The development of the human mandibular joint. *J. Anat.* **1952**, *86*, 326–332. [PubMed]

39. Baume, L.J. Ontogenesis of the human temporomandibular joint. I. Development of the condyles. *J. Dent. Res.* **1962**, *41*, 1327–1339. [CrossRef] [PubMed]

40. Hansson, T.; Oberg, T.; Carlsson, G.E.; Kopp, S. Thickness of the soft tissue layers and the articular disk in the temporomandibular joint. *Acta Odontol. Scand.* **1977**, *35*, 77–83. [CrossRef] [PubMed]

41. Bibb, C.A.; Pullinger, A.G.; Baldioceda, F. Serial variation in histological character of articular soft tissue in young human adult temporomandibular joint condyles. *Arch. Oral Biol.* **1993**, *38*, 343–352. [CrossRef]

42. Ngan, P.W.; Deguchi, T.; Roberts, E.W. *Orthodontic Treatment of Class III Malocclusion*; Benthan Science: Charjah, UAE, 2014; ISBN 978-1-60805-686-6.

43. Singh, M.; Detamore, M.S. Biomechanical properties of the mandibular condylar cartilage and their relevance to the TMJ disc. *J. Biomech.* **2009**, *42*, 405–417. [CrossRef] [PubMed]

44. Wang, L.; Lazebnik, M.; Detamore, M.S. Hyaline cartilage cells outperform mandibular condylar cartilage cells in a TMJ fibrocartilage tissue engineering application. *Osteoarthr. Cartil.* **2009**, *17*, 346–353. [CrossRef] [PubMed]

45. Detamore, M.S.; Athanasiou, K.A. Tensile properties of the porcine temporomandibular joint disc. *J. Biomech. Eng.* **2003**, *125*, 558–565. [CrossRef] [PubMed]

46. Roth, S.; Müller, K.; Fischer, D.C.; Dannhauer, K.H. Specific properties of the extracellular chondroitin sulphate proteoglycans in the mandibular condylar growth centre in pigs. *Arch. Oral Biol.* **1997**, *42*, 63–76. [CrossRef]

47. Kuroda, S.; Tanimoto, K.; Izawa, T.; Fujihara, S.; Koolstra, J.H.; Tanaka, E. Biomechanical and biochemical characteristics of the mandibular condylar cartilage. *Osteoarthr. Cartil.* **2009**, *17*, 1408–1415. [CrossRef] [PubMed]

48. Delatte, M.; Von den Hoff, J.W.; van Rheden, R.E.; Kuijpers-Jagtman, A.M. Primary and secondary cartilages of the neonatal rat: The femoral head and the mandibular condyle. *Eur. J. Oral Sci.* **2004**, *112*, 156–162. [CrossRef] [PubMed]

49. Kalpakci, K.N.; Willard, V.P.; Wong, M.E.; Athanasiou, K.A. An interspecies comparison of the temporomandibular joint disc. *J. Dent. Res.* **2011**, *90*, 193–198. [CrossRef] [PubMed]

50. Detamore, M.S.; Hegde, J.N.; Wagle, R.R.; Almarza, A.J.; Montufar-Solis, D.; Duke, P.J.; Athanasiou, K.A. Cell type and distribution in the porcine temporomandibular joint disc. *J. Oral Maxillofac. Surg.* **2006**, *64*, 243–248. [CrossRef] [PubMed]

51. Wong, G.B.; Weinberg, S.; Symington, J.M. Morphology of the developing articular disc of the human temporomandibular joint. *J. Oral Maxillofac. Surg.* **1985**, *43*, 565–569. [CrossRef]

52. Detamore, M.S.; Orfanos, J.G.; Almarza, A.J.; French, M.M.; Wong, M.E.; Athanasiou, K.A. Quantitative analysis and comparative regional investigation of the extracellular matrix of the porcine temporomandibular joint disc. *Matrix Biol.* **2005**, *24*, 45–57. [CrossRef] [PubMed]

53. Scapino, R.P.; Obrez, A.; Greising, D. Organization and function of the collagen fiber system in the human temporomandibular joint disk and its attachments. *Cells Tissues Organs* **2006**, *182*, 201–225. [CrossRef] [PubMed]

54. Berkovitz, B.K. Collagen crimping in the intra-articular disc and articular surfaces of the human temporomandibular joint. *Arch. Oral Biol.* **2000**, *45*, 749–756. [CrossRef]

55. Plumb, M.S.; Aspden, R.M. The response of elderly human articular cartilage to mechanical stimuli in vitro. *Osteoarthr. Cartil.* **2005**, *13*, 1084–1091. [CrossRef] [PubMed]

56. Almarza, A.J.; Bean, A.C.; Baggett, L.S.; Athanasiou, K.A. Biochemical analysis of the porcine temporomandibular joint disc. *Br. J. Oral Maxillofac. Surg.* **2006**, *44*, 124–128. [CrossRef] [PubMed]

57. Kinoshita, Y.; Maeda, H. Recent developments of functional scaffolds for craniomaxillofacial bone tissue engineering applications. *Sci. World J.* **2013**, *2013*, 863157. [CrossRef] [PubMed]

58. El-Bialy, T.; Uludag, H.; Jomha, N.; Badylak, S.F. In vivo ultrasound-assisted tissue-engineered mandibular condyle: A pilot study in rabbits. *Tissue Eng. Part C Methods* **2010**, *16*, 1315–1323. [CrossRef] [PubMed]

59. Detamore, M.S.; Athanasiou, K.A. Use of a rotating bioreactor toward tissue engineering the temporomandibular joint disc. *Tissue Eng.* **2005**, *11*, 1188–1197. [CrossRef] [PubMed]

60. Anderson, D.E.; Athanasiou, K.A. Passaged goat costal chondrocytes provide a feasible cell source for temporomandibular joint tissue engineering. *Ann. Biomed. Eng.* **2008**, *36*, 1992–2001. [CrossRef] [PubMed]

61. Johns, D.E.; Wong, M.E.; Athanasiou, K.A. Clinically relevant cell sources for TMJ disc engineering. *J. Dent. Res.* **2008**, *87*, 548–552. [CrossRef] [PubMed]

62. Anderson, D.E.; Athanasiou, K.A. A comparison of primary and passaged chondrocytes for use in engineering the temporomandibular joint. *Arch. Oral Biol.* **2009**, *54*, 138–145. [CrossRef] [PubMed]

63. Bailey, M.M.; Wang, L.; Bode, C.J.; Mitchell, K.E.; Detamore, M.S. A comparison of human umbilical cord matrix stem cells and temporomandibular joint condylar chondrocytes for tissue engineering temporomandibular joint condylar cartilage. *Tissue Eng.* **2007**, *13*, 2003–2010. [CrossRef] [PubMed]

64. Wu, Y.; Gong, Z.; Li, J.; Meng, Q.; Fang, W.; Long, X. The pilot study of fibrin with temporomandibular joint derived synovial stem cells in repairing TMJ disc perforation. *Biomed. Res. Int.* **2014**, *2014*, 454021. [CrossRef] [PubMed]

65. Mäenpää, K.; Ellä, V.; Mauno, J.; Kellomäki, M.; Suuronen, R.; Ylikomi, T.; Miettinen, S. Use of adipose stem cells and polylactide discs for tissue engineering of the temporomandibular joint disc. *J. R. Soc. Interface* **2010**, *7*, 177–188. [CrossRef] [PubMed]

66. Costello, B.J.; Kumta, P.; Sfeir, C.S. Regenerative technologies for craniomaxillofacial surgery. *J. Oral Maxillofac. Surg.* **2015**, *73*, S116–S125. [CrossRef] [PubMed]

67. Sunil, P.; Manikandhan, R.; Muthu, M.; Abraham, S. Stem cell therapy in oral and maxillofacial region: An overview. *J. Oral Maxillofac. Pathol.* **2012**, *16*, 58–63. [CrossRef] [PubMed]

68. Zuk, P.A.; Zhu, M.; Mizuno, H.; Huang, J.; Futrell, J.W.; Katz, A.J.; Benhaim, P.; Lorenz, H.P.; Hedrick, M.H. Multilineage cells from human adipose tissue: Implications for cell-based therapies. *Tissue Eng.* **2001**, *7*, 211–228. [CrossRef] [PubMed]

69. Saito, M.T.; Silvério, K.G.; Casati, M.Z.; Sallum, E.A.; Nociti, F.H. Tooth-derived stem cells: Update and perspectives. *World J. Stem Cells* **2015**, *7*, 399–407. [CrossRef] [PubMed]

70. Guo, L.; Li, J.; Qiao, X.; Yu, M.; Tang, W.; Wang, H.; Guo, W.; Tian, W. Comparison of odontogenic differentiation of human dental follicle cells and human dental papilla cells. *PLoS ONE* **2013**, *8*, e62332. [CrossRef] [PubMed]

71. Park, Y.J.; Cha, S.; Park, Y.S. Regenerative applications using tooth derived stem cells in other than tooth regeneration: A literature review. *Stem Cells Int.* **2016**, *2016*, 9305986. [CrossRef] [PubMed]

72. Sedgley, C.M.; Botero, T.M. Dental stem cells and their sources. *Dent. Clin. N. Am.* **2012**, *56*, 549–561. [CrossRef] [PubMed]

73. Silvério, K.G.; Davidson, K.C.; James, R.G.; Adams, A.M.; Foster, B.L.; Nociti, F.; Somerman, M.J.; Moon, R.T. Wnt/β-catenin pathway regulates bone morphogenetic protein (BMP2)-mediated differentiation of dental follicle cells. *J. Periodontal. Res.* **2012**, *47*, 309–319. [CrossRef] [PubMed]

74. d'Aquino, R.; de Rosa, A.; Lanza, V.; Tirino, V.; Laino, L.; Graziano, A.; Desiderio, V.; Laino, G.; Papaccio, G. Human mandible bone defect repair by the grafting of dental pulp stem/progenitor cells and collagen sponge biocomplexes. *Eur. Cell Mater.* **2009**, *18*, 75–83. [CrossRef] [PubMed]

75. Gronthos, S.; Mankani, M.; Brahim, J.; Robey, P.G.; Shi, S. Postnatal human dental pulp stem cells (DPSCs) in vitro and in vivo. *Proc. Natl. Acad. Sci. USA* **2000**, *97*, 13625–13630. [CrossRef] [PubMed]

76. Alge, D.L.; Zhou, D.; Adams, L.L.; Wyss, B.K.; Shadday, M.D.; Woods, E.J.; Gabriel Chu, T.M.; Goebel, W.S. Donor-matched comparison of dental pulp stem cells and bone marrow-derived mesenchymal stem cells in a rat model. *J. Tissue Eng. Regen. Med.* **2010**, *4*, 73–81. [CrossRef] [PubMed]

77. Akkouch, A.; Zhang, Z.; Rouabhia, M. Engineering bone tissue using human dental pulp stem cells and an osteogenic collagen-hydroxyapatite-poly (L-lactide-co-ε-caprolactone) scaffold. *J. Biomater. Appl.* **2014**, *28*, 922–936. [CrossRef] [PubMed]

78. Annibali, S.; Bellavia, D.; Ottolenghi, L.; Cicconetti, A.; Cristalli, M.P.; Quaranta, R.; Pilloni, A. Micro-CT and PET analysis of bone regeneration induced by biodegradable scaffolds as carriers for dental pulp stem cells in a rat model of calvarial "critical size" defect: Preliminary data. *J. Biomed. Mater. Res. B Appl. Biomater.* **2014**, *102*, 815–825. [CrossRef] [PubMed]

79. Mangano, C.; de Rosa, A.; Desiderio, V.; d'Aquino, R.; Piattelli, A.; de Francesco, F.; Tirino, V.; Mangano, F.; Papaccio, G. The osteoblastic differentiation of dental pulp stem cells and bone formation on different titanium surface textures. *Biomaterials* **2010**, *31*, 3543–3551. [CrossRef] [PubMed]

80. Liu, H.C.; E, L.L.; Wang, D.S.; Su, F.; Wu, X.; Shi, Z.P.; Lv, Y.; Wang, J.Z. Reconstruction of alveolar bone defects using bone morphogenetic protein 2 mediated rabbit dental pulp stem cells seeded on nano-hydroxyapatite/collagen/poly(L-lactide). *Tissue Eng. Part A* **2011**, *17*, 2417–2433. [CrossRef] [PubMed]

81. Ikeda, H.; Sumita, Y.; Ikeda, M.; Okumura, T.; Sakai, E.; Nishimura, M.; Asahina, I. Engineering bone formation from human dental pulp- and periodontal ligament-derived cells. *Ann. Biomed. Eng.* **2011**, *39*, 26–34. [CrossRef] [PubMed]

82. Yang, X.; van der Kraan, P.M.; Bian, Z.; Fan, M.; Walboomers, X.F.; Jansen, J.A. Mineralized tissue formation by BMP2-transfected pulp stem cells. *J. Dent. Res.* **2009**, *88*, 1020–1025. [CrossRef] [PubMed]

83. Yang, X.; Walboomers, X.F.; van den Dolder, J.; Yang, F.; Bian, Z.; Fan, M.; Jansen, J.A. Non-viral bone morphogenetic protein 2 transfection of rat dental pulp stem cells using calcium phosphate nanoparticles as carriers. *Tissue Eng. Part A* **2008**, *14*, 71–81. [CrossRef] [PubMed]

84. Kanafi, M.M.; Ramesh, A.; Gupta, P.K.; Bhonde, R.R. Dental pulp stem cells immobilized in alginate microspheres for applications in bone tissue engineering. *Int. Endod. J.* **2014**, *47*, 687–697. [CrossRef] [PubMed]

85. Almarza, A.J.; Athanasiou, K.A. Effects of initial cell seeding density for the tissue engineering of the temporomandibular joint disc. *Ann. Biomed. Eng.* **2005**, *33*, 943–950. [CrossRef] [PubMed]

86. Park, H.; Choi, B.; Hu, J.; Lee, M. Injectable chitosan hyaluronic acid hydrogels for cartilage tissue engineering. *Acta Biomater.* **2013**, *9*, 4779–4786. [CrossRef] [PubMed]

87. Kim, I.L.; Mauck, R.L.; Burdick, J.A. Hydrogel design for cartilage tissue engineering: A case study with hyaluronic acid. *Biomaterials* **2011**, *32*, 8771–8782. [CrossRef] [PubMed]

88. Chung, C.; Burdick, J.A. Influence of three-dimensional hyaluronic acid microenvironments on mesenchymal stem cell chondrogenesis. *Tissue Eng. Part A* **2009**, *15*, 243–254. [CrossRef] [PubMed]

89. Willerth, S.M.; Sakiyama-Elbert, S.E. Combining stem cells and biomaterial scaffolds for constructing tissues and cell delivery. In *The Stem Cell Research Community*; StemBook, Ed.; Harvard Stem Cell Institute: Cambridge, MA, USA, 2008. [CrossRef]

90. Awad, H.A.; Wickham, M.Q.; Leddy, H.A.; Gimble, J.M.; Guilak, F. Chondrogenic differentiation of adipose-derived adult stem cells in agarose, alginate, and gelatin scaffolds. *Biomaterials* **2004**, *25*, 3211–3222. [CrossRef] [PubMed]

91. Finger, A.R.; Sargent, C.Y.; Dulaney, K.O.; Bernacki, S.H.; Loboa, E.G. Differential effects on messenger ribonucleic acid expression by bone marrow-derived human mesenchymal stem cells seeded in agarose constructs due to ramped and steady applications of cyclic hydrostatic pressure. *Tissue Eng.* **2007**, *13*, 1151–1158. [CrossRef] [PubMed]

92. Huang, C.Y.; Reuben, P.M.; D'Ippolito, G.; Schiller, P.C.; Cheung, H.S. Chondrogenesis of human bone marrow-derived mesenchymal stem cells in agarose culture. *Anat. Rec. A Discov. Mol. Cell. Evol. Biol.* **2004**, *278*, 428–436. [CrossRef] [PubMed]

93. Baker, M.I.; Walsh, S.P.; Schwartz, Z.; Boyan, B.D. A review of polyvinyl alcohol and its uses in cartilage and orthopedic applications. *J. Biomed. Mater. Res. B Appl. Biomater.* **2012**, *100*, 1451–1457. [CrossRef] [PubMed]
94. Kobayashi, M.; Chang, Y.S.; Oka, M. A two year in vivo study of polyvinyl alcohol-hydrogel (PVA-H) artificial meniscus. *Biomaterials* **2005**, *26*, 3243–3248. [CrossRef] [PubMed]
95. Kobayashi, M.; Toguchida, J.; Oka, M. Preliminary study of polyvinyl alcohol-hydrogel (PVA-H) artificial meniscus. *Biomaterials* **2003**, *24*, 639–647. [CrossRef]
96. Bodugoz-Senturk, H.; Macias, C.E.; Kung, J.H.; Muratoglu, O.K. Poly(vinyl alcohol)-acrylamide hydrogels as load-bearing cartilage substitute. *Biomaterials* **2009**, *30*, 589–596. [CrossRef] [PubMed]
97. Stammen, J.A.; Williams, S.; Ku, D.N.; Guldberg, R.E. Mechanical properties of a novel PVA hydrogel in shear and unconfined compression. *Biomaterials* **2001**, *22*, 799–806. [CrossRef]
98. Holloway, J.L.; Spiller, K.L.; Lowman, A.M.; Palmese, G.R. Analysis of the in vitro swelling behavior of poly(vinyl alcohol) hydrogels in osmotic pressure solution for soft tissue replacement. *Acta Biomater.* **2011**, *7*, 2477–2482. [CrossRef] [PubMed]
99. Shokrgozar, M.A.; Bonakdar, S.; Dehghan, M.M.; Emami, S.H.; Montazeri, L.; Azari, S.; Rabbani, M. Biological evaluation of polyvinyl alcohol hydrogel crosslinked by polyurethane chain for cartilage tissue engineering in rabbit model. *J. Mater. Sci. Mater. Med.* **2013**, *24*, 2449–2460. [CrossRef] [PubMed]
100. Uematsu, K.; Hattori, K.; Ishimoto, Y.; Yamauchi, J.; Habata, T.; Takakura, Y.; Ohgushi, H.; Fukuchi, T.; Sato, M. Cartilage regeneration using mesenchymal stem cells and a three-dimensional poly-lactic-glycolic acid (PLGA) scaffold. *Biomaterials* **2005**, *26*, 4273–4279. [CrossRef] [PubMed]
101. Kay, S.; Thapa, A.; Haberstroh, K.M.; Webster, T.J. Nanostructured polymer/nanophase ceramic composites enhance osteoblast and chondrocyte adhesion. *Tissue Eng.* **2002**, *8*, 753–761. [CrossRef] [PubMed]
102. Fan, H.; Hu, Y.; Zhang, C.; Li, X.; Lv, R.; Qin, L.; Zhu, R. Cartilage regeneration using mesenchymal stem cells and a PLGA-gelatin/chondroitin/hyaluronate hybrid scaffold. *Biomaterials* **2006**, *27*, 4573–4580. [CrossRef] [PubMed]
103. Thomas, M.; Grande, D.; Haug, R.H. Development of an in vitro temporomandibular joint cartilage analog. *J. Oral Maxillofac. Surg.* **1991**, *49*, 854–856. [CrossRef]
104. Puelacher, W.C.; Wisser, J.; Vacanti, C.A.; Ferraro, N.F.; Jaramillo, D.; Vacanti, J.P. Temporomandibular joint disc replacement made by tissue-engineered growth of cartilage. *J. Oral Maxillofac. Surg.* **1994**, *52*, 1172–1177. [CrossRef]
105. Hagandora, C.K.; Gao, J.; Wang, Y.; Almarza, A.J. Poly (glycerol sebacate): A novel scaffold material for temporomandibular joint disc engineering. *Tissue Eng. Part A* **2013**, *19*, 729–737. [CrossRef] [PubMed]
106. Almarza, A.J.; Athanasiou, K.A. Seeding techniques and scaffolding choice for tissue engineering of the temporomandibular joint disk. *Tissue Eng.* **2004**, *10*, 1787–1795. [CrossRef] [PubMed]
107. Allen, K.D.; Athanasiou, K.A. Scaffold and growth factor selection in temporomandibular joint disc engineering. *J. Dent. Res.* **2008**, *87*, 180–185. [CrossRef] [PubMed]
108. Springer, I.N.; Fleiner, B.; Jepsen, S.; Açil, Y. Culture of cells gained from temporomandibular joint cartilage on non-absorbable scaffolds. *Biomaterials* **2001**, *22*, 2569–2577. [CrossRef]
109. Brown, B.N.; Chung, W.L.; Almarza, A.J.; Pavlick, M.D.; Reppas, S.N.; Ochs, M.W.; Russell, A.J.; Badylak, S.F. Inductive, scaffold-based, regenerative medicine approach to reconstruction of the temporomandibular joint disk. *J. Oral Maxillofac. Surg.* **2012**, *70*, 2656–2668. [CrossRef] [PubMed]
110. Grande, D.A.; Halberstadt, C.; Naughton, G.; Schwartz, R.; Manji, R. Evaluation of matrix scaffolds for tissue engineering of articular cartilage grafts. *J. Biomed. Mater. Res.* **1997**, *34*, 211–220. [CrossRef]
111. Levingstone, T.J.; Matsiko, A.; Dickson, G.R.; O'Brien, F.J.; Gleeson, J.P. A biomimetic multi-layered collagen-based scaffold for osteochondral repair. *Acta Biomater.* **2014**, *10*, 1996–2004. [CrossRef] [PubMed]
112. Farrell, E.; O'Brien, F.J.; Doyle, P.; Fischer, J.; Yannas, I.; Harley, B.A.; O'Connell, B.; Prendergast, P.J.; Campbell, V.A. A collagen-glycosaminoglycan scaffold supports adult rat mesenchymal stem cell differentiation along osteogenic and chondrogenic routes. *Tissue Eng.* **2006**, *12*, 459–468. [CrossRef] [PubMed]
113. Mehrotra, D.; Kumar, S.; Dhasmana, S. Hydroxyapatite/collagen block with platelet rich plasma in temporomandibular joint ankylosis: A pilot study in children and adolescents. *Br. J. Oral Maxillofac. Surg.* **2012**, *50*, 774–778. [CrossRef] [PubMed]
114. Balakrishnan, B.; Joshi, N.; Jayakrishnan, A.; Banerjee, R. Self-crosslinked oxidized alginate/gelatin hydrogel as injectable, adhesive biomimetic scaffolds for cartilage regeneration. *Acta Biomater.* **2014**, *10*, 3650–3663. [CrossRef] [PubMed]

115. Kuo, Y.-C.; Wang, C.-C. Effect of bovine pituitary extract on the formation of neocartilage in chitosan/gelatin scaffolds. *J. Taiwan Inst. Chem. Eng.* **2010**, *41*, 150–156. [CrossRef]

116. Xia, W.; Liu, W.; Cui, L.; Liu, Y.; Zhong, W.; Liu, D.; Wu, J.; Chua, K.; Cao, Y. Tissue engineering of cartilage with the use of chitosan-gelatin complex scaffolds. *J. Biomed. Mater. Res. B Appl. Biomater.* **2004**, *71*, 373–380. [CrossRef] [PubMed]

117. Ma, P.X. Scaffolds for tissue fabrication. *Mater. Today* **2004**, *7*, 30–40. [CrossRef]

118. Beachley, V.; Wen, X. Polymer nanofibrous structures: Fabrication, biofunctionalization, and cell interactions. *Prog. Polym. Sci.* **2010**, *35*, 868–892. [CrossRef] [PubMed]

119. Mendoza-Palomares, C.; Ferrand, A.; Facca, S.; Fioretti, F.; Ladam, G.; Kuchler-Bopp, S.; Regnier, T.; Mainard, D.; Benkirane-Jessel, N. Smart hybrid materials equipped by nanoreservoirs of therapeutics. *ACS Nano* **2012**, *6*, 483–490. [CrossRef] [PubMed]

120. Eap, S.; Morand, D.; Clauss, F.; Huck, O.; Stoltz, J.F.; Lutz, J.C.; Gottenberg, J.E.; Benkirane-Jessel, N.; Keller, L.; Fioretti, F. Nanostructured thick 3D nanofibrous scaffold can induce bone. *Biomed. Mater. Eng.* **2015**, *25*, 79–85. [CrossRef] [PubMed]

121. Keller, L.; Wagner, Q.; Pugliano, M.; Breda, P.; Ehlinger, M.; Schwinté, P.; Benkirane-Jessel, N. Bi-layered nano active implant with hybrid stem cell microtissues for tuned cartilage hypertrophy. *J. Stem Cell Res. Ther.* **2015**, *1*. [CrossRef]

122. Im, G.I.; Shin, Y.W.; Lee, K.B. Do adipose tissue-derived mesenchymal stem cells have the same osteogenic and chondrogenic potential as bone marrow-derived cells? *Osteoarthr. Cartil.* **2005**, *13*, 845–853. [CrossRef] [PubMed]

123. Worster, A.A.; Brower-Toland, B.D.; Fortier, L.A.; Bent, S.J.; Williams, J.; Nixon, A.J. Chondrocytic differentiation of mesenchymal stem cells sequentially exposed to transforming growth factor-β1 in monolayer and insulin-like growth factor-I in a three-dimensional matrix. *J. Orthop. Res.* **2001**, *19*, 738–749. [CrossRef]

124. Catelas, I.; Sese, N.; Wu, B.M.; Dunn, J.C.; Helgerson, S.; Tawil, B. Human mesenchymal stem cell proliferation and osteogenic differentiation in fibrin gels in vitro. *Tissue Eng.* **2006**, *12*, 2385–2396. [CrossRef] [PubMed]

125. Gurevich, O.; Vexler, A.; Marx, G.; Prigozhina, T.; Levdansky, L.; Slavin, S.; Shimeliovich, I.; Gorodetsky, R. Fibrin microbeads for isolating and growing bone marrow-derived progenitor cells capable of forming bone tissue. *Tissue Eng.* **2002**, *8*, 661–672. [CrossRef] [PubMed]

126. Detamore, M.S.; Athanasiou, K.A. Motivation, characterization, and strategy for tissue engineering the temporomandibular joint disc. *Tissue Eng.* **2003**, *9*, 1065–1087. [CrossRef] [PubMed]

127. Almarza, A.J.; Athanasiou, K.A. Evaluation of three growth factors in combinations of two for temporomandibular joint disc tissue engineering. *Arch. Oral Biol.* **2006**, *51*, 215–221. [CrossRef] [PubMed]

128. Detamore, M.S.; Athanasiou, K.A. Evaluation of three growth factors for TMJ disc tissue engineering. *Ann. Biomed. Eng.* **2005**, *33*, 383–390. [CrossRef] [PubMed]

129. Su, X.; Bao, G.; Kang, H. Effects of basic fibroblast growth factor on bone marrow mesenchymal stem cell differentiation into temporomandibular joint disc cells. *Sheng Wu Yi Xue Gong Cheng Xue Za Zhi* **2012**, *29*, 732–736. [PubMed]

130. Kang, H.; Bi, Y.D.; Li, Z.Q.; Qi, M.Y.; Peng, E.M. Effect of transforming growth factor β(1) and insulin-like growth factor-I on extracelluar matrix synthesis of self-assembled constructs of goat temporomandibular joint disc. *Zhonghua Kou Qiang Yi Xue Za Zhi* **2011**, *46*, 541–546. [CrossRef] [PubMed]

131. Fortier, L.A.; Lust, G.; Mohammed, H.O.; Nixon, A.J. Coordinate upregulation of cartilage matrix synthesis in fibrin cultures supplemented with exogenous insulin-like growth factor-I. *J. Orthop. Res.* **1999**, *17*, 467–474. [CrossRef] [PubMed]

132. Sah, R.L.; Chen, A.C.; Grodzinsky, A.J.; Trippel, S.B. Differential effects of bFGF and IGF-I on matrix metabolism in calf and adult bovine cartilage explants. *Arch. Biochem. Biophys.* **1994**, *308*, 137–147. [CrossRef] [PubMed]

133. Kalpakci, K.N.; Kim, E.J.; Athanasiou, K.A. Assessment of growth factor treatment on fibrochondrocyte and chondrocyte co-cultures for TMJ fibrocartilage engineering. *Acta Biomater.* **2011**, *7*, 1710–1718. [CrossRef] [PubMed]

134. Blunk, T.; Sieminski, A.L.; Gooch, K.J.; Courter, D.L.; Hollander, A.P.; Nahir, A.M.; Langer, R.; Vunjak-Novakovic, G.; Freed, L.E. Differential effects of growth factors on tissue-engineered cartilage. *Tissue Eng.* **2002**, *8*, 73–84. [CrossRef] [PubMed]

135. Jiao, Y.; Wang, D.; Han, W.L. Effects of various growth factors on human mandibular condylar cartilage cell proliferation. *Zhonghua Kou Qiang Yi Xue Za Zhi* **2000**, *35*, 346–349. [PubMed]

136. Hanaoka, K.; Tanaka, E.; Takata, T.; Miyauchi, M.; Aoyama, J.; Kawai, N.; Dalla-Bona, D.A.; Yamano, E.; Tanne, K. Platelet-derived growth factor enhances proliferation and matrix synthesis of temporomandibular joint disc-derived cells. *Angle Orthod.* **2006**, *76*, 486–492. [CrossRef] [PubMed]

137. Jazayeri, H.E.; Tahriri, M.; Razavi, M.; Khoshroo, K.; Fahimipour, F.; Dashtimoghadam, E.; Almeida, L.; Tayebi, L. A current overview of materials and strategies for potential use in maxillofacial tissue regeneration. *Mater. Sci. Eng. C Mater. Biol. Appl.* **2017**, *70*, 913–929. [CrossRef] [PubMed]

138. Tollemar, V.; Collier, Z.J.; Mohammed, M.K.; Lee, M.J.; Ameer, G.A.; Reid, R.R. Stem cells, growth factors and scaffolds in craniofacial regenerative medicine. *Genes Dis.* **2016**, *3*, 56–71. [CrossRef] [PubMed]

139. Amini, A.R.; Laurencin, C.T.; Nukavarapu, S.P. Bone tissue engineering: Recent advances and challenges. *Crit. Rev. Biomed. Eng.* **2012**, *40*, 363–408. [CrossRef] [PubMed]

140. Zisch, A.H.; Lutolf, M.P.; Ehrbar, M.; Raeber, G.P.; Rizzi, S.C.; Davies, N.; Schmökel, H.; Bezuidenhout, D.; Djonov, V.; Zilla, P.; et al. Cell-demanded release of VEGF from synthetic, biointeractive cell ingrowth matrices for vascularized tissue growth. *FASEB J.* **2003**, *17*, 2260–2262. [CrossRef] [PubMed]

141. Scheller, E.L.; Krebsbach, P.H. Gene therapy: Design and prospects for craniofacial regeneration. *J. Dent. Res.* **2009**, *88*, 585–596. [CrossRef] [PubMed]

142. Scheller, E.L.; Villa-Diaz, L.G.; Krebsbach, P.H. Gene therapy: Implications for craniofacial regeneration. *J. Craniofac. Surg.* **2012**, *23*, 333–337. [CrossRef] [PubMed]

143. Zhang, X.; Kovtun, A.; Mendoza-Palomares, C.; Oulad-Abdelghani, M.; Fioretti, F.; Rinckenbach, S.; Mainard, D.; Epple, M.; Benkirane-Jessel, N. SiRNA-loaded multi-shell nanoparticles incorporated into a multilayered film as a reservoir for gene silencing. *Biomaterials* **2010**, *31*, 6013–6028. [CrossRef] [PubMed]

144. Yoo, H.S.; Kim, T.G.; Park, T.G. Surface-functionalized electrospun nanofibers for tissue engineering and drug delivery. *Adv. Drug Deliv. Rev.* **2009**, *61*, 1033–1042. [CrossRef] [PubMed]

145. Huang, Z.M.; He, C.L.; Yang, A.; Zhang, Y.; Han, X.J.; Yin, J.; Wu, Q. Encapsulating drugs in biodegradable ultrafine fibers through co-axial electrospinning. *J. Biomed. Mater. Res. A* **2006**, *77*, 169–179. [CrossRef] [PubMed]

146. Park, C.H.; Kim, K.H.; Lee, J.C.; Lee, J. In-situ nanofabrication via electrohydrodynamic jetting of countercharged nozzles. *Polym. Bull.* **2008**, *61*, 521–528. [CrossRef]

147. Ferrand, A.; Eap, S.; Richert, L.; Lemoine, S.; Kalaskar, D.; Demoustier-Champagne, S.; Atmani, H.; Mély, Y.; Fioretti, F.; Schlatter, G.; et al. Osteogenetic properties of electrospun nanofibrous PCL scaffolds equipped with chitosan-based nanoreservoirs of growth factors. *Macromol. Biosci.* **2014**, *14*, 45–55. [CrossRef] [PubMed]

148. Li, G.; Zhang, T.; Li, M.; Fu, N.; Fu, Y.; Ba, K.; Deng, S.; Jiang, Y.; Hu, J.; Peng, Q.; et al. Electrospun fibers for dental and craniofacial applications. *Curr. Stem Cell Res. Ther.* **2014**, *9*, 187–195. [CrossRef] [PubMed]

149. Eap, S.; Keller, L.; Schiavi, J.; Huck, O.; Jacomine, L.; Fioretti, F.; Gauthier, C.; Sebastian, V.; Schwinté, P.; Benkirane-Jessel, N. A living thick nanofibrous implant bifunctionalized with active growth factor and stem cells for bone regeneration. *Int. J. Nanomed.* **2015**, *10*, 1061–1075. [CrossRef]

150. Strub, M.; Van Bellinghen, X.; Idoux-Gillet, Y.; Fioretti, F.; Bornert, F.; Benkirane-Jessel, N.; Kuchler-Bopp, S.; Clauss, F. Maxillary bone regeneration based on nanoreservoirs functionalized ε-polycaprolactone biomembranes in a mouse model of jaw bone lesion. *BioMed Res. Int.* **2017**, in press.

151. Haddad, I.K. Temporomandibular joint osteoarthrosis. Histopathological study of the effects of intra-articular injection of triamcinolone acetonide. *Saudi Med. J.* **2000**, *21*, 675–679. [PubMed]

152. Iida, K.; Kurita, K.; Tange, K.; Yoshida, K. Necrosis of the articular tubercle after repeated injections of sodium hyaluronate in the temporomandibular joint: A case report. *Int. J. Oral Maxillofac. Surg.* **1998**, *27*, 278–279. [CrossRef]

153. Mountziaris, P.M.; Kramer, P.R.; Mikos, A.G. Emerging intra-articular drug delivery systems for the temporomandibular joint. *Methods* **2009**, *47*, 134–140. [CrossRef] [PubMed]

154. Mountziaris, P.M.; Sing, D.C.; Mikos, A.G.; Kramer, P.R. Intra-articular microparticles for drug delivery to the TMJ. *J. Dent. Res.* **2010**, *89*, 1039–1044. [CrossRef] [PubMed]

155. Mountziaris, P.M.; Sing, D.C.; Chew, S.A.; Tzouanas, S.N.; Lehman, E.D.; Kasper, F.K.; Mikos, A.G. Controlled release of anti-inflammatory siRNA from biodegradable polymeric microparticles intended for intra-articular delivery to the temporomandibular joint. *Pharm. Res.* **2011**, *28*, 1370–1384. [CrossRef] [PubMed]

156. Brady, M.A.; Sivananthan, S.; Mudera, V.; Liu, Q.; Wiltfang, J.; Warnke, P.H. The primordium of a biological joint replacement: Coupling of two stem cell pathways in biphasic ultrarapid compressed gel niches. *J. Craniomaxillofac. Surg.* **2011**, *39*, 380–386. [CrossRef] [PubMed]

157. Abou Neel, E.A.; Chrzanowski, W.; Salih, V.M.; Kim, H.W.; Knowles, J.C. Tissue engineering in dentistry. *J. Dent.* **2014**, *42*, 915–928. [CrossRef] [PubMed]

158. Zhu, S.; Zhang, B.; Man, C.; Ma, Y.; Hu, J. NEL-like molecule-1-modified bone marrow mesenchymal stem cells/poly lactic-co-glycolic acid composite improves repair of large osteochondral defects in mandibular condyle. *Osteoarthr. Cartil.* **2011**, *19*, 743–750. [CrossRef] [PubMed]

159. Weng, Y.; Cao, Y.; Silva, C.A.; Vacanti, M.P.; Vacanti, C.A. Tissue-engineered composites of bone and cartilage for mandible condylar reconstruction. *J. Oral Maxillofac. Surg.* **2001**, *59*, 185–190. [CrossRef] [PubMed]

160. Dormer, N.H.; Busaidy, K.; Berkland, C.J.; Detamore, M.S. Osteochondral interface regeneration of rabbit mandibular condyle with bioactive signal gradients. *J. Oral Maxillofac. Surg.* **2011**, *69*, e50–e57. [CrossRef] [PubMed]

161. Keller, L.; Wagner, Q.; Schwinté, P.; Benkirane-Jessel, N. Double compartmented and hybrid implant outfitted with well-organized 3D stem cells for osteochondral regenerative nanomedicine. *Nanomedicine* **2015**, *10*, 2833–2845. [CrossRef] [PubMed]

162. Abukawa, H.; Terai, H.; Hannouche, D.; Vacanti, J.P.; Kaban, L.B.; Troulis, M.J. Formation of a mandibular condyle in vitro by tissue engineering. *J. Oral Maxillofac. Surg.* **2003**, *61*, 94–100. [CrossRef] [PubMed]

163. Girdler, N.M. In vitro synthesis and characterization of a cartilaginous meniscus grown from isolated temporomandibular chondroprogenitor cells. *Scand. J. Rheumatol.* **1998**, *27*, 446–453. [CrossRef] [PubMed]

164. Alhadlaq, A.; Elisseeff, J.H.; Hong, L.; Williams, C.G.; Caplan, A.I.; Sharma, B.; Kopher, R.A.; Tomkoria, S.; Lennon, D.P.; Lopez, A.; et al. Adult stem cell driven genesis of human-shaped articular condyle. *Ann. Biomed. Eng.* **2004**, *32*, 911–923. [CrossRef] [PubMed]

165. Tarafder, S.; Koch, A.; Jun, Y.; Chou, C.; Awadallah, M.R.; Lee, C.H. Micro-precise spatiotemporal delivery system embedded in 3D printing for complex tissue regeneration. *Biofabrication* **2016**, *8*, 025003. [CrossRef] [PubMed]

166. Ackland, D.C.; Robinson, D.; Redhead, M.; Lee, P.V.S.; Moskaljuk, A.; Dimitroulis, G. A personalized 3D-printed prosthetic joint replacement for the human temporomandibular joint: From implant design to implantation. *J. Mech. Behav. Biomed. Mater.* **2017**, *69*, 404–411. [CrossRef] [PubMed]

167. Wang, Y.; Zhang, Y.; Zhang, Z.; Li, X.; Pan, J.; Li, J. reconstruction of mandibular contour using individualized high-density porous polyethylene (Medpor®) implants under the guidance of virtual surgical planning and 3D-printed surgical templates. *Aesthet. Plast. Surg.* **2017**. [CrossRef] [PubMed]

168. Ryu, J.; Cho, J.; Kim, H.M. Bilateral temporomandibular joint replacement using computer-assisted surgical simulation and three-dimensional printing. *J. Craniofac. Surg.* **2016**, *27*, e450–e452. [CrossRef] [PubMed]

169. Green, J.M.; Lawson, S.T.; Liacouras, P.C.; Wise, E.M.; Gentile, M.A.; Grant, G.T. Custom anatomical 3D spacer for temporomandibular joint resection and reconstruction. *Craniomaxillofac. Trauma Reconstr.* **2016**, *9*, 82–87. [CrossRef] [PubMed]

170. Levine, J.P.; Patel, A.; Saadeh, P.B.; Hirsch, D.L. Computer-aided design and manufacturing in craniomaxillofacial surgery: The new state of the art. *J. Craniofac. Surg.* **2012**, *23*, 288–293. [CrossRef] [PubMed]

171. Chen, V.J.; Smith, L.A.; Ma, P.X. Bone regeneration on computer-designed nano-fibrous scaffolds. *Biomaterials* **2006**, *27*, 3973–3979. [CrossRef] [PubMed]

172. Townsend-Nicholson, A.; Jayasinghe, S.N. Cell electrospinning: A unique biotechnique for encapsulating living organisms for generating active biological microthreads/scaffolds. *Biomacromolecules* **2006**, *7*, 3364–3369. [CrossRef] [PubMed]

173. Jayasinghe, S.N. Cell electrospinning: A novel tool for functionalising fibres, scaffolds and membranes with living cells and other advanced materials for regenerative biology and medicine. *Analyst* **2013**, *138*, 2215–2223. [CrossRef] [PubMed]

174. Jessop, Z.M.; Javed, M.; Otto, I.A.; Combellack, E.J.; Morgan, S.; Breugem, C.C.; Archer, C.W.; Khan, I.M.; Lineaweaver, W.C.; Kon, M.; et al. Combining regenerative medicine strategies to provide durable reconstructive options: Auricular cartilage tissue engineering. *Stem Cell Res Ther.* **2016**, *7*, 19. [CrossRef] [PubMed]

175. Li, J.; Hsu, Y.; Luo, E.; Khadka, A.; Hu, J. Computer-aided design and manufacturing and rapid prototyped nanoscale hydroxyapatite/polyamide (n-HA/PA) construction for condylar defect caused by mandibular angle ostectomy. *Aesthet. Plast. Surg.* **2011**, *35*, 636–640. [CrossRef] [PubMed]

176. MacBarb, R.F.; Paschos, N.K.; Abeug, R.; Makris, E.A.; Hu, J.C.; Athanasiou, K.A. Passive strain-induced matrix synthesis and organization in shape-specific, cartilaginous neotissues. *Tissue Eng. Part A* **2014**, *20*, 3290–3302. [CrossRef] [PubMed]

177. Legemate, K.; Tarafder, S.; Jun, Y.; Lee, C.H. Engineering human TMJ discs with protein-releasing 3D-printed scaffolds. *J. Dent. Res.* **2016**, *95*, 800–807. [CrossRef] [PubMed]

MDPI